

**Optical Spectroscopy with Very Large Telescope:
Instrumental Development and Data Interpretation**
The case of the Rocky-Planets Finder ESPRESSO and Spectral
Characterization of BL Lac Objects



Marco Landoni

Department of Mathematics and Physics

University of Insubria - Como

A thesis submitted for the degree of
Doctor of Philosophy in Astronomy and Astrophysics

26th November 2013

Supervisor: Dr. Filippo M. Zerbi
co-Supervisors: Prof. Aldo Treves
Prof. Renato Falomo

*The sudden liberation of our thinking on the very structure of the physical world
was overwhelming*

Chien-Shiung Wu on ^{60}Co β -decay **P** violation experiment.

Abstract

This PhD thesis is focused on one of the main research area in modern Astrophysics: the spectroscopy. Within the current framework of observational astronomy, I carried out the Thesis aiming at the figure of Instrument Scientist who acts as a junction between astronomer and design engineers joining the science and technology in order to contribute to a more consolidated and optimised design of new instrumentations for large experiments.

For this reason, in this Thesis I will present two main parts of my PhD activities that have characterised my entire doctoral training. In particular, I will first introduce ESPRESSO, *the Echelle SPectrograph for Rocky Exoplanet and Stable Spectroscopic Observations*, which will be a new generation extra stable spectrograph at the European Southern Observatory (ESO) Very Large Telescope (VLT). ESPRESSO will be a spectrograph mainly optimised for finding rocky planet orbiting main sequence G stars in the habitable zone through the Radial Velocity (RV) method. I will outline my contribution to ESPRESSO in **Chapter 2** where I illustrate simulations on the expected performances of the detectors used by a main part of the instrument: the Front End Unit. This subsystem is responsible to stabilise the field and pupil of ESPRESSO through active optics and to collect the light from the four telescope and inject it through fiber feeding the spectrograph. I also outline the design of the Exposure Meter of the instrument which is in charge to continuously monitoring the exposure in order to evaluate a critical value, called Mean Time of Exposure (MTE), which is used in order to correct the measured Radial Velocity for the relative Earth motion at the time of observation. For the first time, the exposure will be monitored chromatically allowing a better characterisation of the

behaviour of the MTE and of the overall observation simultaneously. In **Chapter 3** I focus on pure astrophysical research based on spectroscopy of a particular class of Active Galactic Nuclei: the BL Lacertae Objects. These objects are characterised by a strong non-thermal emission which arises from the accreting nucleus. For this reason, spectral features (when present) are extremely diluted making the determination of their redshifts a challenging task. With the adoption of FORS2 spectrograph, in low resolution, at 10mt class VLT I completed a survey of these objects started few years ago and I derived from the complete sample a conspicuous number of properties of the class, including the characterisation of their line-of-sight Mg II absorber systems. Moreover, I will outline the results obtained from observation of a small subsample of strong FERMI γ -rays (and in certain cases VHE emitters) source with ESO X-SHOOTER which combines medium resolution ($R \sim 4000$) and large spectral range. In particular, for the source PKS 0048-097 the determination of its redshift for the first time allowed to deeply investigate its Spectral Energy Distribution and the close environment of the object. The spectra of the other sources in the sample are also illustrated and explicated for particular interesting objects.

Contents

Contents	v
List of Figures	ix
Nomenclature	xviii
1 Introduction	1
2 ESPRESSO: the Echelle SPectrograph for Rocky Exoplanet and Stable Spectroscopic Observations. Design of the Front End and Exposure Meter subsystems	5
2.1 Introduction	5
2.1.1 Exoplanets detection main techniques: Transit and Radial Velocity methods	6
2.1.1.1 An example of planet detection through radial velocity method.	10
2.1.2 ESPRESSO: a general overview of the instrument	12
2.1.2.1 Design concept	12
2.1.2.2 Wavelength calibration	14
2.1.2.3 Coudé train and Front End subsystem - feeding the spectrograph with scientific lights	14
2.1.2.4 Foreseen ESPRESSO mode	15
2.1.2.5 A scientific Pandora box	17
2.2 State of the art at Paranal: Test campaign activities and data analysis	19
2.2.1 Introduction	19

2.2.2	Setup configuration @VLT	20
2.2.2.1	Temperature and wind measurement setup	20
2.2.2.2	PSF and image stability through the tunnels	22
2.2.3	Data analysys	24
2.2.3.1	PSF model	24
2.2.4	Results	27
2.2.4.1	Image quality and relationship with Paranal environment	28
2.2.5	Conclusions	33
2.3	Front-End Subsystem: stabilisation of the field	34
2.3.1	Introduction	34
2.3.2	CCD detector simulation and radiometry	35
2.3.2.1	Determination of optical parameters	37
2.3.3	Radiometric quantities	37
2.3.4	Pinhole slit simulation	40
2.3.5	The algorithm architecture	41
2.3.5.1	Phase (1) - CCD generation	41
2.3.5.2	Phase (2) - Guiding algorithm	42
2.3.6	CCDs under evaluation	43
2.3.6.1	Bright objects cases - Results	47
2.3.6.2	Faint object cases - Results	49
2.3.6.3	Parametric evaluation for faint object guiding	52
2.4	Design of the Exposure Meter subsystem	58
2.4.1	General Introduction	58
2.4.2	Simulations on the expected performances	61
2.4.2.1	Flux received and star model	65
2.4.2.2	Sky model	66
2.4.2.3	$\frac{dp}{d\lambda}$ dispersion function	66
2.4.2.4	PSF model of the Exposure Meter optics	67
2.4.2.5	Fiber image	67
2.4.2.6	Image on the focal plane	69
2.4.2.7	Slit loss and dependence on seeing	69
2.4.2.8	CCD configuration	70

2.4.2.9	Detector simulation for performances evaluation . . .	70
2.4.3	Simulations results and expected performances	72
2.4.3.1	First scientific case - 10 cm s ⁻¹ RV accuracy	76
2.4.3.2	Second scientific case - 1 m s ⁻¹ RV accuracy	80
2.4.3.3	Third scientific case - 10 m s ⁻¹ RV accuracy	82
2.4.3.4	Multimode setup - An introduction to 5 m s ⁻¹ RV accuracy case	83
3	Application of spectroscopy to BL Lacertae objects: from low to medium-high resolution. The case of FORS2 and X-Shooter	85
3.1	An introduction to AGN	85
3.1.1	What is an AGN ?	85
3.1.2	Emission mechanism - Thermal emission from accretion disk, broad line and narrow line regions	88
3.1.2.1	Broad line region	89
3.1.2.2	The narrow-line region	94
3.2	The case of BL Lacertae objects	96
3.2.1	Characteristic of the BL Lacs optical spectra	97
3.3	Observing BL Lacs with FORS2@ESO-VLT. The completion of the sample	98
3.3.1	Introduction	98
3.3.2	The sample	100
3.3.3	The complete BLL@FORS2 sample observed at FORS2-ESO VLT	103
3.3.4	Immediate results	108
3.3.4.1	The BL Lac mean spectrum	125
3.3.5	The relativistic optical beaming factor δ	127
3.3.6	Statistical properties of the whole sample	131
3.3.7	Intervening Mg II system on BL Lac objects observed with FORS2	132
3.4	Medium resolution spectroscopy of bright BL Lac objects with ESO- XSHOOTER	134
3.4.1	Introduction	134

3.4.2	The sample, observation and data reduction	135
3.4.3	The case of FERMI γ -ray BL Lac PKS 0048-097 observed with XSHOOTER	136
3.4.3.1	Introduction	136
3.4.3.2	Spectral analysys	138
3.4.3.3	Intervening MgII and PKS 0048-097 close environ- ment	141
3.4.3.4	Spectral Energy Distribution of PKS 0048-097 . . .	143
3.4.4	Other objects observed. Preliminary results	145
3.4.4.1	Introduction	145
3.4.4.2	The spectra and basic properties	145
3.4.4.3	The peculiar case of MH 2136-428	159
3.5	Future perspective. Spectroscopy of BL Lacs in the E-ELT era . . .	164
3.5.1	Introduction	164
3.5.2	Simulation of BL Lac spectra observed by E-ELT	164
4	ESPRESSO: Foreseen science and outlook	169
5	Conclusions	173
Appendix A	- List of publication	175
References		185

List of Figures

2.1	Transit of a planet detected on the host star [Ribas et al., 2008]. . .	6
2.2	Pictorial representation of the transit method.	7
2.3	Pictorial representation of a planet around a pulsar detected with the Pulsar Timing technique.	8
2.4	An example of radial velocity plot versus time obtained after an observation campaign on the host star (freely taken from en.wikipedia.org Doppler Spectroscopy).	9
2.5	Radial velocity and planet mass limit detection as a function of distance from G2V solar like host star. Pepe et al 2013 in press. . .	12
2.6	Sketch of the ESPRESSO spectrograph optical layout [Spanò et al., 2012]	13
2.7	Coudè Train of ESPRESSO and optical path through the telescope and the tunnels [Cabral et al., 2012].	15
2.8	Top view of the Front-End and the arrival of the four UT beam at the CCL [Riva et al., 2012]	16
2.9	All-sky spatial dipole with the combined VLT (squares) and Keck (circles) α measurements from Webb et al. (2011). Triangles are measures in common to the two telescopes. The blue dashed line shows the equatorial region of the dipole.	18
2.10	Configuration for the proposed environmental tests.	20
2.11	Anemometer used for wind measurements.	21
2.12	Temperature data logger used for temperature measurements. . . .	21
2.13	Optical setup for the image quality measurement at the end side of the delay tunnel.	24

2.14	An example of the PSF of the laser beam recorded by the camera. Horizontal bars represent the area of interest for the full readout while vertical bar is the preliminary computation of the centroid performed by the onboard software of the camera.	25
2.15	An example of the PSF of the laser beam recorded by the camera after the application of gaussian PSF model. Courtesy: ESO Paranal (Document ESO: VLT-TRE-ESP-13520)	27
2.16	Image displacement acquired during the night between 12 and 13 of July 2011.	28
2.17	Comparison between image displacement and temperatures behavior. Wind line (solid blue) refers to the wind temperature at the level of the anemometer.	30
2.18	Correlation between temperature and the wind speed.	30
2.19	Image displacement acquired during the night between 13 and 14 of July 2011 (closed configuration)	31
2.20	Measured FWHM during the 12 to 13 night. Note that spikes are due to non-convergence of the fitting algorithm on bad recorded image.	32
2.21	Standard deviation of the Full Width at half maximum of the image on 10 minutes wide bins	32
2.22	Measured FWHM during the 13 to 14 night in closed ducts configuration. Note that spikes are due to non-convergence of the fitting algorithm on bad recorded image.	33
2.23	Subsampling of the spot position. Red dots are experimental data while the yellow ones are the subsample interpolation in order to better characterise the behaviour of the image displacement on the detector	36
2.24	Quantum Efficiency of a sample of three different TCCD and ESPRESSO System Efficiency (updated at Final Design Review (May 2013)). . .	38
2.25	CCD Sony ICX285 detector Quantum Efficiency. This detector is the baseline for the technical CCD for the ESPRESSO system. . . .	39
2.26	Simulation of a scientific object on the TCCD (no noises considered). . .	40
2.27	Scheme of the guiding algorithm	44

2.28	Workflow of the guiding algorithm. Integration time is computed according to the magnitude of the target and the neutral density filter installed in front of the camera. For instance, table 2.5 gives two general template cases.	45
2.29	Experimental data recorded in Paranal during the observational campaign in July 2011	46
2.30	Perturbations applied to all the configurations: X displacement (top), Y displacement (middle), Seeing variation (Down). The units of the displacement are linear and must be corrected recalling that they are recorder with a F/10 camera.	46
2.31	Simulation results on guiding an object with $m_v \sim 10$. Third and fourth panels show the residual left after the correction of the guiding system	48
2.32	An example of a simulated Front End technical CCD observing object with $m_v \sim 10$ for guiding.	49
2.33	Histograms of the error during a simulation on guiding bright objects. Left upper panel - Histogram of the error as recorded on Paranal on X axis. Right upper panel - Histogram of the error as recorded in Paranal on Y axis. Lower panels represent error after the application of the guiding algorithm	50
2.34	Simulation results on guiding an object with $m_v = 20$	53
2.35	Histograms of the residuals during a simulation on guiding faint objects. Panel legends are the same of Figure 2.33	54
2.36	Pictorial representation of the position of the spot with respect to the requirement (solid circle).	55
2.37	Results of the guiding algorithm performances against detector dark current magnification. The dark current in the legend is in units of $e^- px^{-1} s^{-1}$	55
2.38	RMS error on positioning against detector dark current magnification. The dark current in the legend is in units of $e^- px^{-1} s^{-1}$	56
2.39	Results of the guiding algorithm performances against QE degradation.	56
2.40	RMS error on positioning against QE degradation.	57

LIST OF FIGURES

2.41	ESPRESSO Exposure meter general overall schema.	62
2.42	ESPRESSO exposure meter 3D general view.	63
2.43	ESPRESSO Exposure meter overall efficiency (this curve also considers the whole efficiency of ESPRESSO and includes the Sony ICX 285 detector efficiency)	63
2.44	ESPRESSO Exposure meter light extraction schema.	64
2.45	ESPRESSO Exposure meter overall optical setup.	65
2.46	ESPRESSO Exposure meter ray tracing function. This function allows to known the absolute position (in mm respect to the centre of the CCD) of the image against λ with respect to the dispersion axis.	67
2.47	ESPRESSO Exposure meter PSF function against λ	68
2.48	ESPRESSO Exposure meter PSF function against λ in a pictorial representation.	68
2.49	Seeing vs slit efficiency curve adopted for simulations of the Exposure meter	70
2.50	Simulation of a spectrum obtained in the exposure meter for a M star of $m_v = 15$ assuming seeing of $\sim 1.00''$	73
2.51	Simulation for the exposure time vs magnitude in multiUT mode.	74
2.52	Simulation for the exposure time vs magnitude in singleUT mode.	74
2.53	Flow chart for the strategy adopted for the scientific simulation. Each simulation is repeated 100 times in order to investigate general statistical properties	75
2.54	ESPRESSO Exposure Meter channels	75
2.55	Behavior of the perturbation as seen on the CCD aboard the Exposure Meter	77
2.56	Behavior of the perturbation as seen on the CCD aboard the Exposure Meter	78
2.57	ESPRESSO Exposure Meter performance for 10cm/s goal with $m_v = 10$ with perturbations on the system or atmosphere	78
2.58	ESPRESSO Exposure Meter performances against a chromatic perturbation on the red part (cloud passing through)	80

LIST OF FIGURES

2.59	ESPRESSO Exposure Meter performance for 1m/s scientific goal. No perturbations are applied to the system	81
2.60	ESPRESSO Exposure Meter performance for 1m/s scientific goal with perturbations applied to the system	81
2.61	ESPRESSO Exposure Meter performance for 10 m/s scientific goal without perturbation	83
2.62	ESPRESSO Exposure Meter r.m.s. error on the three channel in multi-UT configuration	84
3.1	Effective potential of a test particle test with mass M in orbit around a Schwarchild Black Hole.	86
3.2	ISCO in function of the black hole spin a	87
3.3	Spectral energy distribution of the radio quiet QSO Mkn586. The UV bump due to thermal radiation generated by the accretion disk is clearly visible in the region 10^{15} - 10^{15} Hz.	88
3.4	Emission lines in the BLR superposed on different spectrum of QSOs with different absolute luminosities.	90
3.5	Multiepoch spectrum of the QSO NGC1097 where double peaked broad $H\alpha$ is clearly spot.	91
3.6	Narrow line region line profile asymmetry. This structure suggests flows of matter in the active nucleus [Lutz et al., 2000].	94
3.7	Narrow line region line spectrum (NIR and FIR) example from the AGN NGC1078 [Lutz et al., 2000].	95
3.8	Optical spectrum of the BL Lac object (2214-313) in which the fea- tures associated to its host galaxy are clearly detected ($z = 0.460$). See Landoni et al 2013, Sbarufatti et al 2009.	99
3.9	Flux calibrated (upper panel) and normalized (lower panel) spec- trum of 1553+113. The spectrum is lacking any intrinsic spectral feature. Absorptions from our galaxy ISM are labeled in green. The telluric absorption are marked. See Landoni et al 2013, Sbarufatti et al 2009.	99

3.10	Top panel: V-magnitude distribution of the observed BLLs in the sample selected adopting the criteria described in the text. Bottom: Fraction of objects of known redshift as a function of the magnitude. Further details and references are reported in Sbarufatti et al. [2006] and Landoni et al. [2013]	101
3.11	Spectra of BLLs sources. Top panel: flux calibrated spectra. Normalized spectra on bottom. Telluric bands are indicated by \oplus , spectral lines are marked by line identification, absorption features from interstellar medium of our galaxy are labeled by ISM, diffuse interstellar bands by DIB. The flux density is in units of 10^{-16} erg cm^{-2} s^{-1} \AA^{-1}	109
3.12	continued	110
3.13	continued	111
3.14	continued	112
3.15	continued	113
3.16	continued	114
3.17	continued	115
3.18	Spectra of QSOs or confirmed non-BLLs sources. Top panel: flux calibrated spectra. Normalized spectra on bottom. Telluric bands are indicated by \oplus , spectral lines are marked by line identification, absorption features from interstellar medium of our galaxy are labeled by ISM, diffuse interstellar bands by DIB. The flux density is in units of 10^{-16} erg cm^{-2} s^{-1} \AA^{-1}	116
3.19	continued	117
3.20	Spectral decomposition (rest frame) for the objects RBS 0337, MS 0622.5-5256, RX J1117.0+2014 and RBS 1899. The solid line shows the fitted spectrum while dots is the observed one.	120
3.21	Mean spectrum of BL Lac objects obtained combining the 23 objects of our campaign in which intrinsic spectral features are detected. The first panel reports the mean spectrum assuming for the continuum a power-law with index $\alpha = 0.90$ (which corresponds to the mean spectral index of the whole BL Lac sample). In the second panel normalised spectrum is shown.	125

3.22	Relation between the thermal disk continuum and MgII emission line luminosity (see Decarli et al. [2011] for details).	128
3.23	Optical beaming factor for the sources observed in the campaign. Red dashed line indicates the lower limit value calculated through Equation 3.27 assuming $z = 0.70$. Filled blue circle are the δ of bona-fide BL Lac objects with Mg II emission line while the open magenta circle are the beaming factor for other intermediate sources (classified as confirmed non-BL Lacs). Dotted line delimit the area of the EW- δ plane where the source are of intermediate nature between pure QSO($\delta \sim 1$)and BL Lacs($\delta >4$).	130
3.24	Incidence rate $\frac{dN}{dz}$ of Mg II absorbers with $0.6 \text{ \AA} < \text{EW } \lambda 2796 < 1.0 \text{ \AA}$ (top) and $\text{EW } \lambda 2796 > 1.0 \text{ \AA}$ (bottom). Figure from [Zhu and Ménard, 2013].	133
3.25	ESO XSHOOTER data reduction pipeline workflow schema (courtesy ESO XShooter User manual, Version 2.0)	137
3.26	PKS0048-097 overall mean spectrum. Atmospheric absorption are labelled by \oplus while calibration artefacts (detectable in the two-dimensional image of the spectrum) are marked with Δ . Emission lines above $\sim 3\text{-}\sigma$ confidence intervals of the SNR of the spectrum are marked with a single vertical line. The expected position of H β at $z = 0.635$ is marked with a dashed line.	139
3.27	PKS 0048-097 [OII] emission line at 6096 \AA , [O III] at 8189 \AA polluted by many resolved atmospheric absorption, and H α emission line at 10751 \AA . The vertical dotted lines represent the expected position of the three emission lines assuming the redshift $z = 0.635$, while the dashed one indicates the position of the barycenter. The red dotted line is the fit to the continuum.	140
3.28	PKS 0048-097 Mg II absorption features at $z = 0.154$ associated with a spiral galaxy at 50 Kpc projected distance from the BL Lac.	141

3.29	An R band image (FoV of $1.1' \times 1.1'$) of the BL Lac object PKS 0048-097 obtained with NTT and SUSI (Melnick et al) by Falomo [1996a] that shows its close environment. The spiral galaxy G1 (panel b) is the Mg II intervening system detected in the very blue part of the spectrum while the Galaxy G2 is a foreground object with respect to the absorption. The panel (a) in the figure shows a deconvolution of the image. The small object nearby PKS 0048-097 is most probably a background galaxy. Panel (c) shows the image of galaxy G1 after the model subtraction, while panel (d) reports the average radial brightness profile of galaxy G1.	142
3.30	PKS 0048-097 spectral energy distribution. The dashed line is the intrinsic SED model, while the solid line represent the flux absorbed by EBL interaction. Green points are from ASDC archive. Red points represent Swift UVOT and XRT data. FERMI spectra FGL1 and FGL2 are indicated, respectively, by blue and green points. The parameters of the model are $\gamma_{\min} = 500$, $\gamma_b = 8.5 \times 10^3$, and $\gamma_{\max} = 5 \times 10^5$, in addition to $n_1 = 2$, $n_2 = 4.1$, $B = 0.46$ G, $K = 3.7 \times 10^4$, $R = 8.2 \times 10^{15}$ cm, and $\delta = 25$. For descriptions of the observations and details of the model, see Tavecchio et al. [2010].	144
3.31	PKS 1553+113 UVB arm (normalised spectrum). Horizontal lines models the echelon orders of the instrument.	146
3.32	PKS 1553+113 VIS arm (normalised spectrum). Same legend of previous figure.	147
3.33	PKS 1553+113 NIR arm (normalised spectrum)	148
3.34	H1722+119 UVB arm (normalised spectrum)	149
3.35	H1722+119 VIS arm (normalised spectrum)	150
3.36	H1722+119 NIR arm (normalised spectrum)	151
3.37	MH2136-428 UVB arm (normalised spectrum)	152
3.38	MH2136-428 VIS arm (normalised spectrum)	153
3.39	MH2136-428 NIR arm (normalised spectrum)	154
3.40	PKS 2554-204 UVB arm (normalised spectrum)	155
3.41	PKS 2254-204 VIS arm (normalised spectrum)	156
3.42	PKS 2254-204 NIR arm (normalised spectrum)	157

3.43	H 2136-428 Ca II systems detected toward the line of sight. Galactic H and K Ca II bands are marked by the label ISM.	159
3.44	MH 2136-428 Ca II systems and ISM K Band de-blend fit. Dashed blue line and dotted red line are respectively the fit for deblending K ISM band and Ca II H band absorption system. The weighted reduced χ^2 for the model is 0.92 with 30 degrees of freedom. The r.m.s. overall error is 0.02.	160
3.45	MH 2136-428 close environment from ESO NTT. The Ca II intervening system detected in the XSHOOTER spectrum arises in the surrounding nebulosity of NGC 7097 at 100 Kpc projected distance from the background BL Lac. S1 and S2 are satellites of NGC 7097 at the same redshift.	161
3.46	MH 2136-428 HST Advanced Camera for Surveys (ACS) snapshot image. The integration time is 780s and adopted filter is F625W. The plate scale is 0.025'' per pixel and the FoV is about 15''x15''. The image clearly shows the presence of a faint galaxy at 3.2'' NW from the BL Lac (labelled as G1).	163
3.47	Aperture effect for different slit dimension projected on the sky. Details are reported in Sbarufatti et al. [2006]	165
3.48	First panel: simulation of a BL Lac spectrum with $V = 17$, $S/N = 2000$, $z = 0.40$ and $N/H = 100$. Aperture correction is 0.35 . Second panel: simulation for a BL Lac spectrum with $V = 20$, $S/N = 500$, $N/H = 40$, $z = 0.70$ and aperture correction of 0.50. For both cases the exposure time is 3600 s and the adopted slit is a 1'' x 1''. The efficiency of the spectrograph is considered similar to the VLT-FORS2. The solid black line is the BL Lac overall spectrum while dashed line is the power law associated to the non thermal emission. Blue dotted line is the superposed host galaxy template spectrum.	166

4.1	XSH-UVB spectrum simulation (SNR 25). Left panel: detection of Ly- α absorption with EW = 100 mÅ, b \sim 100 km s $^{-1}$. Center: Ly- α feature with EW = 200 mÅ, b \sim 50 km s $^{-1}$. Right: Ly- α system with EW = 50 mÅ, b \sim 100 km s $^{-1}$. Dotted line is the best fit.	171
-----	---	-----

Chapter 1

Introduction

The present Thesis work concerns *Observational Astronomy* as it is in recent time considered in the framework of state-of-the-art Astrophysics. In Observational Astronomy nowadays Science and Technology are intimately linked, in a certain sense in the same way Particle Physics Experiments have been carried out in the last decades. The examples of Very High Energy Astrophysics collaborations, such as MAGIC or VERITAS, where astronomers and engineers work strictly together at the same experiment sharing the knowledge of technology and science aimed at the same research target are noticeable, not to mention experiments in accelerators. Such a symbiosis clearly appears during the design of a new instrument (in particular during the conceptual phase) when the Top Level Requirement must be elaborated in order to assess the expected performance, feasibility and reliability of the new system. This phase requires a mutual translation of the requirements and the specifications between the point of view of the engineer and the frame of reference of the Astronomers.

There is a figure, namely the *Instrument Scientist*, who acts within large instrumental projects as the junction figure between astronomers, who think in terms of scientific results and expected performance, and design engineers who declinate the requirements in terms of construction parameters such as optical efficiency, mechanical stability, etc . In the concurrent conceptual design phase, when astronomers and engineers are called to work side by side, the *Instrument Scientist* is called to bridge the science and the technology so to ease the process and con-

tribute to a more solid and viable design.

The present Thesis summarises the Work I have done in my PhD path, i.e. in the last and conclusive phase of my University education. I found already in the early phases of this path the figure of the *Instrument Scientist* intriguing and interesting and I decided to invest my energies in forming myself along this guideline. For this reason, with the help of my Thesis Supervisors, I decided to keep a dual interest for purely scientific arguments on one side and technological development on the other side, both however in the common area of Astronomical Spectroscopy in order to make a synthesis possible.

In details, I first used low to medium/high resolution spectroscopy to study the properties of a population of BL Lacertae objects which are a particular class of Active Galactic Nuclei (AGN). This work is a part of even larger project, started few years ago, aimed at derive as much as possible redshifts using 10m class telescope equipped with modern instrumentations. Thanks to the availability of high quality FORS2 spectroscopic data, I first completed the ZBLLAC survey (<http://archive.oapd.inaf.it/zbllac/>) collecting the spectra of additional 33 sources deriving 5 new redshifts. Moreover, merging all data available from the complete survey I carried out the characterisation of intervening Mg II absorption systems toward the line of sight of BL Lacs and I studied the non thermal properties of the whole sample. The study of Mg II intervening system allowed to clear the fog around a long lived hint on the great excess of Mg II absorption lines in the spectra of BL Lacs. In fact, the survey showed that the number of intervening system is compatible with those expected from $\frac{dN}{dz}$ derived from QSOs spectra . During the PhD I have been trained also on the use and interpretation of data collected with the most recent X-SHOOTER spectrograph at ESO-VLT. In details, I reduced XSHOOTER spectra (collected in service mode) for 5 well known FERMI γ -rays sources deriving the redshift of PKS 0048-097 allowing the study its close environment, its spectral energy distribution from radio to γ -rays and the beaming factor.

From the point of view of advanced technology for astronomical instrumentation, I participated to the definition and design of two subsystem of the third generation VLT spectrograph ESPRESSO : the Front End Unit, which is responsible to collect the light from the telescope and feed the spectrograph through fiber, and

the Exposure Meter unit which is in charge to evaluate the mean time of exposure exploited for the correction of the radial velocity according to flux weighted time of exposure. In details, I have studied the properties of CCD detectors aimed at implementing detailed simulation of the various detectors in order to assess their characteristics suiting both astronomical and engineering requirements. Finally, in the design of the Front End Unit system I also contributed in the definition of the guiding algorithm system which is in charge to stabilise the field during the exposure in order reach 10 cm s^{-1} radial velocity accuracy.

Chapter 2

ESPRESSO: the Echelle SPectrograph for Rocky Exoplanet and Stable Spectroscopic Observations. Design of the Front End and Exposure Meter subsystems

2.1 Introduction

In this section the ESPRESSO instrument will be introduced. The design and definitions are updated at the Final Design Review process that took place on May 2013. Parts of this introduction is freely taken from ESO Messenger Article "ESPRESSO - An Echelle SPectrograph for Rocky Exoplanets Search and Stable Spectroscopic Observations" from Pepe et al 2013 (in press) of which I am a coauthor.

2.1.1 Exoplanets detection main techniques: Transit and Radial Velocity methods

One of the main and most intuitive technique for the detection of extra solar planets in orbit around their host stars is the so called **light curve** or **transit** method. In brief, the idea behind this kind of research is quite simple. Giving the apparent magnitude of the host star, when one of its planet passes in front of its surface the net flux received at the Earth is dimmed and its apparent magnitude raises.. The amount of changes in the detected flux is a function of the solid angle $d\Omega$ subtended by the planet and on the inclination $\sin(i)$ of the plane of the orbit and the observer (placed on the Earth). An example of this light curve is depicted in Figure 2.1 from [Ribas et al., 2008]. In this work, the author measured the radius of a confirmed \sim mass $5 M_{\oplus}$ planet orbiting around the star Gliese 436 (11h 42m 11s, $+26^{\circ} 42' 23''$) of m_v 11 . A pictorial representation of this kind of method for detecting exoplanets is reported in Figure 2.2.

One of the main advantages of this method is that it is able to infer the radius of the detected planet, assuming a model for the dimension of the host star. This last assumption partly holds true when dealing with main sequence stars, where equilibrium model and star equations are well known.

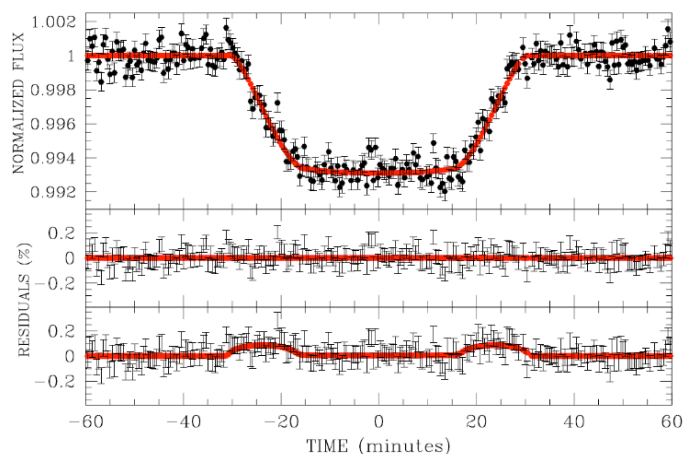


Figure 2.1: Transit of a planet detected on the host star [Ribas et al., 2008].

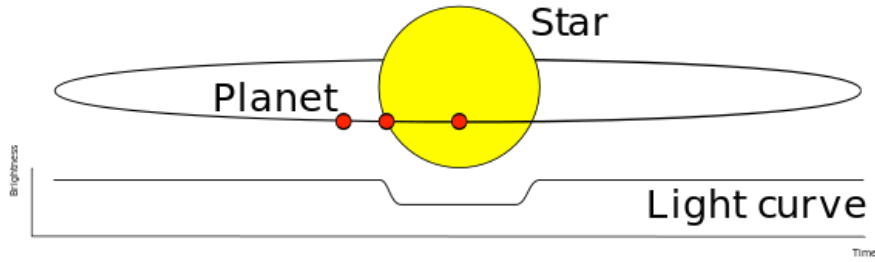


Figure 2.2: Pictorial representation of the transit method.

However, this photometry-based method has two major disadvantages. Planetary transits are only observable for planets whose orbits happen to be aligned with the observation site (telescope). As a rule of thumb, the probability of a planetary orbital plane being directly on the line-of-sight to a host star is the ratio of the diameter of the star to the diameter of the orbit (in small stars, the radius of the planet is also an important factor). About 10 percent of planets with small orbits have such alignment, and the fraction decreases for planets with larger orbits. However, adopting surveys able to study large areas of sky containing thousands or even hundreds of thousands of stars at once, transit surveys can in principle find extrasolar planets at a reasonable rate. For instance, GAIA [Lindgren and Perryman, 1996], Kepler [Koch et al., 1998] or CoRoT [Baglin et al., 2006] missions are or will be used for this kind of activity. The second issue that afflicts the transit method is a high rate of false detections. For instance, the detection of a planet orbiting a red giant branch star could be tricky. In fact, while planets around these stars are much more likely to transit due to the larger size, these transit signals are hard to separate from the main star's brightness light curve as red giants have frequent pulsations in brightness with a period of few hours to days. Red giant stars are also much more luminous and transiting planets block much smaller percentage of light coming from these stars. On the contrary, planets can completely occult a white dwarf which would be easily detectable from Earth. However, due to their small sizes, chance of a planet aligning such a stellar remnant is extremely small as explained before.

In the latter case, a successful method has been exploited for detection of plan-

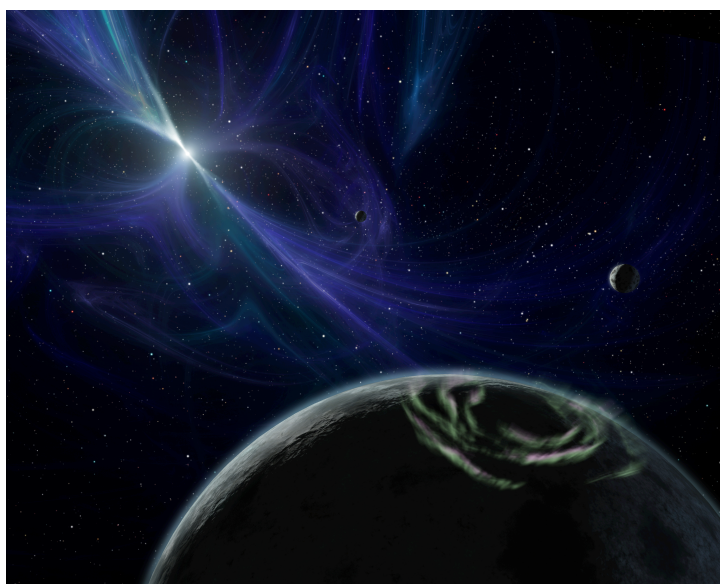


Figure 2.3: Pictorial representation of a planet around a pulsar detected with the Pulsar Timing technique.

ets around pulsars. In particular, since the intrinsic rotation period of a pulsar is so regular (P), slight anomalies in the timing of its observed radio pulses can be used to track the pulsar's motion. Like an ordinary star, a pulsar will move in its own small orbit if it has a planet. Calculations based on pulse-timing observations can then reveal the parameters of that orbit. For instance in 1992 Aleksander Wolszczan and Dale Frail used this method to discover planets around the pulsar PSR 1257+12. [Wolszczan and Frail, 1992]. The detection was quickly confirmed, making it the first confirmation of planets outside the Solar System.

Nevertheless, the state-of-the-art method able to detect planets orbiting around their host stars is the **radial velocity method** which is based essentially on the doppler spectroscopy (see e.g. [Baranne et al., 1979; Cochran and Hatzes, 1994; Mayor and Queloz, 1995; Mayor et al., 1992]). In brief, this method exploits the relative shifts of absorption lines in the star spectrum in order to derive a projected line of sight radial velocity that, combined with other observables, gives the detection and basic properties (such as the mass) of the orbiting planet. Giving a series of observations of the host star spectrum, periodic variations may be de-

tected measuring the wavelength of characteristic spectral absorption lines that increases and decreases regularly over a period of time. An example of this procedure usually yields a radial velocity plot that is reported in Figure 2.4.

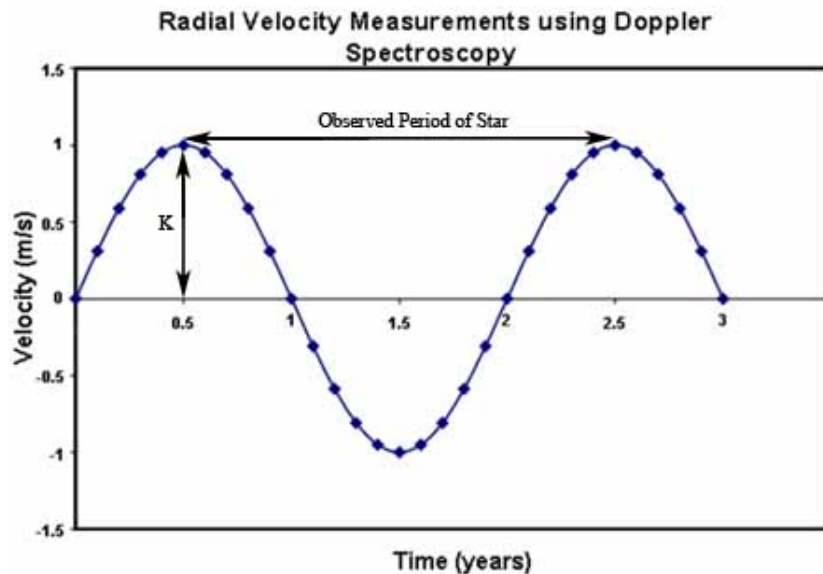


Figure 2.4: An example of radial velocity plot versus time obtained after an observation campaign on the host star (freely taken from en.wikipedia.org Doppler Spectroscopy).

The main problem with radial velocity method is that it can only measure velocity component along the line-of-sight, and so depends on a measurement (or estimate) of the inclination of the planet's orbit to finally determine the planet's mass. If the orbital plane of the planet happens to line up with the line-of-sight of the observer the measured variation in the star's radial velocity is the true value. In the case the orbital plane is tilted away from the line-of-sight, then the true effect of the planet on the motion of the star will be greater than the measured variation in the star's radial velocity, which is only the component along the line-of-sight. As a result, the planet's true mass will be higher than expected.

To correct for this effect, and so determine the true mass of an extrasolar planet, radial-velocity measurements can be combined with astrometric observations, which track the movement of the star across the plane of the sky, perpendicular to the line-of-sight. Astrometric measurements allows researchers to check whether ob-

jects that appear to be high mass planets are more likely to be stellar or sub-stellar objects.

2.1.1.1 An example of planet detection through radial velocity method.

In this example the mass of planet 51 Pegasi (b) orbiting its host star is derived. The radial velocity curve depicted in Figure 2.4 is derived using Doppler spectroscopy to observe the radial velocity of the star which is being orbited by the planet (in a circular orbit). This star velocity shows a periodic variance of ± 1 m s⁻¹ [Mayor and Queloz, 1995], suggesting an orbiting mass that is creating a gravitational pull on this star. From Kepler's third law of planetary motion, the observed period of the planet's orbit around the star (equal to the period of the observed variations in the star spectrum) can be used to determine the distance planet from the star (r) adopting the equation:

$$r^3 = \frac{GM_{star}}{4\pi^2} P_{star}^2 \quad (2.1)$$

where P_{star} is the star observed period and M_{star} is the mass of the host star itself, usually derived from stellar equilibrium models. The velocity of the planet around the star can be calculated using Newton's law of gravitation and the classical definition of centripetal force as expressed in the following equation

$$V_{Planet} = \sqrt{GM_{star}/r} \quad (2.2)$$

The mass of the orbiting planet can be found from its calculated velocity adopting the formula:

$$M_{planet} = \frac{M_{star} V_{star}}{V_{planet}} \quad (2.3)$$

where V_{star} is the velocity of parent star. The observed Doppler velocity, $K = V_{star} \sin(i)$, where i is the inclination of the planet's orbit to the line perpendicular to the line-of-sight. Thus, assuming a value for the inclination of the orbit and for the mass of the star, the observed changes in the radial velocity of the can be used to calculate the mass of the extrasolar planet. In Table 2.1 are given some details on physical observable of known planets orbiting a sun-like star (\sim G2V spectral

class and a mass of $\sim 1 M_{\odot}$).

Planet Mass	Distance (AU)	Radial velocity
Jupiter	1	28.4 m s ⁻¹
Jupiter	5	12.7 m s ⁻¹
Neptune	0.1	4.8 m s ⁻¹
Neptune	1	1.5 m s ⁻¹
Super-Earth (5 M _⊕)	0.1	1.4 m s ⁻¹
Alpha Centauri Bb (1.13 ± 0.09 M _⊕)	0.004	0.51 m s ⁻¹
Super-Earth (5 M _⊕)	1	0.45 m s ⁻¹
Earth	1	0.09 m s ⁻¹

Table 2.1: Planets physical observables and relative measurements.

Planet	Type	MA (AU)	Period	RV (m s ⁻¹)	Spectrograph:
51 Pegasi b	Hot Jupiter	0.05	4.23 d	55.9	First-generation
55 Cancri d	Gas giant	5.77	14.29 y	45.2	First-generation
Jupiter	Gas giant	5.20	11.86 y	12.4	First-generation
Gliese 581c	Super-Earth	0.07	12.92 d	3.18	Second-generation
Saturn	Gas giant	9.58	29.46 y	2.75	Second-generation
α Centauri Bb	Terrestrial	0.04	3.23 d	0.510	Second-generation
Neptune	Ice giant	30.10	164.79 y	0.281	Third-generation
Earth	Habitable	1.00	365.26 d	0.089	ESPRESSO
Pluto	Dwarf	39.26	246.04 y	0.00003	Not detectable

Table 2.2: Known planets and required spectrograph to detect through the radial velocity method (data taken from exoplanets.org).

As shown in Table 2.2 the needed of even more resolved spectrograph is becoming even more compelling in order to study the physical properties and environment of habitable terrestrial planets around main sequence solar like stars. This facts is also supported by Figure 2.5 that shows the correlation between the radial velocity sensitivity to minimum detectable planet mass, assuming a solar like G2V host star.

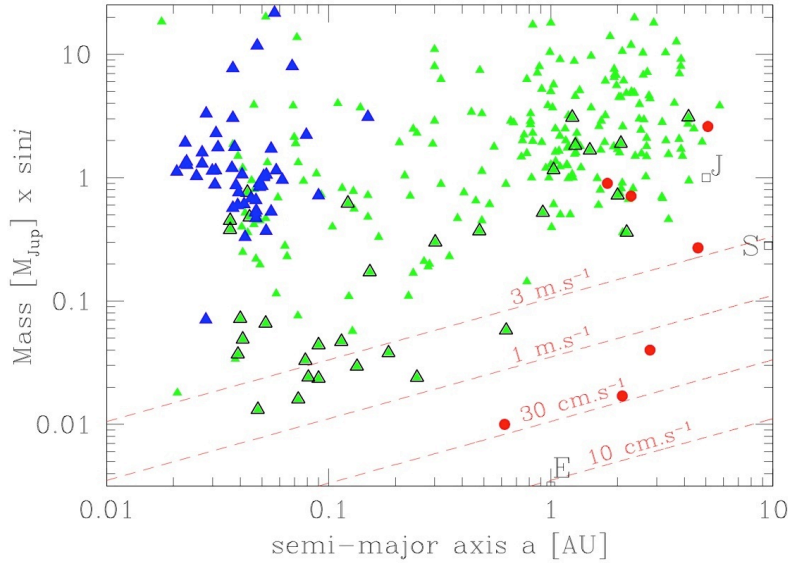


Figure 2.5: Radial velocity and planet mass limit detection as a function of distance from G2V solar like host star. Pepe et al 2013 in press.

2.1.2 ESPRESSO: a general overview of the instrument

2.1.2.1 Design concept

ESPRESSO [Pepe et al., 2010] is a fibre-fed, cross-dispersed, high-resolution, echelle spectrograph. The telescope light is fed to the instrument via a so-called Coudé-Train optical system and within the adoption of optical fibres. ESPRESSO is located in the Combined-Coudé Laboratory (incoherent focus) at the European Southern Observatory (ESO) Paranal site, where a front-end unit can combine the light from up to 4 Unit Telescopes (UT) of the Very Large Telescope (VLT). The target and sky light enter the instrument simultaneously through two separate fibres, which form together the slit of the spectrograph. The full spectrum of an observed scientific object has a wavelength coverage from 380 nm to 780 nm on two large 92 mm x 92 mm CCDs with 10- μ m pixels. A very simple sketch of the optical layout is shown in Figure 2.6 . The aimed precision of 10 cm/sec RMS requires measuring spectral line position changes of 2 nm (physical) in the CCD plane. In order to improve as much as we can the stability and thermal-expansion, the CCD package is made of Silicon Carbide. The package of the CCDs, the surrounding

mechanics and precision temperature control inside the cryostat head and its cooling system, as well as the thermal stability and the homogeneous dissipation of the heat locally produced in the CCDs during operation are of critical importance.

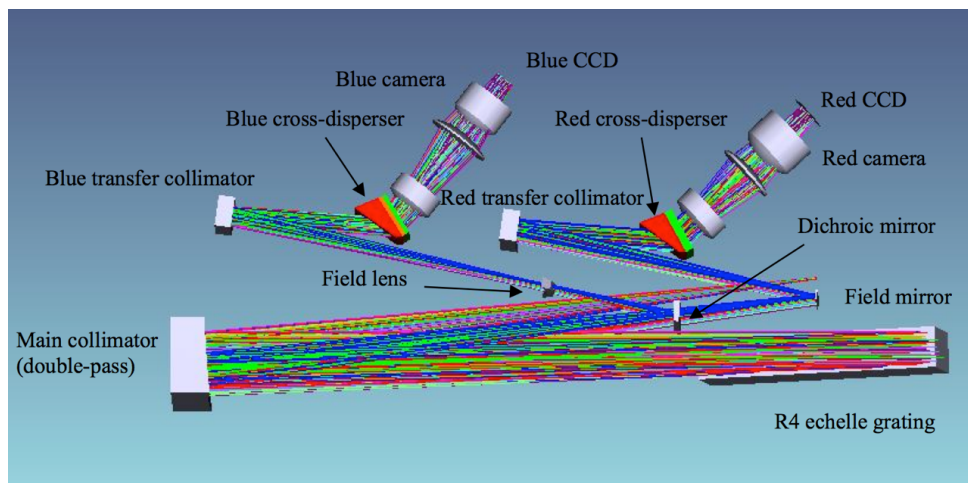


Figure 2.6: Sketch of the ESPRESSO spectrograph optical layout [Spanò et al., 2012]

ESPRESSO is designed to be an **ultra-stable** spectrograph capable of reaching radial-velocity precisions of the order of 10 cm s^{-1} , one order of magnitude better than its predecessor HARPS [Mayor et al., 2003]. This instrument is therefore designed with a totally fixed configuration and for the highest thermo-mechanical stability. The spectrograph optics is mounted in a tri-dimensional optical bench specifically designed to keep the optical system within the thermo-mechanical tolerances required for high-precision RV measurements. The bench is mounted in a vacuum vessel in which 10-5-mbar class vacuum is maintained during the entire duty cycle of the instrument. The temperature at the level of the optical system is required to be stable at the mK level in order to avoid both short-term drift and long-term mechanical instabilities. Such an ambitious requirement is obtained by locating the spectrograph in a multi-shell active thermal enclosure system. Each shell will improve the temperature stability by a factor 10, thus getting from typically Kelvin-level variations in the Combined Coudé Laboratory (CCL) down to mK stability inside the vacuum vessel and on the optical bench.

2.1.2.2 Wavelength calibration

All spectrograph observation through plates or modern CCDs need to be wavelength-calibrated in order to assign to each detector pixel the correct wavelength with a repeatability of the order of $\frac{\Delta\lambda}{\lambda} \sim 10^{-1}$. A necessary condition for this step is the availability of a suitable spectral wavelength reference. While in other spectrograph the wavelength calibration is assed through consolidated standard spectral lamps (such as thorium argon) none of them provide a spectrum sufficiently wide, rich, stable and uniform for this purpose. Therefore, the source for the calibration and simultaneous reference adopted for ESPRESSO is a Laser Frequency Comb (LFC) (see e.g. [Murphy et al., 2007]).

2.1.2.3 Coudè train and Front End subsystem - feeding the spectrograph with scientific lights

ESPRESSO is an instrument designed for the incoherent combined focus of the VLT. Although foreseen in the original plan, such a focus has never been implemented at the VLT. For this reason, the implementation of a Coudè Train is mandatory in order to materialise a focus in the CCL, 40 m far away from the UTs [Cabral et al., 2012]. Unlike any other instrument built so far, ESPRESSO will receive light from any of the four UTs. The light of the single UT scheduled to work with ESPRESSO is then fed into the spectrograph (1-UT mode). Alternatively, the combined light of all the UTs can be fed into ESPRESSO simultaneously (4-UT mode). The Coudè Train picks up the light with a prism at the level of the Nasmyth-B platform and roots the beam through the UT mechanical structure down to the UT Coudè room, and farther to the CCL along the existing incoherent light ducts (see Figure 2.7). The selected concept to convey the light of the telescope from the Nasmyth Focus (B) to the entrance of the tunnel in the Coudè Room (CR) below each UT unit is based on a set of 6 prisms (with some power). The light is directed from the UTs Coudè room towards the CCL using 2 big lenses. The beams from the four UTs converge into the CCL, where mode selection and beam conditioning is obtained thanks to the fore-optics of the Front-End subsystem [Riva et al., 2012].

The Front-End transports the beam received from the Coudè, once corrected for

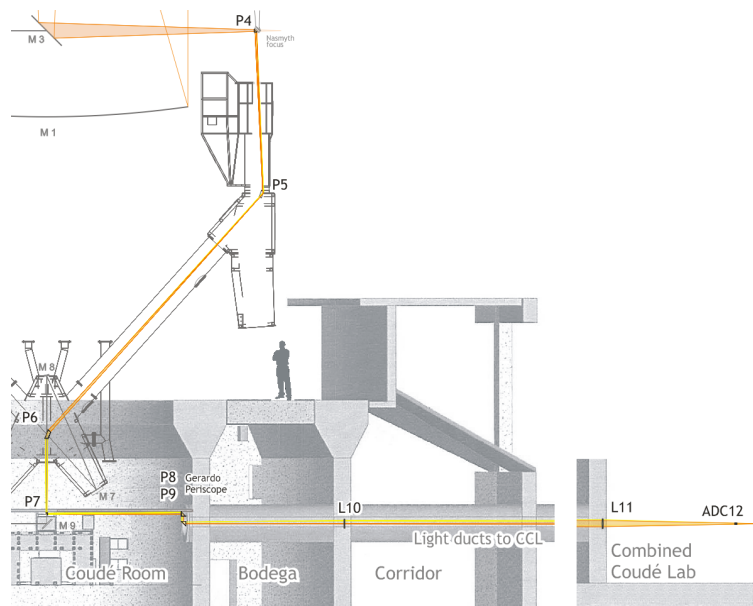


Figure 2.7: Coudé Train of ESPRESSO and optical path through the telescope and the tunnels [Cabral et al., 2012].

atmospheric dispersion by the ADC, to the common focal plane on which the heads of the fibre-to-spectrograph feeding are located. While performing such a beam conditioning the Front-End applies pupil and field stabilization (explained in details in this chapter of the Thesis). They are achieved via two independent control loops each composed of a technical camera and a tip-tilt stage. Another dedicated stage delivers a focusing function. In addition, the Front-End provides the mean to inject calibration light (white and spectral sources) into spectrograph fibre if and when needed. A top view of the Front-End arrangement is shown in Figure 2.8 .

2.1.2.4 Foreseen ESPRESSO mode

ESPRESSO will have three instrumental modes: singleHR, singleUHR and multiMR. Each mode will be available with two different detector read-out modes optimized for low and high-SNR measurements, respectively. In high-SNR (high-precision) measurements the second fiber will be fed with the simultaneous reference, while in the case of faint objects it shall be preferred to feed the second fiber

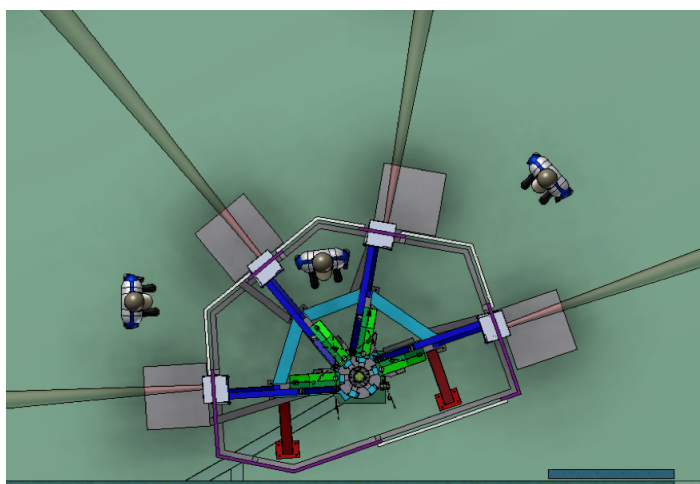


Figure 2.8: Top view of the Front-End and the arrival of the four UT beam at the CCL [Riva et al., 2012]

with sky light. The extreme precision, mandatory for the scientific tasks, will be obtained by adopting and improving concepts implemented in the state-of-the-art HARPS. The light is fed to the spectrograph by means of the front-end unit into optical fibres that scramble the light and provide excellent illumination stability to the spectrograph. The target fibre can be fed either with the light from the astronomical object or the calibration sources. The reference fibre will receive either sky light (faint source mode) or calibration light (bright source mode). In the latter case - the famous simultaneous-reference technique adopted in HARPS - it will be possible to track instrumental drifts down to the cm s^{-1} level. It is assumed that in this mode the measurement is photon-noise limited and detector read-out noise negligible. In the faint-source mode, instead, detector noise and sky background may become significant. In this case, the second fibre will allow to measure the sky background, while a slower read-out and high binning factor will reduce the detector noise. Table 2.3 summarise the expected performance of the overall instruments.

Parameter/Mode	singleHR	multiMR	singleUHR
Wavelength range	380-780 nm	380-780 nm	380-780 nm
Resolving power	134.000	59.000	225.000
Aperture on sky	1.0''	4x1.0''	0.5''
Spectral sampling (average)	4.5 pixels	5.5 pixels (bin x2)	2.5 pixels
Spatial sampling per slice	9.0 (4.5) pixels	5.5 pixels (bin x4)	5.0 pixels
Simultaneous reference	Yes (no sky)	Yes (no sky)	Yes (no sky)
Sky subtraction	Yes (no sim. ref.)	Yes (no sim. ref.)	Yes (no sim. ref.)
Total efficiency	11%	11%	5%
RV precision	< 10 cm s ⁻¹	~ 1 m s ⁻¹	< 10 cm s ⁻¹

Table 2.3: Summary of ESPRESSO’s instrument modes and corresponding performances.

2.1.2.5 A scientific Pandora box

Thanks to its high resolution and stability ESPRESSO will be able to investigate the presence and the basics physical parameters of terrestrial habitable exoplanets around main sequence star from F2V to M4V. In fact, ESPRESSO, being capable of achieving a precision of 10 cm s⁻¹ in terms of radial velocity, will be able to register the signals of Earth-like and massive Earths in the habitable zones (i.e., in orbits where water is retained in the liquid form on the planet surface) around nearby solar-type stars and stars smaller than the Sun. For instance, we recall that our planet pulls a velocity amplitude of 9 cm s⁻¹ onto the Sun, a G2V main sequence star.

Nevertheless, this kind of research is only a tiny fraction of the astrophysical science that this new instrument could be carry on. In particular, it could be possible to study (confirm or deny) the variation of the α fine structure constant and/or variation of the proton-electron ratio mass ratio (μ). At the present moment, Earth-based experiments have revealed no variation in their values. Hence its status as truly constants is amply justified. With the advent of 10-m class telescopes observations of spectral lines of intervening system in the spectra of distant quasars gave the first hints that the fine structure constant might change its value over time, being lower in the past by about 6 ppm (Webb et al., 1999; Murphy et al., 2004). The addition of other 143 VLT-UVES absorbers have revealed a 4- σ

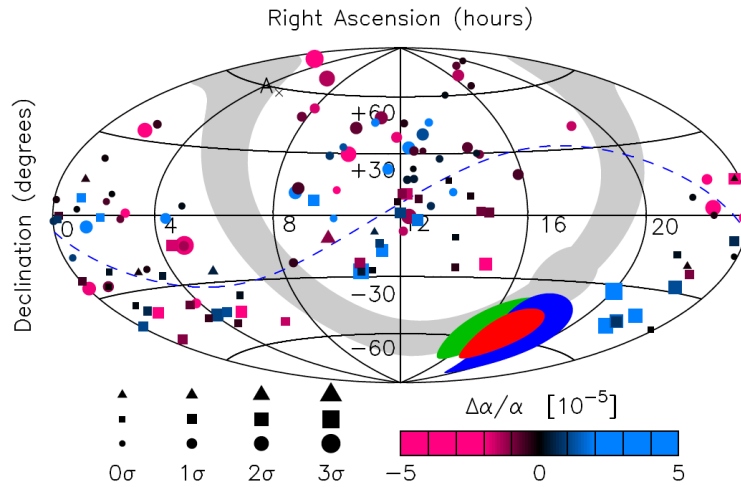


Figure 2.9: All-sky spatial dipole with the combined VLT (squares) and Keck (circles) α measurements from Webb et al. (2011). Triangles are measures in common to the two telescopes. The blue dashed line shows the equatorial region of the dipole.

evidence for a dipole-like variation in α across the sky at the 10 ppm level (King, 2012). This results is shown in Figure 2.9 .

Finally, it will be also possible to study the chemical composition of stars in local galaxies and the metal abundance in the so-called **metal poor stars**. The most metal poor stars in the Galaxy are probably the most ancient fossil records of the chemical composition and thus can provide clues on the pre-Galactic phases and on the stars which synthesized the first metals. Masses and yields of POP III stars can be inferred from the observed elemental ratios in the most metal poor stars [Heger and Woosley, 2010]. ESPRESSO, both in the 1-UT and 4-UT mode will be able to provide spectra with a sufficient resolution and signal to noise ratio for an reliable chemical analysis.

2.2 State of the art at Paranal: Test campaign activities and data analysis

2.2.1 Introduction

As reported in the general description of the instrument, the light coming from the 4 UTs of the VLT are combined in the Coudé Combined Laboratory through the Front End unit. However, the path that the light have to span in order to reach the CCL will most likely induce a deformation on the wavefront and/or tip-tilt on the spot at the focal plane. In order to understand the environmental behaviour where the instrument will be installed and operated, an extensive campaign has been coordinated with the European Souther Observatory ESO. In particular, the following test scheme have been implemented:

- Wind speed in 2 of the VLT incoherent ducts and in P3 / P4 Coudé Room passage
- Temperature record in:
 - Nasmyth platform
 - Coudé Room
 - Combined Coudé Laboratory
- PSF stability of the image at CCL
- Image position stability (tip/tilt) at CCL

The elaboration of the aforementioned information will provide the following information relevant for the optimal optical coupling efficiency between the VLTs Units and ESPRESSO:

- Estimation of the required tip-tilt correction for the Front End Unit
- Air flux in the incoherent ducts
- Temperature record at different times in the year
- Influence of the ducts on the image quality at the CCL

2.2.2 Setup configuration @VLT

We describe in this section the setup for the measurement of temperature, wind and PSF. Further details can be found in Avila G. & Landoni M. , Coud  Room CCL environmental tests. ESO VLT-TRE-ESP-13520.

2.2.2.1 Temperature and wind measurement setup

Temperature measurements were recorded with compact portable devices. Figure 2.12 shows the picture of the sensor. It is an USB Data logger from ATP Messtechnik GmbH. In addition to temperature they provide relative humidity measurements and dew point. They are PC programmable and provide the recorded data in plain text or cvs formats. The resolution is 0.1 degree. Three of them were placed at most relevant points: at the Nasmyth platform to measure the open air temperature, in the middle of the Coud  Room and in the middle of the CCL as indicated in Figure 2.10.

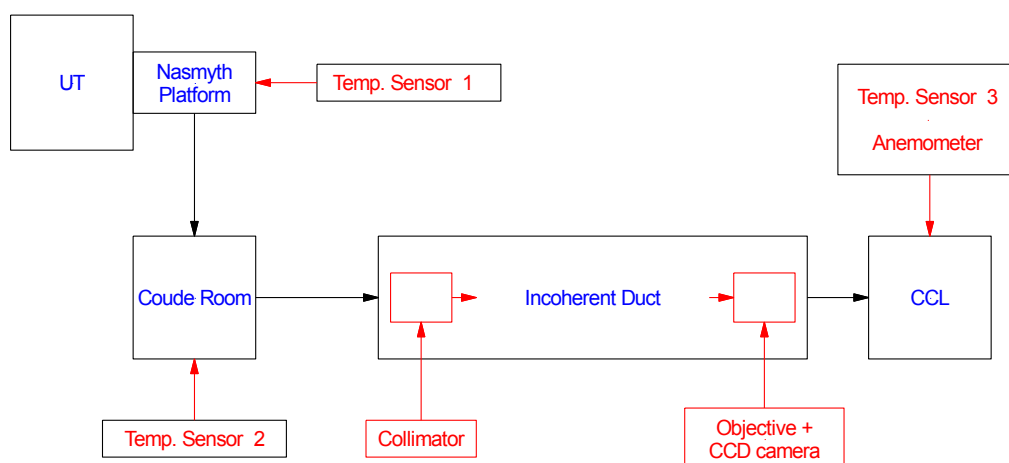


Figure 2.10: Configuration for the proposed environmental tests.

Wind measurements were taken with hot wire anemometers (Hitzedraht-Anemometer PCE-423). They can record very slow fluxes (0.02 m/s) but the big drawback is that they are unidirectional. Figure 2.11 shows the anemometer controller and head. They are not programmable and the recording mode have been fixed to one



Figure 2.11: Anemometer used for wind measurements.



Figure 2.12: Temperature data logger used for temperature measurements.

measurement per second. In order to detect a substantial chimney effect along the tube between P1 and P4 two anemometers will be installed (see Figure 2.10): one at the Nasmyth folded focus where there is a small hole to pass the beam and a second at the passage to the CR, just above M9 (VLT Interferometer). In particular, if the temperature in each Coudè Room is not the same, the wind flux might be different for each duct that reaches the Coudè Combined Laboratory. Consequently the wind speed should be measured for all incoherent ducts. Moreover, since different configurations for the tunnels might be considered, the following configuration for the measurement have been evaluated:

- The incoherent duct is open on both sides and all the coherent ducts (VLTI) are closed. Note that the coherent ducts are closed only on the Delay Line side when the VLTI is not in operation. The incoherent apertures from the CR are always open.
- The incoherent duct is closed on both sides.
- In all the cases the wind sensor has to be placed at around 50 cm inside the duct end.

Note that in the case of UT1 and UT4, where the incoherent ducts intersect the coherent ones, there might be some turbulence at the intersections even if the incoherent ducts are sealed.

2.2.2.2 PSF and image stability through the tunnels

The turbulences that arises inside the tunnel cannot be simulated by a Kolmogorv model [Kolmogorov, 1941] since it considers that the turbulence at small scales are statistically isotropic. However, this assumption holds only for very high Reynolds number.

$$Re = \frac{F_i}{\nu_i} \quad (2.4)$$

where F_i are the inertial forces and ν_i the non-conservative field of forces due to viscosity. Assuming a flow inside a cylindrical tunnel in a newtonian approximation,

the Reynold numbers turns out to be

$$Re = \frac{\rho \mathbf{v} L}{\mu} \quad (2.5)$$

where ρ is the density of the fluid (kg m^{-3}), L is the characteristic linear dimension, \mathbf{v} is the vector fluid velocity and μ is the kinematic viscosity ($\text{m}^2 \text{s}^{-1}$). If a fluid is transported through a pipe (as in the case of the air inside the duct tunnels) the flow is said to be *turbulent* if $Re > 4000$ while, for $Re < 2300$ the flow is laminar. The region between 2300 and 4000 is called *critical Reynolds number* and the flow is said to be in transition between the two regimes.

In the case of the VLT ducts, stratified or laminar fluxes similar to the ones in the VLT-I ducts are expected. A major technique for measuring the image quality would be the adoption of a Shack Hartman wavefront sensor, similar to that applied for adaptive optics. In particular, for a given number of short exposures (of the order of seconds or less) it provides an appropriate average map of the wavefront described by the Zernike coefficients. The point spread function (PSF) and therefore the full width half maximum (FWHM) may be deduced.

However this method requires considerable equipment which is not available in the Coudé Combined Laboratory. For this reason, a simplified method has been proposed instead: the image of a point-like source (optical single mode fibre) generated in the Coudé Room is directly recorded in the CCL with a fast CCD camera. The FWHM is directly measured on the image for different short exposure times. The barycentre or the photocenter of individual images records the tip-tilt low movement of the star.

Figure 2.13 reports the laboratory setup for the intended measurements. On the left side of the delay line an optical fiber of $\sim 10 \mu\text{m}$ is fed by a quasi monochromatic light source. A small F/5 telescope opens the light beam which is then collimated through a long focal lens. After a path of ~ 60 meters the light reaches a simple optics (objective) F/10 that focalize the spot on a CCD camera. It is important to note that a $10 \mu\text{m}$ fiber on F/10 corresponds roughly to $0.026''$ on the sky. Since at the Paranal the median seeing (no adaptive optics considered) is about $0.70''$ [Sarazin et al., 2008] the spot on the detector can be

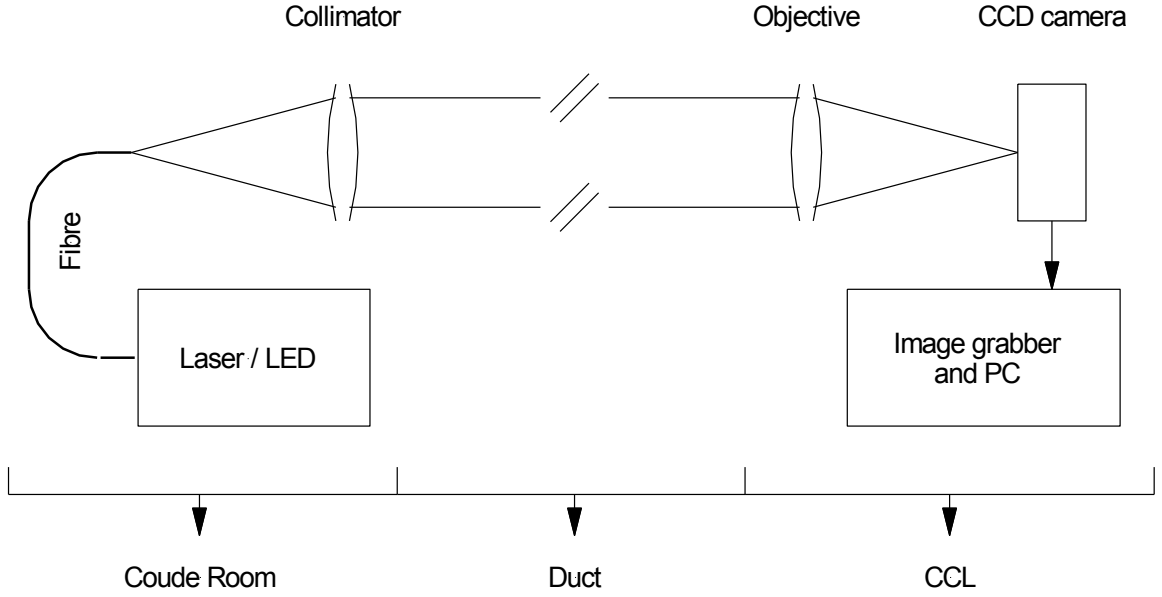


Figure 2.13: Optical setup for the image quality measurement at the end side of the delay tunnel.

reasonable considered as a PSF of a point-like source.

2.2.3 Data analysys

2.2.3.1 PSF model

As noted in the previous chapter, the fiber image should give at the focal plane a good approximation of a the point spread function of an unresolved source. However, as shown in Figure 2.14 the radial profile of the spot is quite similar to a Gaussian Beam profile. A Gaussian beam profile [Svelto, 2010] is a beam of electromagnetic radiation in which the transverse electric field and intensity (irradiance) distributions are described by mean of approsimation of Gaussian functions. These beams are popular when describing the spread function of lasers, as in the case of our experimental setup. In particular, giving the electric field as

$$E(r, z) = E_0 \frac{w_0}{w(z)} \exp \left(\frac{-r^2}{w^2(z)} - ikz - ik \frac{r^2}{2R(z)} + i\zeta(z) \right) , \quad (2.6)$$

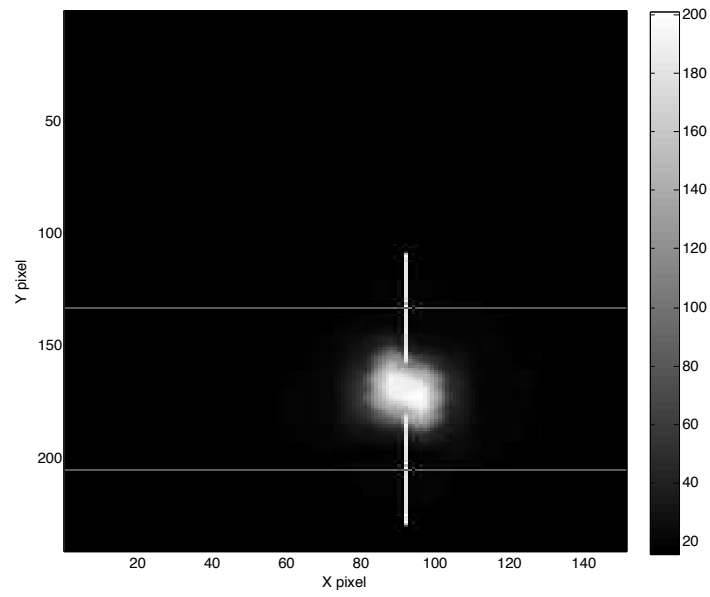


Figure 2.14: An example of the PSF of the laser beam recorded by the camera. Horizontal bars represent the area of interest for the full readout while vertical bar is the preliminary computation of the centroid performed by the onboard software of the camera.

where r is the radial distance from the center axis of the beam,
 z is the axial distance from the beam's narrowest point (the "waist"),
 i is the imaginary unit,
 $k = 2\pi/\lambda$ is the wave number (in rad m),
 $E_0 = |E(0, 0)|$,
 $w(z)$ is the radius at which the field amplitude and intensity drop to $1/e$ and $1/e^2$
 of their axial values,
 $w_0 = w(0)$ is the waist size,
 $R(z)$ is the radius of curvature of the beam's wavefronts,
 $\zeta(z)$ is the Gouy phase shift
 the intensity at radius r in spherical coordinates is given by the equation

$$I(r, z) = \frac{|E(r, z)|^2}{2\eta} = I_0 \left(\frac{w_0}{w(z)} \right)^2 \exp \left(\frac{-2r^2}{w^2(z)} \right), \quad (2.7)$$

where I_0 is the intensity at the center of the beam and η is the characteristic impedance of the medium in which the beam propagates. In our case, the tightness of the beam itself at F/10 allows to properly approximate the spot profile to a true point-like PSF after the application of a low passband filter. The point-like PSF is described by the equation

$$I(q) \approx I'_0 \exp \left(\frac{-q^2}{2\sigma^2} \right), \quad (2.8)$$

where $\text{FWHM} = 2\sqrt{2\ln 2} \sigma \approx 2.3 \sigma$. and q is the distance from the center of the beam. In the case of Gaussian beam profile, $2w = \frac{\sqrt{2} \text{FWHM}}{\sqrt{\ln 2}} = 1.699 \times \text{FWHM}$ where $2w$ is the full width at half maximum at $\frac{1}{e}$ that, for tight beams (0.02"), encompasses about the 99% of the irradiated power. Figure 2.15 shows the result of the adopted approximation. The mean systematical error on the PSF FWHM error is about 20%.

Each recorded image, with a frequency of about 1 Hz, is then reduced through standard MIDAS procedures [Banse et al., 1988]. The data reduction includes standard bias subtraction, cosmic ray removal (if needed). When the raw image is reduced, a gaussian fit is applied adopting the *CENTER/GAUSS* MIDAS recipe. The position of the spot on the detector, instead, is directly recorded by the

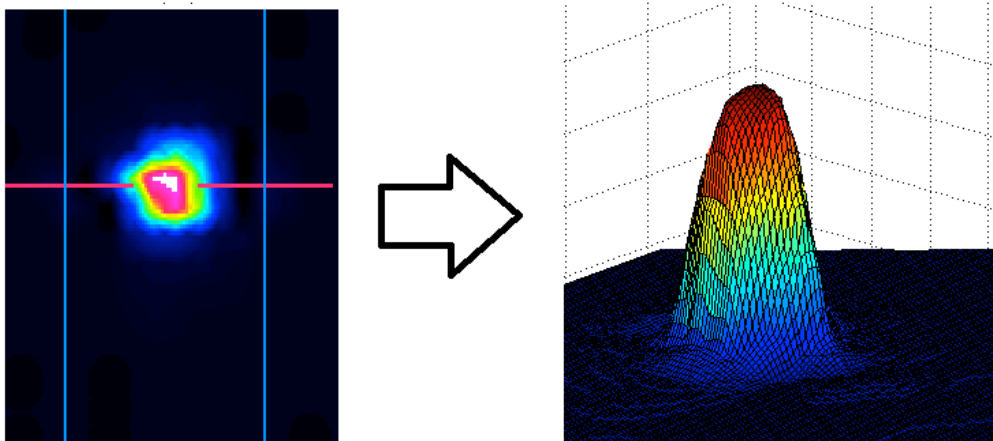


Figure 2.15: An example of the PSF of the laser beam recorded by the camera after the application of gaussian PSF model. Courtesy: ESO Paranal (Document ESO: VLT-TRE-ESP-13520)

detector. Each proposed value for the photometric barycenter computed by the camera itself has been cross-checked with the position proposed by MIDAS after the data reduction.

2.2.4 Results

The campaign (repeated both in the winter and summer chilean seasons) has collected a huge amount of raw data (in particular in terms of FITS image of the image behaviour). The summer data acquisition includes temperatures, wind speed and image displacement (only x and y positions) while in the winter one the image quality (FWHM) has been acquired too. The results are here summarized with significant examples evaluating both the image displacement and the image quality. The overall behaviour of the Paranal environment will be helpful to understand:

- How to design the ESPRESSO Front End unit in terms of stabilization of the field (guiding algorithm).

-
- Definitively point out the needed of adaptive optics at the level of the instrument (or telescope directly)

2.2.4.1 Image quality and relationship with Paranal environment

The data analysis immediately shows that image displacement due to air flows in the ducts has mainly two features. First of all there are some spikes which raise during the whole night and, moreover, a slightly drift along the overall time is also apparent. The image displacements measured in all the campaigns are essentially along the vertical direction. This could drive to infer that a layered thermal stratification of the air exists at the level of the tunnel, instead of a pure turbulent one.

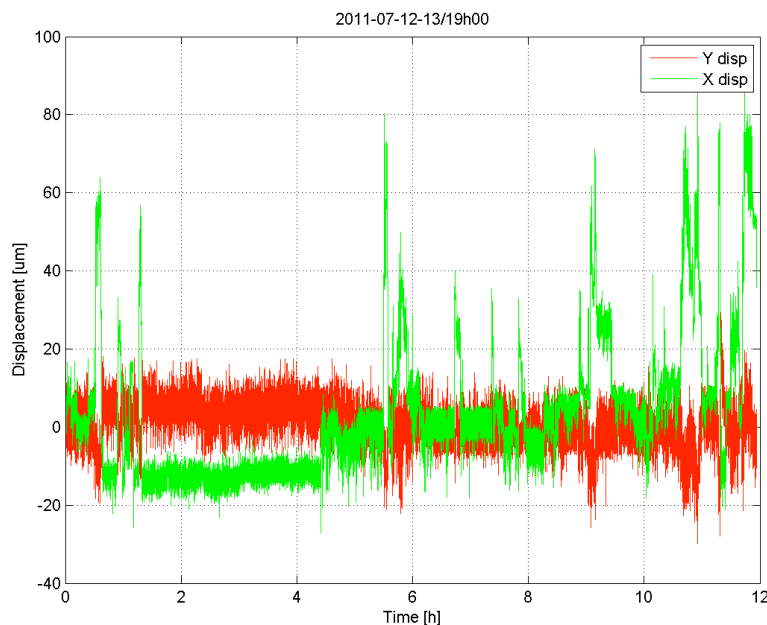


Figure 2.16: Image displacement acquired during the night between 12 and 13 of July 2011.

Figure 2.16 shows an explicative behavior of the centroid displacement during the night. On X axis is represented the time expressed in hours, while in Y is reported the components of the image displacement in microns. As said before,

spikes with displacement of tenth of microns are present. The spikes are sudden event that last usually few minutes; however some of them takes even half an hour. On the other hand it is possible to notice that during the night there are also some plateau where the image is very stable. The characteristics spikes in that night show that the maximum peak within 1 sec is around $50\mu\text{m}$ (the average is around $23\mu\text{m}$). According to the optical configuration, the plate scale is $\sim 390\mu\text{m arcsec}^{-1}$. For this reasons, the displacement on the sky turns out to be $0.12''$ projected on the sky. The stability requirement budget error for the positioning, in order to cope with the ESPRESSO scientific goals, is $0.05''$ rms.

Now, suppose to observe a star of $m_v = 8.00$ in the Johnson UVB V filter. The required exposure time in order to reach, at the level of the recorder spectrum, an accuracy on the radial velocity of about few cm s^{-1} is about 30 minutes. If the exposure starts just before a spike happens, the rms error on the position will be $\sim 0.2''$ which is a factor ~ 5 above the maximum acceptable error on the position of the target on the slit. For this reason, an active control of the field position must be implemented at the level of the front end of the instrument.

The displacement of the PSF has also been correlated with temperature and wind recorder by the instruments adopted as explained in the setup configuration. In Figure 2.17 are shown both the temperatures behavior and the image displacement. A strong correlation between the temperature (taken in proximity of the anemometer) at the entrance of the tunnel into the CCL and PSF tilts seems to appear. Between h2.00 and h4.00 there are both plateau in the temperature and in the displacement while when the temperature starts shacking the spikes of the displacement raise up. From the same figure no strong correlation seems to exist with the other temperature acquired in different location at the VLT.

As expected, the temperature fluctuations are strictly correlated to the wind speed changing that could drive to the conclusion that there is a strict interaction between the turbulence into the tunnel and the vertical displacement of the image (see Figure 2.19). In order to better characterise the turbulence features, a closed configuration for the tunnel has been assesed to evaluate the effect on the image stability. Maintaining the previous setup for the detectors (except for the vertical axis of the camera), both the entrance and the exit of the delay line have been

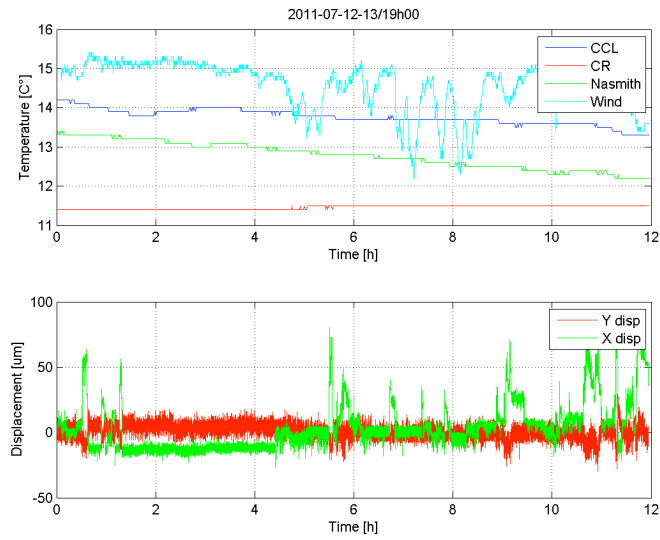


Figure 2.17: Comparison between image displacement and temperatures behavior. Wind line (solid blue) refers to the wind temperature at the level of the anemometer.

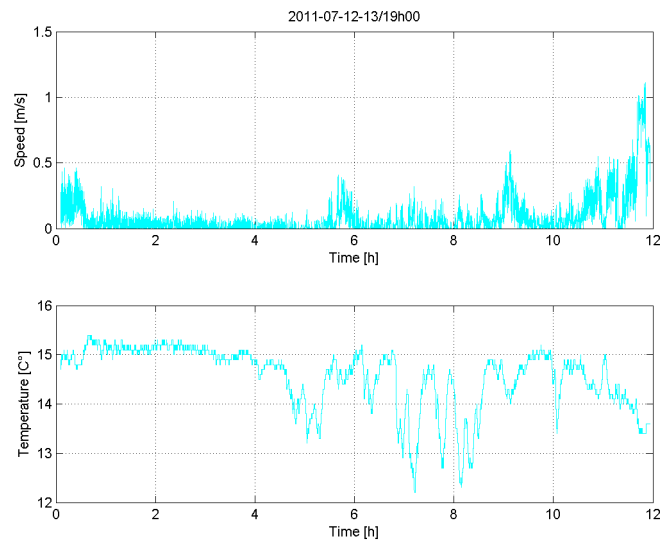


Figure 2.18: Correlation between temperature and the wind speed.

then sealed.

In Figure 2.19 is shown the image displacement in the closed configuration. Note that in this configuration the camera has been rotated along the optical axis of 90 degree due to technical reasons. This clearly demonstrate that during the night there is a predominant displacement along the vertical axis respect to the horizontal one, as detected in the open configurations.

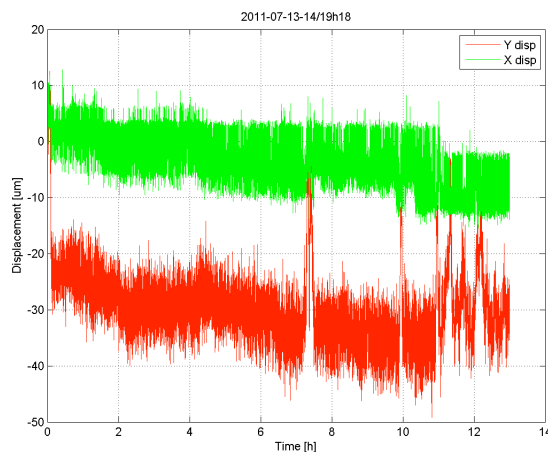


Figure 2.19: Image displacement acquired during the night between 13 and 14 of July 2011 (closed configuration)

From the comparison between open and closed configuration it is clear that the second one shows that the image position is more stable and reliable. The maximum peak-to-valley displacement during a spike is around $35\mu\text{m}$ which is roughly half of the open configuration.

Regarding the image quality in terms of FWHM of the PSF the data analysis shows that it is quite stable along the nights. The behaviour is shown in Figure 2.21

As in the case of image displacement, the PSF of the image has been evaluated also in the closed configuration which provides benefits also to the image quality behavior as shown in Figure 2.22

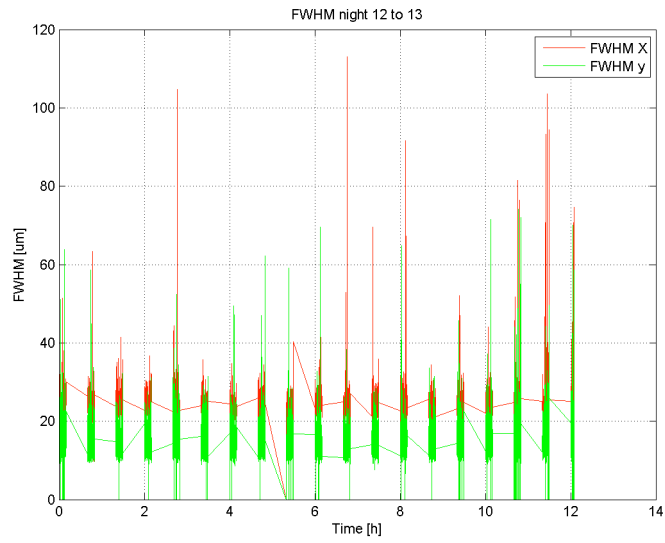


Figure 2.20: Measured FWHM during the 12 to 13 night. Note that spikes are due to non-convergence of the fitting algorithm on bad recorded image.

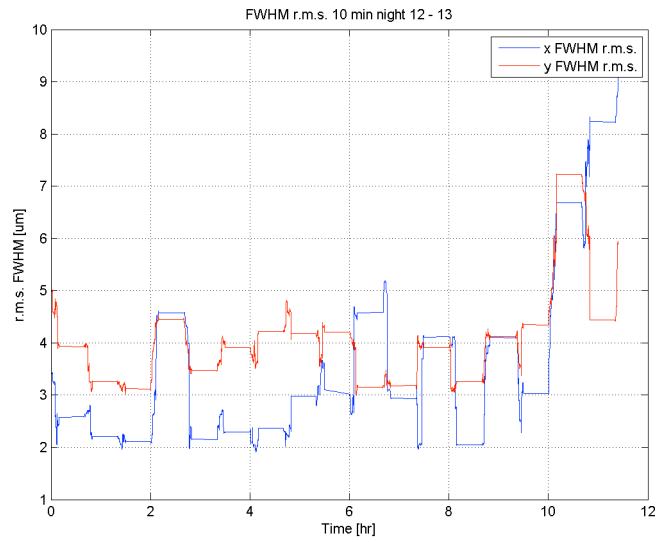


Figure 2.21: Standard deviation of the Full Width at half maximum of the image on 10 minutes wide bins .

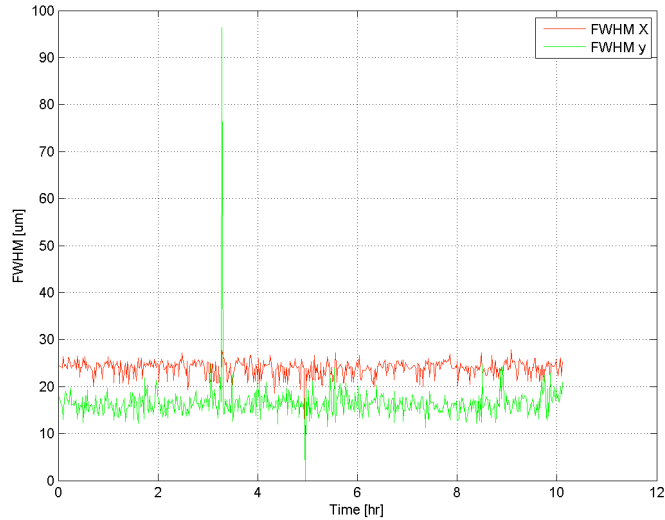


Figure 2.22: Measured FWHM during the 13 to 14 night in closed ducts configuration. Note that spikes are due to non-convergence of the fitting algorithm on bad recorded image.

2.2.5 Conclusions

From the extensive campaign carried out, it is possible to synthesize the following conclusions:

- The Coude delay tunnel impose a displacement to the image. For this reason, an active control of the field at the level of the front end of the instrument is mandatory in order to cope with the positioning requirement ($\epsilon = 0.05''$ rms)
- The displacement occurs suddenly (jumps) and after a various time it really disappear (the photonic centroid of the image goes back to the previous position). Moreover, there seems to exist a correlation between wind into the tunnel and image displacement.
- The measured image quality appears to be more stable than the centroid displacement and it is improved if the tunnel is sealed. In the case of open configuration the rms of PSF size is $\sim 7\mu m$ while in close setup is lower

than $\sim 3\mu m$. For the purposes of ESPRESSO the behaviour of the PSF clearly indicates that **no adaptive optics** is required to fulfill the instrument requirements. Nevertheless, the closed-tunnel setup is overall better than the open one, in terms of centroid stability and also in PSF size stability and dimension which is directly correlated to the image quality.

2.3 Front-End Subsystem: stabilisation of the field

2.3.1 Introduction

The observation campaign in Paranal, illustrated in the previous section, clearly demonstrated that the image stability at the end of the Coudé Train system is not sufficient to guarantee an error on the position accuracy (with respect to the fiber entrance which acts as slit) well below $0.05''$, which is the evaluated requirement for the positioning system in order to reach the stability for the purposes of ESPRESSO (RV stability and SNR directly correlated to severe slit loss in case of bad guiding). For this reason, the aim of the Front End System is the stabilisation of the delivered field and pupil of the telescope and the entire Coudé Train. This task is crucial since it allows the entire ESPRESSO to reach the required performances in terms of stability of the image. The stabilisation algorithm is based on active optics (piezo tip-tilt devices) that will correct low spatial order perturbation (tip tilt) and not high spatial order perturbation since the image quality (in terms of FWHM) is reasonably stable for the purpose of the spectrograph as investigated before.

We will illustrate the following main topics.

- A parametric detector simulator has been set up in order to evaluate the performances of different detector, commercial ones (such as Sony or Kodak detectors) and scientific (e2v or Hamamatzu). In detail the CCD characteristics like RON dark current, QE has been investigated to exploit the expected performance on the sky for the different products.
- A robust version of the centroid calculation based on the computation of

the barycenter adopting Proportional and Integral controller architecture in order to increase the stability of the whole guiding system will be used.

2.3.2 CCD detector simulation and radiometry

In order to exploit the behaviour of the detector and the stabilisation algorithm performance expected on the sky, a numerical model for CCD simulation has been setup. In particular, in the numerical model, the CCDs are essentially characterised by the following parameters:

- Pixel size (μm).
- Number of pixel of the detector (e.g. 511x511).
- Read out noise (in e-).
- Dark Current (in $\text{e- sec}^{-1} \text{ px}^{-1}$).
- Quantum efficiency (on the ESPRESSO spectral range).
- Saturation level (in e- pixel^{-1}) and ADU saturation level.

The main part of the simulation algorithm lies in the generation of the noises, which are function of the parameter of the TCCD. In the next paragraph, we explain the main steps required to simulate an integration of the TCCD in order to validate the Positioning and Guiding Algorithm. In particular, the stabilisation algorithm will be evaluated adopting the displacement obtained through experimental data recorded in Paranal and illustrated in the previous section. Since those measurements have been recorded at 1 Hz, to simulate the real displacement of the image a linear interpolation between one step and the following has been considered. The 1 sec of exposure is then realized by adding 10 images of 0.1sec with the displacement obtained by the linear interpolation illustrated in the pictorial representation of Figure 2.23.

Moreover, the following theoretical assumption are assumed to hold during each simulation:

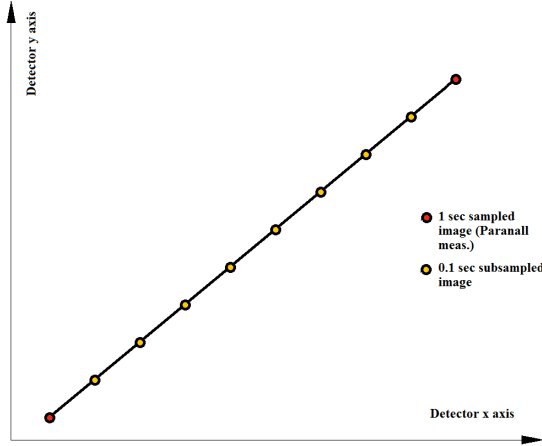


Figure 2.23: Subsampling of the spot position. Red dots are experimental data while the yellow ones are the subsample interpolation in order to better characterise the behaviour of the image displacement on the detector

- The **PSF** (since only point like source are considered) is a **Gaussian function**. In particular, consider the following formula for the spot that it will be sampled on the simulated CCD. $f(x, y) = A \exp\left(-\left(\frac{(x-x_0)^2}{2\sigma_x^2} + \frac{(y-y_0)^2}{2\sigma_y^2}\right)\right)$, where A is the peak in photon s^{-1} of the function, x_0 and y_0 represent the displacement (in pixel unit) of the spot with respect to the origin of the reference system..
- The spot is **symmetric**. In particular, we consider a perfect symmetry of the spot but the algorithm could guide also with an asymmetric one.
- The **reference** flux is considered to be **constant** over the ESPRESSO wavelengths and is $1000 \text{ photons sec}^{-1} \text{ cm}^{-2} \text{ \AA}^{-1}$, assuming an object with apparent magnitude $m_v = 0$. This assumption is reasonable since bolometric correction for different star spectral class (from B to M) slightly modify the bolometric flux received at the level of the Front End stabilisation algorithm subsystem.
- The magnitude of the star is **constant** during the observation (this holds true for the most scientific objects that ESPRESSO will observe).

2.3.2.1 Determination of optical parameters

This paragraph describes the main optical parameters calculated by the algorithm in order to perform the simulation of the CCD. In particular, the **plate scale** of the system will be calculated as

$$PS = \frac{F \times D}{206265} \times 1000 \quad \mu m \text{ arcsec}^{-1} \quad (2.9)$$

where F is defined as F-number times the diameter of the telescope in mm and 1000 is a proportional constant in order to obtain the PS as $\mu m \text{ arcsec}^{-1}$. When the plate scale is constrained, the PSF of the scientific object is simulated as a Gaussian spot. Since the Gaussian function is determined by its variance in the X and Y direction it is necessary to estimate their value that are function of seeing, pixel size and Plate scale. In particular, they are defined as

$$\sigma_x = \sigma_y = \frac{PS \times seeing}{2.35 \times pixel_{size}} \quad \mu m \quad (2.10)$$

where the seeing is given in arc sec and $pixel_{size}$ is the dimension of the pixel in μm . Moreover, if a binning (only squared) is assumed the dimension of the pixel is multiplied by the binning factor.

2.3.3 Radiometric quantities

For each simulation, it is mandatory to estimate how many photons can reach the ESPRESSO Front-End up to the pinhole slit which is responsible to inject the received light into the fiber. Here below are reported the equations that are used in order to perform the estimation, assuming that the scientific object is fully described by its relative visual magnitude (V filter). The received flux between λ and $\lambda + d\lambda$ is calculated as follow

$$\frac{d\phi}{d\lambda} = \phi^* \times \eta(\lambda) \times \eta_{ESPRESSO}(\lambda) \quad (2.11)$$

where ϕ^* is the object flux in photons $\text{sec}^{-1} \text{ cm}^{-2} \text{ \AA}^{-1}$ calculated from its apparent magnitude in V band, $\eta(\lambda)$ is the CCD Quantum Efficiency and $\eta_{ESPRESSO}(\lambda)$ is

the efficiency of the whole ESPRESSO instruments up to the Front End technical CCD. Figure 2.24 shows the diagram of the Quantum efficiency of three different detectors. The solid dashed line represents the estimated efficiency of ESPRESSO system as defined in the PDR document. Figure 2.25 shows the quantum efficiency of the Sony ICX 285 detector which is the baseline one for ESPRESSO (on FDR, May 2013).

Integrating all over the wavelengths that ESPRESSO will observe, the total number of photon per unit area is expressed as:

$$\phi_{sciObj} = \int_{3800}^{8000} \phi^* \times \eta_{ESPRESSO}(\lambda) \times \eta(\lambda) d\lambda \quad (2.12)$$

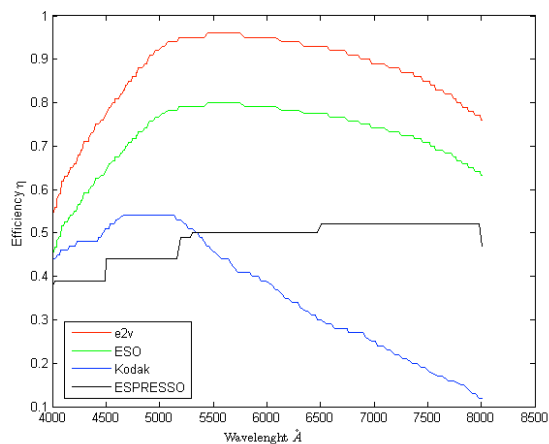


Figure 2.24: Quantum Efficiency of a sample of three different TCCD and ESPRESSO System Efficiency (updated at Final Design Review (May 2013)).

For each pixel of the CCD, it is mandatory to compute the flux received from the star. In particular, adopting the formula

$$N_{photon}^{px} = \int_{x_{min}}^{x_{max}} \int_{y_{min}}^{y_{max}} A \exp \left(- \left(\frac{(x - x_o)^2}{2\sigma_x^2} + \frac{(y - y_o)^2}{2\sigma_y^2} \right) \right) dx dy \quad (2.13)$$

where x and y are the CCD cartesian coordinates and σ_x and σ_y are calculated as explained before. The constant A is defined as $\frac{\phi_{bolometric}}{2\sigma_x\sigma_y\pi}$ ph sec⁻¹ while $X0$ and $Y0$ represent the displacement of the Gaussian spot respect to the center of the

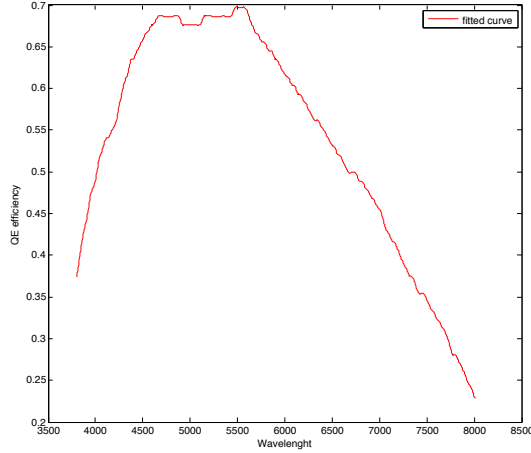


Figure 2.25: CCD Sony ICX285 detector Quantum Efficiency. This detector is the baseline for the technical CCD for the ESPRESSo system.

TCCD. The $\Phi_{bolometric}$ factor is calculated according to Equation 2.12. Note that the double integral is not calculated using an iterative numerical method but using geometric assumptions for the computation of the volume. This is implemented in order to improve the cost of computation.

Finally, the sky background must be evaluated since, for faint objects, the exposure time of the detector aboard the frond end are about 17 sec and the contribution from sky photons is not negligible. Starting from the definition of surface brightness

$$S_v = m_v + 2.5 \log_{10} A \quad (2.14)$$

the magnitude of each pixel is the computed as

$$m_b^{pixel} = S_v - 2.5 \log_{10} \left(\frac{pixel_{size}}{PS} \right)^2 \quad (2.15)$$

The median sky brightness in V band has been assumed as 21.00 mag arcsec⁻², which is a quite good compromise on different lunar phases.

Band	U	B	V	R	I
Magnitude	22.28	22.64	21.61	20.87	19.71

Table 2.4: ESO Paranal observatory mean sky brightness (courtesy European Southern Observatory)

2.3.4 Pinhole slit simulation

In ESPRESSO the slit on the sky is made through the adoption of a pinhole mirror of $1''$ diameter project on the sky (High Resolution mode) and it is also the interface for the fiber injection. On the simulation of the CCD the slit is simulated as a circle with radius equal to $1''$ on the sky centered in the middle of the CCD (which is reasonable the reference point for the system in the simulation). Figure 2.26 shows an example of a simulated CCD (with no noises) in which a star with $m_v = 15$ it is integrated for 0.2 sec, assuming seeing of $1''$.

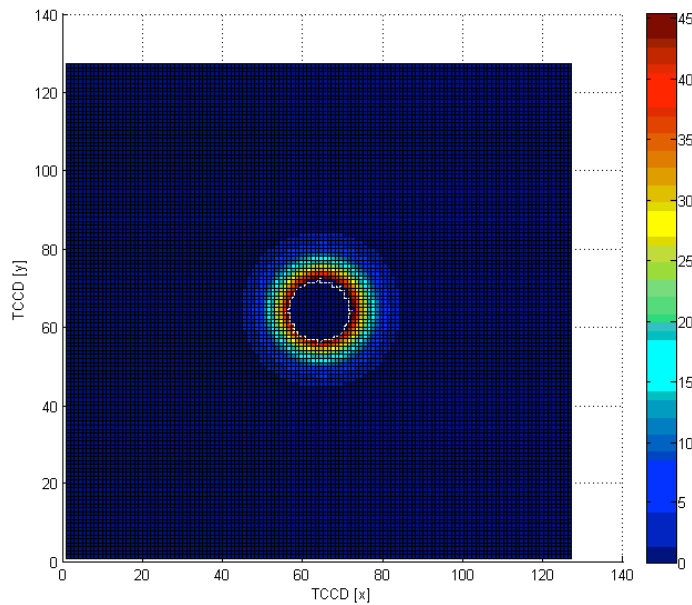


Figure 2.26: Simulation of a scientific object on the TCCD (no noises considered).

2.3.5 The algorithm architecture

In order to evaluate the behaviour of the front end and the technical CCD used for stabilise the field, there are two main phases in the simulations that have been carried out. The first phase (1) regards the generation of the detector image, adopting the theoretical framework explained in the previous section, while the second (2) is only on the evaluation of the guiding algorithm.

2.3.5.1 Phase (1) - CCD generation

Let be n the exposure time (in second) and assume that the physical displacement of the spot (respect to the center of the CCD) are subsampled as explained. For further details on exposure times, representative cases are given in Table 2.5. As a rule of thumb, the integration time of the technical CCD is computed according to the magnitude of the target ($n \propto (2.51)^{-m_v}$) and to the neutral density filter applied on the filter wheel installed in front of the camera

- **Build up** $n \times 10$ CCD in which each pixel contains the flux from the scientific object integrated for 0.1 s. The spot of the scientific object is placed in the position $X_{CCD} = X_{phys}(i) - \Delta X$, $Y_{CCD} = Y_{phys}(i) - \Delta Y$, where ΔX and ΔY are the current correction (zero for the first step) and X_{phys} and Y_{phys} are the absolute spot physical displacement data recorded in Paranal. We do not considered high frequency image blur due to scintillation effect from Kolmogorov perturbation (for further details see the next section).
- **Sum up** the $n \times 10$ CCD
- Add the **sky contribution** on each pixel to the summed CCDs (here in after this sum will be referred only as CCD). The flux (for each pixel) from the sky is calculated as explained in the previous paragraph, considering n as exposure time.
- Subtract the **hole contribution** in the center of the CCD
- **Generate the dark current** signal for each pixel adding a number in which the parameter of the $e^- \text{ sec}^{-1} \text{ px}^{-1}$ is the value of the dark current (from datasheet if available).

-
- **Generate the photon noise** replacing the flux calculated (λt) value of each pixel of the CCD with one drawn from a Poisson distribution (N) in which the parameter of the PDF is the current value of the pixel.

$$Pr(N = k) = \frac{e^{-\lambda t} (\lambda t)^k}{k!} \quad (2.16)$$

- **Generate the readout noise** adding a mask to the CCD generated as a Normal random number with $\mu = 0$ and rms equal to the RON value reported in the datasheet.
- For each pixel **check the saturation level**. If the pixel exceeds the maximum number of electrons allowed in the potential well its value will be fixed at the saturation threshold (reported in the CCD datasheet).
- **Apply the ADC conversion** of the CCD and check if the ADU is saturated. For this reason, the value of each pixel is converted from e- to ADU through the ccd-gain factor (e- ADU⁻¹). In case of saturation, the value of the pixel is forced to $2^{ADU_{bits}}$, where ADU_{bits} are the number of bits available to the electronics of CCD for the readout.

2.3.5.2 Phase (2) - Guiding algorithm

In this phase, the CCD generated in Phase(1) is given as the input for the guiding algorithm under evaluation.

- Performe a standard σ -clipping on the CCD in order to enhance the signal-to-noise ratio of the image. In particular, in this steps the background is subtracted since only pixels above a certain threshold are considered, while the others below the threshold are forced to be zero. In this way, the photo-center is calculated without systematic deviation introduced by the detector and background biases. The threshold is computed in a small region of the CCD away from the target in order to give a reasonable estimation of the background used for the computation of previous step.

-
- Calculate the centroid adopting the canonical baricenter formula for the X and Y coordinate (X_{BARY} and Y_{BARY}).
 - Calculate error in the X and Y position as $\Delta X_{ERR} = X_{BARY} - X_{REF}$ and $\Delta Y_{ERR} = Y_{BARY} - Y_{REF}$ where X_{REF} and Y_{REF} are the reference desired position (for the simulation it is the center of the hole which is coincident with the center of the TCCD).
 - Update the integral error (Integral error) and the total integration time.
 - Update the correction position X and Y adopting a P.I. control architecture, where K_p is the proportional constant and K_i is the integral constant according to equation

$$X(t+1) = X(t) + K_p \times X_{err} + \frac{K_i \times Integral_{ErrorX}}{TOTAL_{IntegrationTime}} \quad (2.17)$$

$$Y(t+1) = Y(t) + K_p \times Y_{err} + \frac{K_i \times Integral_{ErrorY}}{TOTAL_{IntegrationTime}} \quad (2.18)$$

- Step to point 1, Phase (1), if the integration in not yet completed.

Figure 2.27 and 2.28 shows the block diagram and the general workflow of the analysis.

2.3.6 CCDs under evaluation

Different technical CCDs have been evaluated starting from the high performance e2v-detector, implemented in most of scientific instruments, that has the drawback of a USB and Ethernet interface moving to less performing detectors (Kodak and Sony) that also enable the Ethernet GIGE vision interface. We have considered two different template cases in order to stress the performances of the detector both in high and low speed acquisition range. Based onto scientific goal a bright and a faint object template case has been defined basically to identify requirements for RON dark current and Quantum Efficiency.

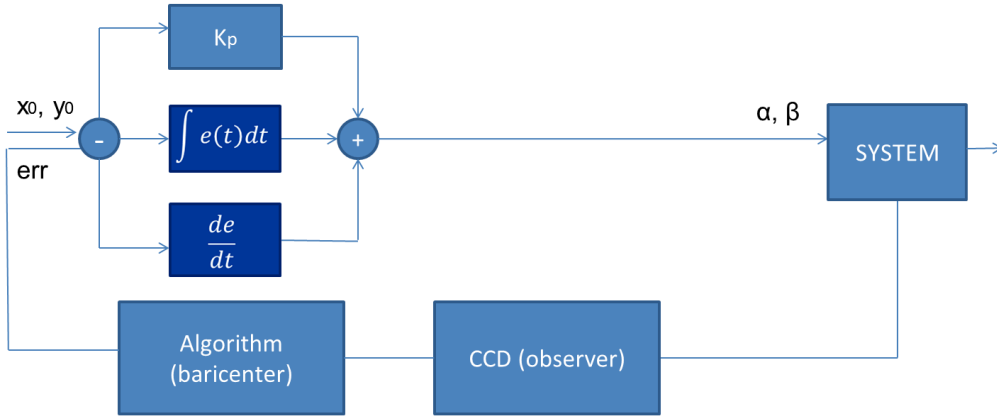


Figure 2.27: Scheme of the guiding algorithm

The displacement disturbances adopted are relative to the experimental data measured in Paranal during the second observational campaign (see Figure 2.29 and 2.30). In particular the most severe condition has been taken into account.

	Faint object	Bright objects
Apparent Magnitude	$m_v = 20$	$0 \leq m_v \leq 8$
Scientific exposure time	~ 45 mins (10 m s ⁻¹ RV acc.)	1 to 20 mins (10 cm s ⁻¹)
Number of corrections	100	100 or better
Correction period	18 s	0.1s or better
Sky brightness	21 mag arcsec ⁻²	21 mag arcsec ⁻²
rms error max	< 0.05	< 0.05 or better

Table 2.5: Template case adopted for the algorithm evaluation.

To evaluate the algorithm performances the most severe displacement recorded in Paranal has been considered. In addition we added a non-physical step variation of the seeing which overestimates its real possible modification. However, for sake of simplicity no image blur due to scintillation has been considered since we take into account only the integrated effect of the Kolmogorov perturbation spectrum on the image quality which directly reflects into the size of the seeing disk. The barycenter algorithm is anyway quite insensitive to any real seeing variation. Figure 2.30 illustrates the real system situation taken into account. For

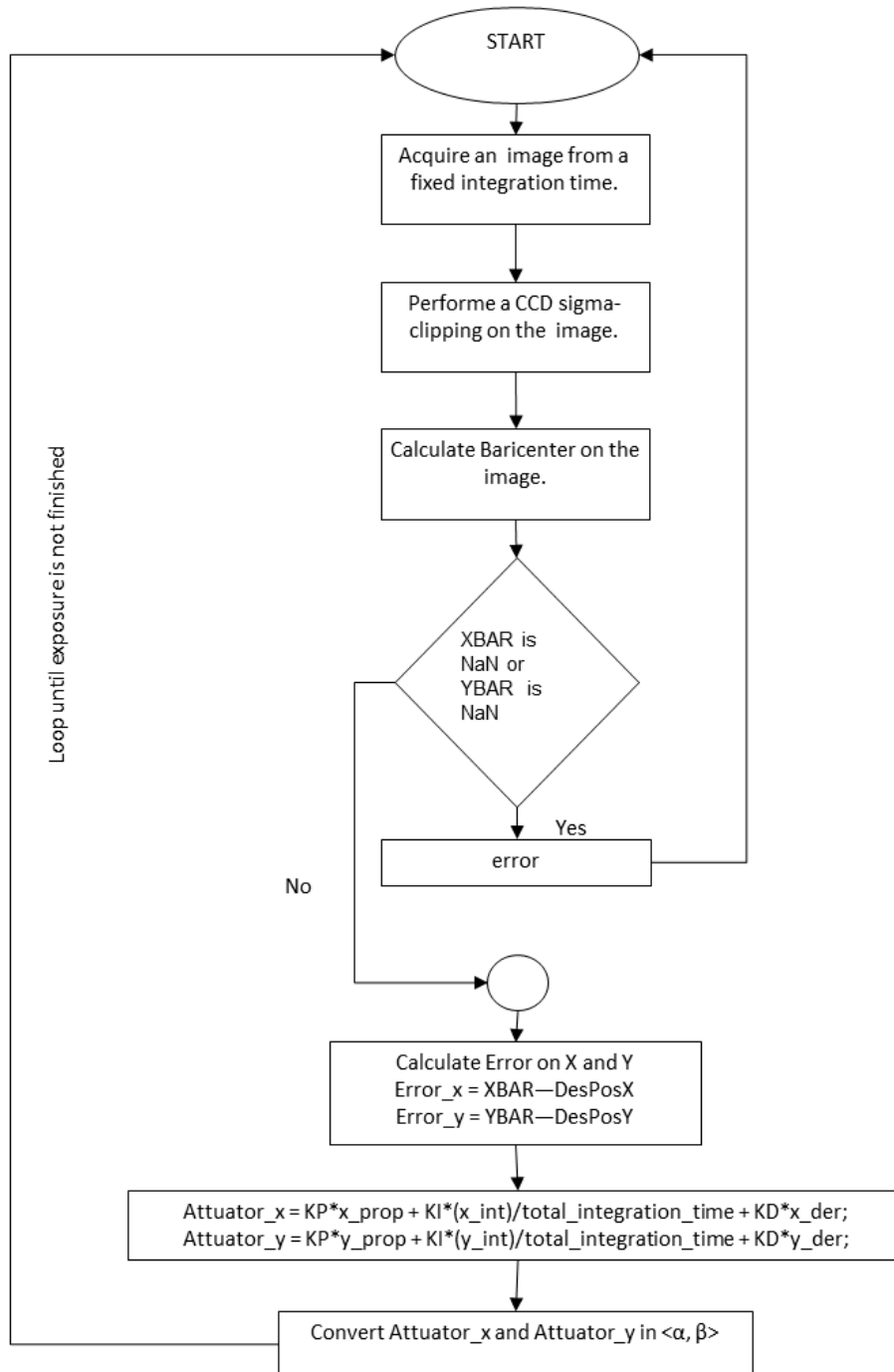


Figure 2.28: Workflow of the guiding algorithm. Integration time is computed according to the magnitude of the target and the neutral density filter installed in front of the camera. For instance, table 2.5 gives two general template cases.

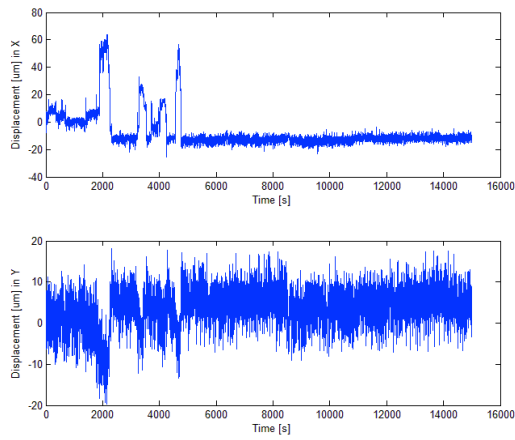


Figure 2.29: Experimental data recorded in Paranal during the observational campaign in July 2011

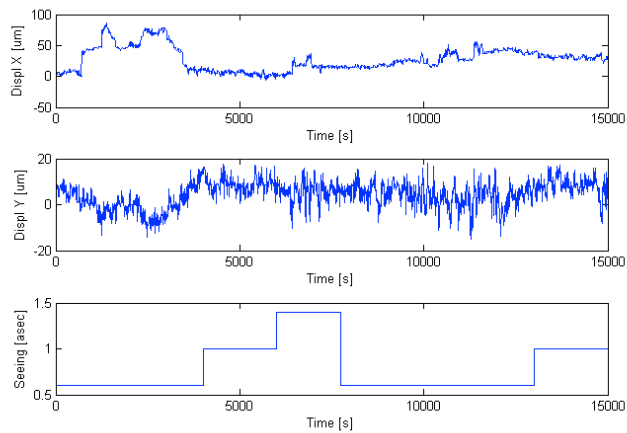


Figure 2.30: Perturbations applied to all the configurations: X displacement (top), Y displacement (middle), Seeing variation (Down). The units of the displacement are linear and must be corrected recalling that they are recorder with a F/10 camera.

instance, an improvement (next steps) of the model will be achieved through the introduction of the scintillation model described by Kolmogorov spectrum of atmospheric perturbation. For each simulation carried out, the following parameter will be calculated in order to infer the general behaviour of the algorithm:

- Maximum error (correction residual) displacement
- Average error in order to be sure that no systematic effects are injected by the guiding system
- RMS on the mean error vector , where the mean error vector is defined as

$$\begin{pmatrix} \frac{\sum_i^N e_x(i)}{N} \\ \frac{\sum_i^N e_y(i)}{N} \end{pmatrix} \quad (2.19)$$

and the modulus, defines as $\sqrt{\sigma_x^2 + \sigma_y^2}$ must be lower than $0.05''$ in order to guarantee the required precision.

It is also important here to stress the fact that the guiding errors (or correction residuals) which are referred throughout the Chapter are the quantity (expressed in arc sec or linear unit¹) which are left after the application of the correction computed by the system. In particular $\epsilon = X_{ref} - X_{actual}$, where ϵ is the residual (as explained above), X_{ref} is the desired position and X_{actual} is the actual position of the object on the slit.

2.3.6.1 Bright objects cases - Results

When guiding the field through a bright target object, the performance of the algorithm are always **shot noise** limited and, for each detector under evaluation, the RMS error on the position is far below the desired accuracy ($\epsilon \sim 0.003$ or less). In fact, considering the signal-to-noise ratio CCD equation [Howell, 2006]

$$\frac{S}{N} = \frac{N_\star}{\sqrt{N_\star + n_{pix}(N_{sky} + N_D + N_R^2)}} \quad (2.20)$$

¹In F/8, which is the optical layout of the front end unit, the plate scale is $\sim 310 \mu\text{m arcsec}^{-1}$

where N_\star are the counts received from the target object, n_{pix} is the number of pixel considered, N_{sky} are the photons falling on the CCD from the sky background, N_D are the counts due to dark current and N_R are the read out noise per pixel. In the case of very low magnitude, N_{sky} , N_D and N_R are negligible when compared to N_\star so the snr equation turns out to be

$$\frac{S}{N} = \frac{N_\star}{\sqrt{N_\star}} \propto \sqrt{N_\star} \quad (2.21)$$

and the resulting image is said to be shot noise limited. For this reason, the detector characteristic such as the readout noise or the dark current are negligible and the overall performance of the system are only affected by the quantized nature of the light. In order to cope with very bright magnitude, the Front End guiding system is equipped with a filter wheel that will be configured with 5 neutral density filters with Optical depth OD of 1, 2, 3, 4 and 5. For example, in Table 2.6 is shown the configuration for the filter wheel against target magnitude.

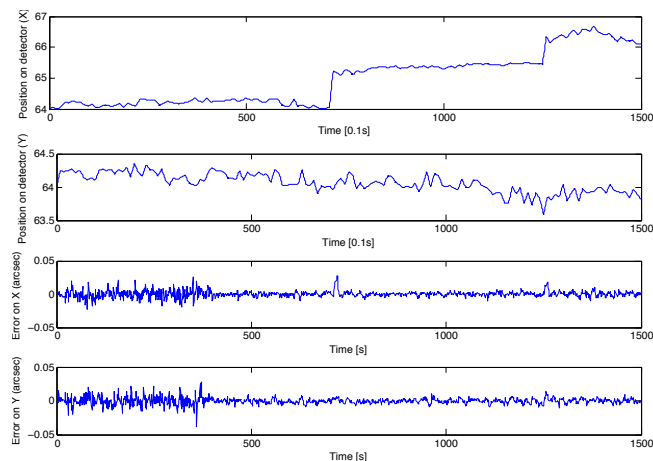


Figure 2.31: Simulation results on guiding an object with $m_v \sim 10$. Third and fourth panels show the residual left after the correction of the guiding system

As shown in Figure 2.31 the residuals induced by the guiding systems are negligible with respect to actual displacement, although severe perturbation are applied to the system. Measurements and consequent action on the PI controller are shot noise limited. In particular Box 3 and 4 of Figure 2.31 report the residuals

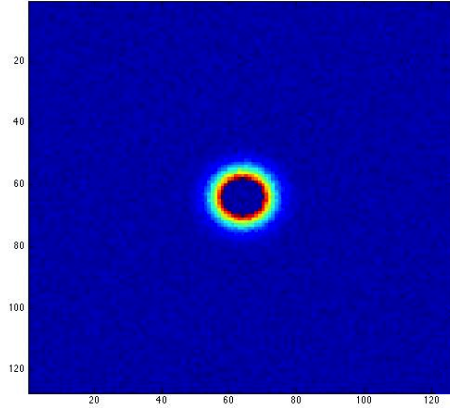


Figure 2.32: An example of a simulated Front End technical CCD observing object with $m_v \sim 10$ for guiding.

mv	20th-2th	11-9th	8-7th	6-4h	3-2	1-0
OD	*	1	2	3	4	5
ExpTime	0.1s to 17s	0.1	0.1	0.1	0.1	0.1

Table 2.6: CCD readout times and Neutral density filter configuration for bright objects. Binning 2x2 is assumed. Gain 3.2 e-/ADU is also considered.

of guiding systems after the application of correction. Figure 2.32 shows a pictorial representation of a simulated CCD as seen aboard the Front End guiding system while results of the entire simulation are given in Table 2.7. The results are also reported through histograms in Figure 2.33.

2.3.6.2 Faint object cases - Results

When the Front End Unit has to cope with faint object for guiding task the situation is more challenging. In particular, starting from the SNR equation (Equation 2.20) for $m_v \geq 18$ the image recorded at the level of the detector begin to be background and readout noise dominated. For instance, if the sky brightness is roughly the same reported in Table 2.3.3 an exposure of 1 second (assuming a detector with $6.45 \mu\text{m}$ and 2x2 binning) imprint ~ 14 e- on the detector. For

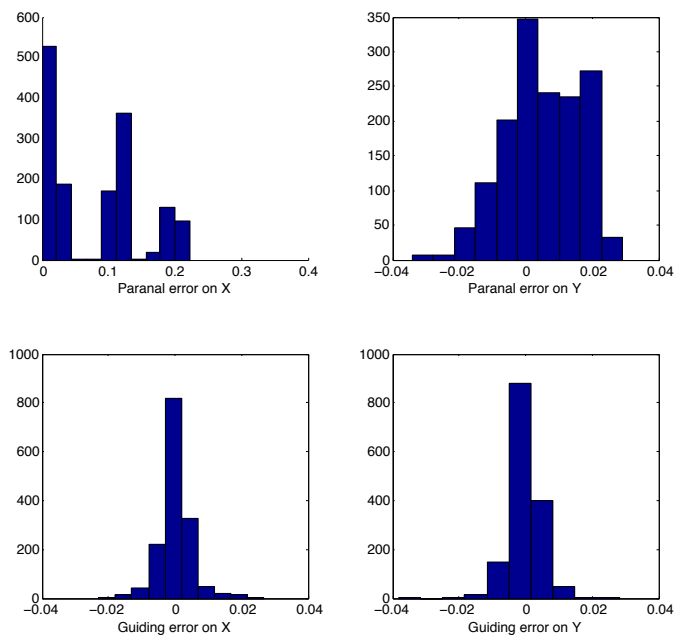


Figure 2.33: Histograms of the error during a simulation on guiding bright objects. Left upper panel - Histogram of the error as recorded on Paranal on X axis. Right upper panel - Histogram of the error as recorded in Paranal on Y axis. Lower panels represent error after the application of the guiding algorithm

Coordinate	Quantity	Measured value
x	Max residual	0.05''
	Mean residual	$5.8'' \times 10^{-6}$
y	Max residual	0.026''
	Mean residual	$3.8'' \times 10^{-7}$
Overall residual RMS	Residual vector	0.0057''

Table 2.7: Algorithm performance evaluation for object with $m_v \sim 10$ (bright case).

the faintest considered magnitude ($m_v \sim 20$) the typical exposure times for the technical CCD of the Front End are about ~ 17 secs (which is calculated considering the typical scientific exposure time and the required SNR ratio of the image obtained at the TCCD in order to perform guiding) the flux received from the sky is ~ 240 e-. The baseline detector (Sony ICX-285) possesses a full well capacity of ~ 20.000 e-, a readout noise of 8 e- and a negligible dark current ($\leq 0.003e^{-}s^{-1}px^{-1}$). For this reason $\sim 1\%$ of the full well capacity is occupied by the background that it is also a factor 30 with respect to the readout noise. Another crucial quantity that significantly affects the overall performance at faint magnitude is the detector quantum efficiency. As noted in the previous section, the guiding of bright object is a straightforward task and the CCD characteristic only affect marginally the overall performance. Nevertheless, this assumption does still not hold at higher magnitude. For all of these reasons, simulations have been carried out with the baseline Sony ICX 285 detector and its parameters. Moreover, additional simulations have been performed modifying the basic CCD parameter (starting from an high level one e2v detector, see Figure 2.24) in order to investigate (and, possibly, mitigate) the consequent effect on the system. Finally, it is worthy to note that the detector considered (ICX 285AL) possesses in the camera implementation choosed (BigEye G132G cooled) the on-chip binning in only one direction (vertical). When guiding faint objects, the CCDs of the Front End Unit are configured in order to achieve a 2x2 binning in order to reduce the effect of

the readout noise. In this case, since only one direction is directly binned on chip the readout noise considered during simulation is $\sim \sqrt{2}\text{RON}$ in order to take into account a quadrature summation of the noise during the binning off chip (which is implemented with a FPGA aboard the camera).

In Figure 2.36, 2.35 and in the pictorial representation of Figure 2.36 we report the obtained result for the guiding algorithm when a faint object $m_v = 20$ is considered. Table 2.8 illustrates the performances obtained after running.

Coordinate	Quantity	Measured value
x	Max residual	0.90''
	Mean residual	$1.0'' \times 10^{-3}$
y	Max residual	0.06''
	Mean residual	$8.0'' \times 10^{-4}$
Overall residual RMS	Residual vector	0.0310''

Table 2.8: Algorithm performance evaluation for object with $m_v \sim 20$ (faintest case).

2.3.6.3 Parametric evaluation for faint object guiding

An additional analysis has been carried out in order to quantify the effect of different quantum efficiency and detector dark current onto the algorithm performance. Considering the previous results, we focus the attention on the faint-object ($m_v \sim 20$) template case which is the most critical one. In particular, **dark current** and **quantum efficiency peak** will be parametrically modified in order to asses a detailed analysis on the performances. It must be reminded here that the measured displacements used to evaluate the guiding performance refer only to the tunnels for incoherent light combination between Coudè Room and CCL, as illustrated in the previous chapter. Results are presented in Figure 2.37, 2.38, 2.39 and 2.40.

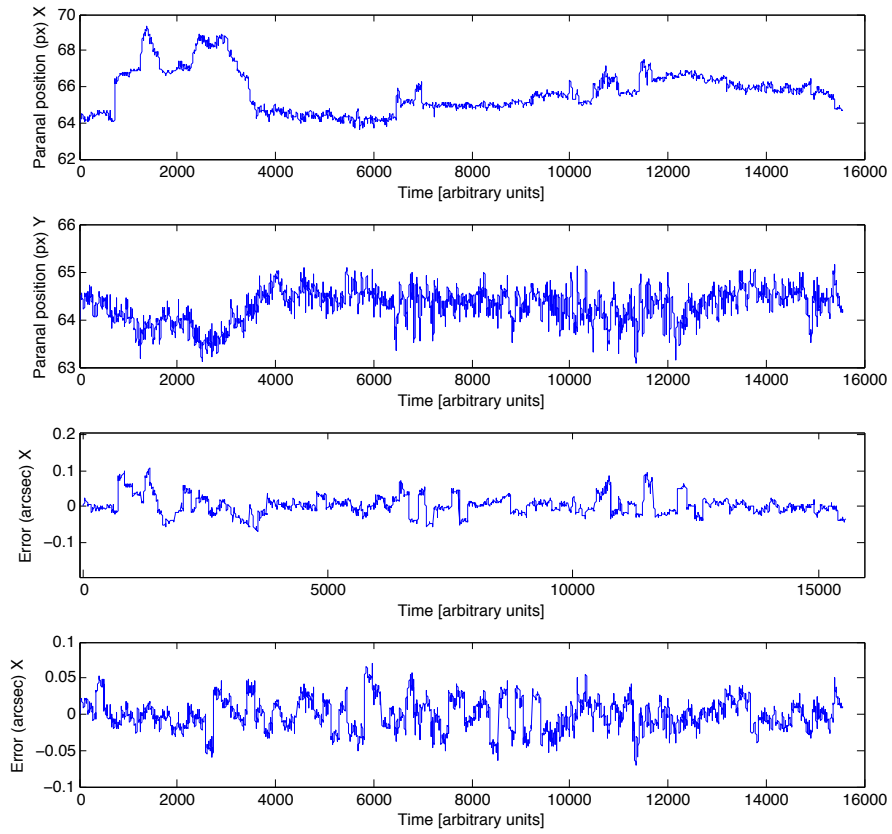


Figure 2.34: Simulation results on guiding an object with $m_v = 20$.

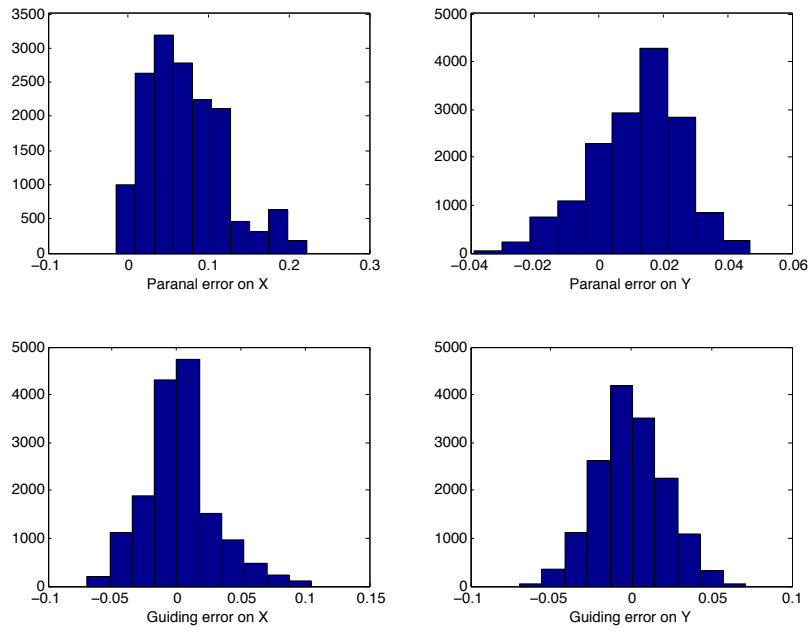


Figure 2.35: Histograms of the residuals during a simulation on guiding faint objects. Panel legends are the same of Figure 2.33

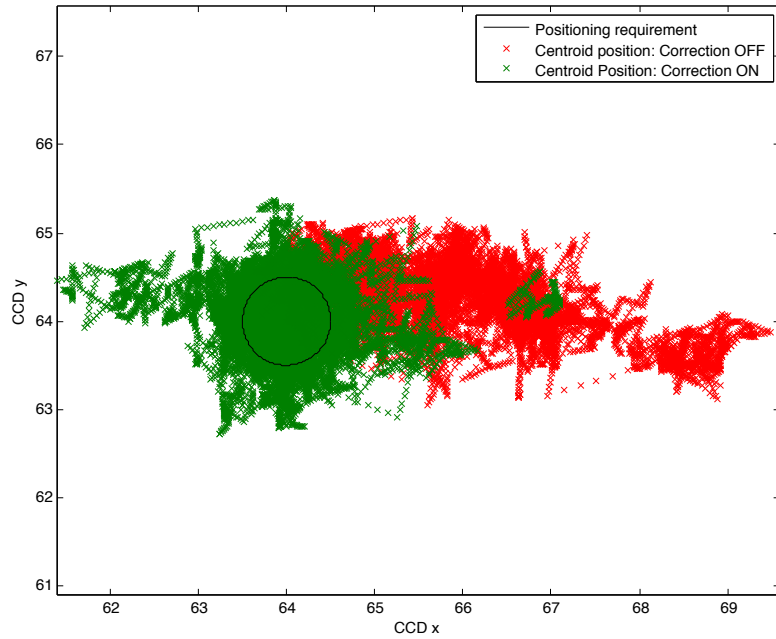


Figure 2.36: Pictorial representation of the position of the spot with respect to the requirement (solid circle).

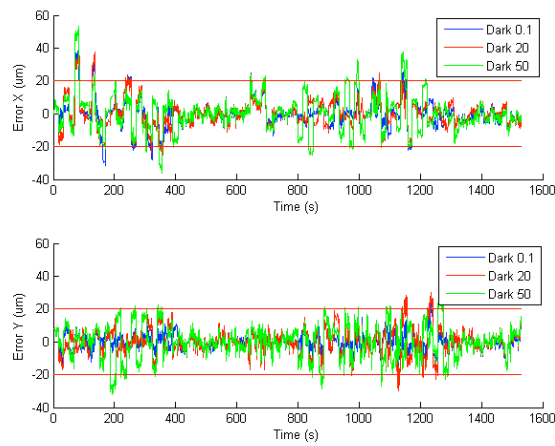


Figure 2.37: Results of the guiding algorithm performances against detector dark current magnification. The dark current in the legend is in units of $e^- px^{-1} s^{-1}$.

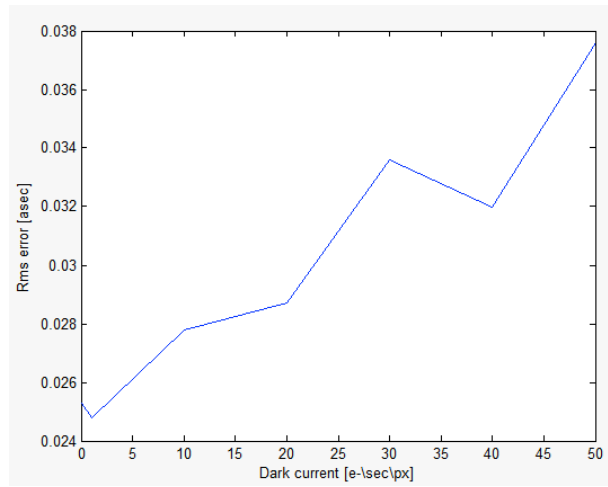


Figure 2.38: RMS error on positioning against detector dark current magnification. The dark current in the legend is in units of $e^- px^{-1} s^{-1}$.

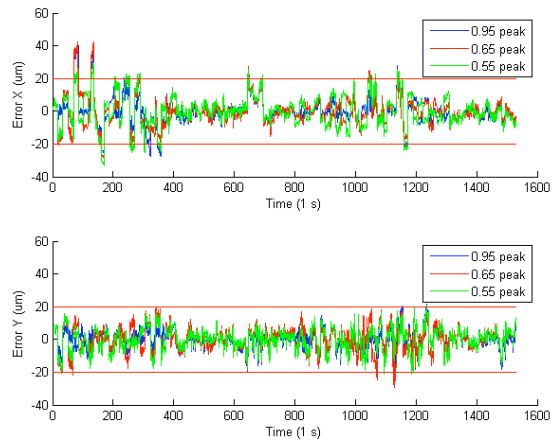


Figure 2.39: Results of the guiding algorithm performances against QE degradation.

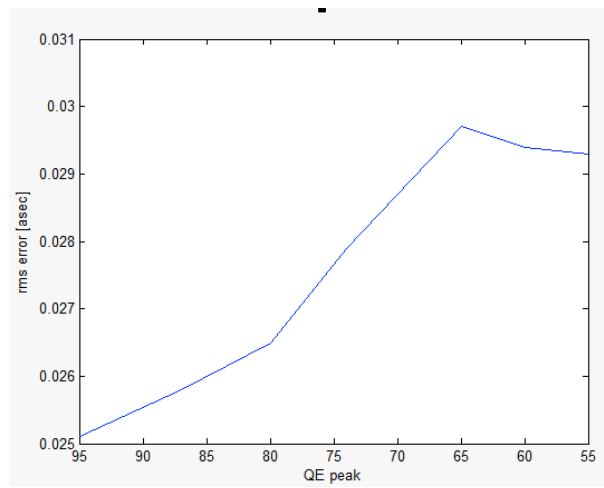


Figure 2.40: RMS error on positioning against QE degradation.

2.4 Design of the Exposure Meter subsystem

2.4.1 General Introduction

When a spectrum of a star is obtained in order to measure its radial velocity, defined as $V_{rad} = V(t) \times \sin(i)$, it must be corrected taking into account the relative speed of the observer which is at rest with respect to the Earth. For this reason, the spectroscopic shift z_{obs} measured by an Earth-bound observer must be converted to the corresponding barycentric shift z_B that would be measured by an observer at rest relative to the Solar System barycenter (SSB) and at zero gravitational potential. In the case of ESPRESSO, the key problem is to know to which precision the transformation can be computed and what are the main factors limiting the accuracy. Movements of the SSB relative to the Galactic center and the Local group are not considered here.

The general formula connecting observed and barycentric shifts [Lindgren and Dravins, 2003] is given by

$$1 + z_b = (1 + z_{obs}) \times \left(1 - \frac{\Phi_{obs}}{c^2} - \frac{|\vec{v}_{obs}|}{2c^2}\right)^{-1} \times \left(1 + \frac{\vec{k} \cdot \vec{v}_{obs}}{c}\right) \quad (2.22)$$

where

1. Φ_{obs} is the gravitational potential measured at the location of the observer.
2. \vec{v}_{obs} is the velocity vector of the observer respect to the Solar System barycenter.
3. \vec{k} is a unit vector pointing from the observer to the target.

The stellar coordinates (expressed in $\langle \alpha, \delta \rangle$) must be known much better than $0.35''$, otherwise varying systematic errors on the line of sight and thus on the barycentric correction will be introduced on yearly time scale. While the coordinate can be assumed to be known in general to much better than $0.35''$ the mean time of the exposure (which is flux weighted) must be known with accuracy in order to perform the correction according to the 1-momentum of the time of exposure. The 1st momentum of a function is generally defined as $\mu'_n = \int_{-\infty}^{\infty} (x - c)^n f(x) dx$.

Given that definition, the Mean Time of Exposure (MTE) is defined as

$$MTE = \frac{\int_{TE}^{TS} tf(t)dt}{\int_{TE}^{TS} f(t)dt} \quad (2.23)$$

where t is the time, $f(t)$ is the measured flux at time t and TS , TE are the start time and the end time of the scientific exposure. MTE might be very different from just the mean value of TS and TE , especially when the atmospheric conditions change significantly during the exposure. In other planet-finder spectrograph like HARPS North and HARPS South the correction is assessed using a simple exposure meter based on a photomultiplier counter and no chromatic effects are investigated. In the case of ESPRESSO, the Exposure Meter is made by two main components: a simple grating (150 lines/mm) and a technical camera equipped with a CCD. In particular, the grating disperses the small portion of the scientific light that feeds the exposure meter and the MTEs are calculated on, let's say, three different channels (which are a slices of the spectrum obtained at the level of the CCD) following the formulas

$$MTE_1 = \frac{\int_{TE}^{TS} tf_1(t)dt}{\int_{TE}^{TS} f_1(t)dt} \quad (2.24)$$

$$MTE_2 = \frac{\int_{TE}^{TS} tf_2(t)dt}{\int_{TE}^{TS} f_2(t)dt} \quad (2.25)$$

$$MTE_3 = \frac{\int_{TE}^{TS} tf_3(t)dt}{\int_{TE}^{TS} f_3(t)dt} \quad (2.26)$$

where $f_1(t)$, $f_2(t)$ and $f_3(t)$ is the integrated measured flux on the relative channel on the spectrum. The number of channels considered in this Chapter has been tuned according to two main parameters. The first one is the wavelength coverage, which is 4000 - 8000 angstroms that yields a sampling of about 1300 Å per channel. This value is sufficient to have a reasonable spectral sampling and enough signal to maintain the error on the computed MTE below the specific. Nevertheless, since both dimensions and numbers of channels are software tunable a further development of this Thesis could be the investigation of a greater number

of channels and/or their dynamical adjustment according to target magnitude or scientific objectives.

The adoption of multi-channel MTE allows to obtain a very precise measurement of the MTE according not only to the spectral type of star that it is observed but also against chromatic atmosphere perturbation. In particular, as reported in the following sections, the MTE could vary significantly between the three channels. The most challenging situation is materialised when the scientific object is observed under sky condition in which a thin cloud passes in front of the target. In this case, the MTE could be significantly different in the blue and red region of the spectrum. In fact, assuming that the covering factor is reasonable, the flux received in the blue part of the spectrum is roughly constant while in the middle/near infrared region the luminosity is significantly dimmed. This dimming is caused by a reduced atmosphere transmission efficiency, due to absorption of red-der photons by molecules of the water vapor in the thin clouds. For this reason, the use of a simple spectrum at the level of the exposure meter allows to capture variation of the MTE according to the wavelength, significantly reducing the error on the RV, in comparison to the calculation of the MTE only on integrated (white) light as shown in the results section of this chapter.

The design of the ESPRESSO exposure meter has been assessed in order to comply with the requirement of radial velocity precision measurement. In particular, starting from three top level requirement of accuracy (10 cm s⁻¹ single UT high resolution, 1 m s⁻¹ single UT high resolution, 5 m s⁻¹ for multi-UT and 10 m s⁻¹ single UT high resolution) the exposure meter design allow to maintain the error induced on the measurement of MTE below the photonic accuracy reached at the level of the scientific echelle spectrum. For example, suppose to observe an $m_v = 8$ class-G star with the scientific goal to measure the shift of its absorption lines on the photosphere with an accuracy of 10 cm s⁻¹. The MTE calculated by the Exposure Meter must be below the error induced on the scientific spectrum of the star by the photonic accuracy and, for this reason, the measure on the scientific spectrum will only be shot-noise limited.

The Exposure Meter (shown in Figure 2.42) works on the same spectral band of the scientific Echelle grating[Spanò et al., 2012]. In particular, the spectral bandwidth is 380nm to \sim 800nm. However, from 380nm to 400 nm the exposure meter is completely blind due to a pass band filter that is required by the exposure meter diffraction grating in order to avoid the overlap of the orders with $m > 1$. The total efficiency of the exposure meter (which includes atmosphere, telescope, slit losses and fiber link efficiency) is presented Figure 2.43. The calculation also considers the quantum efficiency of the Sony ICX285, which is the baseline detector. The optical design of this small subsystem is very similar to that of other spectrographs. The Exposure meter receives the light from the fiber link that will feed ESPRESSO. This extra light comes due to the fact that the F/number of the fibers and that of the spectrograph are different. This situation yields a phenomena called Focal Ratio Degradation (FRD). In particular, about 3% of the light coming from the fiber will never reach the echelle of ESPRESSO and would be otherwise lost. Briefly, as reported in Figure 2.44, the photons coming from the fiber are extracted by the adoption of a small crowned mirror designed to match the halo of FRD (2) and then are focused onto a bundle of fibers (3) that reproduces the same fiber interface entrance on both sides. The recovered light will then feed the exposure meter. In Figure 2.45 the general optical layout aboard the exposure meter is shown. A very general pictorial representation of the subsystem is given in Figure 2.41. The collimator is a standard Edmund triplet (30229 A.1) made out by N-F2 and N-BK7, and the refocusing is obtained through the same objective. A Richardson disperser grating will be mounted into the collimated beam, while a filter wheel will be equipped with neutral filter in order to cope with different star brightnesses. As pointed out before, in order to cut the blue wavelength up to 400nm a custom coating will be assessed in order to avoid order overlapping. The useful Exposure meter bandwidth will be then \sim 400-800nm.

2.4.2 Simulations on the expected performances

In order to characterise the expected performance of the Exposure Meter on the on-sky regime a long series of simulation have been carried out. This section presents the theoretical background in order to understand it and the obtained

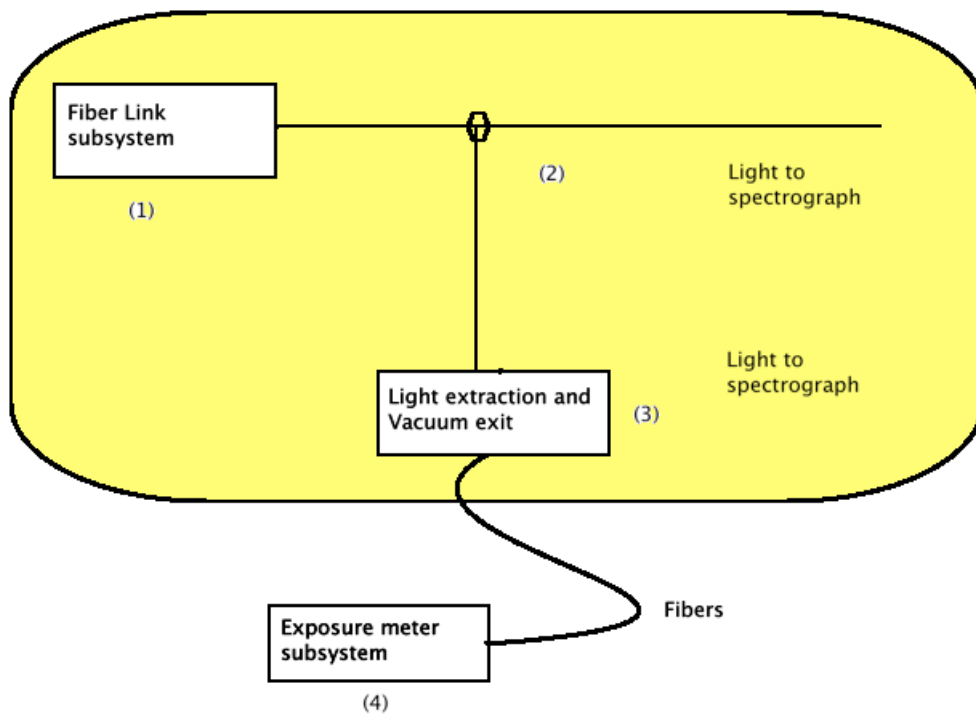


Figure 2.41: ESPRESSO Exposure meter light extraction schema.

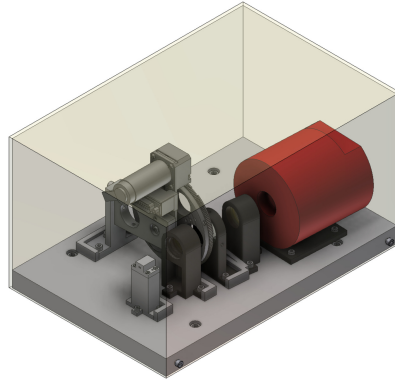


Figure 2.42: ESPRESSO exposure meter 3D general view.

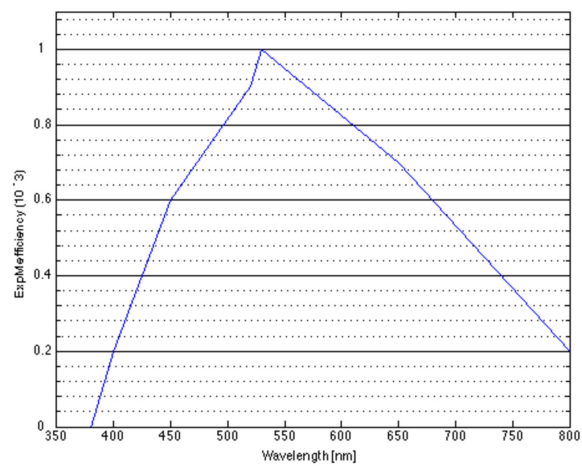


Figure 2.43: ESPRESSO Exposure meter overall efficiency (this curve also considers the whole efficiency of ESPRESSO and includes the Sony ICX 285 detector efficiency)

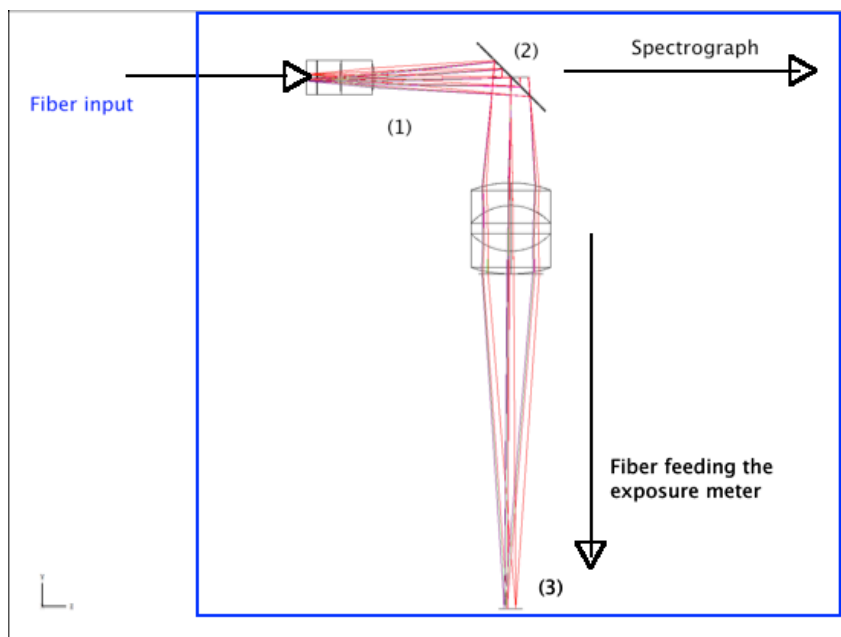


Figure 2.44: ESPRESSO Exposure meter light extraction schema.

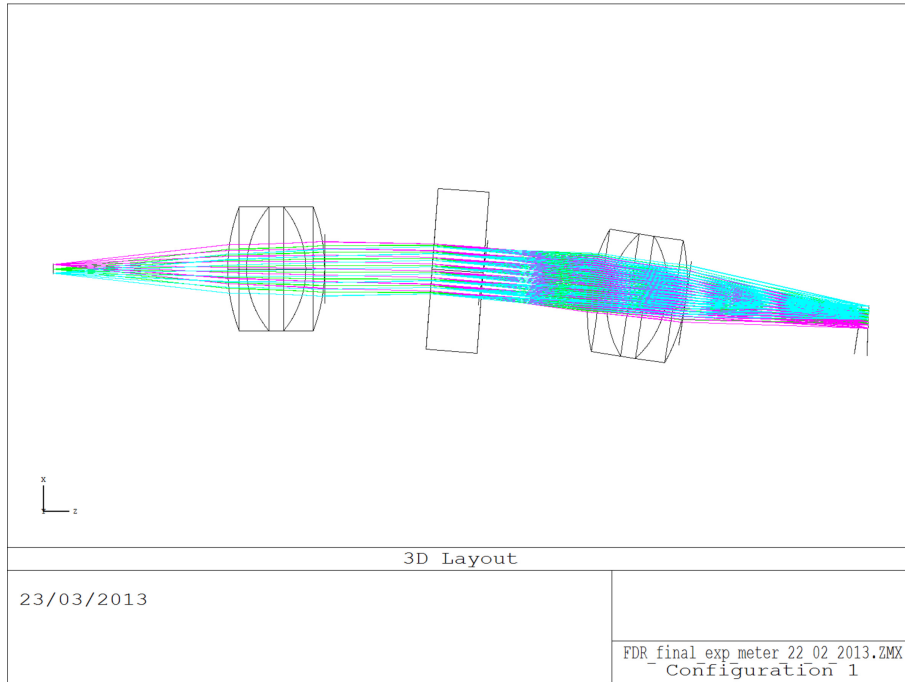


Figure 2.45: ESPRESSO Exposure meter optical setup.

results which confirm the feasibility of the designed instrument for the on sky regime.

2.4.2.1 Flux received and star model

Stars are modeled as a blackbody radiator. In particular, the differential flux received between λ and $\lambda + d\lambda$ is computed as

$$d\phi = B(\lambda, T) \times ExpM_{efficiency}(\lambda) \times \frac{\lambda}{hc} \times \phi^* \times 10^{\frac{-m_v}{2.5}} d\lambda \quad (2.27)$$

where $B(\lambda, T)$ is the Plank law (in units of $\text{erg cm}^{-2} \text{s}^{-1} \text{cm}^{-1}$) defined as

$$B_\lambda(T) = \frac{2hc^2}{\lambda^5} \frac{1}{e^{\frac{hc}{\lambda k_B T}} - 1} \quad (2.28)$$

and ϕ^* is a normalisation constant such that the differential flux density at 5550 Å is 1000 photons $\text{s}^{-1} \text{cm}^{-2} \text{Å}^{-1}$ for a 0th magnitude star in the V Band

Stellar class	Surface temperature	m_v
BV1 - main sequence (blue)	~ 25.000 K	from 0th to 20th
GV5 - main sequence (yellow)	~ 5.300 K	from 0th to 20th
MV7 - main sequence (red to brown)	~ 2.500 K	from 0th to 20th

Table 2.9: Star spectral types and properties considered for the performed simulations.

(Johnson UVB filter) and m_v is the apparent magnitude of the star considered. $ExpM_{efficiency}$ is a function that takes into account the efficiency reported in Figure 2.43. Since the design approach of the exposure was such that three chromatic channels will be used for the calculation of the MTE, simulations have been performed considering different stellar spectral classes, whose properties are reported in Table 2.9.

2.4.2.2 Sky model

The sky emission is modeled as a simple power-law assuming that the sky surface brightness is $\sim 21 m_v \text{ arcsec}^{-1}$ in the visible V band. In the case of high resolution mode and multi-UT mode, the subtended area is 0.785 arcsec^2 . For this reason and for the quite short exposure time of the Exposure Meter TCCD its contribution is negligible (at least up to 19th-20th magnitude).

2.4.2.3 $\frac{d_p}{d\lambda}$ dispersion function

For the simulation is mandatory to know the position of the image of the fiber in function of the wavelength. In Figure 2.46 the function that models the position of the image against the wavelength of the choosed grating is plotted. It will be adopted for the numerical simulations in order to properly emulate the spectrum obtained on the CCD of the Exposure Meter. The dispersion power of the grating is of the order of $6 \times 10^{-4} \text{ mm } \text{\AA}^{-1}$. Note that, despite a very little non linear dispersion which appears in complete ray tracing, the peak to valley between the two edge is less than $4\mu\text{m}$, which is of the order of a fraction of the detector pixel. For this reason, the dispersion can be safely considered constant. In the spatial direction (Y) the position is constant along the CCD ($\pm 0.1 \text{ px}$ peak to valley).

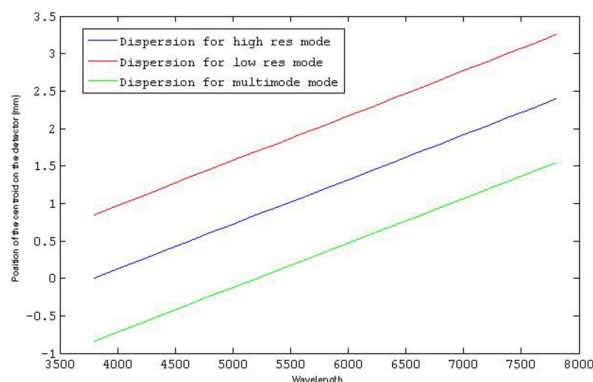


Figure 2.46: ESPRESSO Exposure meter ray tracing function. This function allows to know the absolute position (in mm respect to the centre of the CCD) of the image against λ with respect to the dispersion axis..

For all of these reasons, the function could be assumed to be of the form

$$\frac{dp}{d\lambda} \sim 6 \times 10^{-4} \text{ mm } \text{\AA}^{-1} \quad (2.29)$$

2.4.2.4 PSF model of the Exposure Meter optics

Through the adoption of ray tracing (Zemax analysis) the point spread function of the Exposure Meter has been evaluated. The PSF is quite stable though different wavelength but slightly differences appear (in the order of few pixels). The PSF is reasonably assumed to be gaussian. In particular, Figure 2.47 illustrates the PSF dimension (in μm) while Figure 2.48 shows what appears on the detector when an impulsive signal (Dirac delta-function) is applied in front of the overall exposure meter optics.

2.4.2.5 Fiber image

The image of the fiber for the considered case (Multi UT mode, Ultra High resolution 1UT or High resolution 1UT) is modeled through the drawing of the relative polygon on the detector matrix. They are reported in Table 2.10:

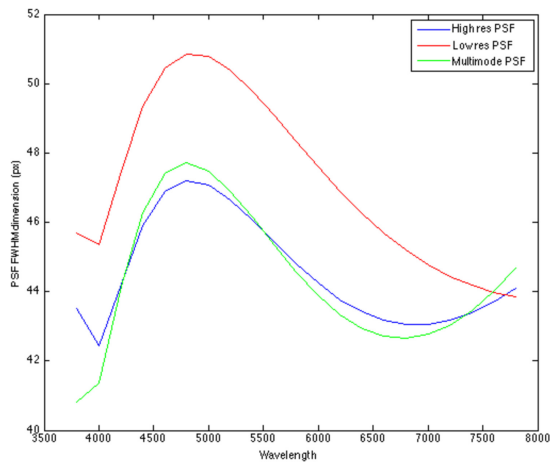


Figure 2.47: ESPRESSO Exposure meter PSF FWHM function against λ in a pictorial representation. The slightly difference between the three ESPRESSO modes are apparent due to different optical path through the overall Exposure Meter subsystem to the detector.

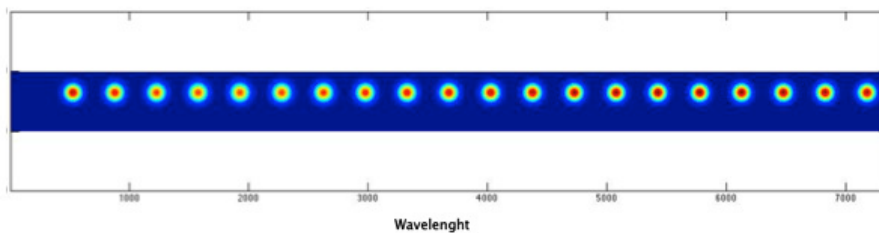


Figure 2.48: ESPRESSO Exposure meter PSF function against λ in a pictorial representation.

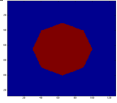
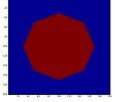
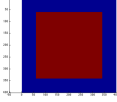
Mode	Description	Image
Single 1UT UHR mode	Octagonal fiber of 70 μm	
Single 1UT HR mode	Octagonal fiber of 140 μm	
Multi-UT mode	Rectangular fiber of $\sim 280 \mu\text{m}$	

Table 2.10: Image fibers on the focal plane and configuration.

2.4.2.6 Image on the focal plane

At the level of the detector the images of the fibers reported in Table 2.10 must be corrected for the PSF function described in the previous sections. The equation ¹takes into account the canonical definition of convolution in a discrete domain:

$$Image_{detector}(i, j) = Image_{fiber} \otimes PSF(\lambda) = \sum_{j=-\infty}^{j=+\infty} \sum_{i=-\infty}^{i=+\infty} Image(i, j) \times PSF(m-i, m-j) \quad (2.30)$$

2.4.2.7 Slit loss and dependence on seeing

The seeing at wavelength λ follows the formula

$$S(\lambda) = S_{5500\text{\AA}} \left(\frac{\lambda}{5500\text{\AA}} \right)^{-\frac{1}{6}} \quad (2.31)$$

where S_{5500} is the seeing measured at 5500 \AA . This relation obviously affects the amount of light that enter the spectrograph since the subtended slit is a pinhole of $\sim 1''$ for the High Resolution mode. For the simulation a mean seeing of $1''$ is assumed (up to $m_v \sim 15$, for m_v greater than 15 $\sim 0.80''$ seeing is assumed) and the efficiency due to slit-loss is considered. For instance, at 5500 \AA the efficiency for a seeing of $1''$ is about 50%. In other words, only 50% of the scientific light is

¹The ∞ obviously appears in the theoretical definition. It will be substituted with the detector dimensions.

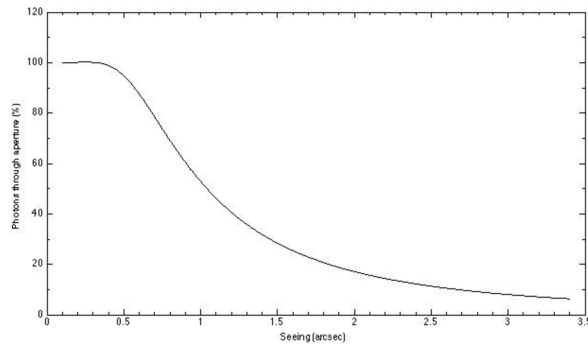


Figure 2.49: Seeing vs slit efficiency curve adopted for simulations

able to reach the spectrograph while the remnant photons are back reflected for the guiding system [Landoni et al. \[2012b\]](#); [Riva et al. \[2012\]](#). The seeing-efficiency curve is reported in Figure 2.49. The behaviour has been assessed in two ways, numerical and analytical, in order to ensure a good estimation of the slit loss related to seeing effect. The analytical expression for the slit loss is given by the Equation 2.32.

$$f = 1 - \frac{1}{\exp\left(\sqrt{\log 2} \frac{\Phi f}{SP\Phi_s}\right)^2} \quad (2.32)$$

where Φf is the pinhole diameter, Φ_s is the seeing and SP is scale plate of the optical system.

2.4.2.8 CCD configuration

The frequency for the readout of the technical CCD of the Exposure Meter has been evaluated taking into account noises from the detector, accuracy on the measurement on the flux and computational overhead. In Table 2.11 are reported the readout frequencies adopted for the simulation that are a baseline for the on-sky regime (note that T is the exposure time of scientific object).

2.4.2.9 Detector simulation for performances evaluation

This section presents the algorithm adopted to generate a generic image of the Exposure Meter CCD detector. The result is used in order to evaluate the performance of the overall system. For numerical reason, the spectrum is simulated

RV	UTs m_v limit	Read frequency	CCD gain and bin
10 cm s ⁻¹	1UT - m_v 10	$T/1000$ or less	High , 2x2 bin
1 m s ⁻¹	1UT - m_v 15	$T/100$ or less	Low , 2x2 bin
10 m s ⁻¹	1UT - m_v 20	$T/10$	Low, 2x2 bin
5 m s ⁻¹	multiUT - m_v 20	$T/10 * (nUT)$	Low, 2x2 bin

Table 2.11: CCD configuration for the Exposure meter. T is the scientific exposure time and nUT is the number of UTs considered in the case of multiUT observation mode

dividing in bin of $\sim 20\text{\AA}$. Starting from the definition of the received differential flux, wavelength dispersion and PSF a CCD is generated as follow:

1. Compute the number of photon received from the scientific object in a bin of 20\AA by the integration of Equation 2.27. In particular, the total number of photon received in a 20\AA wide bin is

$$ph_{bin}^{start} = \int_{bin_{start}}^{bin_{end}} B(\lambda, T) \times ExpM_{efficiency}(\lambda) \times \frac{\lambda}{hc} \times \phi^* \times 10^{-\frac{m_v}{2.5}} d\lambda \quad (2.33)$$

2. Compute the number of photon received in a bin of a 20\AA from the sky by the integration of the formula

$$ph_{bin}^{start} = \int_{bin_{start}}^{bin_{end}} 2 \times 10^{-17} \times ExpM_{efficiency}(\lambda) \times \frac{\lambda}{hc} \times \phi^* \times 10^{-\frac{m_v}{2.5}} d\lambda \quad (2.34)$$

The differential flux of $10^{-17} \text{ erg cm}^{-2} \text{ s}^{-1} \text{\AA}^{-1}$ correspond to the mean sky background level at ESO Paranal .

3. Draw the image of a fiber (according to which mode is under simulation, see Table 2.10) in the detector at the position $\frac{bin_{start}+bin_{end}}{2}$ adopting the relation $(\frac{\lambda}{\Delta\lambda})$ reported in Figure 2.46 and imposing that the total number of counts is such that it is equal to the number of scientific photon plus the photons received from the sky (energy conservation). Uniform illumination of the fiber image is assumed.

-
4. Apply Equation 2.30 in order to convolve the drawn image with the instrumental PSF response at wavelength $\frac{bin_{start}+bin_{end}}{2}$
 5. Add the result to the overall image (which contains the draws of each fiber in their proper positions).
 6. Repeat from step 1 until $bin_{end} = 8000 \text{ \AA}$.
 7. Apply the binning adopting a resize of the image.
 8. Multiply the overall results for the integration time considered.

At this point, the image generated is saved and stored for further computation (in particular for the theoretical MTE, that must be compared with the measured one after detector noises) and the noises from the detector are generated in the same way that it is explained in Section 2.3.5.1. In Figure 2.50 it is reported the result of the simulation of the Exposure Meter detector for an MV5 spectral type class with apparent magnitude $m_v = 15$. The first panel shows the obtained detector at the end of the generation (with noises) while the second panel shows the extracted spectrum (in ADU).

2.4.3 Simulations results and expected performances

The performance of the exposure meter, in terms of accuracy and precision of the MTE calculation, has been evaluated starting from the most common scientific cases requirement. In particular, the simulation framework has been stressed in two different situations: a **zero order evaluation** in which it is assumed to observe the scientific target with no perturbation at the level of the atmosphere or on the instrument itself and a **second order evaluation** in which a chromatic perturbation is considered. As noted in the previous sections, when a chromatic perturbation occurs, the received flux is dimmed especially in the red part of the received light. This situation is typical when observing the target through a thin cloud.

As an overall consideration, the flow diagram of Figure 2.53 reports in detail how a generic simulation of a scientific exposure has been implemented. Briefly, knowing the required exposure time for reaching desired radial velocity accuracy,

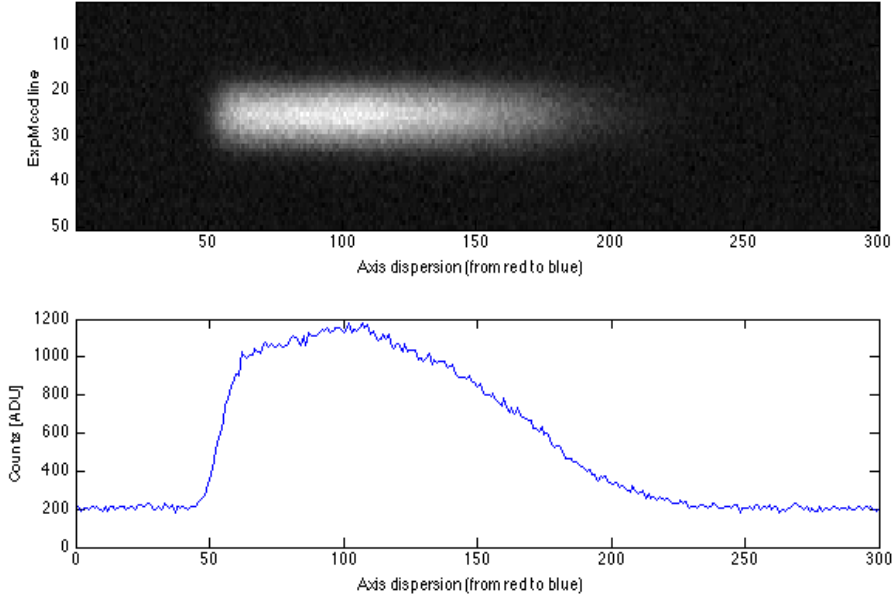


Figure 2.50: Simulation of a spectrum obtained in the exposure meter for a M star of $m_v = 15$ assuming seeing of $\sim 1.00''$

the TCCDs of the Exposure meter are read out (in this case, simulated) and stored for the final computation of the MTE. The integration times (readout frequencies) of the TCCD are investigated in Table 2.11. In particular, the accuracy on RMS radial velocity on the scientific spectrum is defined as

$$\text{rms}(\text{m s}^{-1})_{\text{photon}} = \frac{K}{S/N_{5500\text{\AA}}} \quad (2.35)$$

where K is a constant which depend on the characteristic of the spectrograph (e.g. resolution, detector noises, etc.). For instance, as a rule of thumb, in the case of HARPS [Mayor et al., 2003] for a G2V star a RV of $\sim 1 \text{ m s}^{-1}$ is reached when the S/N is about 100 per pixel, as illustrated by Equation 2.35 assuming $K = 100$. The approximate exposure time vs magnitudes are depicted in Figure 2.52 and Figure 2.51 (Pepe et al 2013, ESO Messenger in press). In particular, Figure 2.52 refers to 1UT mode while Figure 2.51 to multiUT (4) configuration mode.

Finally, the simulation software performs the calculation of the MTEs in each

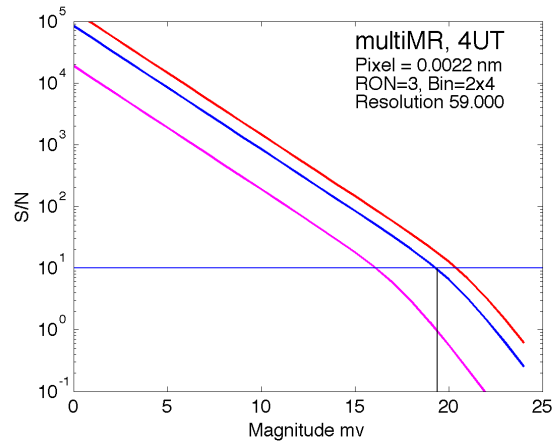


Figure 2.51: Simulation for the exposure time vs magnitude in multiUT mode. Purple solid line represent $t_{exp} = 60$ s, blue is $t_{exp} = 1200$ s and red is $t_{exp} = 3600$ s.

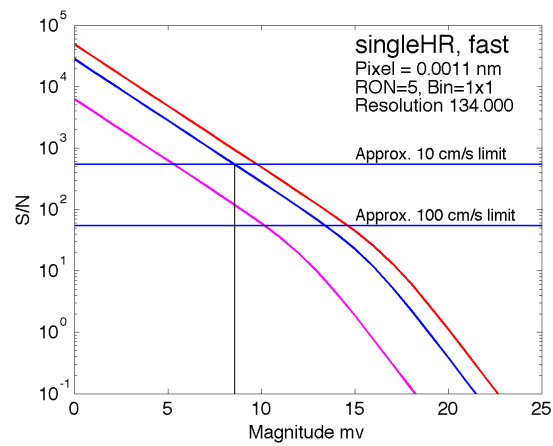


Figure 2.52: Simulation for the exposure time vs magnitude in singleUT mode. Legend is the same of Figure 2.51

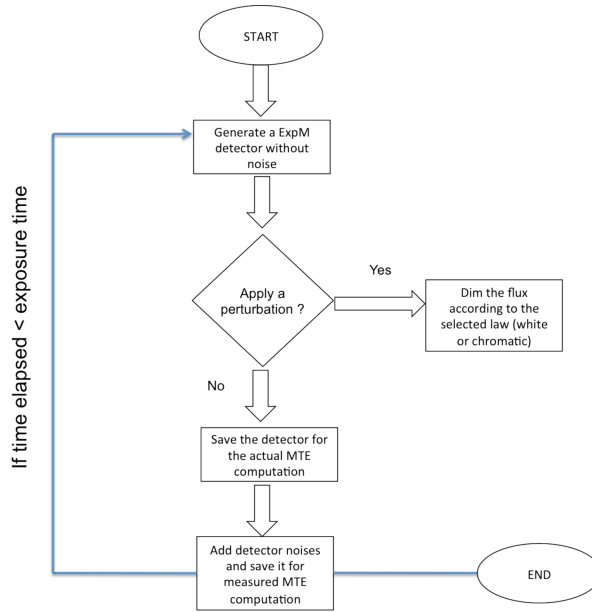


Figure 2.53: Flow chart for the strategy adopted for the scientific simulation. Each simulation is repeated 100 times in order to investigate general statistical properties.

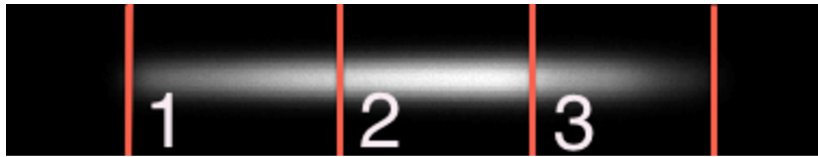


Figure 2.54: ESPRESSO Exposure Meter channels.

channel on ideal ccd (noise free) in order to evaluate its actual value, and on real ccd with relative noises (as explained in the previous sections). The differences between the actual value and the simulated one (after noises) is then converted in RV accuracy error induced by the exposure meter assuming that, in the worst case, an error of 0.6s corresponds to 1 cm/s in the RV measurement. This is, of course, the worst case since the value depends on the declination of the target. For the simulation, dependences on $\langle \alpha, \delta \rangle$ are not investigated.

Simulations are repeated 100 times in order to investigate the r.m.s. error and the general behaviour of the system. The channels, which simulations refer

to, are indicated by the pictorial representation of Figure 2.54. We stress again the fact that the dispersion axis is inverted at the level of the focal plane in which the detector lies (from red to blue). It is also important here to recall the general aim and algorithm behind each simulation. In particular, starting from the scientific exposure time (T) needed to reach the photonics accuracy in function of the magnitude target (see e.g. Figures 2.51, 2.52) n noise-free images with integration time of $\frac{T}{n}$ (see Table 2.11) are generated (and possibly blurred in case of perturbation). Then, the MTE (which is the actual noise free value) is computed. The n CCD images passes throughout the chain of all noises that must be considered (photon noise, dark current, RON, etc) following the simulation procedure also adopted in par. 2.3.5. The MTE is then calculated on the actual (noisy) CCD images. The difference between the actual value of MTE and the measured one is then computed and converted in RV error according to the fact that 0.6s of error is about 1 cm s^{-1} on the measured star RV. The overall process is repeated 100 times in order to investigate statistical properties (in terms of rms, for example). Results are presented both in tabular and graphical format. The data reduction of CCDs frames is assumed to be easy to compute and no particular tasks are considered at this level of approximation. In particular, for each frame the background is computed in a small region away from the spectrum (median value of about 10×10 pixels) and then it is subtracted from the overall frame. The fluxes in each channel (used for the computation of the MTE) are then obtained summing up pixels belonging to that channel (column of the CCD). In order to enhance the SNR for very faint sources it is suggested to use only the central 3 or 5 lines of the spatial axis of CCD since their SNR is sufficient enough for the computation of MTE. As in the case of aperture photometry, trying add more pixels for faint sources also increase the noises although much more signal is contained in the aperture.

2.4.3.1 First scientific case - 10 cm s^{-1} RV accuracy

In order to evaluate the performance of the designed Exposure Meter for the 10 cm/s scientific goal, the simulations start with the assumption of the integration time needed for reach this accuracy at the level of the scientific spectrum (from

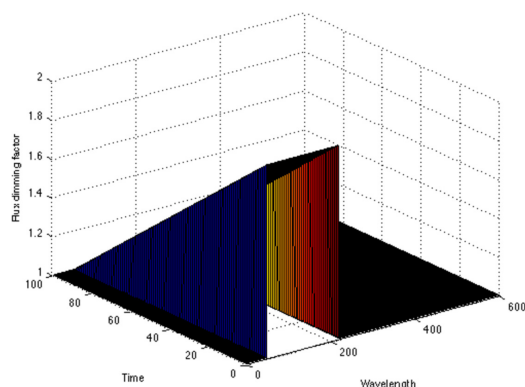


Figure 2.55: Behavior of the perturbation as seen on the CCD aboard the Exposure Meter.

now, referred as photonic accuracy). In particular, the limit magnitude for the 10 cm/s is $m_v = 10$ since the required integration time for the photonic accuracy of 10 cm/s is about 1.6 hours. For $m_v < 10$ the error induced on the calculation of the MTE by the Exposure Meter is negligible ($\ll 1$ cm/s) and the accuracy on the scientific spectrum is always shot-noise limited. Moreover, for magnitude $m_v < 2$ the exposure meter is not required since the integration time should be very short (less than 10 seconds). However, since in the optical design a filter wheel has been implemented the Exposure Meter could be used with a read out frequency limited by the maximum sampling frequency of the camera (12 fps, for instance) or less if needed.

For $m_v = 10$, the limit case, two simulation has been assessed. In the first one, no perturbation are applied on the system or on the atmosphere. Results are presented in Figure 2.57 and 2.58 and Table 2.12 and 2.13 . In particular, for the 100 simulations the error induced by the Exposure Meter on the channels are presented in the boxes of Figure 2.57 for the spectral type B,G and M investigated while r.m.s. error are tabulated in Table 2.12 and 2.13 . The second case considers a chromatic perturbation modelled by the function of Figure 2.55 where its behaviour can be seen. The effect of the perturbation on the spectra at the level of the exposure meter, plotted against time, could be spotted in Figure 2.56. The second order simulations carried out also adopt symmetric perturbation in time, in order to better emulate the actual sky condition on different exposures.

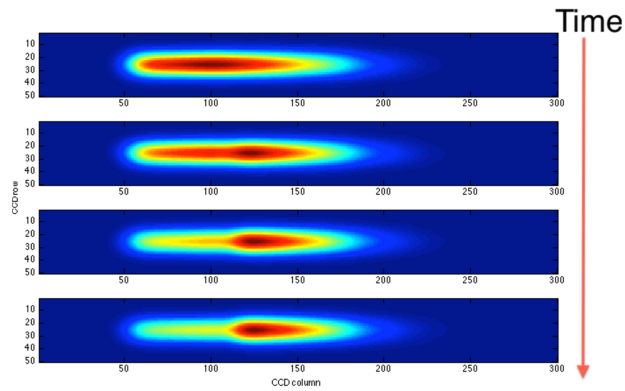


Figure 2.56: Behavior of the perturbation as seen on the CCD aboard the Exposure Meter.

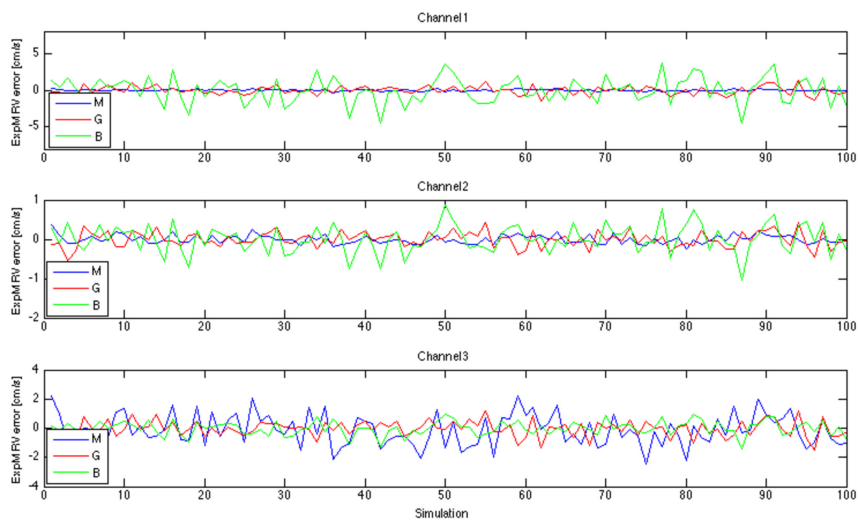


Figure 2.57: ESPRESSO Exposure Meter performance for 10cm/s goal with $m_v = 10$ with perturbations on the system or atmosphere.

Channel / Spectral type	B	G	M
r.m.s error on Channel 1	1.2 cm/s	0.5 cm/s	0.1 cm/s
r.m.s error on Channel 2	0.3 cm/s	0.2 cm/s	0.2 cm/s
r.m.s error on Channel 3	0.4 cm/s	0.5 cm/s	1.3 cm/s

Table 2.12: Root mean square error for 10cm s^{-1} scientific goal, $m_v = 10$ and no perturbation on the system

Channel / Spectral type	B	G	M
r.m.s error on Channel 1	2.5 cm/s	0.8 cm/s	0.1 cm/s
r.m.s error on Channel 2	0.3 cm/s	0.3 cm/s	0.2 cm/s
r.m.s error on Channel 3	0.5 cm/s	0.6 cm/s	1.5 cm/s

Table 2.13: Root mean square error for 10cm s^{-1} scientific goal, $m_v = 10$ with perturbation applied on the system

Is a chromatic exposure meter a must-have device ? Comparison between spectrum and white light

It is now important to note that the use of the small spectrum at the level of the exposure meter significantly reduce the error on the MTE when such a perturbation occurs at the level of the atmosphere. In particular, if the MTE is calculated only on the integrated white light for this simulation it gives a value of $2.9377\text{e}+03$ s. The MTE, since a perturbation occurred, is obviously different from the simple half value of the integration time (which is 3000s in this case).

However, when inspecting the MTE on channel 1 (red) and channel 3 (blue) the results are significantly different since in the red band less light reached the instrument due to the perturbation (note that the situation could be exactly symmetric if the perturbation occurs in the blue part instead of happening in the red one. In detail, $\text{MTE}(\text{Ch1}) = 2.6550\text{e}+03$ and $\text{MTE}(\text{Ch3}) \sim 3000\text{s}$. Now, comparing the MTE on channel 1 with the MTE on white light gives a difference of ~ 282 s that corresponds to a worst case error of ~ 4.7 m/s. For this reason, the correction of the relative shift of a stellar absorption line in the red region of the spectrum using only the MTE calculated on the integrated light would cause an error of several meters per second. These kind of consideration also apply for the next simulations of 1m/s and 10 m/s of scientific goals. In the case of multi-UT mode no perturba-

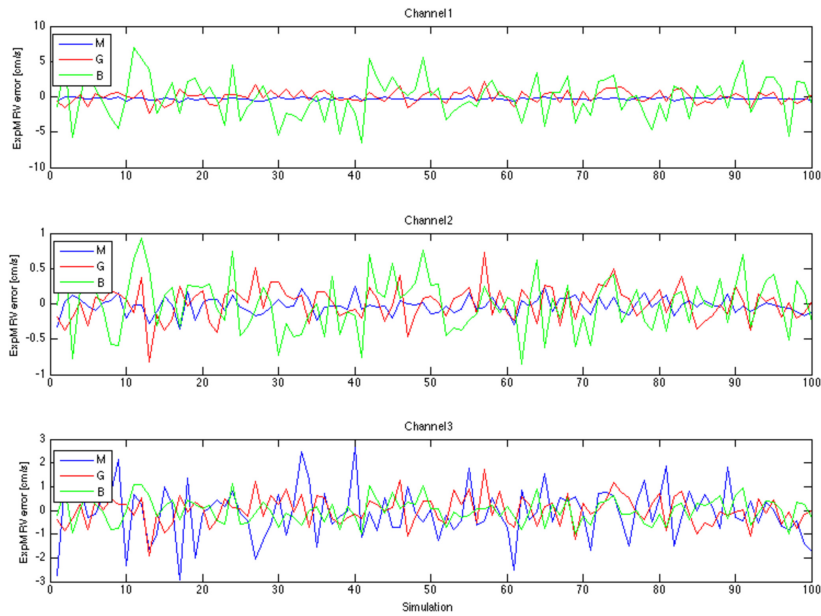


Figure 2.58: ESPRESSO Exposure Meter performances against a chromatic perturbation on the red part (cloud passing through).

tion are applied since the light comes from different arms of the instrument and the sky conditions could also be slightly different.

2.4.3.2 Second scientific case - 1 m s^{-1} RV accuracy

As in the previous case, two kind of simulations have been carried out. For 1 m s^{-1} the limit magnitude is $m_v = 15$ since the exposure time needed to reach the desired accuracy is about 1.5 hours. For magnitude $m_v < 15$ the error induced by the exposure meter is negligible in comparison to the requirement of the 1 m s^{-1} accuracy and, in any case, the error induced by this subsystem is lower than the photonic precision reached at the level of the scientific spectrum. Results are reported in Figures 2.59, 2.60 and Tables 2.14, 2.15.

The adoption of a spectrum, as illustrated in the previous scientific case, reduced significantly the error when the chromatic perturbation occurred. In particular, if the system only adopt the MTE on the integrated white light, the error on the red part of the spectrum for inaccurate Earth-motion correction would be of about several meters per second.

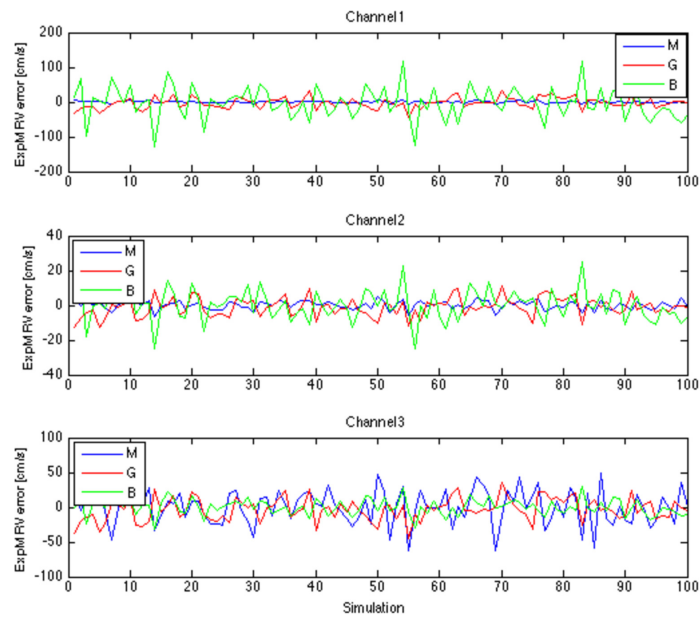


Figure 2.59: - ESPRESSO Exposure Meter performance for 1m/s scientific goal. No perturbations are applied to the system

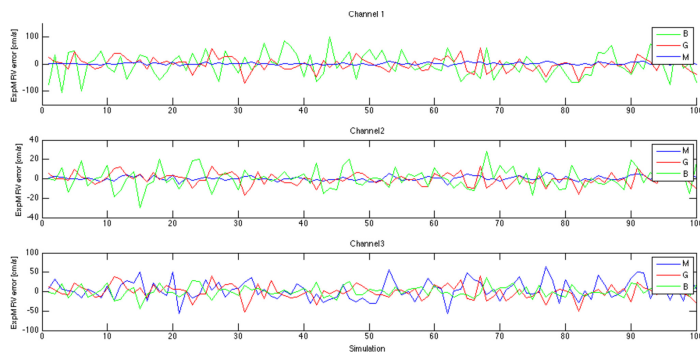


Figure 2.60: - ESPRESSO Exposure Meter performance for 1m/s scientific goal with perturbations applied to the system

Channel / Spectral type	B	G	M
r.m.s error on Channel 1	0.30 m/s	0.1 m/s	0.05 m/s
r.m.s error on Channel 2	0.1 m/s	0.05 m/s	0.1 m/s
r.m.s error on Channel 3	0.12 m/s	0.15 m/s	0.2 m/s

Table 2.14: Root mean square error for 1 m s^{-1} scientific goal, $m_v = 15$ without perturbation applied on the system

Channel / Spectral type	B	G	M
r.m.s. error on Channel 1	0.37 m/s	0.20 m/s	0.1 m/s
r.m.s. error on Channel 2	0.10 m/s	0.10 m/s	0.2 m/s
r.m.s. error on Channel 3	0.10 m/s	0.15 m/s	0.25 m/s

Table 2.15: Root mean square error for 1 m s^{-1} scientific goal, $m_v = 15$ **with** perturbation applied on the system

2.4.3.3 Third scientific case - 10 m s^{-1} RV accuracy

For the 10 m s^{-1} accuracy scientific case the limit magnitude is about 19-20 (worst case considered for the simulation). For brighter object (e.g. $m_v = 16, 18$) the error induced by the exposure meter in its channels is negligible (less than 1 m s^{-1}) compared to the photonic accuracy reached at the level of the scientific spectrum. For this reason, the measurements are shot noise limited and not affected by the error that occurs on the MTE computed by adopting the designed Exposure Meter. Since, in this case, the requirements are quite loose and reasonable perturbations affects the MTE for an amount that is less than 10 m s^{-1} only a zero order simulation has been carried out. Results are reported in Figure 2.61 and Table 2.16.

Channel / Spectral type	B	G	M
r.m.s error on Channel 1	2.5 m/s	2.2 m/s	0.7 m/s
r.m.s error on Channel 2	1.0 m/s	0.95 m/s	1 m/s
r.m.s error on Channel 3	1.5 m/s	2.0 m/s	3 m/s

Table 2.16: Root mean square error for 10 m s^{-1} scientific goal, $m_v \sim 20$ **without** perturbation applied on the system

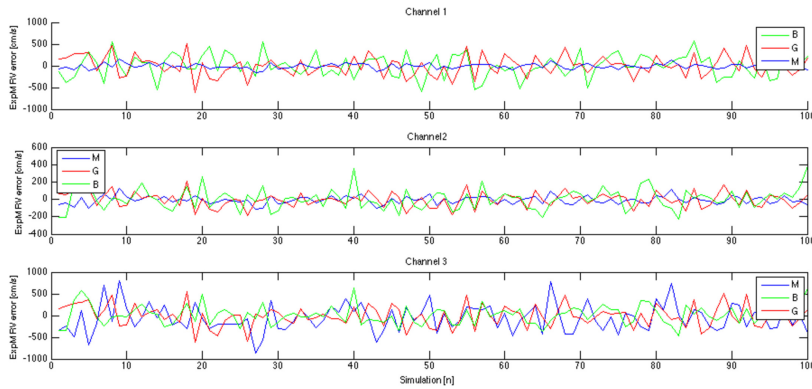


Figure 2.61: - ESPRESSO Exposure Meter performance for 10 m/s scientific goal without perturbation

2.4.3.4 Multimode setup - An introduction to 5 m s⁻¹ RV accuracy case

In the case of multi-UT observation mode, the spectrograph and the exposure meter collect the light from the scientific target from more than 1 telescope. For this reason, the flux received is n -times that received from only one UT. As a representative case, a simulation for an $mv = 20$ object has been carried out. In particular, in order to reach a photonic accuracy of 5 m s⁻¹ an exposure of 3h is required with only one UT. This integration time is quite high in comparison to a typical exposure time in an Observation Block (less than 2 hours). However, adopting 4-UT configuration the time needed is reduced by a factor of 4 since 4 telescopes feed the spectrograph simultaneously. In Figure 2.62 and Table 2.17 are reported the errors induced by the exposure meter with a configuration of 4-UT, adopting parameters reported in Table 2.11.

Channel / Spectral type	B	G	M
r.m.s error on Channel 1	3.2 m/s	3.0 m/s	1.1 m/s
r.m.s error on Channel 2	1.6 m/s	2.4 m/s	2.0 m/s
r.m.s error on Channel 3	1.6 m/s	2.8 m/s	3.0 m/s

Table 2.17: ESPRESSO Exposure Meter r.m.s. error on the three channel in multi-UT configuration

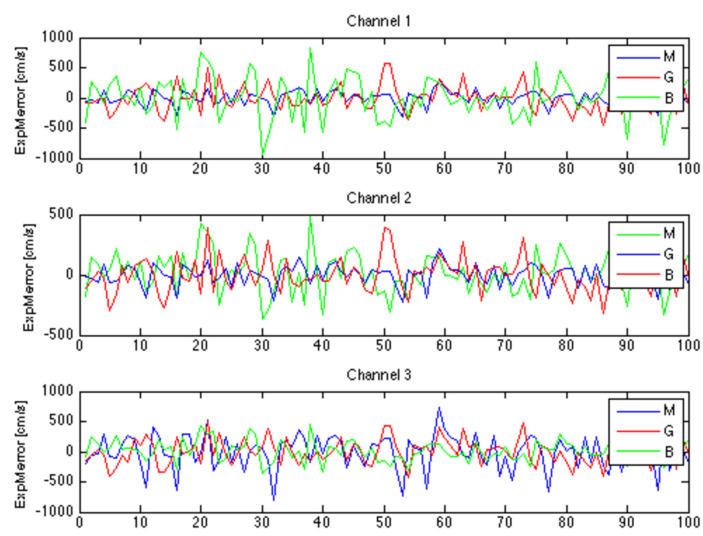


Figure 2.62: - ESPRESSO Exposure Meter r.m.s. error on the three channel in multi-UT configuration

Chapter 3

Application of spectroscopy to BL Lacertae objects: from low to medium-high resolution. The case of FORS2 and X-Shooter

3.1 An introduction to AGN

3.1.1 What is an AGN ?

Active galactic nuclei (AGN) are astrophysical sources characterised by a strong emission of electromagnetic radiation. The power of which is of the order of 10^{42} - 10^{48} erg s⁻¹. The emitting region is extremely compact and usually its volume is about 1 pc³. The radiation is emitted across the overall electromagnetic spectrum, from radio to Very High Energy (VHE) γ -rays. For the brightest sources the bolometric luminosity is of the order 10^{47} erg s⁻¹. According to the Eddington luminosity,

$$L_{bol} \leq L_{Edd} = \frac{4\pi GM_{\bullet} m_p c}{\sigma_t} \quad (3.1)$$

which implies that $M_{\bullet} \geq 7 \times 10^8 M_{\odot}$. The gravitational radius R_s for this mass is $R_s = \frac{2GM}{c^2}$ that turns out to be $R_s = 2.1 \times 10^{14}$ cm. This value is comparable with the one reported for the emitting region estimated through the time

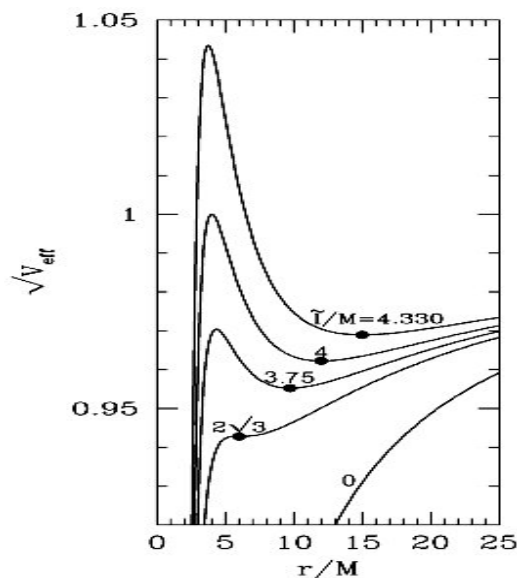


Figure 3.1: Effective potential of a test particle test with mass M in orbit around a Schwarchild Black Hole.

scale variability of the source (assuming causality connection). For this reason, the currently accepted paradigm for AGN emission is that the released power is supported by the accretion of matter onto a Super Massive Black Hole (SMBH) which dissipates its potential gravitational energy . If the central black hole has a mass M_{\bullet} , the energy released *per unit mass* is then

$$\Delta E_{acc} = \frac{GM}{R_{isco}} \quad (3.2)$$

where R_{isco} is the inner stable circular orbit. Assuming a spherical Schwarchild metric, it is safe to assume $R_{isco} \sim R_{grav} = \frac{2GM}{c^2}$ and the energy released per unit mass is $\Delta E = \epsilon \Delta M c^2 \sim 0.1 m c^2$. The mass-energy conversion efficiency ϵ is maximum when a highly rotating Kerr black hole with angular momentum J is consider. In this case, the energy released per unit mass would be $\Delta E \sim 0.40 \Delta M c^2$ (see also Figures 3.2, 3.2).

It is also important to note that the inner stable circular orbit is also a function of the Black Hole spin, as illustrated in Figure 3.2.

For QSOs objects, where typical luminosities are of the order of $L \sim 10^{46} \text{ erg s}^{-1}$

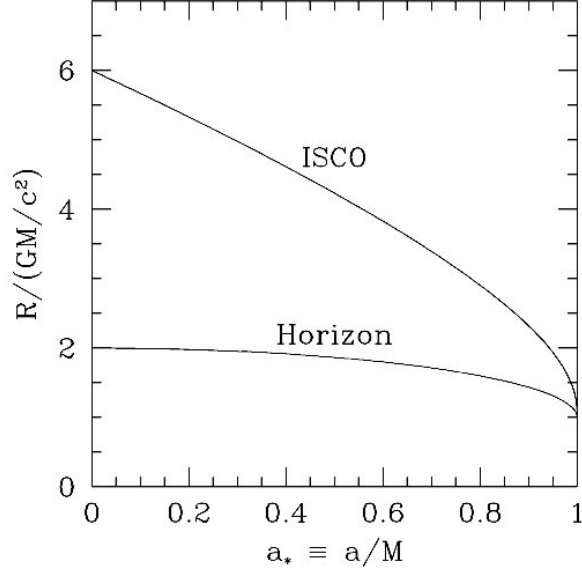


Figure 3.2: ISCO in function of the black hole spin a .

the accretion rate requires ΔM of $1 M_{\odot} \text{ yr}^{-1}$ while for X-ray binaries luminosities are of the order of $L \sim 10^{39} \text{ erg s}^{-1}$ implying $10^{-7} M_{\odot} \text{ yr}^{-1}$. The mass accretion rate is also related, as illustrated in previous equations, to the Eddington Luminosity. In fact, ΔM is related to the accretion luminosity as $\Delta M = \frac{L_{acc}}{\epsilon c^2}$. The maximum luminosity is related to the Eddington luminosity, which is the maximum power sustained by the AGN (balance between force due to radiation pressure and force of gravity). For this reason, combining equations one obtains

$$\Delta M = \frac{L_{acc}}{\epsilon c^2} < \frac{4\pi G M m_p}{\epsilon c \sigma_t} \quad (3.3)$$

which implies that the black hole growth is governed by the equation $M \leq M_0 e^{\frac{t}{\tau}}$

$$M(t) \leq M_0 e^{\frac{t}{\tau}} \quad (3.4)$$

where τ is the Salpeter growth time defined as

$$\tau = \frac{\epsilon c \sigma_t}{4\pi G m_p} \sim 5 \times 10^7 \text{ yr} \quad (3.5)$$

3.1.2 Emission mechanism - Thermal emission from accretion disk, broad line and narrow line regions

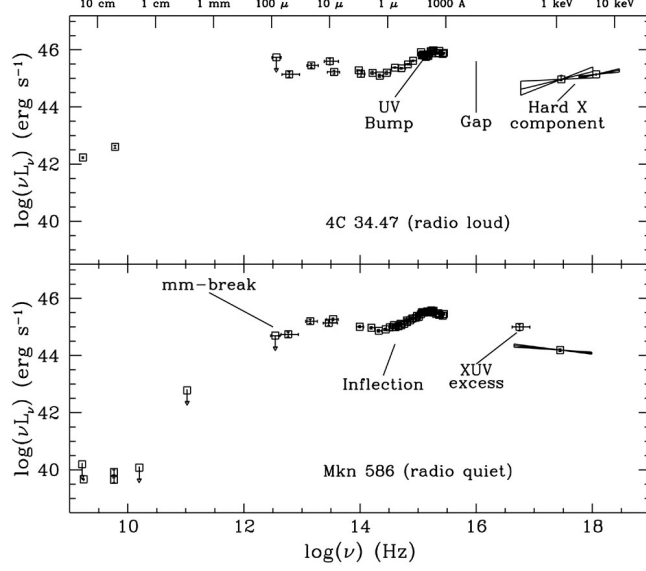


Figure 3.3: Spectral energy distribution of the radio quiet QSO Mkn586. The UV bump due to thermal radiation generated by the accretion disk is clearly visible in the region $10^{15} - 10^{15}$ Hz.

In general, the optical to UV spectrum of QSOs and AGN is dominated by thermal emission deriving from the accretion disk which is formed by accreted matter. The material, spiralling through the disk, releases gravitational energy and angular momentum before reaching the event horizon. The energy loss due to viscosity and friction could be safely modelled as an ensemble of thin ring, all emitting as blackbody radiator. In particular, the energy released between r and $r + dr$ in the elementary interval time dt is

$$\frac{dE}{dt} = \frac{3GM\Delta M}{4\pi r^3} \times \left(1 - \left(\frac{r_{in}}{r}\right)^{1/2}\right) \quad (3.6)$$

Integrating all over the radii one has

$$L = \int_{r_{ISCO}}^{+\infty} 2\pi r \frac{3GM\Delta M}{8\pi r^3} \times \left(1 - \left(\frac{r_{in}}{r}\right)^{1/2}\right) dr \quad (3.7)$$

According to the Virial Theorem, the total emitted luminosity could also be expressed as

$$L = \frac{1}{2} \frac{GM\Delta M}{r_{in}} \text{ erg s}^{-1} \quad (3.8)$$

which simply states that half of the power released from accretion goes into radiation produced by friction in the accretion disk. As spotted before, each disk of radii dr emits as a blackbody radiator. For this reason, the luminosity of the disk between r and $r + dr$ is

$$dL = \frac{GM\Delta M}{2r} dr = 2(2\pi r dr) \sigma T^4(r) \quad (3.9)$$

The temperature $T(r)$ is could then be expressed as

$$T(r) = \left(\frac{3GM\Delta M}{8\pi\sigma R_{int}^3} \right)^{\frac{1}{4}} \left(\frac{R_{int}}{r} \right)^{\frac{3}{4}} \text{ K} \quad (3.10)$$

Differentiating $T(r)$ with respect to dr it is possible to estimate the accretion disk temperature. In particular

$$T_{disk}(r) = \frac{dT(r)}{dr} = 0 = \left(\frac{24c^6 \Delta M}{125\pi\sigma G^2 M^2} \right)^{\frac{1}{4}} = \left(\frac{95c^5}{125k\sigma GM} \frac{1}{\epsilon} \frac{L_{disk}}{L_{Eddington}} \right)^{\frac{1}{4}} \quad (3.11)$$

Considering a Kerr black hole with maximum angular momentum J , $R_{int} \sim \frac{5}{8} R_{Schw}$ and a typical mass of a SMBH ($\sim 10^8 M_{\odot}$) $T_{disk} \sim 7 \times 10^5 \text{ K}$. At the level of the spectrum, the contribution of the accretion disk could be spotted by the so called big blue bump that can be easily observed in QSOs UV spectra. An example of a SED where the big blue bump is clearly detectable is reported in Figure 3.3. The size of the emitting region in common Active Galactic Nuclei is of the order of our Solar System, producing the light of a nearly a trillion (10^{12}) stars in a very small compact region. This evaluation is also obtained through the study of short time-scale variability of the nuclei brightness.

3.1.2.1 Broad line region

In the accepted paradigm of AGN structure, the accretion disk is surrounded by relative cold gaseous halos which generate emission lines by fluorescence in gas

clouds surrounding the central black hole. In fact, in most AGNs the UV, visible or infrared spectra show broad line component ($1000 \leq \text{FWHM} \leq 20000 \text{ km s}^{-1}$) typical of photoionized gases at $T \sim 10^4 \text{ K}$. The average of different spectra of AGNs shows that BLR lines are extremely similar over a wide range of luminosity as illustrated in Figure 3.4.

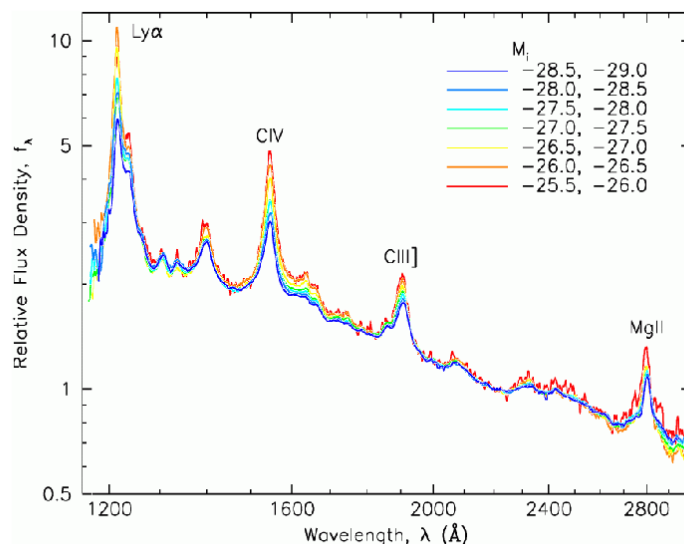


Figure 3.4: Emission lines in the BLR superposed on different spectrum of QSOs with different absolute luminosities.

The broad line profiles could also be exploited in order to study kinematics properties of the source since, for the most part, the profiles tell us about the kinematic of the BLR itself. For instance, a very common technique based on Virial Theorem allows to estimate the mass of the central engine starting from the profile of the BLR which reflect the dynamic of the gravitational potential (related to the FWHM velocity Δv) of the central black hole, as illustrated in Equation 3.12 (where R is the BLR radius which can be inferred from multiple scale relations, see e.g. [Kaspi et al. \[2005\]](#)).

Moreover, a relatively small subset of AGNs show double-peaked BLR profiles that are characteristic of rotation (see Figure 3.5). This characteristic tell us that

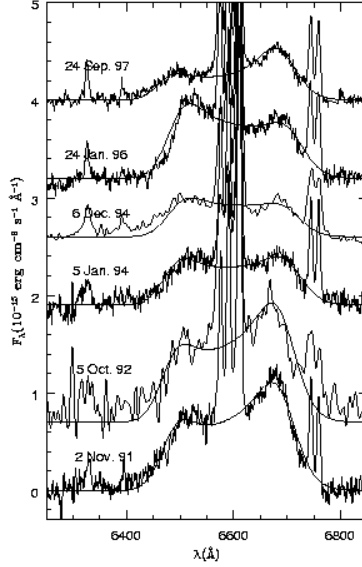


Figure 3.5: Multiepoch spectrum of the QSO NGC1097 where double peaked broad $H\alpha$ is clearly spot.

probably accretion disks are not symmetric or axisymmetric.

$$M_{\bullet} \propto \frac{\Delta V^2 R}{G} \quad (3.12)$$

As explained, emission lines in the BLR are generated through the photoionization of the gas from the continuum generated by the accretion disk. Since no forbidden lines are detectable in the BLR densities are quite high, of the order of $10^{10} n_e \text{ cm}^{-3}$. The ionization level of the BLR is usually defined as :

$$U = \frac{1}{n_e c} \int_{13.6\text{eV}}^{+\infty} \frac{F_{\nu}}{h\nu} d\nu \quad (3.13)$$

U depends on the intrinsic luminosity of the source F_{ν} , on the distance from the ionizing source and on the density n_e of free electrons. The ionization parameter could also be derived through indirect measurement. In particular, it may be derived from the intensity ratio of the [OIII] $\lambda 5007$ and [OII] $\lambda 3727$ [Penston et al., 1990]. In details, considering the equation of ionization balance for species

i one has

$$N_i^0 = \frac{1}{4\pi r^2 N_e} \int_{\nu_i}^{+\infty} \frac{L_\nu \alpha_{\nu_i}}{h\nu \alpha_i} d\nu = N_i^+ N_e \alpha_i \quad (3.14)$$

The ratio of number of particles in the ionized state, to that in the non-ionized state is thus

$$\frac{N_i^+}{N_i^0} = \frac{1}{4\pi r^2 N_e} \int_{\nu_i}^{+\infty} \frac{L_\nu \alpha_{\nu_i}}{h\nu \alpha_i} d\nu \quad (3.15)$$

The recombination coefficients, α_i are independent of photon frequency. Defining a ionization parameter Γ which is species-independent as

$$\Gamma = \frac{1}{4\pi r^2 N_e c} \int_{\nu_0}^{+\infty} \frac{L_\nu}{h\nu} d\nu \quad (3.16)$$

With this model, it is possible to refer to the ratio of ionization, which is species dependent, as

$$\frac{N_i^+}{N_i^0} = \frac{\alpha_{\nu_i}}{\alpha_i} c\Gamma \quad (3.17)$$

The integral in 3.16 is the number of ionizing photons coming from the source. When divided by $4\pi r^2$, this becomes the surface density of ionizing photons. In the case where $N_e \sim N_p$, this density of photons is then compared with the density of material. In other words, Γ describes how many ionizing photons there are per atom.

$$\Gamma = \frac{Q(H^0)}{4\pi r^2 c N_H} \sim \frac{\langle N_{ph} \rangle}{\langle N_H \rangle} \quad (3.18)$$

Broad lines typically seen in quasars only occur for permitted and semi-permitted transitions. In addition to the emission lines of the hydrogen (Lyman and Balmer series) and helium, the commonly ions include

- Permitted lines of lithium-like ions (from s -shell electrons). For instance, the strongest lines are C IV $\lambda 1549$, N V $\lambda 1240$, O VI $\lambda 1035$, Mg II $\lambda 2798$, and Si IV $\lambda 1400$.
- Permitted lines of Fe II that are usually blended due to instrument resolution and intrinsically high density at high temperature which cause doppler

broadening and blending. In the broad line region, forbidden lines are suppressed. Combining this fact with the presence of semiforbidden lines places a constrain on the density of the BLR. The density of the broad line region is estimated to be of the order of 10^8 or 10^9 atom cm^{-3} .

The temperature of the BLR is assumed to be $T_e \sim 15000$ K. This value is derived from the ratio of Fe III and Fe II, adopting the Saha equation, and from the simultaneous presence of the C III] λ 1909 and absence of C III λ 977. The mass and the size of the BLR can be estimated in the following way (for sake of simplicity we will refer to H β hydrogen transition). The luminosity of the H β emission line is defined as

$$L(H\beta) = N_e N_p \alpha_{H\beta}^{eff} h\nu_{H\beta} fV \quad (3.19)$$

where f is the filling factor and V the considered volume. The total mass of the ionized gas is thus

$$\mathcal{M} = (N_p m_H + N_{He} m_{He}) fV \sim 1.3 N_p m_H fV \quad (3.20)$$

Combining Equation 3.19 and 3.20 the total mass of the BLR is thus defined as

$$\mathcal{M} = 1.3 m_H \frac{L(H\beta)}{N_e \alpha_{H\beta}^{eff} h\nu_{H\beta}} \quad (3.21)$$

A typical luminosity for the H β emission line is $L(H\beta) = 10^9 L_\odot$. Assuming $N_e \sim 10^9 \text{ cm}^{-3}$ the BLR mass turns out to be $40 M_\odot$. The volume in which this mass of gas is contained is

$$V = \frac{4}{3} \pi r^3 = \frac{\mathcal{M}}{1.4 N_p m_H f} \quad (3.22)$$

The typical radius for the BLR can be also derivated from the equations illustrated before. In particular, R is defined as

$$R \sim 0.015 f^{-\frac{1}{3}} \left(\frac{10^9}{N_e} \right)^{\frac{2}{3}} \text{ pc} \quad (3.23)$$

Operationally, the BLR radius could also be obtained through the adoption of scaling relation involving continuum luminosity (e.g λL_λ at $\lambda = 5100\text{\AA}$, see e.g.

Kaspi et al. [2005]). Assuming median value, one has that the BLR size is therefore only a few tenths of a light year which is unresolvable also with modern telescopes and innovative instrumentation.

3.1.2.2 The narrow-line region

The Narrow Line Region is located between 10 pc e 1 Kpc from the accreting black hole. Dispersion velocities inferred from the FWHM of the lines are quite variable but, in general, they are below 1000 km s^{-1} . A lot of forbidden lines are present in the NLR spectrum, suggesting the idea that the NLR is a low density region. The gaseous content in the narrow line region is in general optically thick ($\tau \gg 1$). Nevertheless, in some objects, the high ratio $\text{He II } \lambda 4686 / \text{H}\beta$ allow also to infer that optically thin NLR clouds could also exist. The mean electron density and temperature are of the order of $10^3 - 10^4 \text{ cm}^{-3}$ and $\sim 1.5 \times 10^4 \text{ K}$. The ionization parameter, defined as in the case of BLR, is of the order of 10^{-2} . The NLR is

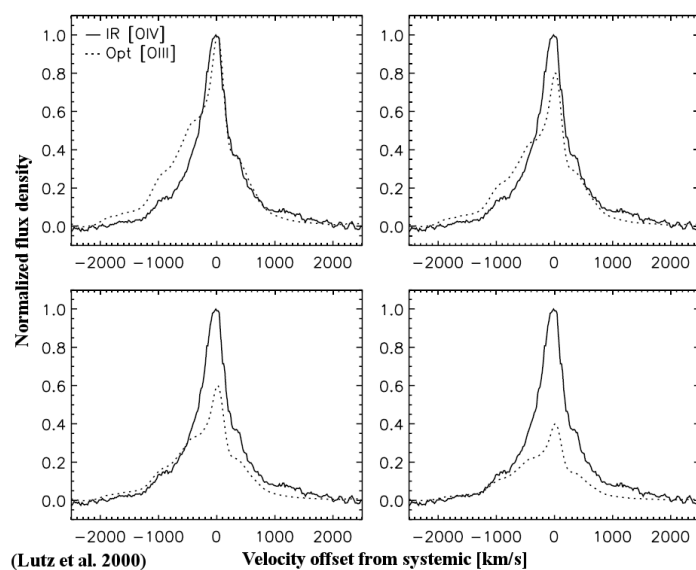


Figure 3.6: Narrow line region line profile asymmetry. This structure suggests flows of matter in the active nucleus [Lutz et al., 2000].

organized as a stratified structure. In the inner region, the photoionization of the low density gaseous nebule is only due to the central accreting black hole. The most

intense emission lines that could be measured in the spectrum are the doublet [OIII] $\lambda\lambda$ 5007, 4959, [NII] and [SII]. The external region is called Extended Emission Line Region (EELR). The kinematic deduced from the structure of the narrow emission lines reflects the potential of the galaxy itself and not the gravitational potential well of the central black hole, as in the case of the Broad Line region. It is worth noticing that in some cases, the profile of the emission lines from NLR are found to be asymmetric suggesting that outflows due to winds could be present (see Figure 3.6).

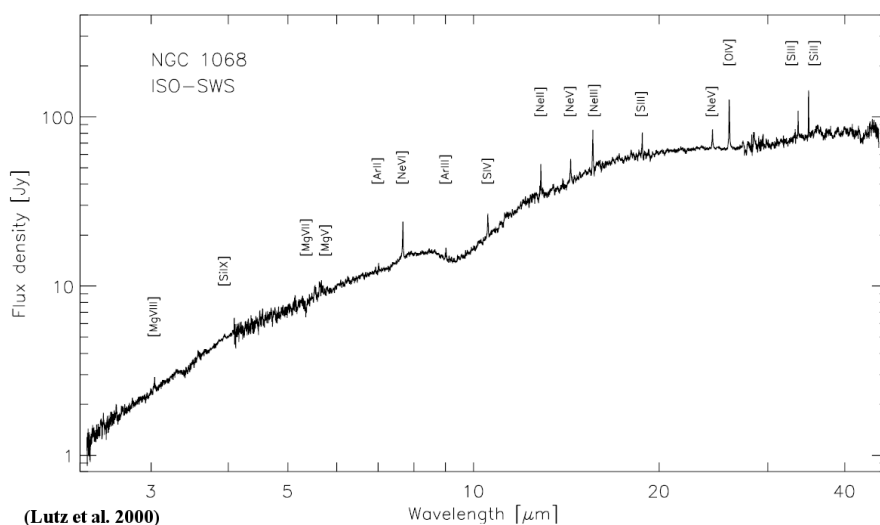


Figure 3.7: Narrow line region line spectrum (NIR and FIR) example from the AGN NGC1078 [Lutz et al., 2000].

As in the case of the Broad Line Region, the mass of NLR can be estimated from numerous diagnostic ratios measured through properties of the emission lines (see e. g. [Peterson, 1997]). In particular, typical densities of the NLR are of the order of 10^{-3-5} atom cm^{-3} and its total mass is of the order of several million of solar masses. A sample spectrum of NLR is shown in Figure 3.7.

3.2 The case of BL Lacertae objects

BL Lac objects are a particular class of AGN essentially characterized by [Peterson, 1997]

- Absence or extreme weakness of spectral features in the optical spectrum.
- Flat radio spectrum
- Large and rapid variability in all spectral bands
- High optical polarization
- Large X and γ -ray luminosities
- Superluminal motion

BL Lacs are grouped with Flat Spectrum Radio Quasars (FSRQ), due to the same characteristics, except for line weakness, into the *blazar* class. The common structure of all radio-loud AGNs [Urry and Padovani, 1995] is thought to be given by a central SMBH, surrounded by an accretion disk and ionized gas clouds, which emit the spectral lines. As explained in the previous paragraph, these clouds are divided into a Broad Line Region (BLR), closer to the black hole, and a Narrow Line Region (NLR), at a greater distance. On the same plane of the accretion disk, an optically thick torus of gas and dust is also present. The black hole also powers a relativistic jet, orthogonal to the accretion disk, which accounts for the large scale radio emission. In this scenario, a BL Lac is seen when the line of sight is close to the jet direction. The relativistic beaming of the radiation emitted in the jet easily explains the main characteristics of this class (e.g. the rapid and large variability, the high polarization, the superluminal motions). Their spectral energy distribution (SED) is characterized by two broad peaks. The low energy maximum is usually explained as the synchrotron emission by a population of highly relativistic electrons accelerated in the relativistic jet, while the higher energy one is interpreted as Inverse Compton emission of the same population of electrons interacting with seed photons produced from the synchrotron radiation (Synchrotron Self Compton, SSC) or photons from the external environment (External Compton), depending on the model [Ghisellini et al., 1998].

3.2.1 Characteristic of the BL Lacs optical spectra

The main characteristic of the optical spectrum of BL Lacs is that the lines (from the BLR, NLR or from its host galaxy) can be very faint, if present at all. For this reason the first definition of the class required that the equivalent width (EW) of the strongest emission line should be less than 5\AA rest frame. This definition has been often criticized as arbitrary, because it does not correspond to intrinsic physical differences in the objects. In fact [Scarpa and Falomo \[1997\]](#) showed that in blazars emission line properties vary smoothly across the 5\AA limit. Several other classification criteria were proposed for BL Lacs. For example, [Plotkin et al. \[2010\]](#) adopted a limit on the intensity of the CaII continuum break around 4000\AA (CaII break $< 25\%$) when selecting BL Lacs from the SDSS while [Landt et al. \[2004\]](#) adopts the relative strength of [OII] and [OIII] narrow lines, but the question is still open.

Nevertheless, the extreme weakness (or absence) of the lines is easily explained by the emission mechanism model mentioned above. The light from the host galaxy, which has been found to be a giant elliptical with $M_r = -22.80 \pm 0.10$ [[Sbarufatti et al., 2005a](#)] responsible of the absorption lines, and the radiation from the BLR and NLR (emission lines) in first approximation are emitted isotropically, while the non-thermal continuum emitted by the jet is doppler-enhanced (δ) due to relativistic effect ($P_{received} = \delta^4 P_{emitted}$). When the line of sight is aligned with the jet and the beaming increases, the line flux remains constant, while the continuum flux increase reducing the equivalent width of spectral lines. Another paradigm usually taken into account for explaining the absence of the emission lines from the Broad Line Region is based on a particular kind of accretion disk, which is radiatively inefficient. This kind of disk is called ADAF, Advection Dominated accretion Flow which essentially postulates that most of the accretion power is not released in the disk (which is geometrically thick and optically thin) but it is carried away in a direct accretion beyond the event horizon. Further details could be found in [Narayan and Yi \[1994\]](#) and references therein.

3.3 Observing BL Lacs with FORS2@ESO-VLT.

The completion of the sample

3.3.1 Introduction

As illustrated before, BL Lac objects are a particular class of Active Galactic Nuclei (AGN) characterized by a quasi featureless optical spectra. Their emission is in fact strongly dominated by the non-thermal continuum arising from the relativistic jet aligned towards the line of sight of the observer. The featureless nature of their optical spectra makes the determination of their redshifts (and, as a consequence of their distance) a very challenging task. Deep imaging studies of BL Lac objects carried out using both ground based and space observatories show that they are hosted in luminous giant ellipticals (see e.g. [Urry et al. \[2000\]](#) , [Falomo et al. \[2000\]](#), [Sbarufatti et al. \[2005a\]](#)). For this reason, in addition to the non thermal emission, there is always a thermal contribution due to the stellar component of the host galaxy. Sometimes, like in other AGN, some emission lines generated by fluorescence in gas clouds surrounding the central black hole, can be present. Finally as in the case of QSOs, absorption lines due to intervening gas in the halo of foreground galaxies can be observed in the spectra of BL Lacs (e.g. [Stoche and Rector \[1997\]](#)). In this latter case, if the BL Lac object does not exhibits other intrinsic features the intervening absorptions put a lower limit to the redshift of the source.

In the past decade a number of projects were carried out to determine the redshift of BL Lac objects. Most of these works were based on optical spectra collected with 4 m class telescopes, and are therefore limited by relatively low signal-to-noise ratio, low spectral resolution and limited wavelength range (e.g. [Falomo et al. \[1993b\]](#); [Stickel et al. \[1993\]](#); [Veron-Cetty and Veron \[1993\]](#); [Falomo et al. \[1994b\]](#); [Falomo \[1996b\]](#); [Landt et al. \[2001\]](#); [Rector and Stoche \[2001\]](#)).

The detectability of spectral features depends on the brightness of the nuclear source. During low brightness states, intrinsic absorption features can be more easily revealed, while during high states one can better discover intervening absorption systems. Nevertheless, the strong contribution from the non-thermal continuum, illustrated in the previous paragraph, drastically lowers the equivalent width of the

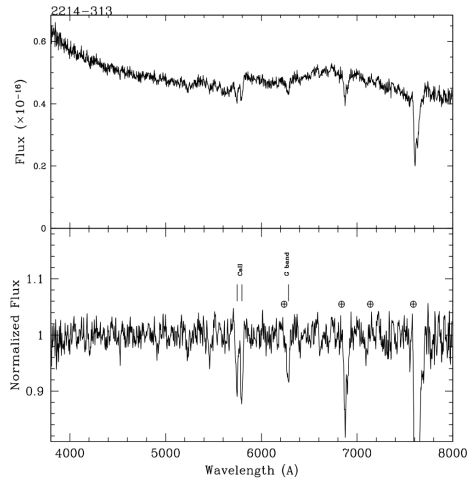


Figure 3.8: Optical spectrum of the BL Lac object (2214-313) in which the features associated to its host galaxy are clearly detected ($z = 0.460$). See Landoni et al 2013, Sbarufatti et al 2009.

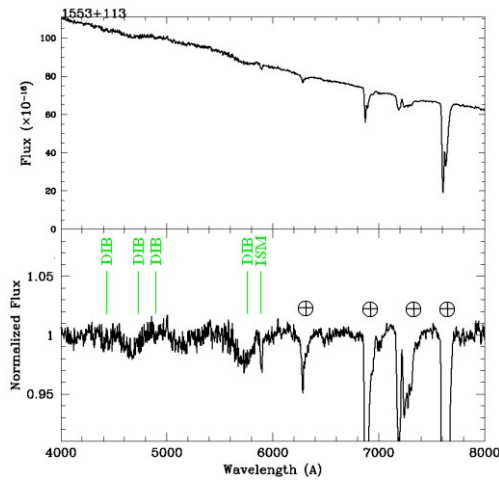


Figure 3.9: Flux calibrated (upper panel) and normalized (lower panel) spectrum of 1553+113. The spectrum is lacking any intrinsic spectral feature. Absorptions from our galaxy ISM are labeled in green. The telluric absorptions are marked. See Landoni et al 2013, Sbarufatti et al 2009.

intrinsic spectral features making their detection challenging. For these reasons, more systematic work aimed at obtain high signal-to-noise spectra of BL Lacs was started [Sbarufatti et al., 2006]. In particular, exploiting the capabilities of FORS1 and FORS2 at the 8-m Very Large Telescopes (VLT) of the European Southern Observatory (ESO) spectra for a sample of 69 objects, extracted from the lists of BL Lacs by Padovani & Giommi *Sedentary Survey* [Padovani and Giommi, 1995], have been secured. This high quality spectroscopic data forms the first collection of homogeneous and high quality spectra of BL Lacs from which a number of properties (in addition to the redshift or a redshift lower limit) can be extracted (the work in part reported in this Thesis).

Figure 3.8 and Figure 3.9 show examples of optical spectra for two BL Lacs objects. In the first case we report the spectrum of the well known TeV source PG1553+113 obtained with VLT + FORS2. As shown, no intrinsic features are apparent yielding this powerful source with an unknown redshift. In the second case, the absorption features of the host galaxy (CaII H K and the stellar G Band) of 2214-313 are detected with high confidence allowing us to derive a firm value for the redshift of the source (more details can be found in this Thesis and on website archive.oapd.inaf.it/zbllac/).

The content of this Chapter is published in the article **ESO Very Large Telescope Optical Spectroscopy of BL Lacertae Objects. IV. New Spectra and Properties of the Full Sample** (Landoni et al. [2013]) aimed to complete the survey mentioned before and to derive the overall properties of the class from the complete sample. Throughout the Thesis, we consider the following cosmological parameters: $H_0 = 70 \text{ km s}^{-1} \text{ Mpc}^{-1}$, $\Omega_m = 0.27$ and $\Omega_\Lambda = 0.73$.

3.3.2 The sample

The sample of BLLs (and candidates) observed with the ESO Very Large Telescope has been selected from two extended catalog of BLLs: the Padovani & Giommi (1995) [Padovani and Giommi, 1995] collection and the Sedentary Survey (SS; Giommi et al. [1999], Giommi et al. [2005]). The first list contains all objects identified as BLLs, belonging to the complete samples existing at the time of its compilation, selected in the radio, optical, and X-ray bands (e.g., the 1 Jy survey,

Stickel et al. [1991]; Palomar-Green survey [PG]; Extended Medium Sensitivity Survey [EMSS]). It also includes sources from the Hewitt and Burbidge [1993] and [Véron-Cetty and Véron, 2003] catalogs. More details are given in Landoni et al. [2013] and Sbarufatti et al. [2006].

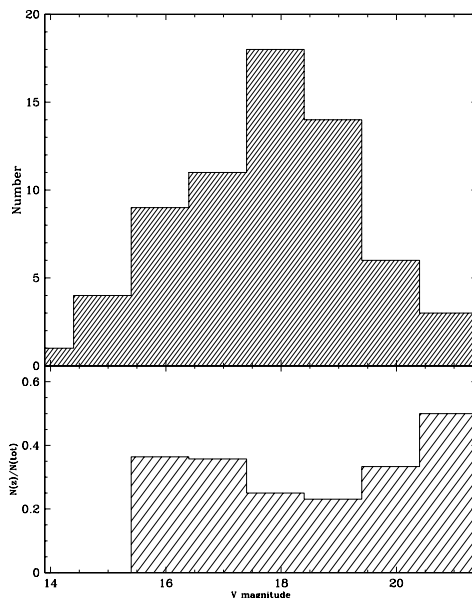


Figure 3.10: Top panel: V-magnitude distribution of the observed BLLs in the sample selected adopting the criteria described in the text. Bottom: Fraction of objects of known redshift as a function of the magnitude. Further details and references are reported in Sbarufatti et al. [2006] and Landoni et al. [2013].

According to the 11th Veron-Cetty catalog of AGN objects [Véron-Cetty and Véron, 2003] at the time of the first scheduling of the overall campaign in 2003, 797 sources were known as candidate or confirmed BL Lacs and 313 objects of the list were left without a reliable measure of their redshift. In order to select sources well observable from the Paranal site only the sources with $\delta < 15$ were considered. With this cutoff a total of 169 BL Lacs objects still remains of unknown redshift. From this set, objects with apparent magnitude $V < 21$ were selected in order to secure an acceptable SNR ratio spectrum for each source. The campaign obtained time for the observation of 88 sources, selected combining the

~ 155 objects well observable with FORS2 from the catalogs mentioned above. In Figure 3.10 we report a synthetic statistic about the distribution of the BLL observed magnitude versus the redshift hit rate for redshift bin.

3.3.3 The complete BLL@FORS2 sample observed at FORS2-ESO VLT

Source Name	z	V	α	SNR	References
PKS 0019+058	> 0.49	18.10	0.65	120	Sbarufatti et al 2009 - AJ 137:337-346
PKS 0047+023	> 0.82	19	0.61	80	Sbarufatti et al 2006 AJ 132:1-19
PKS 0048-09	> 0.30	16.10	0.95	250	Sbarufatti et al 2006 AJ 132:1-19
GC 0109+224	> 0.10	14.9	0.85	200	This work
GC 0109+224	> 0.25	14.80	0.82	380	Sbarufatti et al 2009 - AJ 137:337-346
RBS 0231	> 0.41	18.90	1.00	20	Sbarufatti et al 2009 - AJ 137:337-346
PKS 0140-059	> 0.46	19.20	0.45	65	This work
1RXS J022716.6+020154	0.457	18.90	0.83	100	Sbarufatti et al 2005 AJ 129:559-566
RBS 0337	0.232	16.50	1.30	130	This work
PKS 0302-623	1.350	18.30		150	This work
PKS 0306+102	0.862	21.20	0.47	20	Sbarufatti et al 2005 AJ 129:559-566
1RXS J031615.0-26074	0.443	18.10	1.20	130	Sbarufatti et al 2005 AJ 129:559-566
PKS 0338-214	0.223	17.90	0.27	210	Sbarufatti et al 2005 AJ 129:559-566
RBS 0499	> 0.45	19.10	1.00	40	This work
PKS 0410-519	1.254	17.40		70	This work
PKS 0420+022	2.278	18.80		90	Sbarufatti et al 2006 AJ 132:1-19
PKS 0422+00	> 0.31	16.30	0.88	230	Sbarufatti et al 2006 AJ 132:1-19
PKS 0426-380	1.105	18.60	0.70	100	Sbarufatti et al 2005 AJ 129:559-566
PKS 0439-299	> 0.68	20.80	0.30	30	This work

PKS 0443-387	0.537	17.30		140	This work
RBS 0589	>0.45	17.50	1.20	130	This work
ZS 0506+056	> 0.15	16	0.92	200	This work
PMN J0529-3555	0.323	20.20		30	This work
PKS 0539-543	1.191	17.90		70	This work
1RXS J055806.6-383829	0.302	16.80	1.21	280	Sbarufatti et al 2005 AJ 129:559-566
PKS 0607-605	1.1	18.10		50	This work
MS 0622.5-5256	0.513	19.90	0.90	45	This work
PKS 0627-199	>0.63	19.30	0.56	50	Sbarufatti et al 2006 AJ 132:1-19
PKS 0723-00	0.127	16.00		250	Sbarufatti et al 2006 AJ 132:1-19
PKS 0735+17	> 0.18	16.30	0.84	160	This work
PKS 0808+019	1.148	18.40	0.93	140	Sbarufatti et al 2005 AJ 129:559-566
OJ-131	0.539	17.90	0.44	100	This work
PKS 0823-223	>0.911	15.70	0.47	220	Sbarufatti et al 2009 - AJ 137:337-346
H0841+1256	>2.48	18.10		100	Sbarufatti et al 2006 AJ 132:1-19
1WGA J1012.2+063	0.727	17.60	0.80	200	Sbarufatti et al 2005 AJ 129:559-566
RX J1022.7-0112	> 0.30	17.10	1.34	100	This work
RX J1023.9-4336	> 0.24	16.30	1.28	200	This work
PKS 1057-79	0.581	16.20	0.73	90	Sbarufatti et al 2009 - AJ 137:337-346
PKS B1056-113	> 0.27	17.20	0.66	100	This work
1ES 1106+244	> 0.37	18.70	0.78	40	This work
RX J1117.0+2014	0.140	16.50	0.98	130	This work

PKS 1145-676	0.210	18.60		80	Sbarufatti et al 2009 - AJ 137:337-346
OM 280	> 0.20	16.10	0.79	100	Sbarufatti et al 2009 - AJ 137:337-346
1ES 1212+078	0.137	17.40	1.17	100	Sbarufatti et al 2006 AJ 132:1-19
RX J1241.8-1455	> 0.32	17.30	1.05	140	This work
1ES 1239+069	> 0.47	18.70	1.00	50	This work
1ES 1248-296	0.382	19.50	0.92	50	Sbarufatti et al 2006 AJ 132:1-19
PKS 1250-33	0.856	20.10	0.48	30	Sbarufatti et al 2005 AJ 129:559-566
PKS 1256-229	0.481	17.90	0.31	170	Sbarufatti et al 2005 AJ 129:559-566
4C 12.46	> 0.37	18.20	0.43	70	This work
1ES 1320+084N	1.50	19.00		50	Sbarufatti et al 2006 AJ 132:1-19
PKS 1349-439	>0.39	16.90	0.82	240	Sbarufatti et al 2006 AJ 132:1-19
OQ 012	> 0.63	18.60	0.29	120	Sbarufatti et al 2009 - AJ 137:337-346
OQ 240	> 0.10	14.60	1.00	170	This work
1RXS J144505.9-032613	> 0.51	17.70	1.21	100	Sbarufatti et al 2006 AJ 132:1-19
1RXS J150343.0 154107	>0.38	17.90	1.52	40	Sbarufatti et al 2006 AJ 132:1-19
OR 103	1.833	16.40		150	This work
RBS 1478	> 0.50	19.20	0.95	50	This work
PKS 1519-273	1.297	17.80	0.51	170	Sbarufatti et al 2005 AJ 129:559-566
PMN J1539-0658	> 0.80	19.90	0.50	50	Sbarufatti et al 2009 - AJ 137:337-346
HB89 1553+113	>0.09	13.90	0.84	250	Sbarufatti et al 2006 AJ 132:1-19
H1722+119	>0.17	14.80	1.30	350	Sbarufatti et al 2006 AJ 132:1-19
PKS 1815-553	1.633	21.40		10	This work

PKS 1830-589	> 0.45	18.10	0.65	100	Sbarufatti et al 2009 - AJ 137:337-346
PKS 2012-017	>0.94	17.70	0.49	130	Sbarufatti et al 2006 AJ 132:1-19
OW 080	> 0.47	18.80	0.42	90	This work
1RXS J213151.7-251602	>0.86	19.00	1.28	70	Sbarufatti et al 2006 AJ 132:1-19
RBS 1752	0.448	17.80	1.45	90	Sbarufatti et al 2009 - AJ 137:337-346
PKS 2131-021	1.284	19.20	0.29	80	Sbarufatti et al 2006 AJ 132:1-19
MH 2133-449	>0.98	19.70	1.02	60	Sbarufatti et al 2006 AJ 132:1-19
MH 2136-428	>0.24	15.60	0.84	490	Sbarufatti et al 2006 AJ 132:1-19
OX 183	0.870	19.50	0.16	50	This work
RX J22174-3106	0.460	19.70	0.90	50	Sbarufatti et al 2006 AJ 132:1-19
PKS 2223-114	0.997	21.40	0.31	20	Sbarufatti et al 2006 AJ 132:1-19
PKS 2233-148	> 0.65	18.50	0.15	170	Sbarufatti et al 2006 AJ 132:1-19
RBS 1899	> 0.53	19.20	0.93	60	This work
RBS 1915	0.243	17.30	1.09	160	Sbarufatti et al 2009 - AJ 137:337-346
PKS 2254-204	>0.47	17.10	0.86	220	Sbarufatti et al 2006 AJ 132:1-19
1RXS J231027.0-371926	>1.03	19.60	1.15	80	Sbarufatti et al 2006 AJ 132:1-19
RX J2319.6+1611	> 0.97	17.80	0.96	100	This work
1ES 2322-409	> 0.16	16.50	0.84	60	This work
MS 2342.7-1531	>1.03	21.50	1.02	20	Sbarufatti et al 2006 AJ 132:1-19
TXS 2346+052	0.419	18.70	0.06	80	Sbarufatti et al 2009 - AJ 137:337-346
1RXS J235730.1-171801	>0.85	18.10	1.44	150	Sbarufatti et al 2006 AJ 132:1-19
1RXS J235730.1-171801	> 0.63	17.90	1.40	110	Sbarufatti et al 2009 - AJ 137:337-346

PKS 2354-021	0.812	20.40	0.67	30	Sbarufatti et al 2005 AJ 129:559-566
--------------	-------	-------	------	----	--------------------------------------

Table 3.1: BL Lacs candidate source observed from ESO
VLT with FORS2 spectrograph.

The spectra of the sources reported in Table 3.1 were obtained in Service Mode using the FOcal Reducer and a low dispersion Spectrograph (FORS2, Seifert et al. [2000]). The observations of the last run which this Thesis refers to (labelled as This Work in Table 3.1) took place between April 2008 and June 2008 at VLT-UT1 (Antu) and from September 2008 to February 2009 at VLT-UT2 (Kueyen). The spectrograph was configured with a 300V+I grism with a slit of 2'' achieving the spectral range of 3800 - 8300 Å with a dispersion of $\sim 3.2 \text{ \AA pixel}^{-1}$. The seeing during the observation was in the range 0.65''-2.50'' with an average of 1.20'' (rms $\sim 0.4''$). Although these observations were carried on in 2008, the data processing started in late 2010 due to problems related to flat field calibrations.

Data reduction was performed using the IRAF package with the adoption of standard procedures. In particular, for each target we performed bias subtraction, flat fielding and bad pixels or cosmic rays rejection. For each object we obtained from 2 to 6 individual exposure frames that were then combined into a single average image. The wavelength calibration was achieved using the spectra of a Helium Neon Argon lamp reaching an accuracy of $\sim 3 \text{ \AA}$ rms. Even though the overall program did not require photometric conditions during observations, checking the weather database at Paranal, the sky was clear during most of the time. This enabled us to flux calibrate our spectra using standard stars [Oke, 1990].

The flux calibration was assessed through the relative photometric calibration of the acquisition image and the overall uncertainty is $\Delta m \sim 0.1 \text{ mag}$ (rms). Finally, each spectrum has been de-reddened applying the extinction law described in Cardelli et al. [1989] assuming the E_{B-V} values computed by [Schlegel et al., 1998].

3.3.4 Immediate results

In this section I will refer to the objects observed during Period P81 and P82. For the other objects of the sample reported in Table 3.1 see [Sbarufatti et al., 2005b]; [Sbarufatti et al., 2006]; [Sbarufatti et al., 2009] and [Landoni et al., 2013] for overall further details. From the spectroscopic point of view we consider as *bona-fide* BL Lac the sources that either have a featureless spectrum or in which their intrinsic features have equivalent width (EW) $< 5 \text{ \AA}$. Based on this classifi-

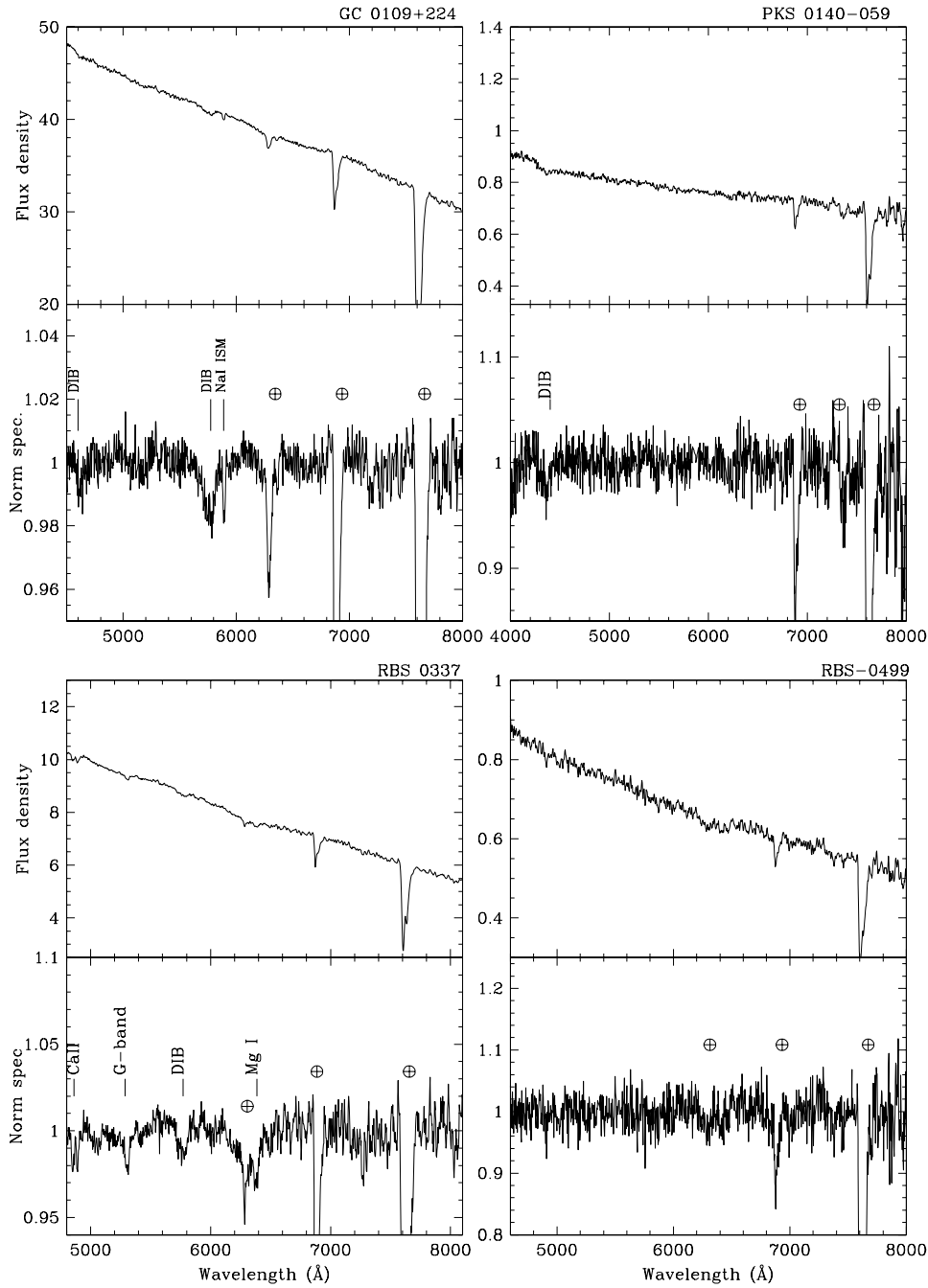


Figure 3.11: Spectra of BLLs sources. Top panel: flux calibrated spectra. Normalized spectra on bottom. Telluric bands are indicated by \oplus , spectral lines are marked by line identification, absorption features from interstellar medium of our galaxy are labeled by ISM, diffuse interstellar bands by DIB. The flux density is in units of $10^{-16} \text{ erg cm}^{-2} \text{ s}^{-1} \text{ \AA}^{-1}$.

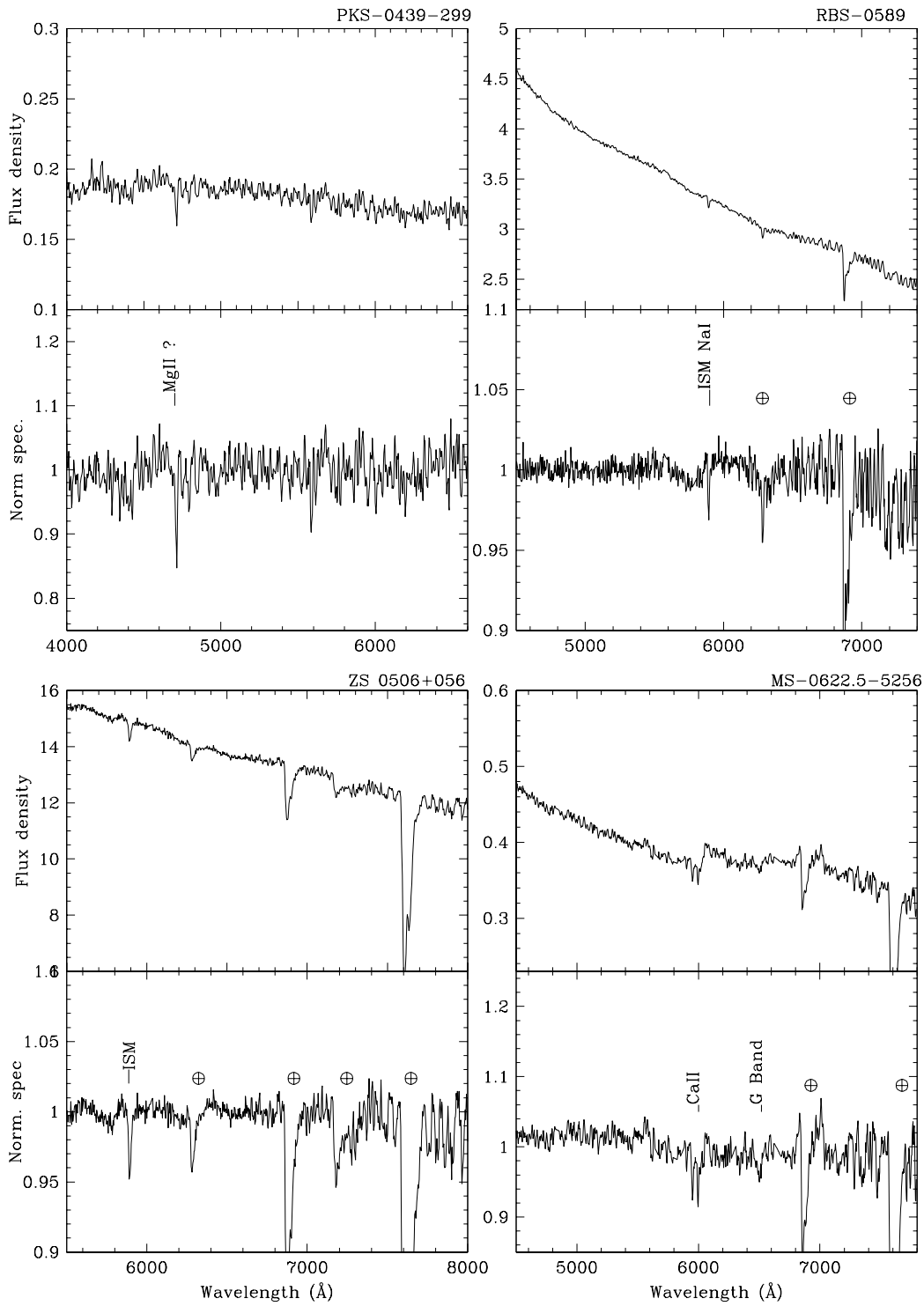


Figure 3.12: continued

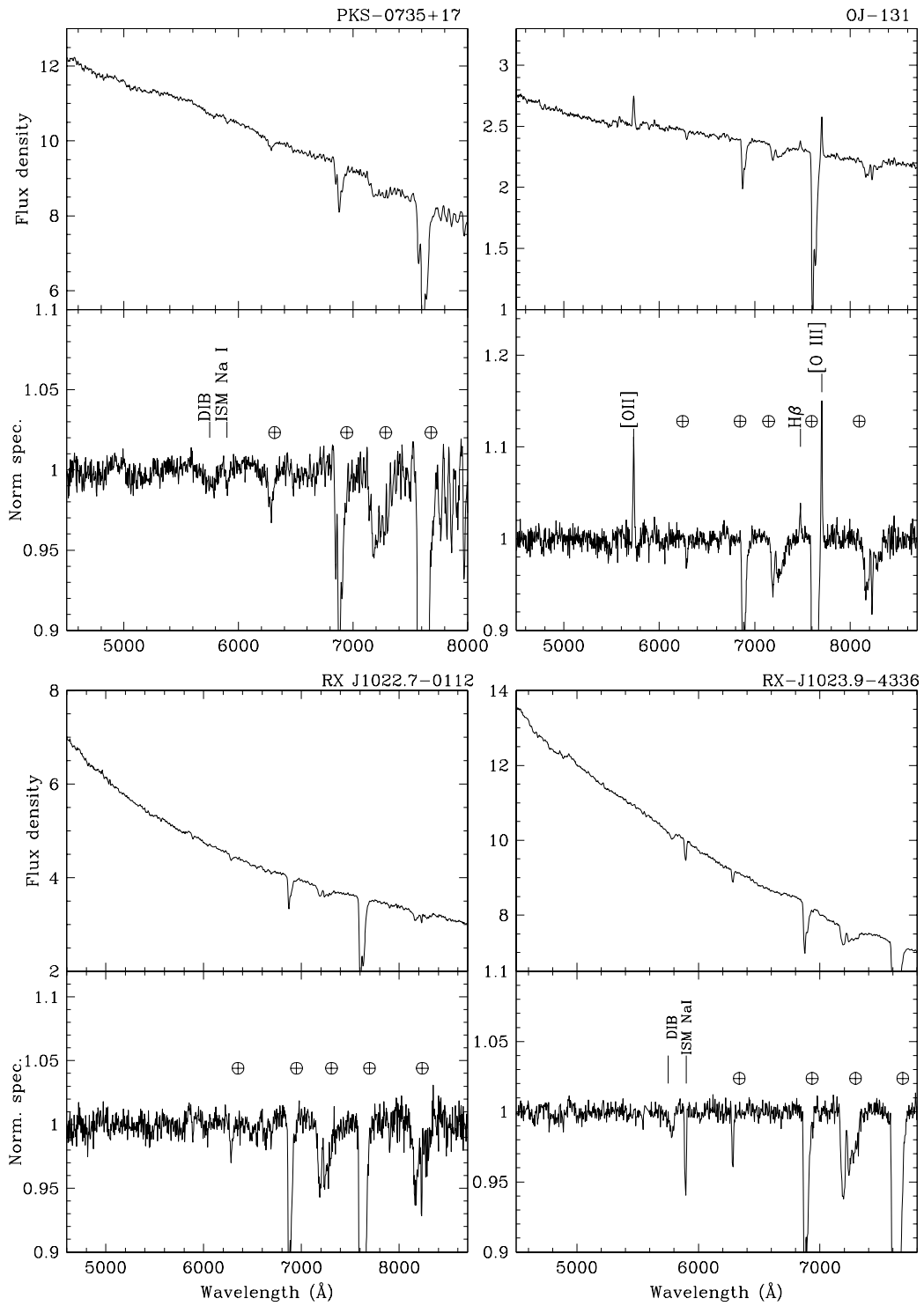


Figure 3.13: continued

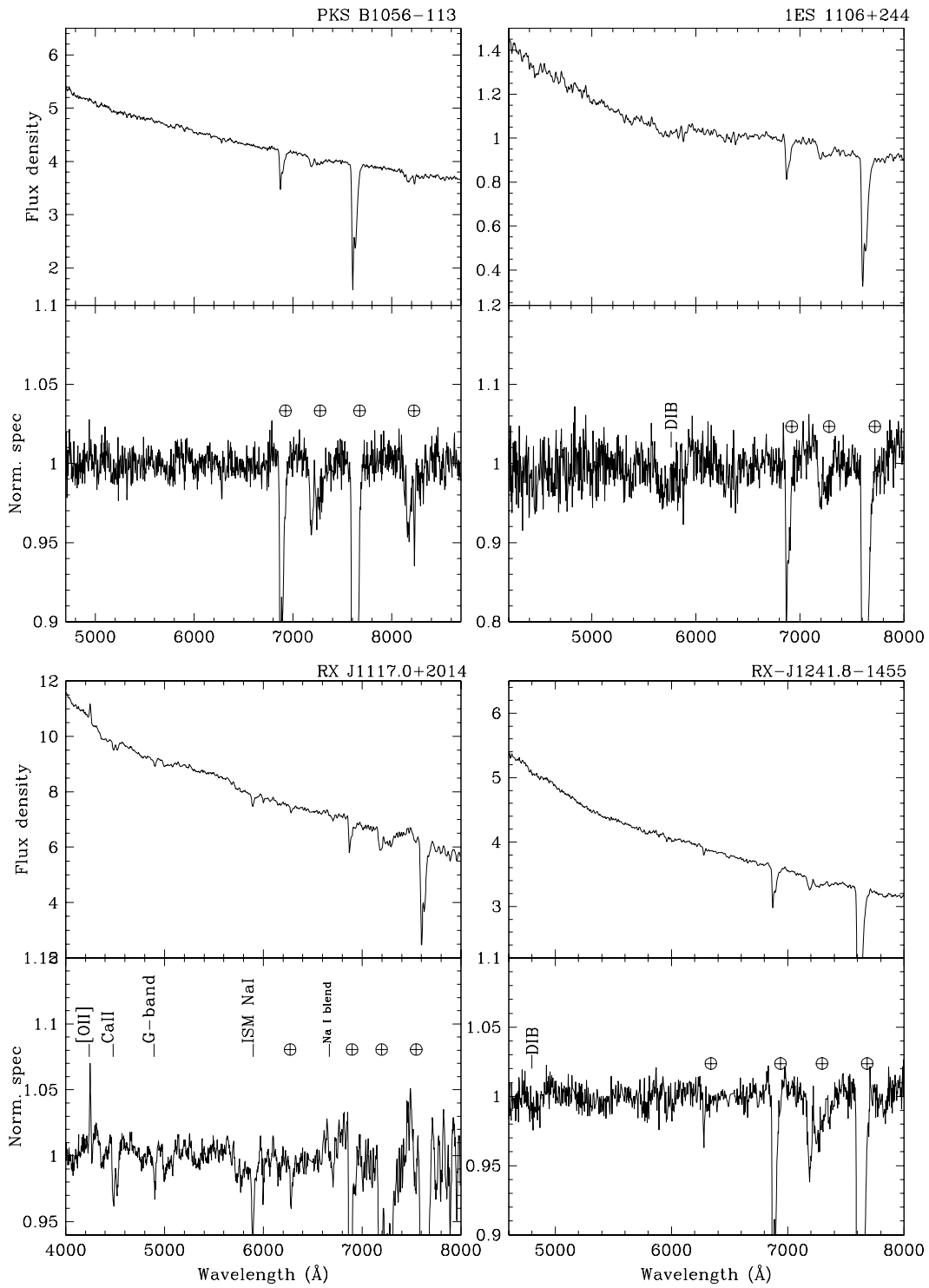


Figure 3.14: continued

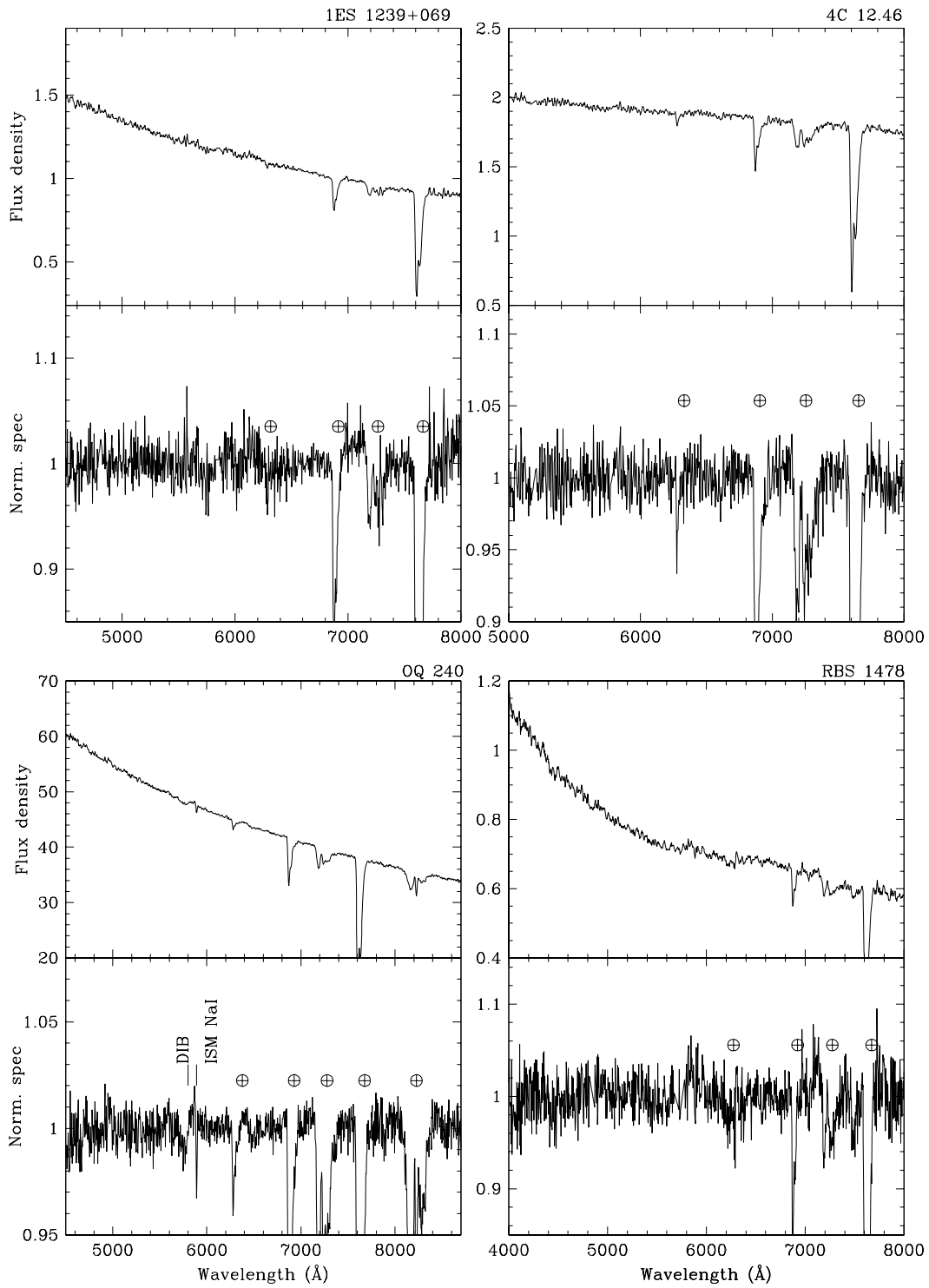


Figure 3.15: continued

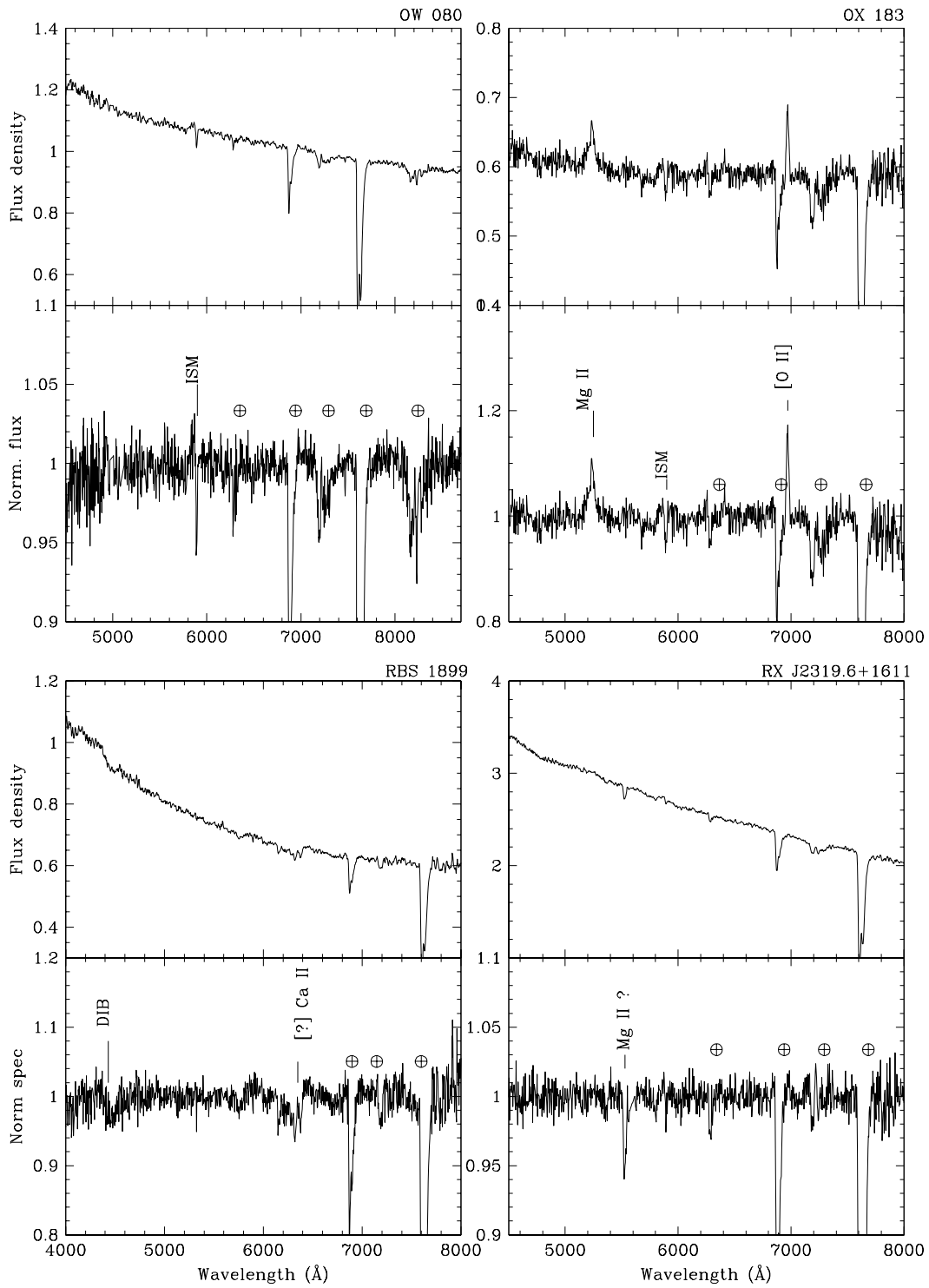


Figure 3.16: continued

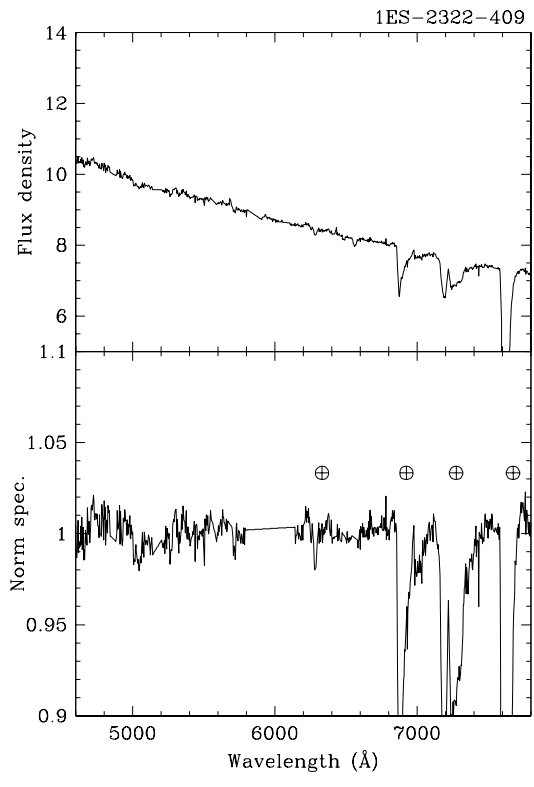


Figure 3.17: continued

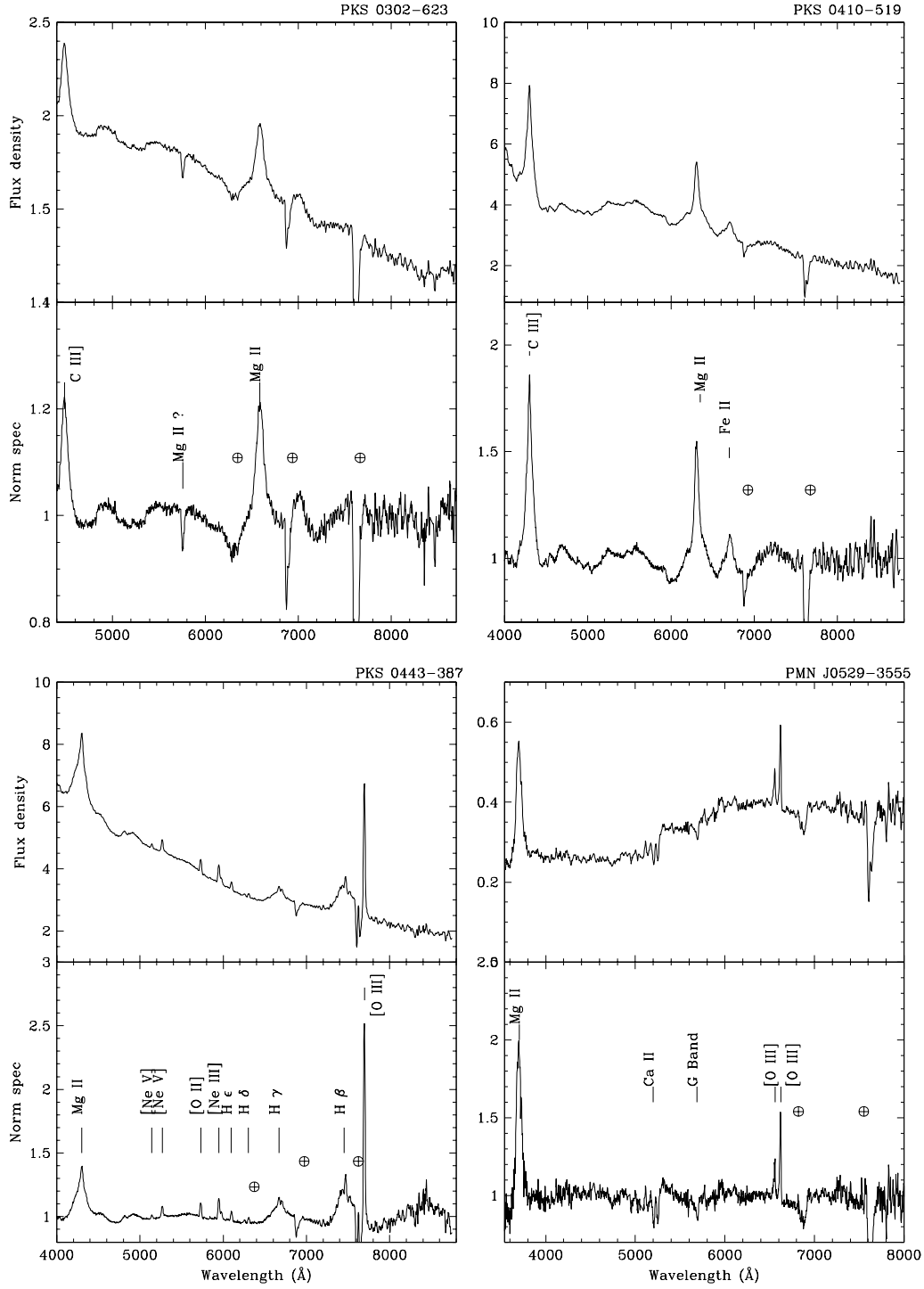


Figure 3.18: Spectra of QSOs or confirmed non-BLLs sources. Top panel: flux calibrated spectra. Normalized spectra on bottom. Telluric bands are indicated by \oplus , spectral lines are marked by line identification, absorption features from interstellar medium of our galaxy are labeled by ISM, diffuse interstellar bands by DIB. The flux density is in units of $10^{-16} \text{ erg cm}^{-2} \text{ s}^{-1} \text{ \AA}^{-1}$.

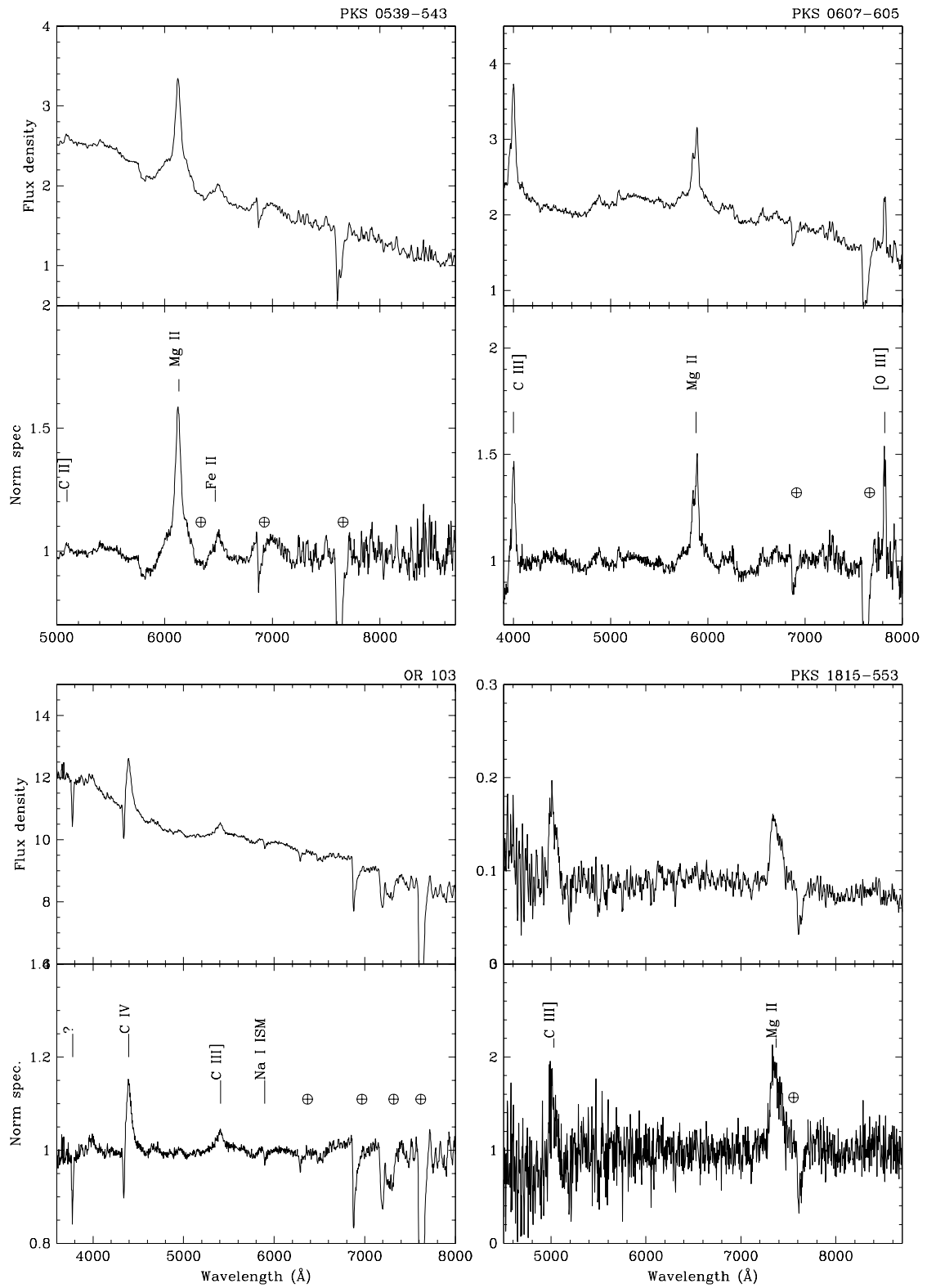


Figure 3.19: continued

cation we confirm the BL Lac nature for 25 objects . Their spectra are reported in Figure 3.11 to Figure 3.17 while confirmed non-BL Lac spectra are shown in Figure 3.18 to Figure 3.19. All BL Lac spectra can be accessed at the website <http://www.oapd.inaf.it/zbllac/> In particular, 20 sources have no intrinsic lines, 3 of them show weak absorption features arising from their host galaxy and other 3 show weak narrow emission lines. For only one object (OX 183) a weak broad emission line is apparent. We identify spectral features arising from the source or from intervening systems with the atomic species (if applicable) while the Diffused Interstellar Bands are marked with the label DIB. Telluric absorption are indicated by the symbol \oplus . The identification of the lines, their equivalent width, full width at half maximum and redshift estimation are given in Table 3.2 for BL Lac objects and in Table 3.3 for the other sources.

As explained in the Introduction of this chapter, the emission of BL Lac objects in the optical region is well characterised by a superposition of a non-thermal component, arising from the accreting nucleus, and a thermal one that originates from its host galaxy. In particular, the emission from the nucleus can be described by a power-law model $F_\lambda \propto \lambda^{-\alpha}$ while the galaxy contribution can be modeled by an elliptical galaxy template spectrum with $M_{host} = -22.90 \pm 0.50$ [Sbarufatti et al., 2005a]. For the objects that do not present host galaxy absorption features we fitted the continuum adopting a single power law, while for the BL Lac where galactic absorption are detected we performed the fit by adding the host galaxy template contribution, following procedure described in [Sbarufatti et al., 2006];[Sbarufatti et al., 2009]. Resulting power law indexes are reported in Table 3.2. The mean value is $\alpha_{mean} = 0.87 \pm 0.35$ which is consistent with result for power law indexes obtained in [Sbarufatti et al., 2005b]; [Sbarufatti et al., 2006];[Sbarufatti et al., 2009] ($\alpha_{mean} = 0.90 \pm 0.40$). Following the procedure described in [Sbarufatti et al., 2005b] we measured the minimum detectable equivalent width (EW_{min}) for each spectrum. All the candidate in the spectrum with EW above the minimum value has been carefully identified and cross checked with the original bidimensional frames (which are 2 or more per each source). Spectral parameters, line properties and relative identification and minimum equivalent width for the BL Lac objects investigated in this Thesis are reported in Table 3.2.

For the objects in which no spectral features are detectable (e.g. the case of BLL

0Q 240) we applied the procedure fully illustrated in Sbarufatti et al. [2005b] Sbarufatti et al. [2006] in order to infer a lower limit on the redshift of each source. Assuming that the BL Lac host galaxy is a giant elliptical with $M_{host} = -22.90 \pm 0.50$ if one measures the minimum equivalent width and the R nucleus apparent magnitude it is possible to derive a lower limit on the z of the source adopting the equation

$$EW_{obs} = \frac{(1+z) \times EW_0}{1 + \rho/A(z)} \quad (3.24)$$

where EW_{obs} is the observed minimum equivalent width, EW_0 is the equivalent width of the feature in the host galaxy template of Kinney et al. [1996], ρ is the nucleus-to-host flux ratio, z is the redshift and $A(z)$ is the aperture correction. The lower limits are reported in Table 3.2 . Spectral decompositions for BL Lacs with detected host galaxies are reported in Figure 3.20.

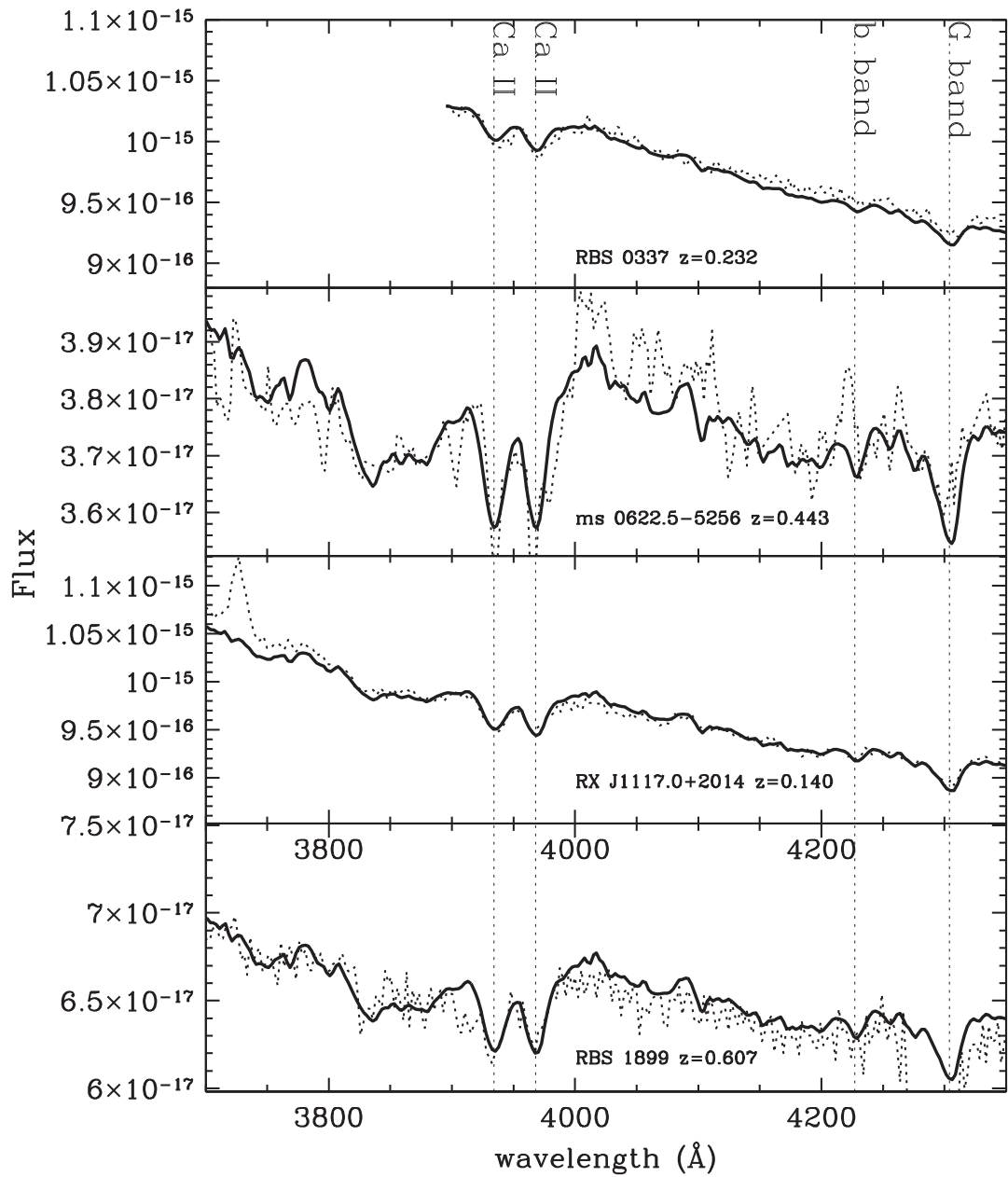


Figure 3.20: Spectral decomposition (rest frame) for the objects RBS 0337, MS 0622.5-5256, RX J1117.0+2014 and RBS 1899. The solid line shows the fitted spectrum while dots is the observed one.

Object	z	α	R	EW_{min}	Line ID	λ	z_{line}	Type	FWHM kms^{-1}	$EW_{obs}(\text{\AA})$
GC 0109+224	> 0.10	0.85	14.20	0.11						
PKS 0140-059	> 0.46	0.45	18.50	0.45						
RBS 0337	0.232	1.30	16.00	0.35	Ca II	4850	0.233	g		$+0.60 \pm 0.15$
					Ca II	4889	0.232	g		$+0.55 \pm 0.15$
					G Band	5304	0.232	g		$+0.80 \pm 0.13$
					Mg I	6375	0.233	g		$+1.00 \pm 0.18$
RBS 0499	> 0.45	1.00	18.60	0.65						
PKS 0439-299	> 0.68	0.30	20.10	1.00	Mg II (?)	4708	[0.68]	i		$+2.15 \pm 0.50$
RBS 0589	> 0.45	1.20	17.00	0.20						
ZS 0506+056	> 0.15	0.92	15.30	0.18						
MS 0622.5-5256	0.513	1.00	19.30	0.65	Ca II	5953	0.513	g		$+1.50 \pm 0.20$
					Ca II	6002	0.513	g		$+1.45 \pm 0.20$
					G Band	6501	0.512	g		$+1.40 \pm 0.40$
PKS 0735+17	> 0.18	0.84	15.70	0.20						
OJ-131	0.539	0.44	17.20	0.25	[O II]	5736	0.539	e	1200 ± 150	-1.15 ± 0.30
					H β	7481	0.539	e	1100 ± 100	-0.70 ± 0.15
					[O III]	7703	0.538	e	1250 ± 100	-2.50 ± 0.20
RX J1022.7-0112	> 0.30	1.34	16.60	0.20						

RX J1023.9-4336	> 0.24	1.28	15.80	0.12						
PKS B1056-113	> 0.27	0.66	16.50	0.20						
1ES 1106+244	> 0.37	0.78	18.20	0.65						
RX J1117.0+2014	0.140	1.40	16.10	0.40	[O II]	4245	0.139	e	1200 ± 120	-1.20 ± 0.20
					Ca II	4489	0.140	g		+0.70 ± 0.15
					Ca II	4522	0.140	g		+0.60 ± 0.10
					G Band	4908	0.140	g		+0.70 ± 0.20
					Na I Blend	6710	0.139	g		+1.10 ± 0.40
RX J1241.8-1455	> 0.32	1.05	16.80	0.20						
1ES 1239+069	> 0.47	1.00	18.10	0.35						
4C-12.46	> 0.37	0.43	17.60	0.30						
OQ-240	> 0.10	1.00	14.20	0.15						
RBS 1478	> 0.50	0.95	18.60	0.50						
OW-080	> 0.47	0.42	18.10	0.25						
OX-183	0.870	0.16	18.70	0.50	Mg II	5236	0.870	e	4400 ± 300	-5.80 ± 1.60
					[O II]	6970	0.870	e	1100 ± 200	-3.50 ± 0.70
RBS 1899	> 0.53	0.93	18.60	0.45						
RX J2319.6+1611	> 0.97	0.96	17.20	0.25	Mg II (?)	5527	[0.97]	i		+1.50 ± 0.30
1ES 2322-409	> 0.16	0.84	15.90	0.32						

Table 3.2: Spectral line parameters for the BL Lac objects.

Object ¹	α	R	LineID	λ	z_{line}	Type	FWHM kms ⁻¹	EW _{obs} (Å)
PKS 0302-623	1.350	17.70	C III]	4485	1.349	e	5500 ± 300	-20.00 ± 2.00
			Mg II (?)	5756	[1.056]	i		+2.50 ± 0.30
			Mg II	6585	1.350	e	7000 ± 300	-35.00 ± 8.00
PKS 0410-519	1.254	17.10	C III]	4300	1.252	e	5200 ± 300	-63.50 ± 5.00
			Mg II	6310	1.253	e	3400 ± 300	-48.00 ± 6.00
PKS 0443-387	0.537	16.80	Mg II	4298	0.535	e	7400 ± 500	-53.50 ± 3.00
			[Ne V]	5143	0.537	e	1100 ± 100	-0.60 ± 0.20
			[Ne V]	5268	0.537	e	1500 ± 200	-2.60 ± 0.30
			[O II]	5730	0.537	e	1200 ± 100	-2.50 ± 0.20
			[Ne III]	5946	0.537	e	2000 ± 300	-5.30 ± 0.60
			H ϵ	6098	0.537	e	1200 ± 200	-1.70 ± 0.30
			H δ	6304	0.537	e	1050 ± 150	-0.90 ± 0.20
			H γ	6670	0.537	e	5300 ± 400	-30.00 ± 3.00
			H β	7455	0.534	e	5300 ± 400	-30.00 ± 3.00
[O III]	7697	0.537	e	1100 ± 100	-35.00 ± 8.00			
PMN J0529-3555	0.323	19.20	Mg II	3705	0.323	e	6400 ± 400	-90.30 ± 10

¹Description of columns: (1) Object name (5) Barycenter of the line (6) Redshift of the line; (7) Line type e: emission line from BL Lac; g: absorption line from BL Lac host galaxy; i: absorption line from intervening system; (8) Full Width at half maximum; (9) Measured equivalent width

			Ca II	5206	0.323	g		$+4.60 \pm 0.70$
			Ca II	5250	0.323	g		$+4.50 \pm 0.50$
			G Band	5689	0.323	g		$+4.50 \pm 0.50$
			[O III]	6560	0.323	e	1300 ± 100	-4.70 ± 0.80
			[O III]	6623	0.323	e	1100 ± 200	-9.80 ± 1.20
PKS 0539-543	1.191	17.60	C II]	5097	1.191	e	3200 ± 300	-1.40 ± 0.30
			Mg II	6135	1.191	e	4000 ± 400	-50.00 ± 8.00
PKS 0607-605	1.100	17.30	C III]	4000	1.095	e	3400 ± 300	-30.90 ± 3.00
			Mg II	5880	1.100	e	4000 ± 300	-45.50 ± 4.00
			[O II]	7821	1.100	e	1100 ± 100	-13.50 ± 2.00
OR 103	1.833	15.70	Mg II (?)	3778	[0.349]	i		$+2.80 \pm 0.5$
			C IV	4393	1.834	e	5200 ± 300	-13.50 ± 2.00
			C III]	5410	1.833	e	4800 ± 400	-5.00 ± 0.70
PKS 1815-553	1.633	20.80	C III]	5030	1.634	e	6800 ± 600	-92.00 ± 13.00
			Mg II	7370	1.632	e	6100 ± 400	-115.00 ± 15.00

Table 3.3: Spectral measurement for objects that are not classified as bona fide BL Lacs (QSOs for example)

3.3.4.1 The BL Lac mean spectrum

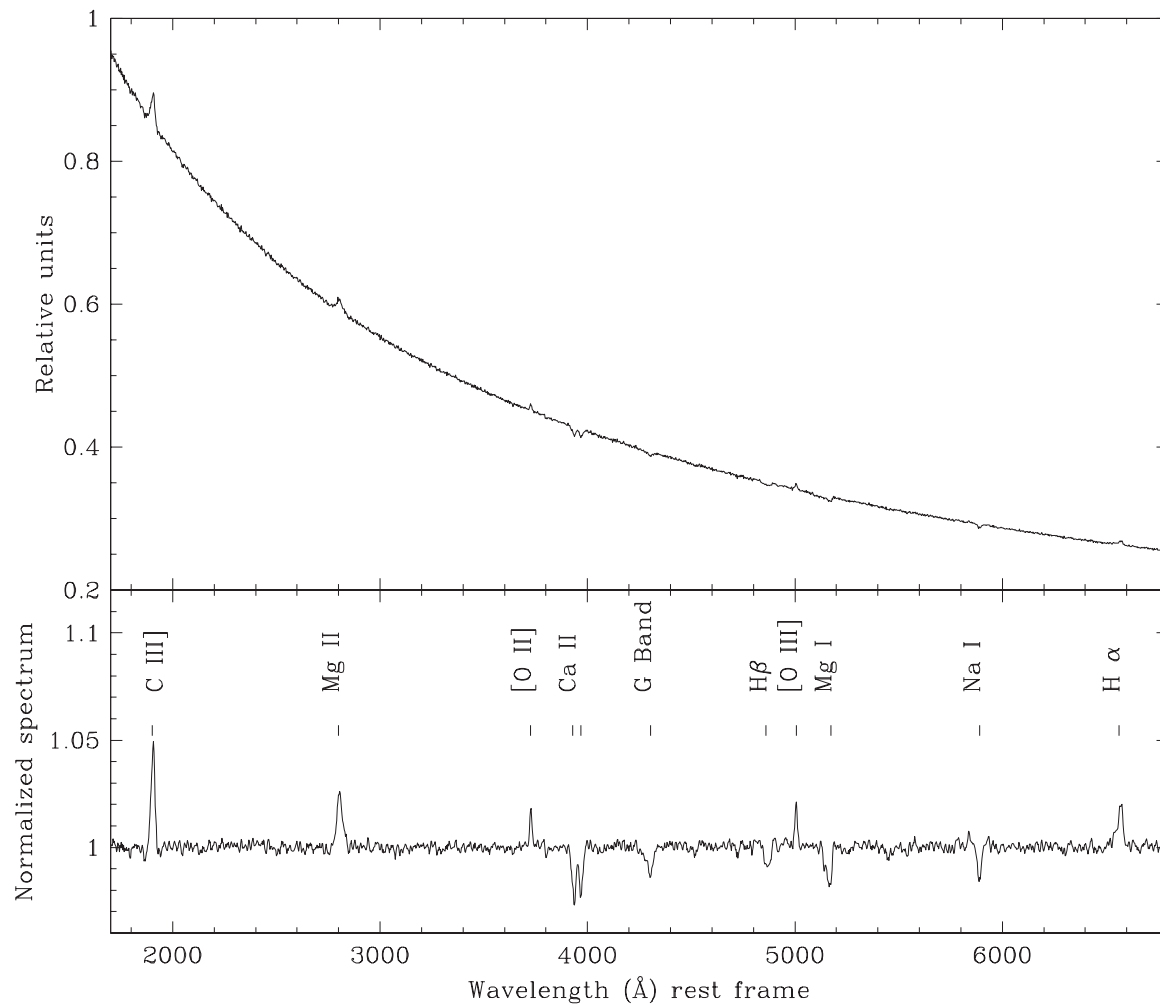


Figure 3.21: Mean spectrum of BL Lac objects obtained combining the 23 objects of our campaign in which intrinsic spectral features are detected. The first panel reports the mean spectrum assuming for the continuum a power-law with index $\alpha = 0.90$ (which corresponds to the mean spectral index of the whole BL Lac sample). In the second panel normalised spectrum is shown.

Ion ¹	λ	EW	FWHM (kms ⁻¹)	EW range	FWHM range	$\frac{N_{obs}}{N_{tot}}$	Type
C III]	1909	1.20 ± 0.10	4000 ± 350	[1.30; 1.90]	[2000; 4000]	3/4	e
Mg II	2800	1.00 ± 0.20	3500 ± 200	[0.30; 3.20]	[1900; 6100]	9/13	e
[O II]	3727	0.30 ± 0.10	1300 ± 200	[0.10; 2.50]	[1000; 4700]	9/18	e
Ca II	3934	0.80 ± 0.20		[0.30; 6.10]		12/17	g
Ca II	3968	0.65 ± 0.10		[0.40; 4.20]		12/17	g
G Band	4305	0.75 ± 0.10		[0.42; 4.00]		12/17	g
H β	4862	0.25 ± 0.10		[0.50; 3.00]		2/14	g
[O III]	5007	0.50 ± 0.10	1100 ± 200	[0.80; 1.47]	[500; 2400]	3/14	e
Mg I	5162	0.90 ± 0.20		[0.26; 14.00]		3/12	g
Na I	5892	0.40 ± 0.10		[1.00; 3.00]		2/6	g
H α	6563	0.90 ± 0.15	1300 ± 200	*	*	1/3	e

Table 3.4: Mean BLL spectrum parameters.

In order to better characterise the spectrum of BL Lac objects, we constructed a mean optical spectrum combining the normalized spectra of the 23 sources, belonging to the whole sample, with z measured through intrinsic emission or absorption lines. In details, for each spectrum we first carefully removed spectral regions contaminated by telluric, interstellar medium or intervening absorption system (such as the Mg II, see next sections) and then we corrected the spectrum to rest frame reference by adopting the measured z . We finally averaged the spectra according to their signal-to-noise ratio. The obtained mean spectrum is reported in Figure 3.21 and it covers the spectral range $1800 \text{ \AA} \sim 6700 \text{ \AA}$, rest frame. The first panel shows the mean spectrum assuming for the continuum a power-law with index $\alpha = 0.90$ while the normalised spectrum is reported in the bottom panel. We measured the spectral features detectable on the average spectrum reporting the line identification, equivalent width and full width at half maximum in Table 3.4. It is important to point out that, due to the large difference in BL Lacs of the

¹Description of columns: (1) Ion identification; (2) Rest frame wavelength; (3) Measured equivalent width (4) Full width at half maximum (5) Equivalent width measurement range (6) Full width at half maximum measurement range (7) Ratio between number of detections and number of spectra in which the line could be measures (8) Type of line: e: emission line from BL Lac; g: absorption line from BL Lac host galaxy;

ratio between the non-thermal emission and the thermal one associated to stellar component arising from their host galaxy, the mean BL Lac spectrum cannot be considered as representative as that of QSOs. Nevertheless, it illustrates emission or absorption lines that could be measured in individual objects. In particular, absorption lines from the host galaxy are always present in the spectrum but their detectability depends both on SNR ratio and on the nucleus-to-host ratio of the source. The emission lines instead could be missing .

3.3.5 The relativistic optical beaming factor δ

The emission mechanism of BL Lac objects is essentially dominated by the non-thermal emission which arises from synchrotron photons generated by the relativistic jet. Due to its high $\Gamma = \frac{1}{\sqrt{1-\beta^2}}$ Lorentz factor and considering the low angle subtended by the cone of the jet and the line of sight, the relativistic doppler beaming $\delta = \frac{1}{\Gamma(1-\cos\theta)}$ plays an important role in the understating of the physics behind these kind of source. In fact, as a first property, it must to be recalled that the received power from the jet is relativistic, boosted according to the formula $P_{received} = \delta^4 P_{emitted}$. In various emission model mechanism (see e.g. [Tavecchio et al. \[1998\]](#)) the δ doppler factor is derived from theoretical assumption on the radiative region mixed up with observable physical quantities, such as X-ray fluxes, SED, etc.

For instance, in the radio emission, the relativistic beaming of the jet is revealed in BL Lac in the frequent appearance of jets with superluminal velocities. This is also required in high energy emissions (in γ -rays) by the short time scale of variability, which can be accommodated in a standard SSC model (e.g. [Tavecchio et al. \[1998\]](#)) only invoking large Doppler beaming factors. In order to derive a relativistic doppler factor calculated from the observable quantities in the optical band and following the unified model of Active Galactic Nuclei, we assume that the optical emission arising from the nuclear component is basically the superposition of a two major component. The thermal emission of luminosity L_{th} , associated with a disk structure, and a non thermal one L_{nth} , which dominates the output received power in BL Lac objects. Since the former component is assumed to be isotropic (at least in a first rough approximation) and the latter supposedly is

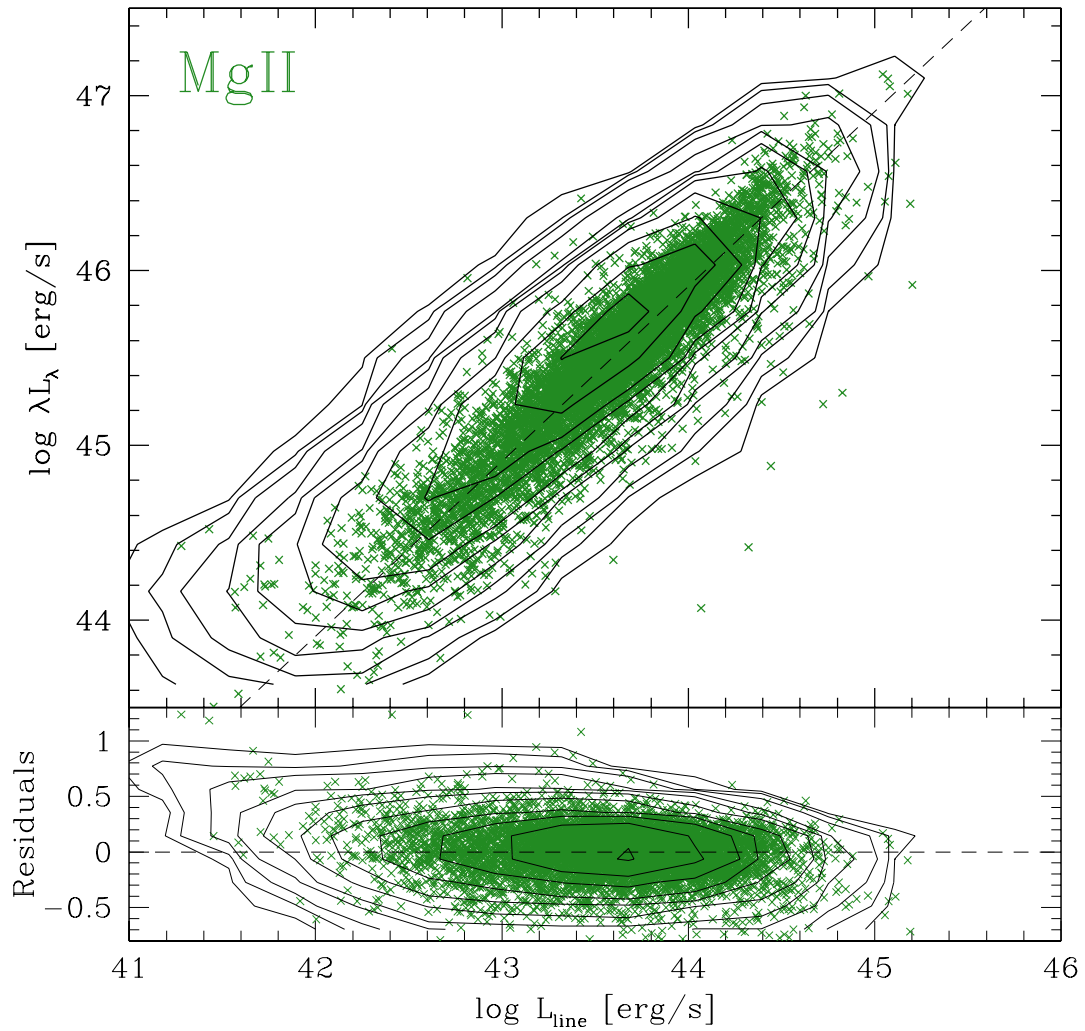


Figure 3.22: Relation between the thermal disk continuum and MgII emission line luminosity (see Decarli et al. [2011] for details).

beamed, we can define as beaming factor (see e.g. Farina et al. [2012]; Landoni et al. [2012a])

$$\delta_{opt} = \frac{L_{tot}}{L_{thermal}} \quad (3.25)$$

where $L_{tot} = L_{thermal} + L_{NonThermal}$. We further assume that the thermal components (accretion disk) of BL Lac objects can be described as that of quasars. The large collection of Type I AGN spectra available in the SDSS allows to find relations between the broad line luminosity L_{line} and the continuum (thermal) luminosity for Type I quasars. They are generally expressed in the form

$$\log \frac{\lambda L_{\lambda}(\lambda_{ref})}{L_{line}} = K \quad (3.26)$$

For simplicity, we refer only to Mg II relation (see Figure 3.22) since it is the tightest one ($K = 1.91 \pm 0.26$, $\lambda_{ref} = 3000$, see Decarli et al. [2011]; Shaw et al. [2012]). Taking into account the contribution of the cosmological redshift and combining Equation 3.25 and 3.26 with the usual definition of the Equivalent Width, one has

$$\delta = (1 + z) \times \frac{\lambda_{ref}}{10^K \times EW} \quad (3.27)$$

δ is obviously equal to ~ 1 , within the dispersion, in the case Type I quasar. When a broad Mg II line is observed in a BL Lac object Eq. 3.27 gives an estimate of the beaming. If no emission line is detected one can still use Eq. 3.27 and from the upper limit on the equivalent width deduce a lower limit on δ . We suppose that the redshift is such that the relation can be applied because the Mg II emission line is within band of observation and we also consider the positive $1-\sigma$ dispersion on the relation, which yields $K = 2.17$. In particular, for featureless BL Lacs we assume $z \sim 0.7$ while for the BL Lac in which the redshift is known we use the actual value for the redshift. The wide-spread criterion of defining a BL Lac a Type I AGN with line $EW < 5$, which was adopted also in this paper, therefore translates through Eq. 3.27 in $\delta \gtrsim 4$ which is a more physical definition. In other words, the criteria illustrated in the equation simply states that in BL Lacs the non thermal output power is at least a factor 4 higher than the thermal one.

In Figure 3.23 we show the lower limit relation expressed in Eq. 3.27 for the beaming factor of BL Lacs with no broad emission lines (dashed line) and the

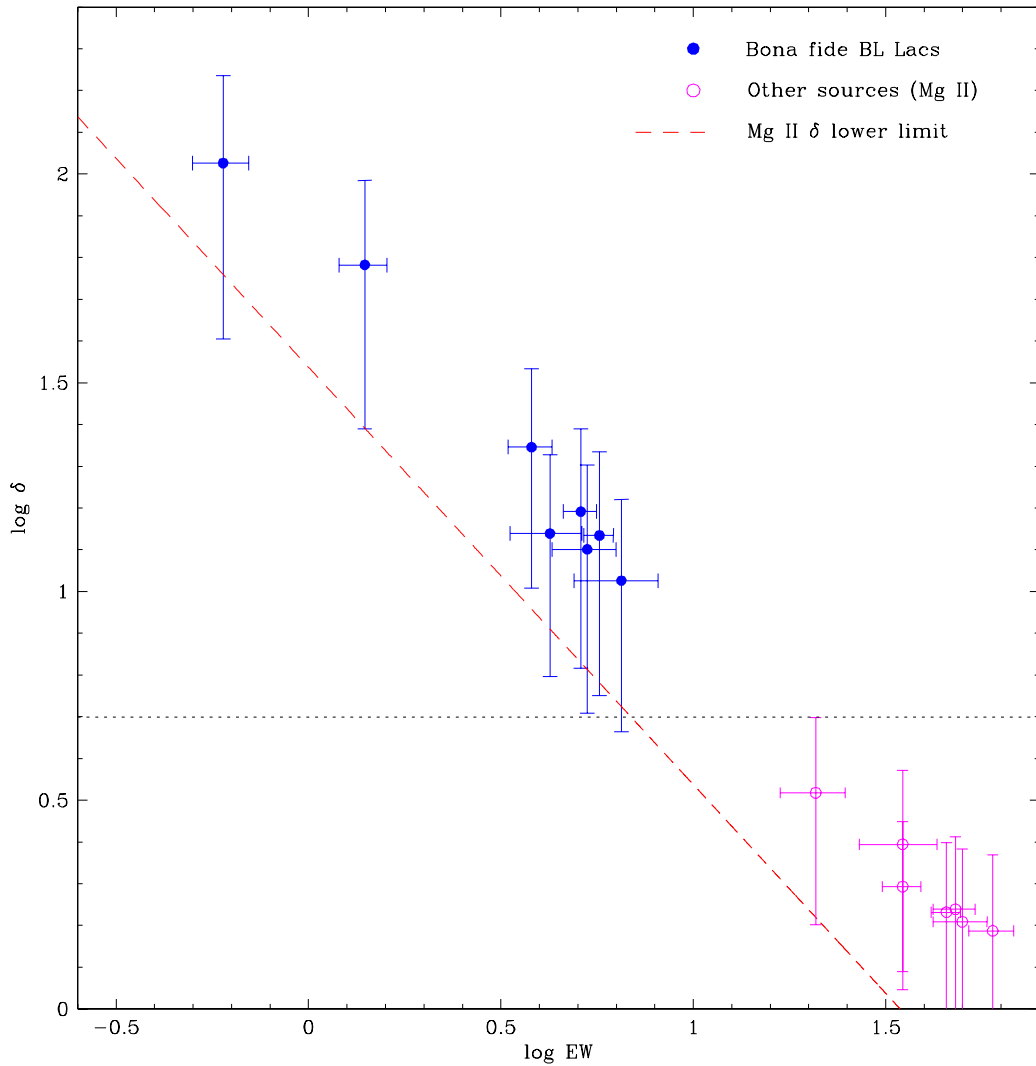


Figure 3.23: Optical beaming factor for the sources observed in the campaign. Red dashed line indicates the lower limit value calculated through Equation 3.27 assuming $z = 0.70$. Filled blue circle are the δ of bona-fide BL Lac objects with Mg II emission line while the open magenta circle are the beaming factor for other intermediate sources (classified as confirmed non-BL Lacs). Dotted line delimit the area of the EW- δ plane where the source are of intermediate nature between pure QSO($\delta \sim 1$) and BL Lacs($\delta > 4$).

actual value of δ for the sources in which the broad Mg II emission line is detected (filled blue circle). We note that ~ 7 BL Lac candidates considered in our complete sample have spectral properties that do not completely satisfy the criterion for BL Lac classification. On the other hand, these objects differ also from the typical spectrum of Type I AGN. Interesting enough they have their optical beaming factor (open magenta circle of Figure 3.23) much larger of that of quasar, where δ should be ~ 1 , suggesting a substantial non-thermal emission from the nucleus which indicates that the objects are indeed of intermediate nature between BL Lac and quasars.

3.3.6 Statistical properties of the whole sample

Thanks to the high quality optical spectra, we confirmed as bona-fide BL Lacs **69** sources while **15** have been classified as QSOs or FSRQs. The remaining 4 objects are stars (in particular 1 main sequence star and three white dwarf misclassified in the original catalogs).

For the sources that have been classified as bona-fide BL Lac we were able to measured a spectroscopic redshift for **23** of them. In particular, in **12** sources we clearly detected the absorption features from their host galaxy and in **15** objects emission lines are observable. Broad emission lines (such as Mg II or C III]) are detected in only **10** BL Lacs.

We measured the luminosity of Mg II emission lines in all the sources in which the line is detected. The mean value is $\log L(MgII) \sim 42.40 \pm 0.30$, where $L(MgII)$ is in erg s^{-1} . This value is lower of an order of magnitude of that of quasars which is $\log L(MgII) \sim 43.60 \pm 0.45$ [Shen et al., 2011] but the dispersions are rather larger. For the remaining **46** sources we inferred a redshift lower limit as illustrated in the previous section .

The full dataset, with spectra and line identification, is also available in electronic form at the website <http://www.oapd.inaf.it/zbllac/>.

3.3.7 Intervening Mg II system on BL Lac objects observed with FORS2

In 1997 [Stocke and Rector \[1997\]](#) claimed that a strong excess of a factor ~ 4 on the number of Mg II intervening system is apparent in the spectra of BL Lac objects, with respect to those of quasars. Since BL Lac objects are extragalactic sources it is reasonable to expect that their spectra could present absorption features from intervening systems but a strong excess of Mg II system could appear as a selection effect and/or an intrinsically properties of the source. A more exotic explanation involves the gravitational lensing of the BL Lac source. As reported in [Stocke and Rector \[1997\]](#) BL Lac objects with foreground Mg II absorbers could be microlensed by stars associated with the absorbing gas. The background AGN is a radio-loud quasar associated with its common emission line but the action of the foreground stellar screen is to preferentially amplify the continuum of the background source.

In order to confirm or partially reject this claimed excess we analysed our FORS2 BL Lac sample aimed to characterise the Mg II detected intervening systems. In our sample there are 7 confirmed BL Lacs objects in which absorption systems are detected. These absorptions are interpreted as Mg II intervening systems on our line of sight toward the BL Lac. In particular, the total number of absorbing systems is $N_{obs} = 8$, partly associated with BL Lacs with unknown redshift. The most natural interpretation is that the features are due to intervening MgII at $\lambda_{rest} = 2800$. The features associated to intervening Mg II systems are observable in our sample in the redshift interval $z_{min} \sim 0.5$ and $z_{max} \sim 1.5$. The total number of BL Lacs we consider is $n_t = 69$ (23 with redshift measured and 46 lower limits on z) and those which have $z < z_{min}$ are 13. Therefore, excluding sources with $z < z_{min}$ the number of BL Lacs which can contribute to the observed absorptions is at most 56. On the other hand the minimum number which for sure contributes to the statistics of the absorbers is 8, which are the observed systems associated to BL Lacs in our sample, plus the number of BL Lacs without intervening absorptions with $z > z_{min}$ that are 20.

Following [Zhu and Ménard \[2013\]](#), who consider QSOs in the SDSS, for an arbitrary pointing direction the normalised mean number of MgII absorbers with EW

$\gtrsim 1 \text{ \AA}$ is $n_Q \sim 0.40$ in the redshift range given above. This value is obtained numerically integrating the curve reported in Figure 3.24 bottom panel. Within

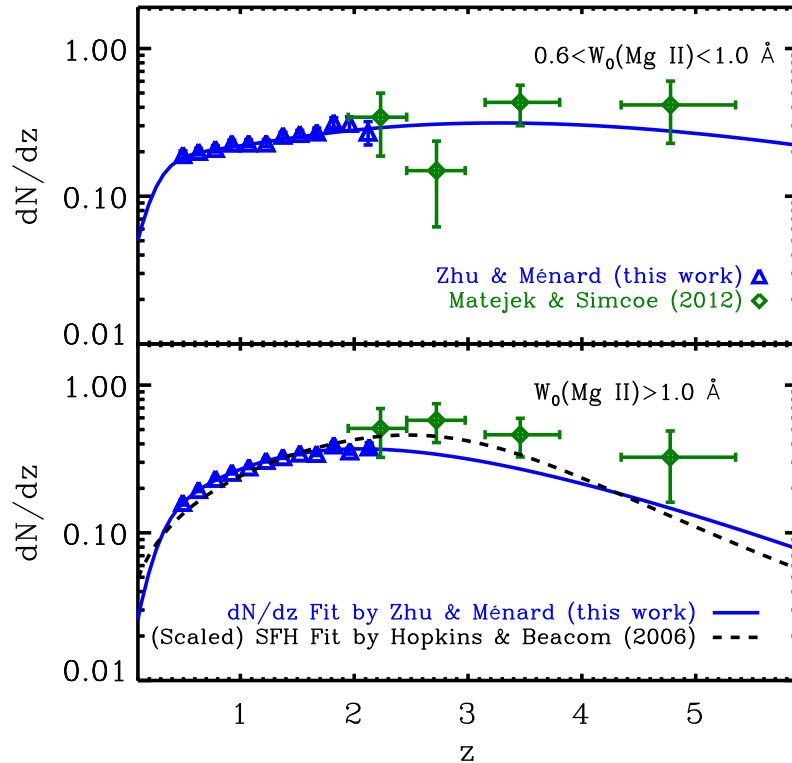


Figure 3.24: Incidence rate $\frac{dN}{dz}$ of Mg II absorbers with $0.6 \text{ \AA} < EW \lambda 2796 < 1.0 \text{ \AA}$ (top) and $EW \lambda 2796 > 1.0 \text{ \AA}$ (bottom). Figure from [Zhu and Ménard, 2013].

these assumptions we expect that the number of Mg II absorption systems is $11 < N_{exp} < 22$. Since in our sample we observe $N_{obs} = 8$ intervening systems we do not confirm the suggestion of Stocke and Rector [1997] and we conclude that absorbers related to BL Lacs are not more numerous than those associated to QSOs. Moreover, since the distribution of Mg II intervening system for BL Lac appears to be similar of those of quasars, the number of observed absorption system could suggest that the BL Lacs without z in our sample should have low value for their redshift, in order to comply with the discussed statistical properties for intervening system.

3.4 Medium resolution spectroscopy of bright BL Lac objects with ESO-XSHOOTER

3.4.1 Introduction

As illustrated in the previous section, observation with a 8 mt class telescope equipped with a low/medium resolution spectrograph allowed to measure redshift for a conspicuous percentage of BL Lacs for which the z were unknown when observed with other telescopes (4 mt for instance). Nevertheless, some γ -ray TeV bright sources were left without z also with 8-mt FORS2 spectra.

A first solution of this problem is to increase the SNR ratio of the observed spectra using even larger telescopes or perform spectroscopy in the NIR band of the electromagnetic spectrum. This approach is suitable both for higher redshift sources, where rest frame optical and UV emission lines from the active nucleus and absorption lines from the host move in the observed NIR band, and for low-intermediate redshift sources, where strong emission and absorption lines are available to measure precisely the redshift. For all of these reasons, we decided to observe a small subset of bright γ -ray sources with XSHOOTER [Vernet et al., 2011] spectrograph at ESO-VLT.

Sbarufatti et al 2009 proposed a filler program, to be carried out under non-optimal seeing condition, aimed at the observation of 6 sources selected following the criteria : **(a)** sources confirmed as featureless BL Lacs by VLT+FORS optical spectroscopy; **(b)** source lacking high S/N IR spectroscopy in the literature; **(c)** source detected in the γ -ray or TeV domain. An additional observational constraint requires that the selected sources must have $\delta < 20^\circ$ and $14 < m_v < 17$ in order to ensure high S/N spectra with reasonable exposure times.

VLT equipped with XSHOOTER observations produced for the first time UV to NIR spectroscopy for these sources. The high expected S/N allowed the detection of faint spectral features. The UV part of the spectrum has been used to model the non-thermal continuum that is subtracted from the optical and IR spectra in order to maximize our capability to detect host galaxy spectral lines. In the case of a featureless spectrum we determinate a more stringent redshift lower limit exploiting the fact that host galaxies are candles, as done for our previous VLT+FORS

Date ^{(a)1}	Seeing ^(b)	Channel ^(c)	Slit ^(d)	R ^(e)	t_{exp} ^(f)	N ^(g)	SNR ^(h)
05 Jul 2010	1.22	UVB	$1.6'' \times 11''$	3300	2720	4	34
		VIS	$1.5'' \times 11''$	5400	2460	6	32
		NIR	$1.5'' \times 11''$	3500	1440	6	28
18 Aug 2010	0.84	UVB	$1.6'' \times 11''$	3300	2720	4	24
		VIS	$1.5'' \times 11''$	5400	2460	6	24
		NIR	$1.5'' \times 11''$	3500	1440	6	24

Table 3.5: Journal of Observations of PKS0048-097

Date ^(a)	Seeing ^(b)	Channel ^(c)	Slit ^(d)	R ^(e)	t_{exp} ^(f)	N ^(g)	SNR ^(h)
28 Apr 2010	1.80	UVB	$1.6'' \times 11''$	3300	410	4	150
		VIS	$1.5'' \times 11''$	5400	410	6	130
		NIR	$1.5'' \times 11''$	3500	410	6	80

Table 3.6: Journal of Observations of PG 1553+113

observations. More details are reported in the Proposal P85-43030 (PI: Sbarufatti B.).

3.4.2 The sample, observation and data reduction

The following sources, with the reported setup, have been observed with ESO-XSHOOTER at the Very Large Telescope.

We obtained UVB (3100-5500 Å), Optical (5600-10.000 Å) and near-IR (10.100-15.000 Å) spectra of the each target using the ESO Very Large Telescope (UT2 - *Kueyen*) equipped with X-Shooter in Service Mode. The spectra were secured using the Nodding configuration for the instrument, according to the Journal of Observations reported from Table 3.5 to Table 3.8.

The data reduction was carried out using the X-Shooter Data Reduction Pipeline (version 2.0.0, see [Goldoni et al. \[2006\]](#)) in Polynomial Mode adopting the config-

Date ^(a)	Seeing ^(b)	Channel ^(c)	Slit ^(d)	R ^(e)	t_{exp} ^(f)	N ^(g)	SNR ^(h)
28 Apr 2010	1.80	UVB	$1.6'' \times 11''$	3300	240	4	60
		VIS	$1.5'' \times 11''$	5400	240	6	60
		NIR	$1.5'' \times 11''$	3500	240	6	50

Table 3.7: Journal of Observations of H 1722+119

Date ^(a)	Seeing ^(b)	Channel ^(c)	Slit ^(d)	R ^(e)	t_{exp} ^(f)	N ^(g)	SNR ^(h)
28 Apr 2010	1.80	UVB	$1.6'' \times 11''$	1360	240	4	50
		VIS	$1.5'' \times 11''$	1360	240	6	45
		NIR	$1.5'' \times 11''$	3500	1360	6	30
05 May 2010	1.80	UVB	$1.6'' \times 11''$	1360	240	4	50
		VIS	$1.5'' \times 11''$	1360	240	6	45
		NIR	$1.5'' \times 11''$	3500	1360	6	30

Table 3.8: Journal of Observations of PKS2254-204

uration recommended by ESO.

In particular, for each observation, we calculated the Master Bias Frames and Master Flat Frames for each channel selecting carefully the proper slit values reported in Table 3.5 - 3.8. We also obtained the bidimensional mapping required by the pipeline software stack to resample the Echelle Orders. Finally, for each channel, we computed the sensitivity functions required by the pipeline to calibrate in flux the spectra. We normalized in relative units the obtained spectra in order to proper juxtapose the three arms.

In case of multiple observation (PKS 0048-097 and PKS 2254-204) since no significant spectral differences were apparent between the two spectra we averaged them in order to improve the overall signal-to-noise ratio. For instance, the XSHOOTER Pipeline Workflow schema, taken from the Official ESO User Manual, is reported in Figure 3.25.

3.4.3 The case of FERMI γ -ray BL Lac PKS 0048-097 observed with XSHOOTER

3.4.3.1 Introduction

PKS 0048-097 ($m_V = 15$) is a bright, strongly variable [Pica and Smith, 1983] and best studied BL Lac object [Falomo et al., 1993a, 1994a; Stickel et al., 1993; Wills et al., 1992]. Despite many spectroscopical studies [Sbarufatti et al., 2006; Stickel et al., 1993] it remains one of the few bright sources with unknown redshift. Imaging studies of the source were unable to detect its host galaxy [Falomo, 1996a]. Moreover, the upper limits to the brightness of the host galaxy derived

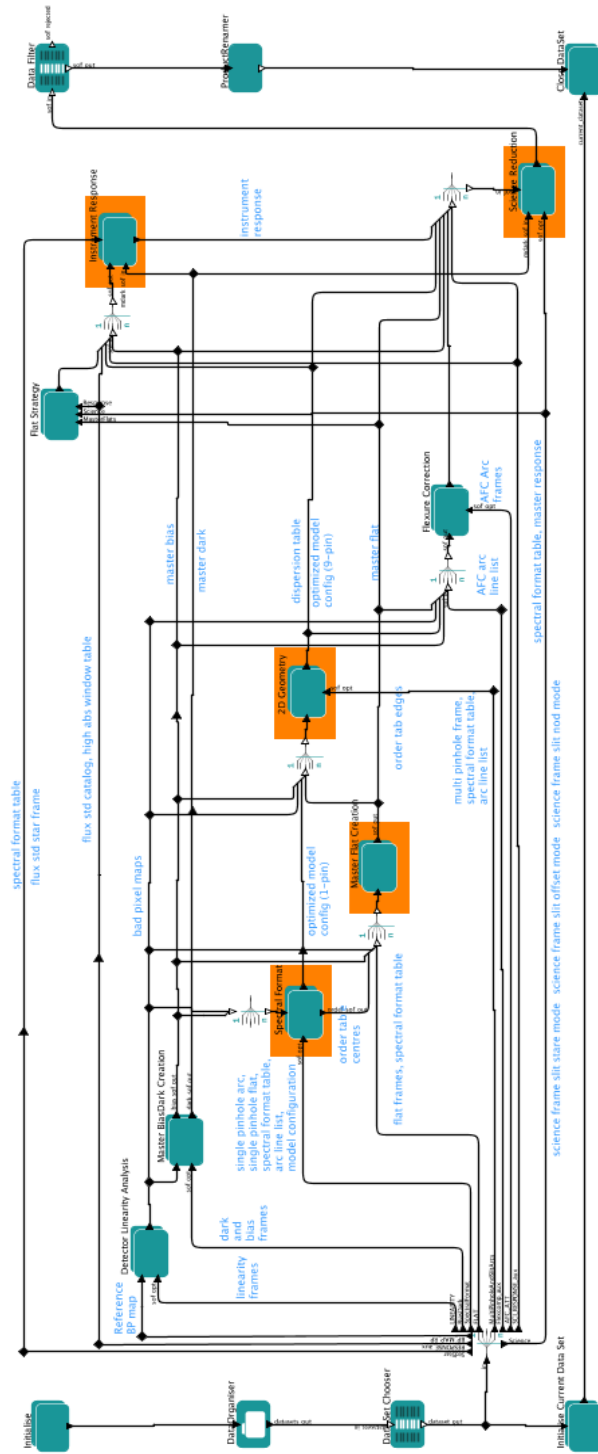


Figure 3.25: ESO XSHOOTER data reduction pipeline workflow schema (courtesy ESO XShooter User manual, Version 2.0)

Table 3.9: Measurements of spectral lines observed (referred to the mean spectrum of each arm). The observed λ column is referred to the barycenter of the line.

Line	λ [\AA]	z	FWHM [km s^{-1}]	EW [\AA]
Mg II 2796.35	3228.20 ± 0.20	0.1544 ± 0.0001		0.59 ± 0.16
Mg II 2803.53	3236.60 ± 0.20	0.1544 ± 0.0001		0.45 ± 0.12
[O II] 3727.40	6096.20 ± 1	0.635 ± 0.0004	680 ± 100	0.79 ± 0.39
[O III] 5006.84	8189.20 ± 1	0.635 ± 0.0004	400 ± 100	0.92 ± 0.44
H α 6562.80	10751.10 ± 5	0.638 ± 0.001	1900 ± 130	3.00 ± 1.20

from Optical and NIR imaging suggest lower limits to the redshift of $z > 0.3$, even $z > 0.5$ [Falomo, 1996a; Kotilainen et al., 1998]. Nevertheless, the observation of the source with XSHOOTER allowed us both to measure a firm redshift for this well known source and to study the close environment of the BL Lac. In particular, in Figure 3.26, we show the mean spectrum of PKS 0048-097 obtained after the complete data reduction with X-SHOOTER.

3.4.3.2 Spectral analysis

PKS 0048-097 clearly shows that its continuum is dominated by the contribution of non-thermal emission, which can be described by a power law of the form $F(\lambda) = \lambda^{-\alpha}$ ($\alpha \sim 0.9$). In addition to many telluric absorption lines, it is possible to clearly detect the intervening Galactic absorption of Ca II (EW $0.16 \text{ \AA} - 0.05 \text{ \AA}$) and Na I (EW $0.10 \text{ \AA} - 0.07 \text{ \AA}$). The flux calibration was cross checked using the relative photometric calibration of the acquisition image. The R band magnitude of PKS 0048-097 is found to be 17.3 ± 0.3 , which corresponds to a low brightness of the source. In the literature, the R magnitude of the source is reported to be between 14.74 and 16.22 (Fan and Lin [2000]). In this case, the combination of the high quality instrumentation, in terms of throughput and spectral resolution, and the low brightness of the source clearly favoured the detection of the faint emission lines.

Starting from the spectrum reported in Figure 3.26 we searched for intrinsic emission or absorption features above or below $\sim 3\sigma$ SNR ratio of the spectrum with the additional condition that the features are clearly detectable in both in-

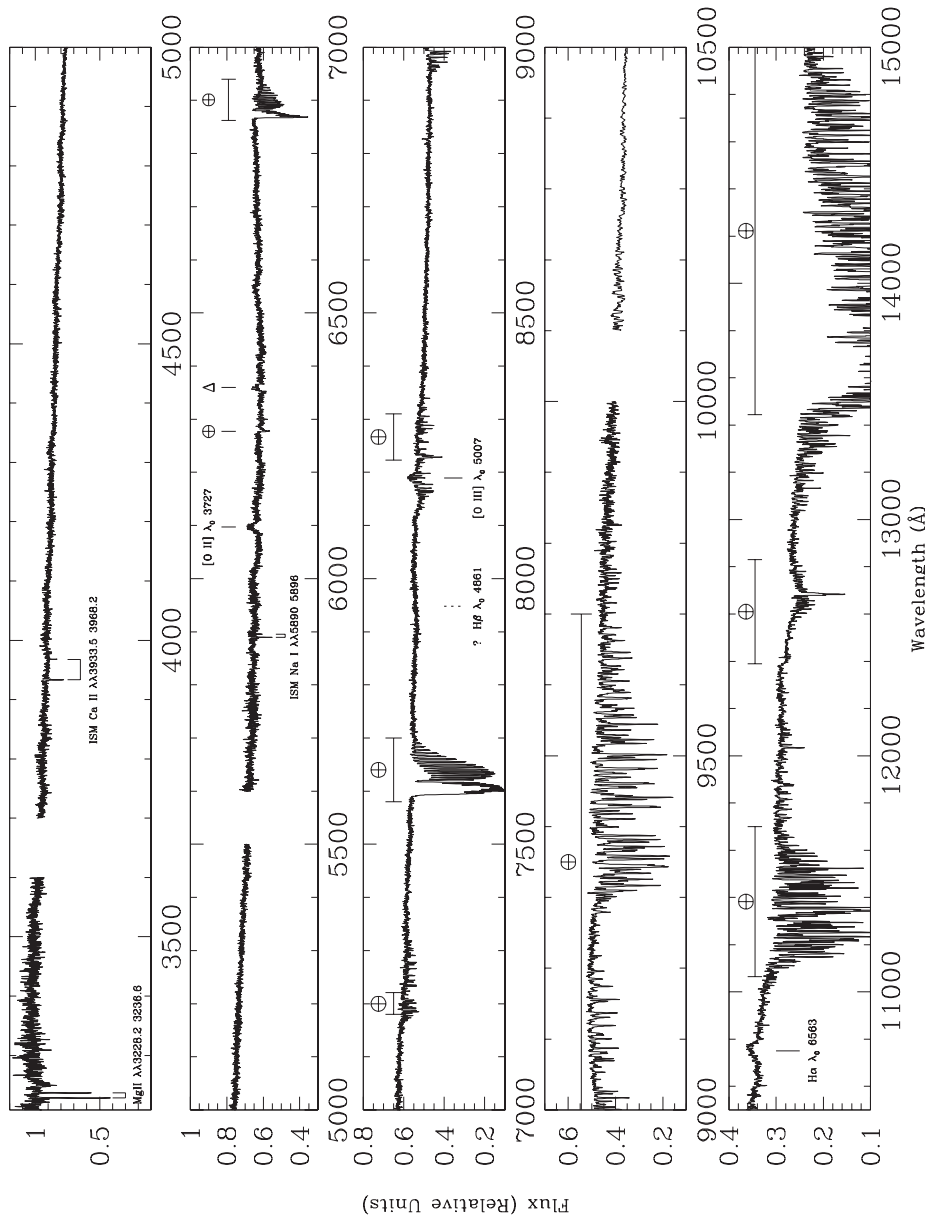


Figure 3.26: PKS0048-097 overall mean spectrum. Atmospheric absorption are labelled by \oplus while calibration artefacts (detectable in the two-dimensional image of the spectrum) are marked with Δ . Emission lines above $\sim 3\text{-}\sigma$ confidence intervals of the SNR of the spectrum are marked with a single vertical line. The expected position of $H\beta$ at $z = 0.635$ is marked with a dashed line.

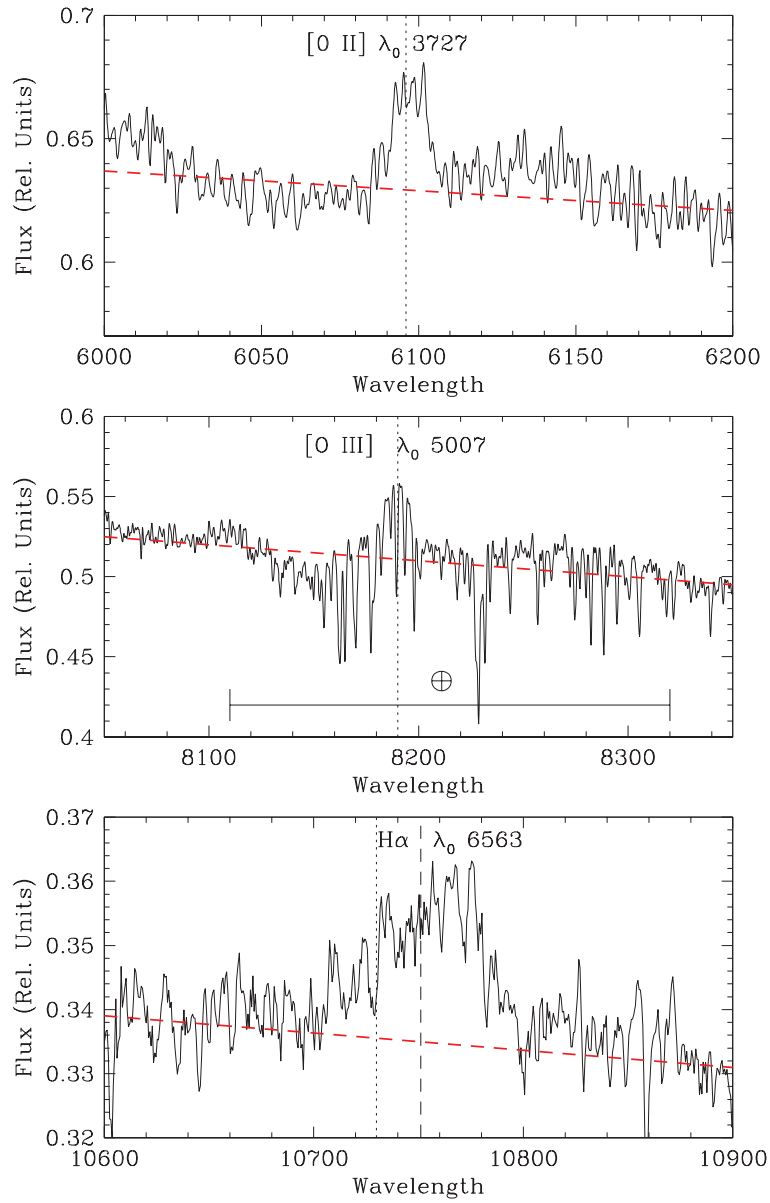


Figure 3.27: PKS 0048-097 [OII] emission line at 6096 \AA , [O III] at 8189 \AA polluted by many resolved atmospheric absorption, and $\text{H } \alpha$ emission line at 10751 \AA . The vertical dotted lines represent the expected position of the three emission lines assuming the redshift $z = 0.635$, while the dashed one indicates the position of the barycenter. The red dotted line is the fit to the continuum.

dividual spectra and do not correspond to obvious defects in the two-dimensional image. This procedure detected three emission lines (see Figure 3.26 and 3.27 and Table 3.9) at $\lambda = 6096\text{\AA}$, $\lambda = 8189\text{\AA}$, and $\lambda = 10751\text{\AA}$. The line at $\lambda = 6096\text{\AA}$ was tentatively detected by Rector and Stocke [2001] (EW 0.3 \AA). It is important at this point to stress the fact that no previous near-IR observation of comparable spectral resolution was present in the literature. We identify the first two lines as [O II] ($\lambda_0 = 3727\text{\AA}$) and [O III] ($\lambda_0 = 5007\text{\AA}$) from which a consistent redshift of $z = 0.635$ is derived. The third emission line ($\lambda = 10751\text{\AA}$) is identified as $\text{H}\alpha$, which corresponds to $z = 0.638$. The small velocity difference ($\sim 600 \text{ km s}^{-1}$) measured between the redshifts derived from these narrow and broad emission lines is not uncommon in quasars (see e.g. Boroson [2005]). We therefore assume that a reliable estimate of the redshift of PKS 0048-097 is $z = 0.635$.

3.4.3.3 Intervening MgII and PKS 0048-097 close environment

In the UV part of the spectrum (around $\lambda \sim 3200$) two narrow absorption features at $\lambda\lambda 3228.20 \text{ \AA} 3236.60 \text{ \AA}$ (see Figure 3.28) are clearly detectable and the straightforward interpretation of this absorption system is an intervening Mg II absorption system at redshift $z = 0.154$. To search for objects associated with this absorption, we investigated the environment around the target using a high-resolution deep image of the field, in the R band, obtained with ESO NTT and SUSI [Falomo, 1996a].

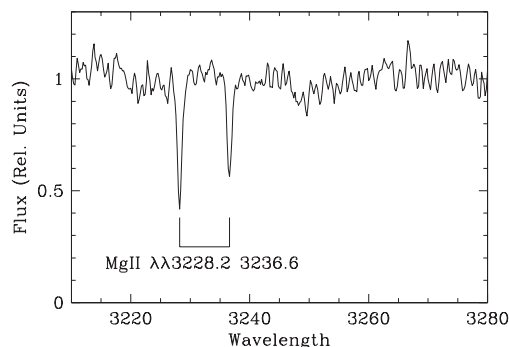


Figure 3.28: PKS 0048-097 Mg II absorption features at $z = 0.154$ associated with a spiral galaxy at 50 Kpc projected distance from the BL Lac.

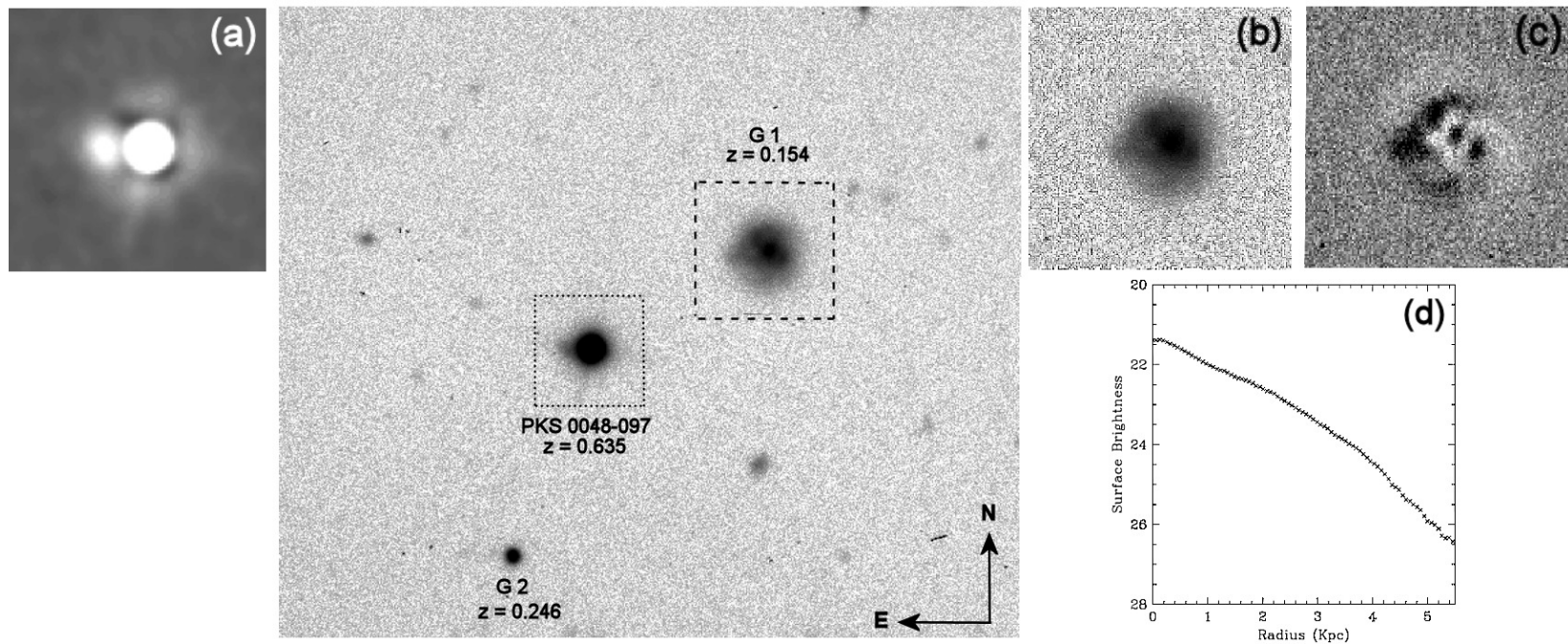


Figure 3.29: An R band image (FoV of $1.1' \times 1.1'$) of the BL Lac object PKS 0048-097 obtained with NTT and SUSI (Melnick et al) by Falomo [1996a] that shows its close environment. The spiral galaxy G1 (panel b) is the Mg II intervening system detected in the very blue part of the spectrum while the Galaxy G2 is a foreground object with respect to the absorption. The panel (a) in the figure shows a deconvolution of the image. The small object nearby PKS 0048-097 is most probably a background galaxy. Panel (c) shows the image of galaxy G1 after the model subtraction, while panel (d) reports the average radial brightness profile of galaxy G1.

The close companion galaxy ($m_R = 22.5$) that is $2.5''$ east of PKS 0048-097 (see panel (a) of Figure 3.29) and previously detected by Falomo et al. [1990] is too faint to be associated with the absorption system at $z = 0.154$ and it is probably a background galaxy. The spiral galaxy G1 ($m_r = 19.2$) at $\sim 23''$ north-west of the BL Lac corresponding to a 50 kpc projected distance at redshift $z = 0.154$ [Stickel et al., 1993] is the obvious galaxy associated with the observed Mg II absorption. This galaxy ($M_r = -20.57$) is found to have a disturbed morphology (see panel (b), (c), and (d) of Figure 3.29) after model subtraction and a scale length of ~ 5 Kpc. This is a rare case-study of absorption system at low redshift (see e.g. Kacprzak et al. [2011]) in which the counterpart can be reliably investigated using an imaging analysis. The column density inferred from the Mg II features by adopting the Voigt profile-fitting method is $\log N_{MgII}^a = 13.20$ atoms cm^{-3} .

3.4.3.4 Spectral Energy Distribution of PKS 0048-097

PKS 0048-097 is a well known γ -ray emitter observed with FERMI in the band 100 MeV - 10 GeV and its high energy spectrum could be well accommodated by the adoption of a single power law ($\alpha_0 = 2.38 \pm 0.24$). Assuming the extrapolation of this power law measured with FERMI to the TeV band, we calculated the expected emission after correction for the EBL absorption [Domínguez et al., 2011] and based on the derived redshift. The EBL interaction reduces the intrinsic flux above 50 GeV by a factor of 1.7 and above 300 GeV by a factor of 60.

In Figure 3.30, we reported the overall spectral energy distribution (SED) of PKS 0048-097 collected for multifrequency data by Tavecchio et al. [2010]. We fitted the data using a standard leptonic one-zone model considering synchrotron and synchrotron self-Compton (SSC) radiation mechanism (see Tavecchio et al. [1998, 2010]). We report two curves: the dashed line shows the intrinsic emission, while the solid one takes into account the absorption by EBL photons, assuming the estimate of Domínguez et al. [2011]. Despite adopting different approaches and methods, models for the EBL are in significant agreement in the spectral region interesting for absorption of GeV-TeV photons (see discussion and comparison in Domínguez et al. [2011]). The one-zone models satisfactorily reproduce the SED above the IR band, below which the emission is self-absorbed in the region that

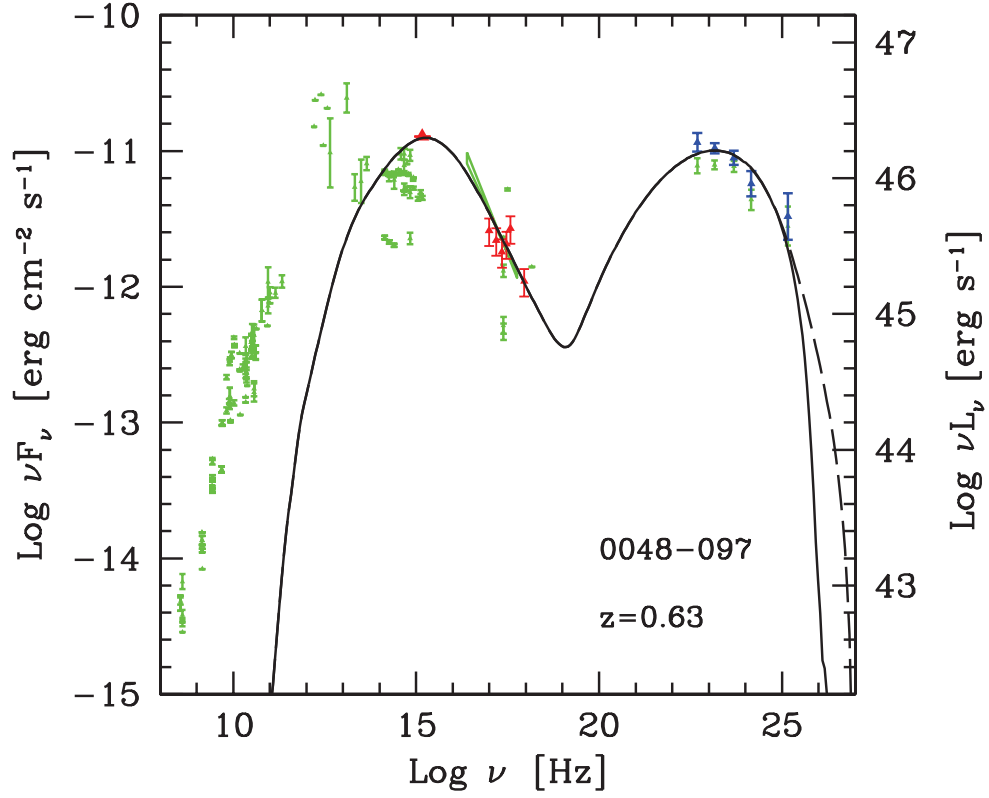


Figure 3.30: PKS 0048-097 spectral energy distribution. The dashed line is the intrinsic SED model, while the solid line represent the flux absorbed by EBL interaction. Green points are from ASDC archive. Red points represent Swift UVOT and XRT data. FERMI spectra FGL1 and FGL2 are indicated, respectively, by blue and green points. The parameters of the model are $\gamma_{\min} = 500$, $\gamma_b = 8.5 \times 10^3$, and $\gamma_{\max} = 5 \times 10^5$, in addition to $n_1 = 2$, $n_2 = 4.1$, $B = 0.46$ G, $K = 3.7 \times 10^4$, $R = 8.2 \times 10^{15}$ cm, and $\delta = 25$. For descriptions of the observations and details of the model, see [Tavecchio et al. \[2010\]](#).

we consider. The emission at lower frequencies is therefore produced in a more distant, transparent, region of the jets, and is irrelevant to the modelling of the high frequency SED.

3.4.4 Other objects observed. Preliminary results

3.4.4.1 Introduction

In this section we illustrate the reduced spectrum obtained for the other objects in the XSHOOTER observed sample. These results will be published in a paper in preparation (Landoni et al 2014). Briefly, for the TeV sources PG 1553+113 and H1722+119 we found that their spectra are completely featureless. Also the FERMI source PKS 2254-204 shows a completely non-thermal dominated spectra. The same consideration apply for MH 2136-428 but, in this case, an intervening Ca II H-K band system at $z \sim 0.008$ allows to study environment of the source.

3.4.4.2 The spectra and basic properties

Here below we report the normalised spectra of each of the sources. Spectral measurements on each source are reported in Table 3.10. In particular, we report also the minimum equivalent width which must be compared with those measured on FORS2 spectra. In the case of XSHOOTER, the EW_{\min} are about a factor ~ 10 lower than those measured with FORS2. This will allow us (in the mentioned forthcoming paper) to derive stringent lower limit for their redshift applying the procedure described in [Sbarufatti et al., 2006].

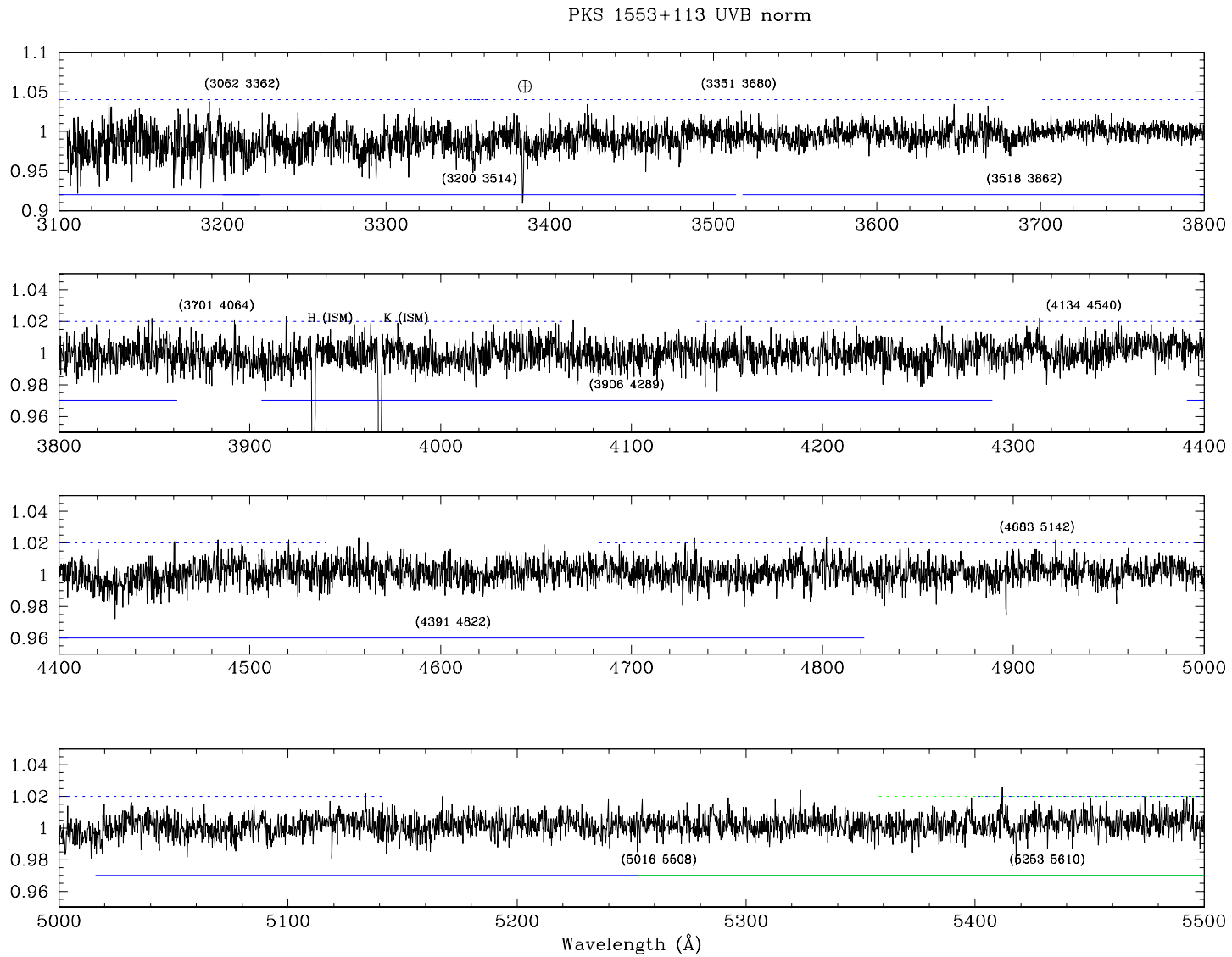


Figure 3.31: PKS 1553+113 UVB arm (normalised spectrum). Horizontal lines models the echelon orders of the instrument.

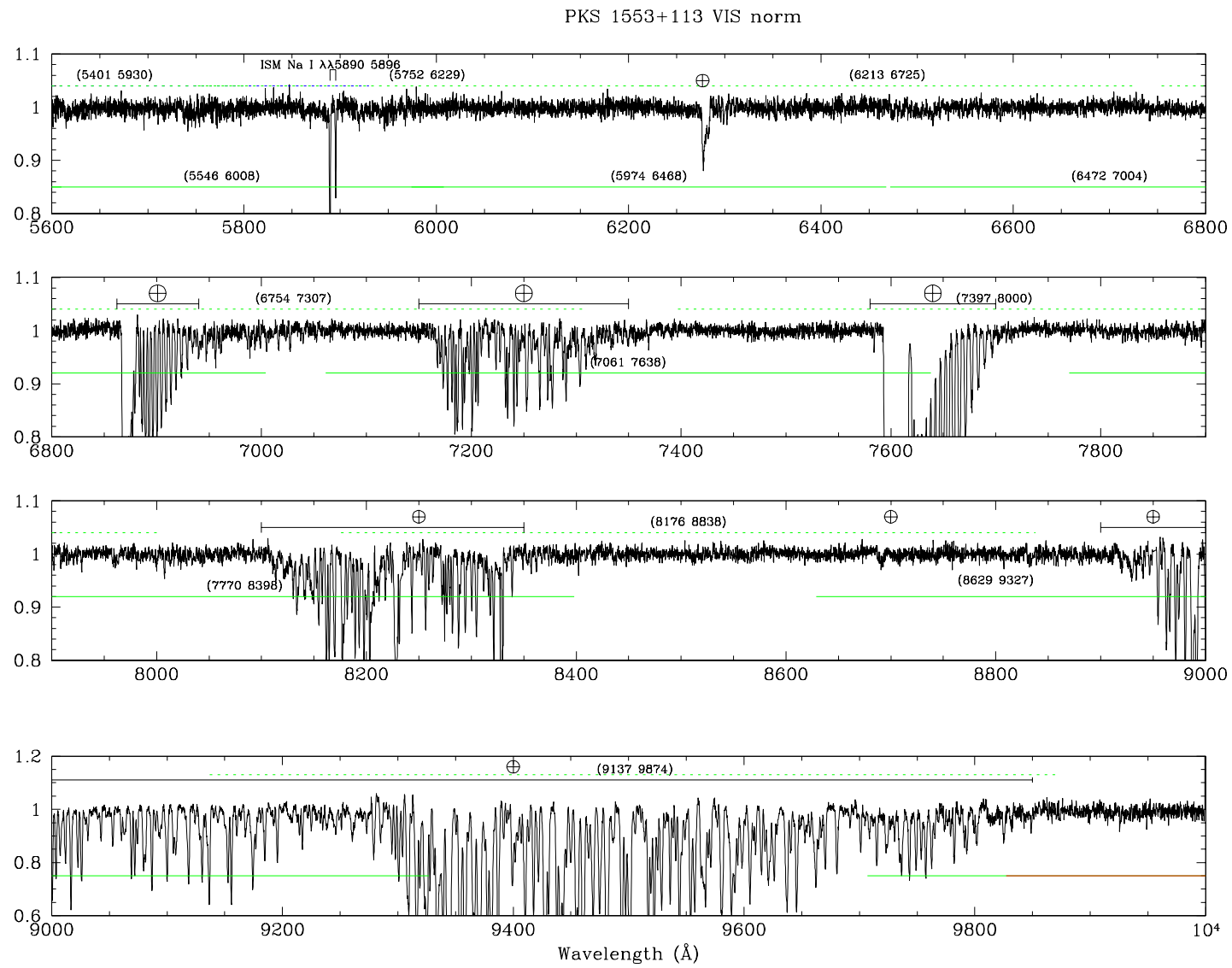


Figure 3.32: PKS 1553+113 VIS arm (normalised spectrum). Same legend of previous figure.

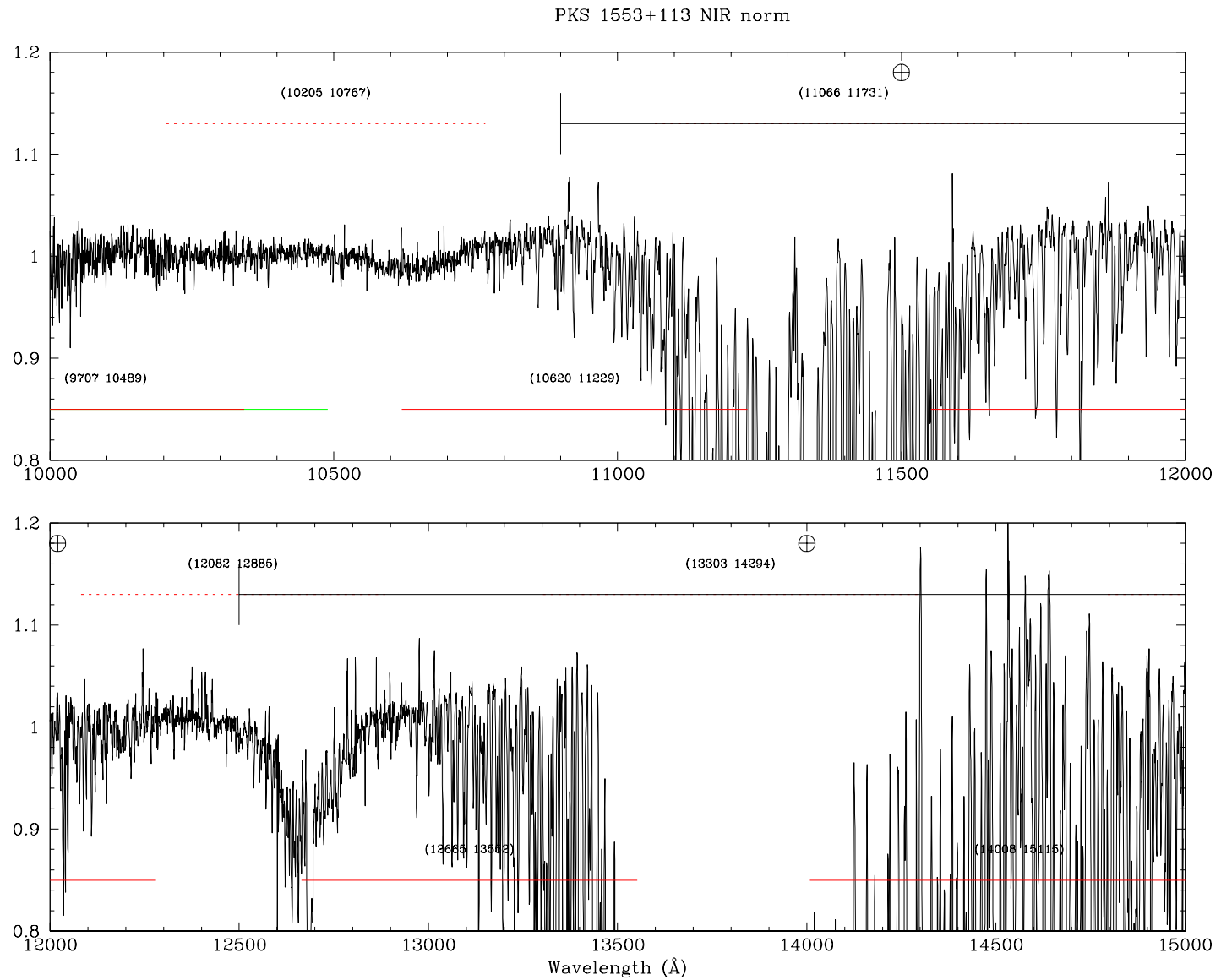


Figure 3.33: PKS 1553+113 NIR arm (normalised spectrum)

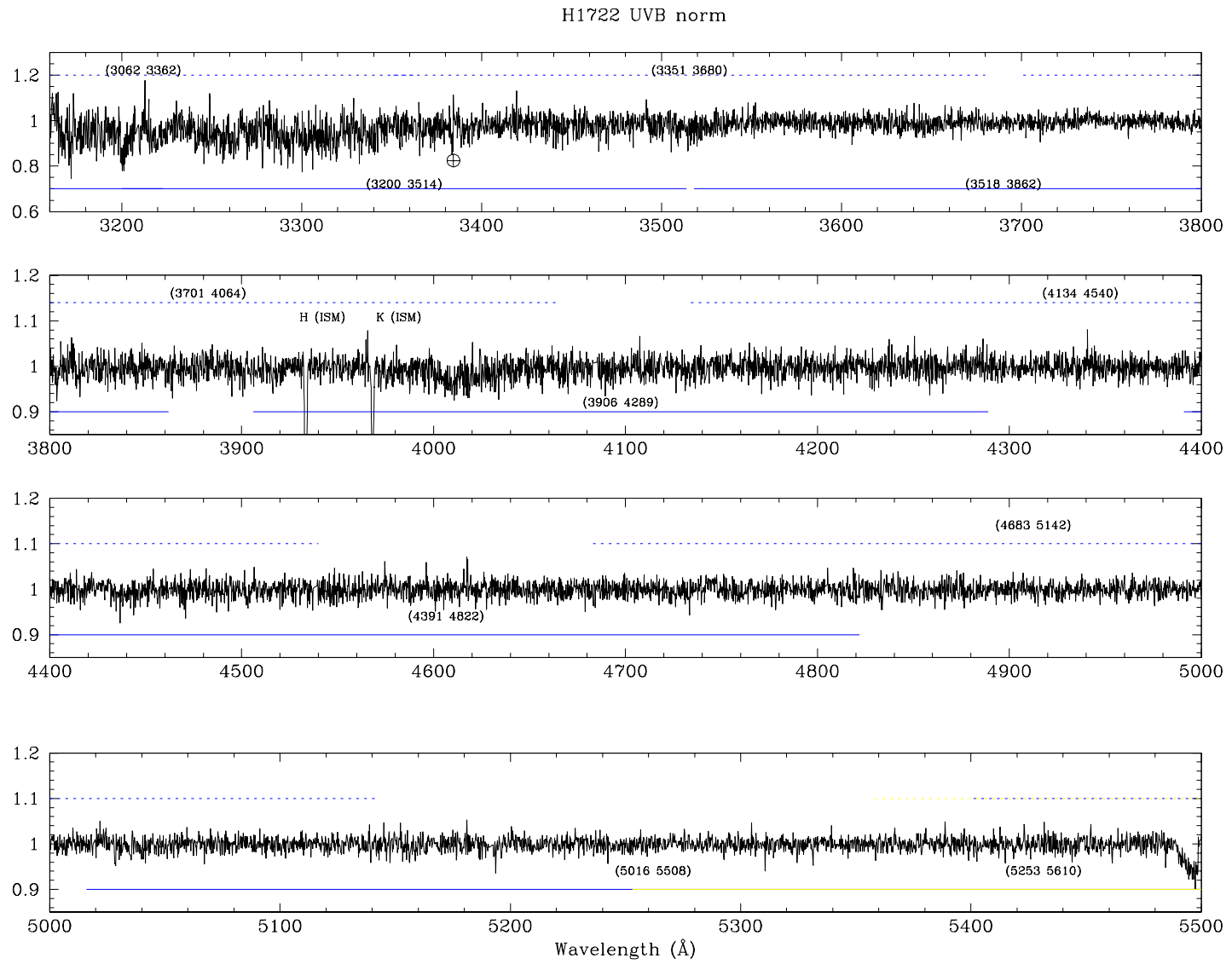


Figure 3.34: H1722+119 UVB arm (normalised spectrum)

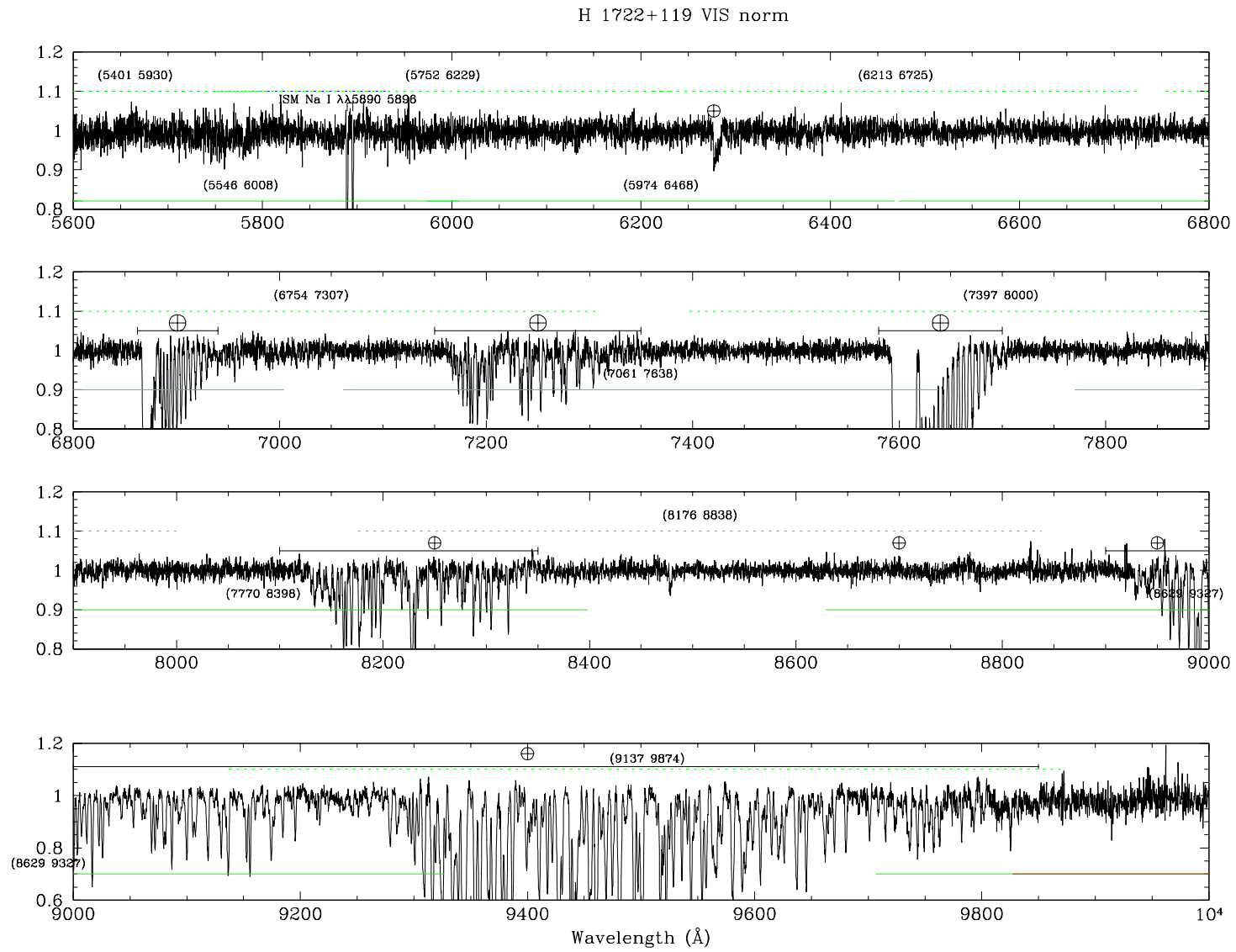


Figure 3.35: H1722+119 VIS arm (normalised spectrum)

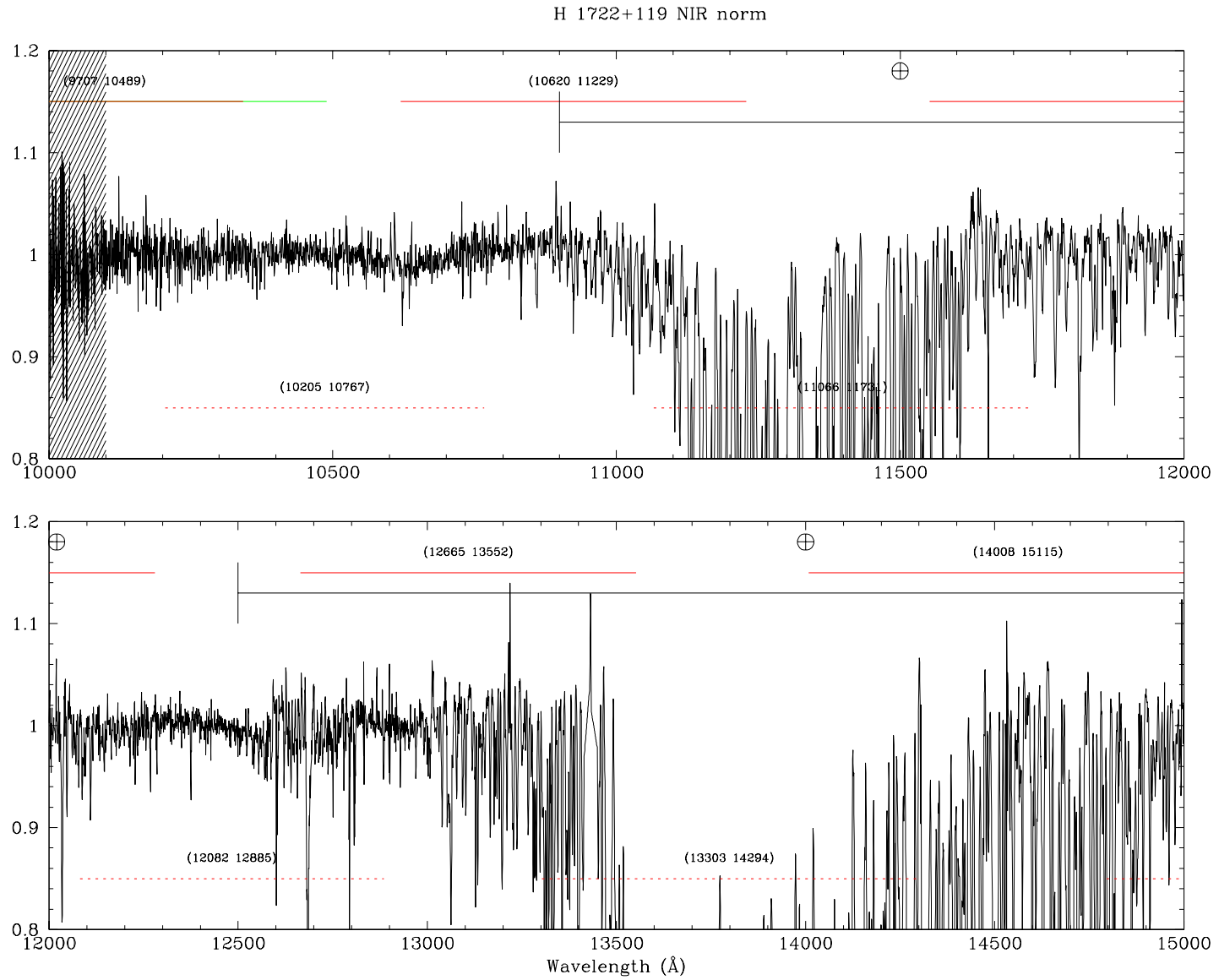


Figure 3.36: H1722+119 NIR arm (normalised spectrum)

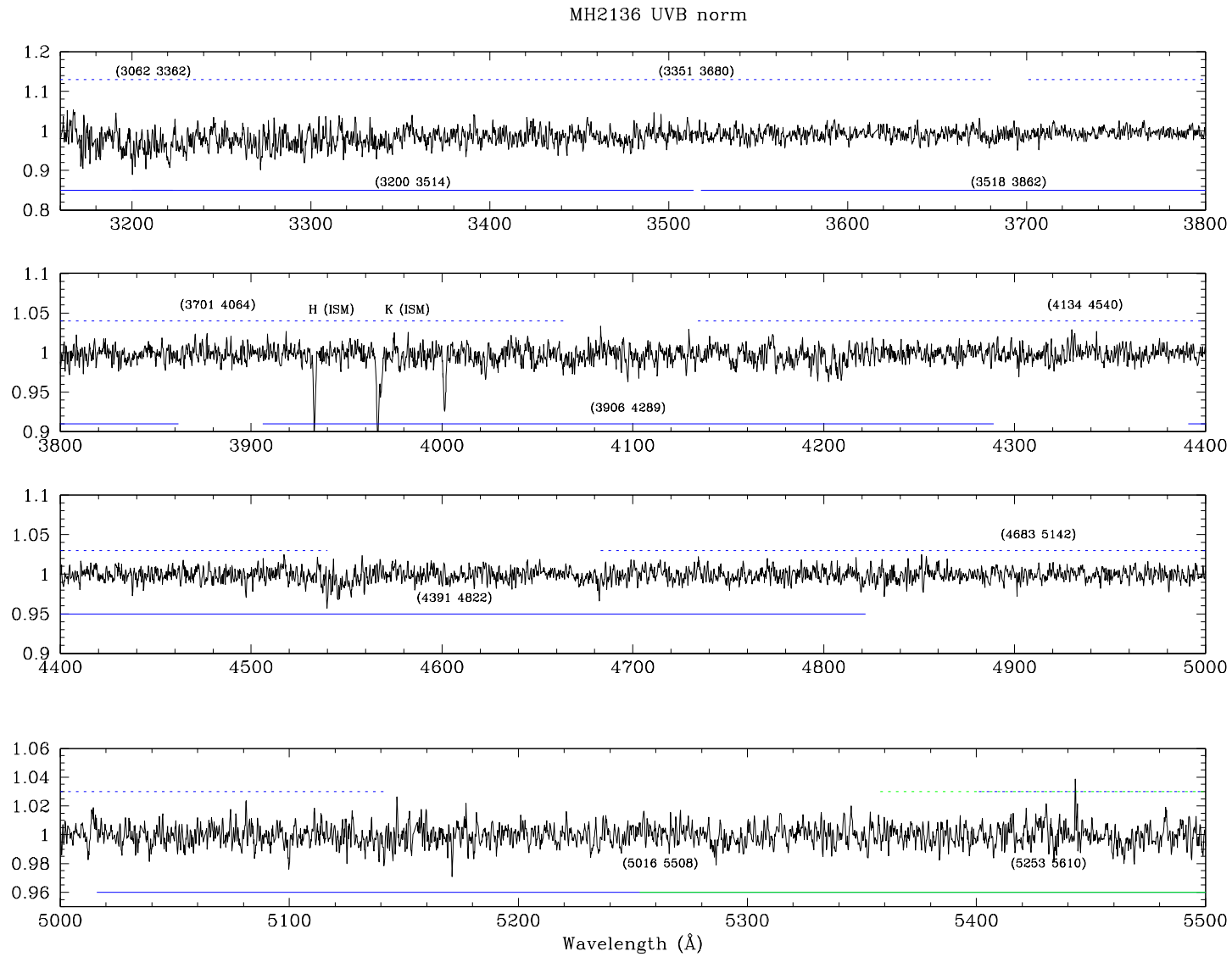


Figure 3.37: MH2136-428 UVB arm (normalised spectrum)

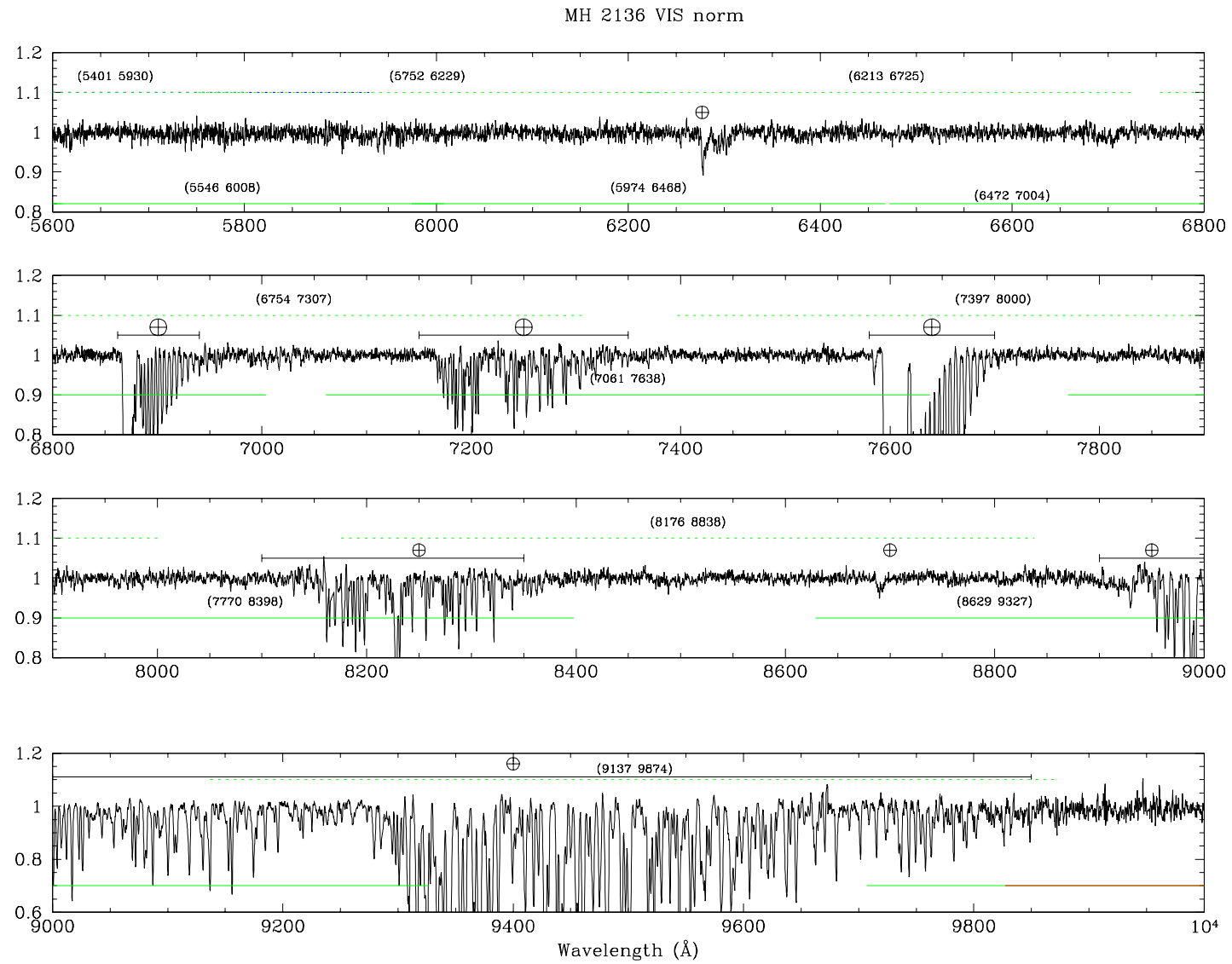


Figure 3.38: MH2136-428 VIS arm (normalised spectrum)

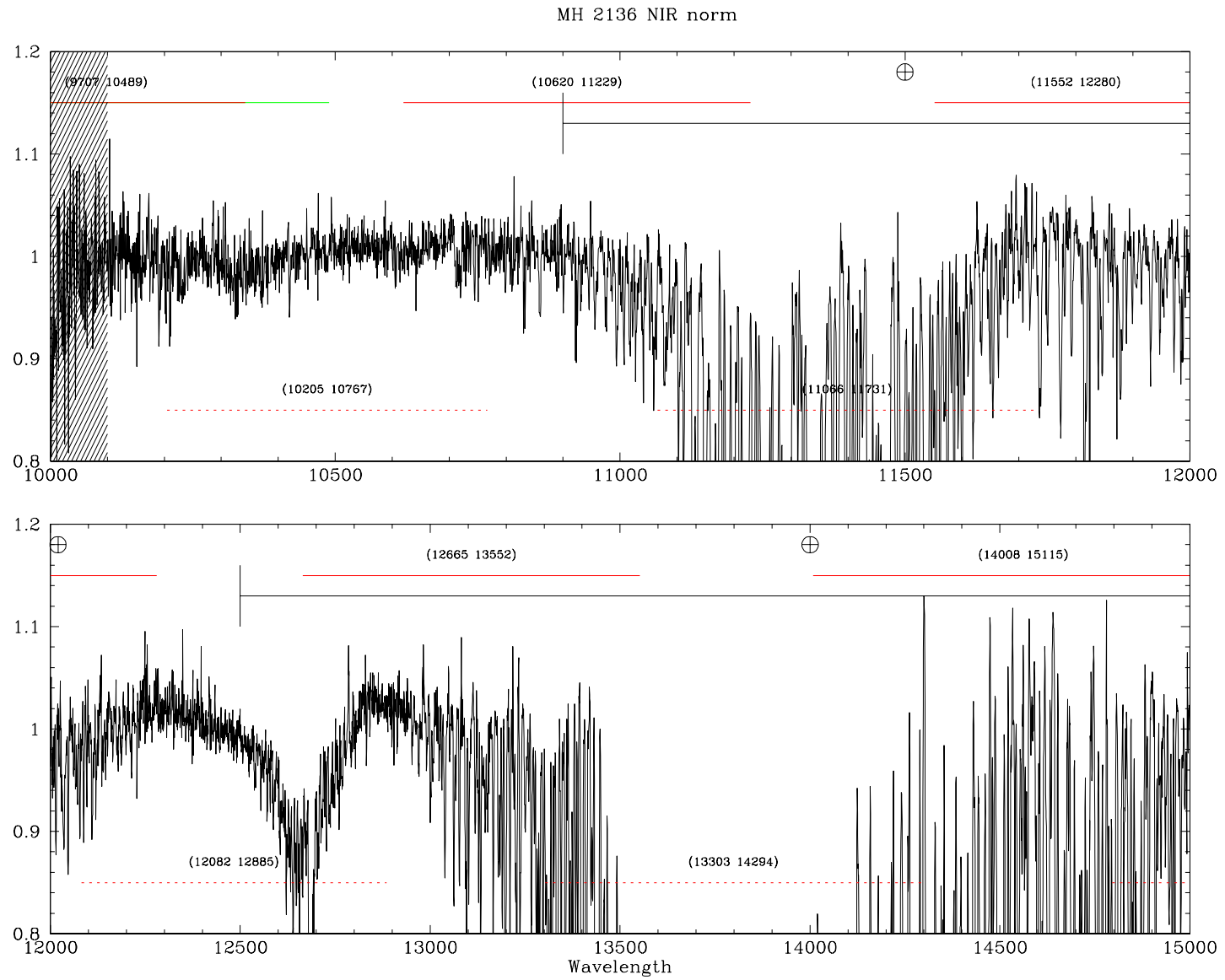


Figure 3.39: MH2136-428 NIR arm (normalised spectrum)

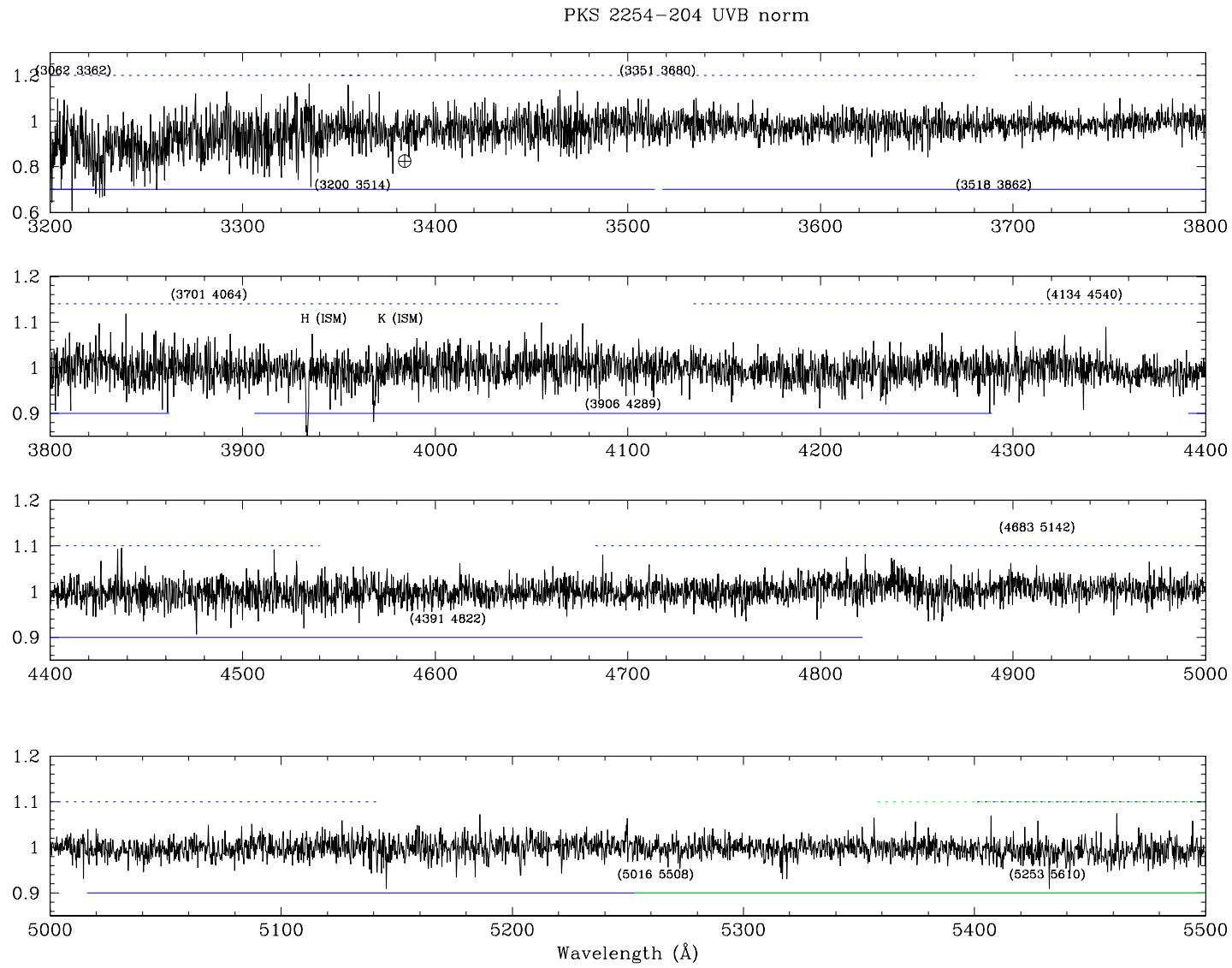


Figure 3.40: PKS 2554-204 UVB arm (normalised spectrum)

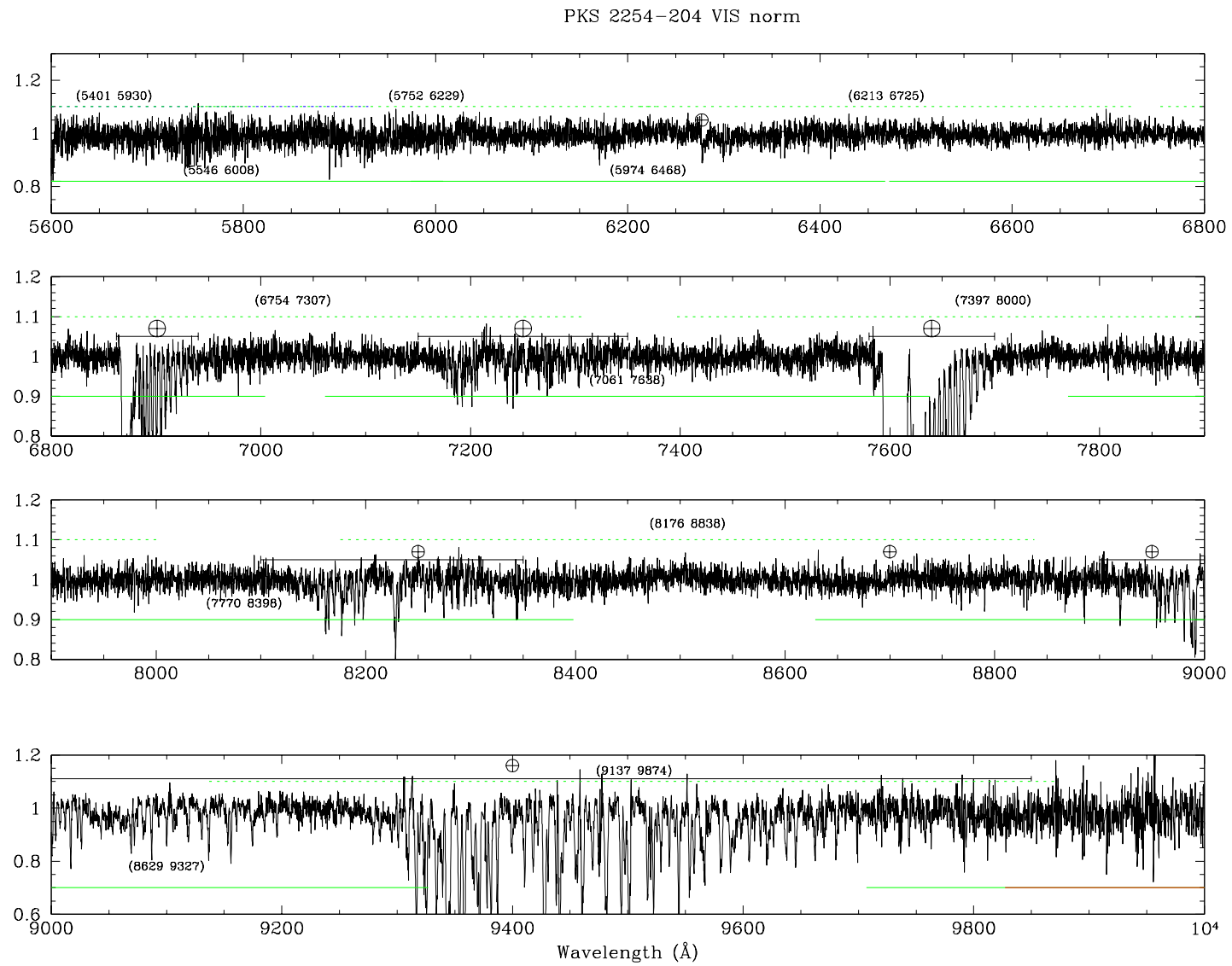


Figure 3.41: PKS 2254-204 VIS arm (normalised spectrum)

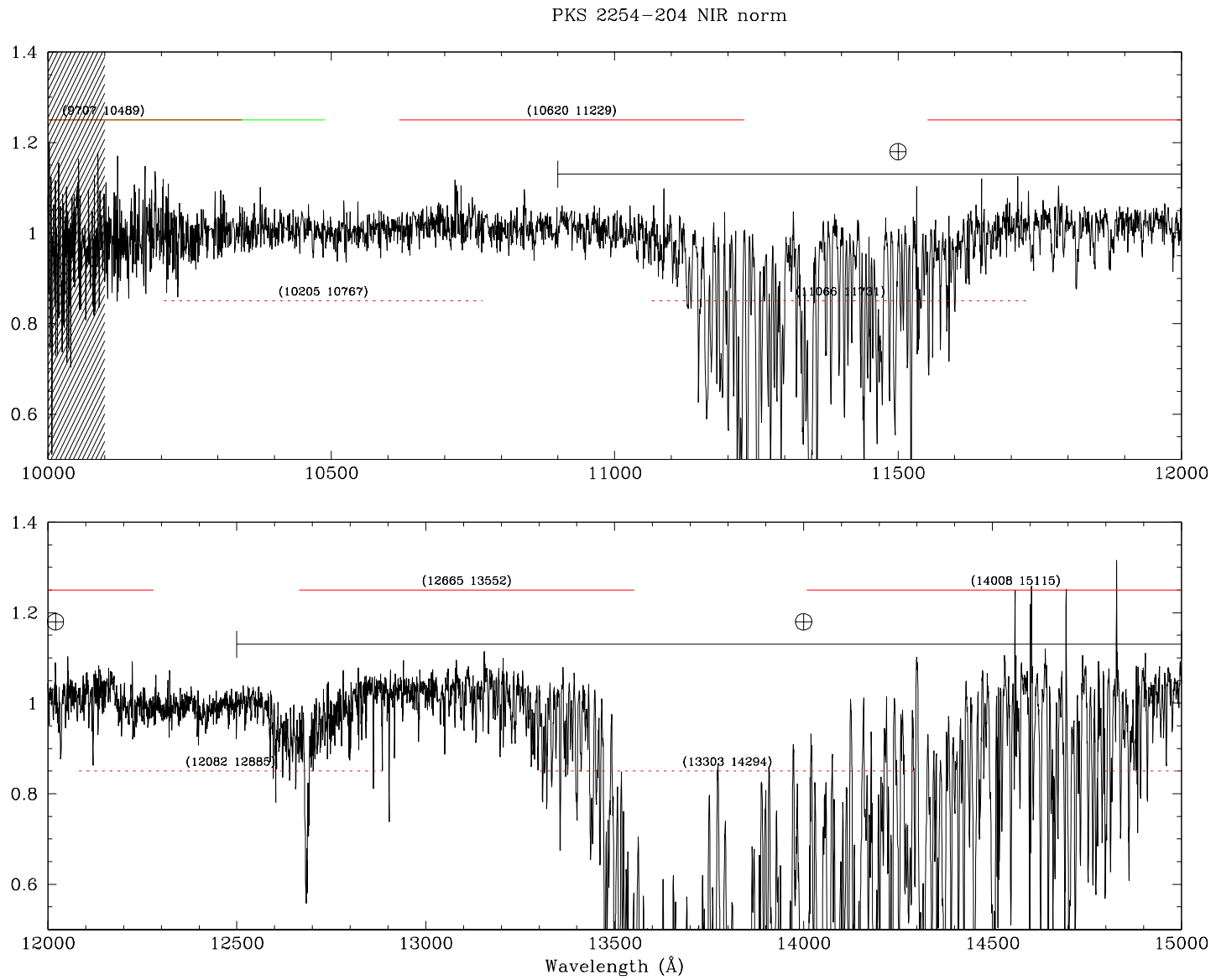


Figure 3.42: PKS 2254-204 NIR arm (normalised spectrum)

Object ¹	z	α	R	EW_{min}	Line ID	λ	z_λ	Type	EW
PG 1553+113		0.82	14.00	0.06 U - 0.05 V - 0.31 N	Ca II (ISM)	3933.30	-	g	0.37 ± 0.02
					Ca II (ISM)	3968.10	-	g	0.22 ± 0.02
					Na I (ISM)	5889.20	-	g	0.30 ± 0.03
					Na I (ISM)	5895.30	-	g	0.20 ± 0.03
H 1722+119		0.80	14.40	0.13 U - 0.07 V - 0.20 N	Ca II (ISM)	3933.40	-	g	0.45 ± 0.02
					Ca II (ISM)	3968.20	-	g	0.30 ± 0.02
					Na I (ISM)	5889.20	-	g	0.62 ± 0.03
					Na I (ISM)	5895.30	-	g	0.50 ± 0.05
MH 2136-428	> 0.008	0.65	15.60	0.05 U - 0.05 V - 0.31 N	Ca II (ISM)	3933.40	-	g	0.14 ± 0.02
					Ca II (ISM)	3968.20	-	g	0.10 ± 0.04
					Ca II (H)	3966.40	0.0084	i	0.15 ± 0.02
					Ca II (K)	4001.20	0.0084	i	0.10 ± 0.02
PKS 2254-204		0.70	17.10	0.10 U - 0.10 V - 0.30 N	Ca II (ISM)	3933.40	-	g	0.20 ± 0.05
					Ca II (ISM)	3967.70	-	g	0.10 ± 0.04

Table 3.10: Spectral parameters for the XSH objects

¹(1) Object name; (2) average redshift (or lower limit); (3) power-law spectral index; (4) R magnitude measured on the spectrum; (5) Minimum equivalent width detectable in the three arms (U = UVB, V = VIS and N = NIR); (6) Line identification (7) Barycenter of the line (8) Redshift of the line; (9) Line type e: emission line from BL Lac; g: absorption line from BL Lac host galaxy; i: absorption line from intervening system; (11) Measured equivalent width

3.4.4.3 The peculiar case of MH 2136-428

MH 2136-428 is a bright BL Lac object ($m_r = 15.36$) discovered by [Hawkins et al. \[1991\]](#) through its strong optical variability ($\Delta m \sim 1.0$). The source appeared in an optical survey carried out in 1977, with the UK 1.2 Schmidt telescope, aimed at detect quasars on the ESO/SERC field . The survey yielded two BL Lac objects selected on their optical variability, highly polarisation and radio loudness (including MH 2136-428).

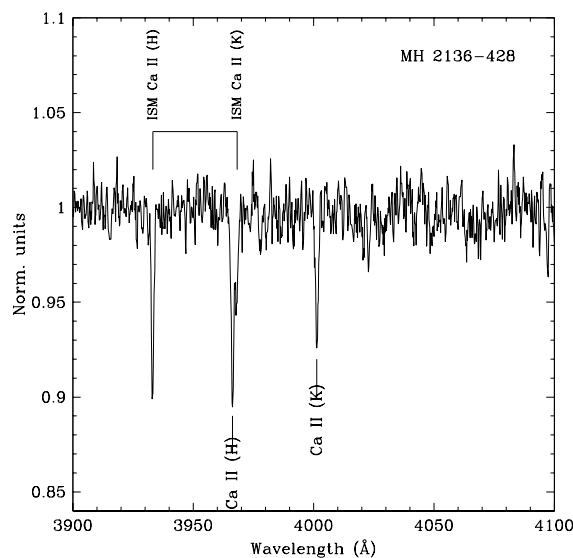


Figure 3.43: H 2136-428 Ca II systems detected toward the line of sight. Galactic H and K Ca II bands are marked by the label ISM.

Previous spectroscopical studies of this source ([Hawkins et al. \[1991\]](#), [Sbarufatti et al. \[2006\]](#) and [Shaw et al. \[2013\]](#)) failed to detect intrinsic or absorption lines leaving the object completely featureless.

The XSHOOTER spectrum also shows that the overall spectrum of MH 2136-428 exhibit a strongly dominated non-thermal continuum that arises from the active nucleus which can be firmly described by a single power-law of the form $F(\lambda) = \lambda^{-\alpha}$, where $\alpha \sim 0.70$. The measured spectral index is well consistent with previous observation of this source [[Sbarufatti et al., 2006](#)]. The lack of intrinsic spectral features ([Sbarufatti et al. \[2006\]](#), [Shaw et al. \[2013\]](#)) in the large spectral

band 3200 - 15.0000 Å is also confirmed.

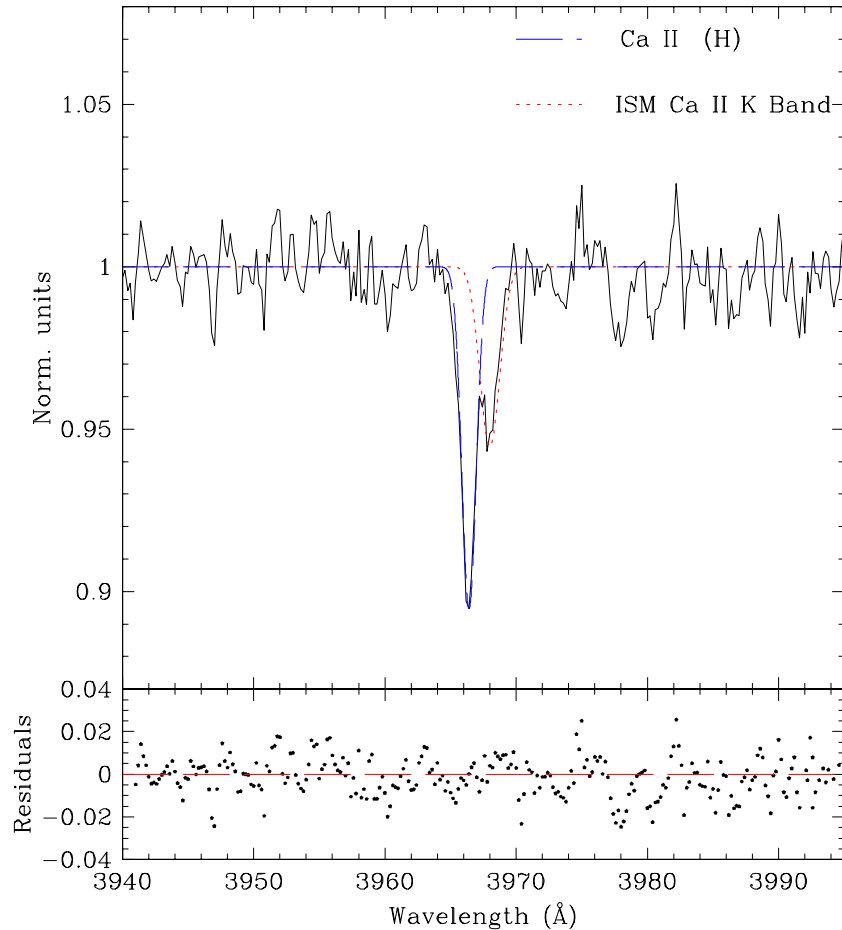


Figure 3.44: MH 2136-428 Ca II systems and ISM K Band de-blend fit. Dashed blue line and dotted red line are respectively the fit for deblending K ISM band and Ca II H band absorption system. The weighted reduced χ^2 for the model is 0.92 with 30 degrees of freedom. The r.m.s. overall error is 0.02.

However, we clearly detected two narrow absorption lines above $\sim 3\text{-}\sigma$ of the signal-to-noise ratio at 3966.40 Å and 4001.40 Å that we interpret as intervening system on the line of sight of MH 2136-428 (Figure 3.43). The first one is blended with the Ca II K band absorption that arises in our Galaxy. In order to measure the properties of both lines we fitted them with two gaussian profiles, assuming a

model for the Ca II K band absorption derived from observations of other BL Lacs objects with X-Shooter in the same program. The results of the fitting procedure is reported in Figure 3.44. The most straightforward interpretation considering the ratio of the wavelength is a Ca II intervening system at $z = 0.0085$. The close environment which also confirms the interpretation is illustrated in Figure 3.45.

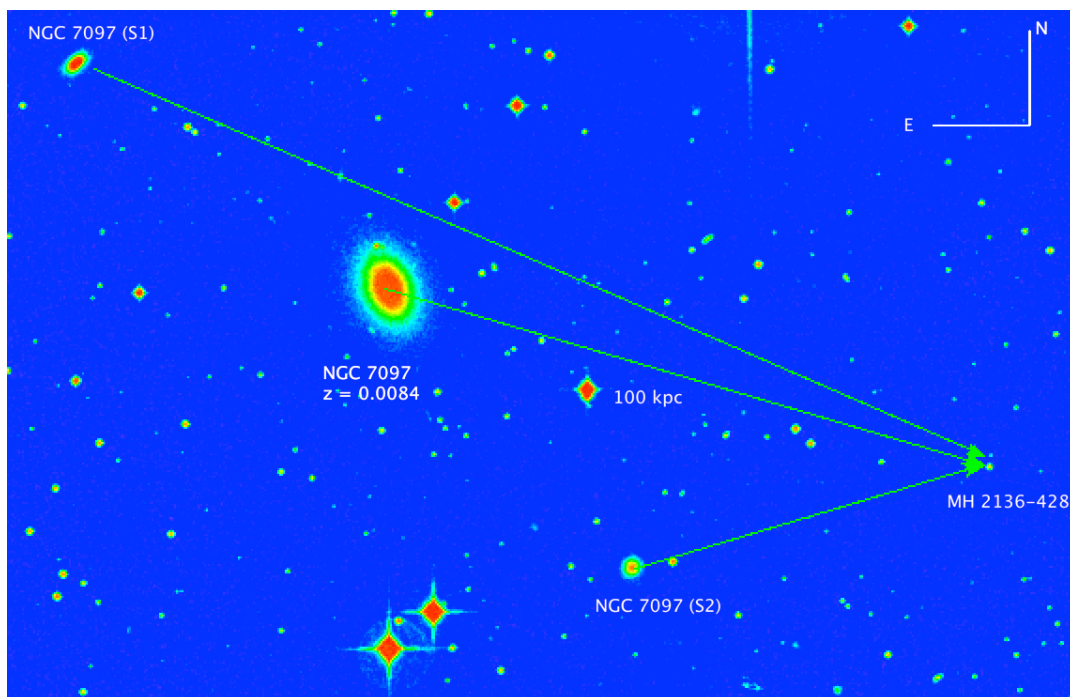


Figure 3.45: MH 2136-428 close environment from ESO NTT. The Ca II intervening system detected in the XSHOOTER spectrum arises in the surrounding nebosity of NGC 7097 at 100 Kpc projected distance from the background BL Lac. S1 and S2 are satellites of NGC 7097 at the same redshift.

We also found that this BL Lac was imaged with the Advanced Camera for Surveys (ACS) aboard the Hubble Space Telescope [Ubeda and et al., 2012] using the High Resolution Channel (HRC). In particular, two frames have been acquired adopting the filter F625W for a total integration time of 780s. In Figure 3.46 we report the field of view around MH 2136-428. We measured the apparent magnitude of the source that turns out to be $m_{F625W} \sim 16.00$. The image of the BLL is unresolved, as confirmed by the comparison with the point spread function derived with TinyTim [Krist et al., 2011]. The analysis of the image carried out

with AIDA [Uslenghi and Falomo, 2011] also reveals that no significant extended surround nebulosity due to BLL host galaxy is detectable, leaving the radial surface brightness of the source best fitted only by the PSF model. Furthermore, at $\sim 3''$ North-West from the BL Lac a faint spiral galaxy (labelled as G1 in Figure 3.46) is clearly detected. The apparent magnitude of G1 is $m_{G1} = 20.90$ and the relative surface brightness profile is well fitted by a Sersic profile yielding a R_{eff} of $\sim 1''$. From the expected absolute magnitude of typical spiral galaxies we reasonably infer that the redshift of G1 is $0.40 \leq z_{G1} \leq 0.60$. Within this assumption, its absolute magnitude is $-21.70 \leq M_V^{G1} \leq -20.00$ and the projected distance from MH 2136-428 turns out to be $20 \leq d \leq 30$ kpc. We searched for possible Mg II absorption feature imprinted by G1 in the BL Lac spectrum. No absorption lines compatible with the Mg II doublet transition above the instrumental sensitivity ($EW_{min} \sim 0.03 \text{ \AA}$) are revealed in the range $\sim 3900 - 4500 \text{ \AA}$. Although we do not know if G1 is a foreground or background object, the absence of Mg II absorption (if G1 is foreground with respect to BL Lac) it is not unexpected since, as noted by Chen et al. [2010], about 40% of isolated galaxy at $\rho \leq 100h^{-1}$ kpc from a background QSO do not imprint Mg II spectral signature in its spectrum.

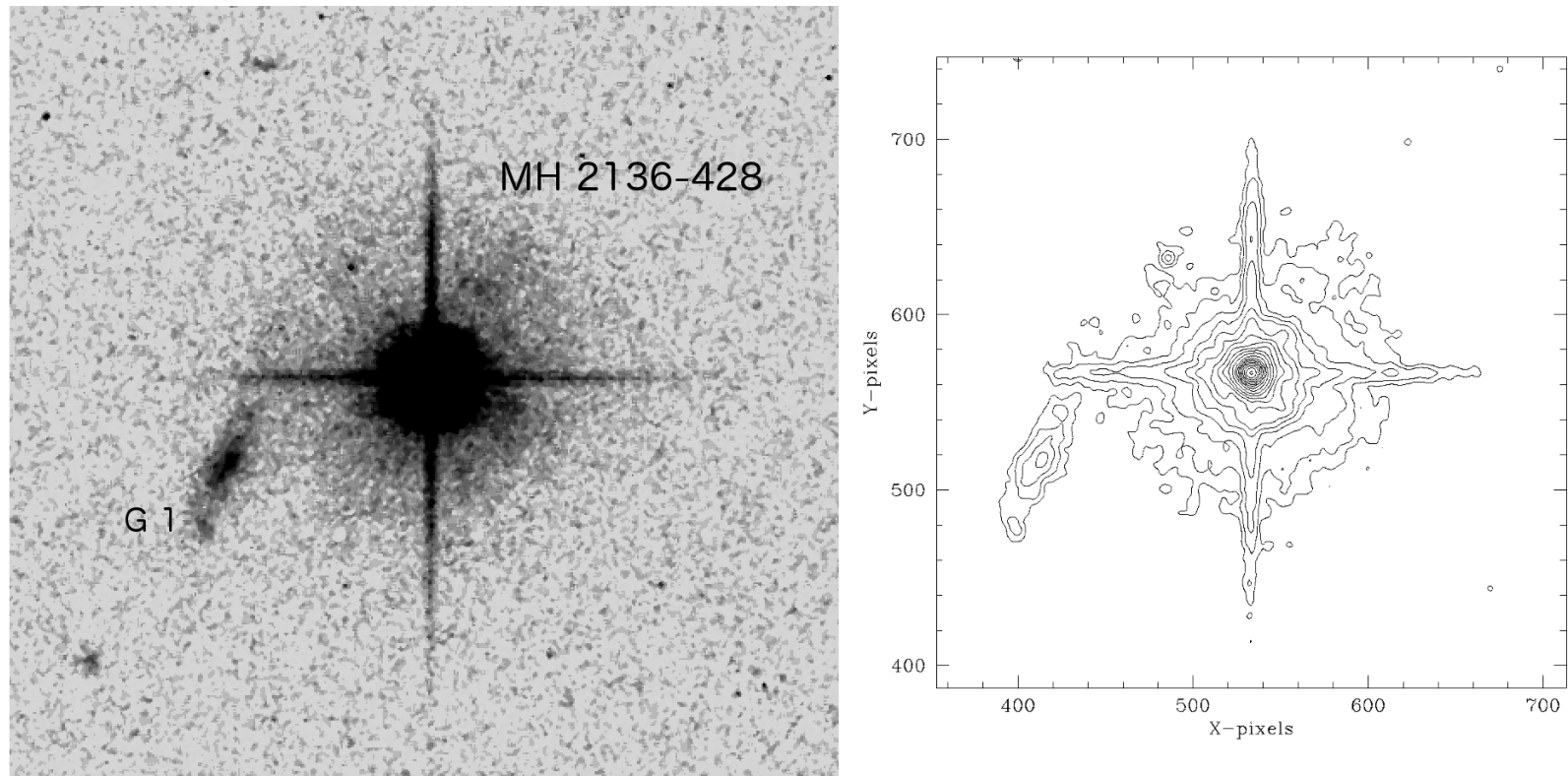


Figure 3.46: MH 2136-428 HST Advanced Camera for Surveys (ACS) snapshot image. The integration time is 780s and adopted filter is F625W. The plate scale is $0.025''$ per pixel and the FoV is about $15'' \times 15''$. The image clearly shows the presence of a faint galaxy at $3.2''$ NW from the BL Lac (labelled as G1).

3.5 Future perspective. Spectroscopy of BL Lacs in the E-ELT era

3.5.1 Introduction

In the spectrum of a BL Lac object the absorption lines associated to the stellar components of the host galaxy are always present. On the other hand, their detectability depends both on the S/N ratio and on the nucleus to host ratio (N/H) of the source. With the state of the art 8-mt class telescopes and modern instrumentation it is possible to obtain spectra with S/N about 100 and $R \sim 2000$ for object of $V \sim 17$ (assuming exposure time of ~ 1 hour). For sources with $V \gtrsim 20$ the situation is even worse since the S/N typically drops below 50. This limits the capability to detect the host galaxy features either for the sources with high intrinsic N/H ratio and for faint objects. In this chapter we illustrated that it is possible to overcome the problem either increasing the SNR ratio or the spectral resolution as in the case of X-SHOOTER.

For this reason, in order to significantly improve these limits, a future 40-mt class telescope like the European Extreme Large Telescope (E-ELT) is mandatory to investigate these kind of objects. In particular, the adoption of even larger telescope equipped with low resolution FORS2-like spectrograph allows to study the host galaxy features in the spectra of BL Lacs in which the nucleus to host ratio is extremely high. In this section it will be illustrated how E-ELT equipped with a FORS2 like spectrograph could detected host galaxy features for high N/H ratio sources with different magnitude and redshift assuming reasonable exposure times.

3.5.2 Simulation of BL Lac spectra observed by E-ELT

Assuming that the BL Lac spectrum is the sum of a non thermal emission, modelled with a power law, and a stellar component described by a giant elliptical galaxy [Kinney et al., 1996] we performed the simulation of two cases. We consider an exposure time of 3600 s and a spectrograph with a dispersion of $\sim 1.0 \text{ \AA} / \text{pixel}$, with an efficiency similar to the VLT-FORS2. We take into account a standard galaxy characterised by $M_r = -23$ and $R_{eff} = 10 \text{ kpc}$. We adopted an aperture

correction for a slit of $1'' \times 1''$, similarly to the aperture effect correction fully described in Sbarufatti et al. [2006]. Briefly, the fraction of starlight lost δ_{mag} due to slit effect depends on the redshift of the object and in the simulations this fact is taken into account assuming that N/H ratio apparent at the level of the spectrograph is higher than the N/H ratio intrinsic of the source. We adopted an aperture effect $A(z)$ described by curves reported in Figure 3.47 .

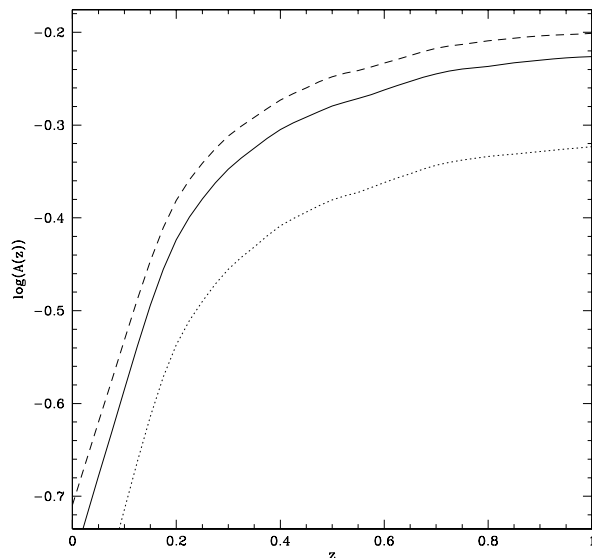


Figure 3.47: Aperture effect for different slit dimension projected on the sky. Details are reported in Sbarufatti et al. [2006]

The results of the simulations are presented in Figure 3.48 . In the first case (top panel), the E-ELT can obtain a spectrum with $S/N \sim 2000$ for an object with $V = 17$ and $z = 0.40$. The features associated to the host galaxy are clearly detectable with an intrinsic N/H up to 100 in the band $5200 - 6200 \text{ \AA}$. The second simulation (bottom panel) is carried out assuming $V = 20$ and $z = 0.70$. In this case, the S/N ratio of the spectrum is ~ 500 and the intrinsic N/H ratio limit reached is ~ 40 . We note that the use of the E-ELT allows to increase the S/N ratio of the spectra of a factor ~ 20 for the first case and ~ 10 for the latter respect to typical S/N ratios reached with the VLT.

In the light of these results, we are confident that the advent of 40-mt telescope

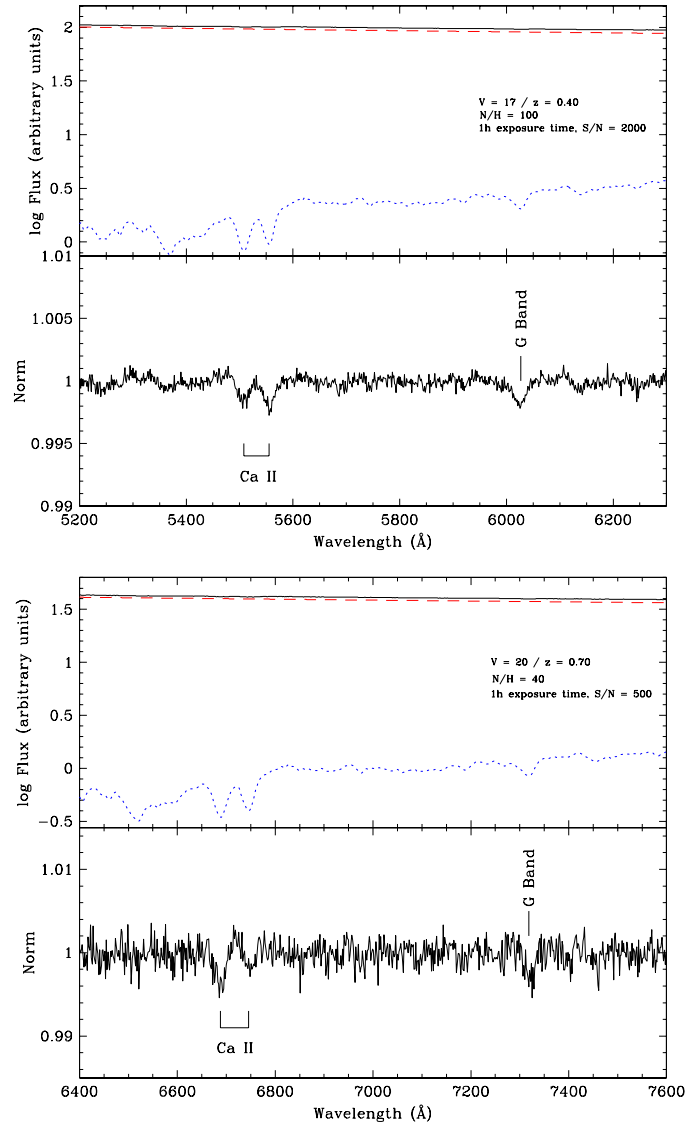


Figure 3.48: First panel: simulation of a BL Lac spectrum with $V = 17$, $S/N = 2000$, $z = 0.40$ and $N/H = 100$. Aperture correction is 0.35 . Second panel: simulation for a BL Lac spectrum with $V = 20$, $S/N = 500$, $N/H = 40$, $z = 0.70$ and aperture correction of 0.50. For both cases the exposure time is 3600 s and the adopted slit is a $1'' \times 1''$. The efficiency of the spectrograph is considered similar to the VLT-FORS2. The solid black line is the BL Lac overall spectrum while dashed line is the power law associated to the non thermal emission. Blue dotted line is the superposed host galaxy template spectrum.

instrumentation can significantly decrease the fraction of BL Lacs that are still left without z .

Chapter 4

ESPRESSO: Foreseen science and outlook

According to the latest schedule, ESPRESSO will be commissioned at the Very Large Telescope in Paranal in late 2016. A lot of science, as explained in the introduction of this Thesis, will be carried out through the adoption of this revolutionary instrument which, for the first time, will deliver a 16mt equivalent class telescope on the Earth. In this small Chapter I want to present the outlook for a foreseen scientific project in which I want to be involved. As reported in Chapter 3 I spent a lot of time in my PhD studying the optical spectral properties of BL Lac. As in the case of PKS 0048-097 or in a lot of sources in the ZBLLAC campaign intervening systems on the line of sight are apparent, but in only few cases deeply investigations of the physical condition of the absorbing gas are possible. This is caused in part due to low resolution (which is not sufficient to resolve singular absorption in the clouds or derive stringent physical parameters) and due to low SNR especially with high z sources. This issue is directly linked with a new project carried on in collaboration with my supervisors Prof. A. Treves and Prof. R. Falomo. In particular, at the moment of the submission of this Thesis we are issuing a proposal at ESO-XSHOOTER aimed at obtaining high quality spectra of candidate high-redshift BL Lacs. Thanks to superior quality of spectroscopical XSHOOTER data we want to confirm the BL Lac nature of the candidates and exploiting their Ly- α absorber at $z \geq 1.70$ in order to firmly constraint their redshift and study the distribution of the absorbers toward the line of sight of BL Lacs.

In details, the confirmed high-redshift BL Lac objects will allow us to probe the cosmic evolution of the class which is a 20 years controversial issue. In fact, BL Lac objects form an elusive class of low power AGN that, contrary to the case of QSOs, appear to not evolve or anti-evolve with the cosmic time. Moreover, the claimed evolution appears to be dependent on the wavelength range adopted for surveys. In particular, radio selected BL Lacs seem to be positively evolving as in the case of QSOs while those selected in the X-ray band appear to anti-evolve with the cosmic time. This issue is mainly induced by very paucity of high redshift objects. Using the complete SDSS optically selected sample of BL Lacs (see e.g. [Plotkin et al., 2010]) we selected 6 BL Lac candidates with possibly $z \geq 1.6$ to obtain good SNR and high spectral resolution over a wide spectral range with X-SHOOTER. The existence of BL Lacs at high redshift in the adopted survey would disprove the proposed anti evolution picture yielding a direct confirmation that the recent proposed anti evolution of the class is strongly biased by selection effects (see e.g. [Giommi et al., 2012]). In order to assess the feasibility of this observations, we simulated the spectrum of a BL Lac object in which Ly- α absorbers are present according to the signal to noise ratio obtained from the ESO Exposure Time Calculator (ETC). The adopted values for the simulations are similar to those observed using HST/COS observation of Lyman- α detected intervening systems toward the line-of-sight of the BL Lac PKS 1553+113 [Danforth et al., 2010] and results are reported in Figure 4.1.

Nevertheless, the faint magnitude of the sources ($V \sim 19$) allow to obtain reasonable but not excellent signal-to-noise ratio. Moreover, the medium resolution does not allow to deeply probe any structure on absorption features (multiple systems at the same redshift or resolve different clouds that cause the absorption itself). The advent of ESPRESSO in 4-UT mode will allow to obtain an higher (or comparable) SNR (at least a factor of 2 assuming same exposure time) *combining* the high resolution suitable for the investigation of complex absorber structure. Despite of the fact that, high resolution spectrographs are currently available at 10 mt class telescopes (e.g. UVES@VLT) they are limited to magnitude around $V = 18$ if desired SNR would be ~ 20 -30. With the advent of ESPRESSO in 4-UT mode the limit magnitude will be pushed away with the great advantage to maintain reasonable overall exposure times. For example, according to the most

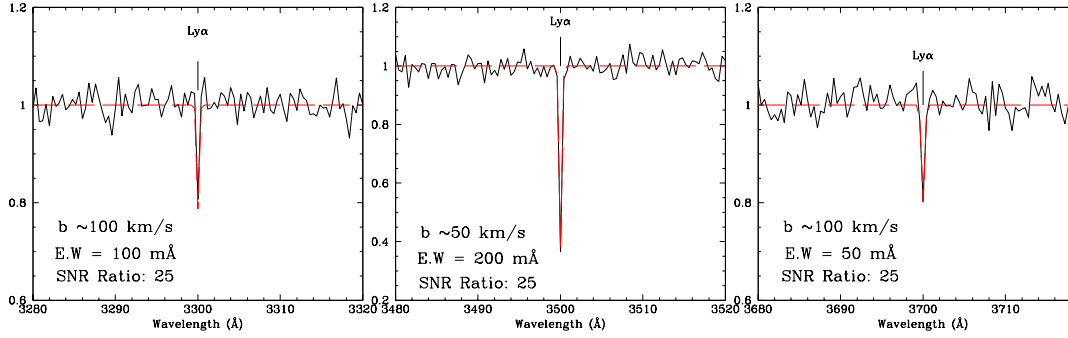


Figure 4.1: XSH-UVB spectrum simulation (SNR 25). Left panel: detection of Ly- α absorption with $EW = 100 \text{ mÅ}$, $b \sim 100 \text{ km s}^{-1}$. Center: Ly- α feature with $EW = 200 \text{ mÅ}$, $b \sim 50 \text{ km s}^{-1}$. Right: Ly- α system with $EW = 50 \text{ mÅ}$, $b \sim 100 \text{ km s}^{-1}$. Dotted line is the best fit.

recent Exposure Time Calculator for ESPRESSO a SNR of 20 is reached 1 hour in for an object of 20th magnitude. This value should be compared with that obtained with UVES ETC which is less than 10 for the same object. On the light of these considerations, we are confident that the advent of this new generation spectrograph in the VLT era will allow for the first time to study from the ground faint sources at high redshift with the greatly benefit of combining high resolution and suitable SNR ratio to deeply investigate intervening absorbers (and associated system) toward the line of sight of this elusive class of objects.

Chapter 5

Conclusions

Aimed at achieve the basic knowledge behind the professional figure of the *Instrument Scientist*

I presented in this Thesis the results of my work on the application of low and medium/high resolution spectroscopy to the study of a particular class of Active Galactic Nuclei, the BL Lacertae objects. The work was specially aimed to the interpretation of spectroscopic observations and consequent redshift determination. In details I completed the analysis and interpretation of a a survey started few years ago (www.oapd.inaf.it/zbl1lac/). Through this work I learned how to use and how to scientifically interpret data obtained with ESO-FORS2 (a first generation spectrograph) and ESO-X-SHOOTER.

I also presented in this thesis my personal contribution to the definition and design of a new ultra high resolution spectrograph for planet finding and cosmological research: ESPRESSO@VLT. Through this activity I learned how to work in a large Instrumental Project where I contributed with simulations of the expected performance of the Front End Subsystem and Exposure Meter Subsystem, to be compared with the top level astronomical requirements for the instrument.

The most relevant result, in terms of personal formation, of my PhD educational path resides in the synergy between the aforementioned areas, which allowed me to achieve the basic formation as an *Instrument Scientist*, the professional figure I aim to for the future.

Appendix A - List of publication

Title: On the redshift of the bright BL Lacertae object PKS 0048-097

Authors: Landoni, M.; Falomo, R.; Treves, A.; Sbarufatti, B.; Decarli, R.; Tavecchio, F.; Kotilainen, J.

Publication: Astronomy & Astrophysics, Volume 543, id.A116, 5 pp.

Publication Date: 07/2012

Origin: EDP Sciences

Astronomy Keywords: BL Lacertae objects: individual: PKS 0048-097, galaxies: active

DOI: 10.1051/0004-6361/201219114

Bibliographic Code: 2012A&A...543A.116L

Abstract: Aims: We attempt to determine the spectroscopic redshifts of bright BL Lac objects, which have proven difficult to measure.

Methods: We use the spectra acquired using the newly available spectrograph X-Shooter at the European Southern Observatory Very Large Telescope, which combines high resolution with a large wavelength range, to obtain ultraviolet to near-infrared spectra of BL Lacs.

Results: Our observations of PKS 0048-097 detect three emission lines, which permit us to derive a redshift $z = 0.635$. Moreover, we discover a Mg II absorption system at $z = 0.154$ that is associated with a foreground spiral galaxy a 50 kpc of projected distance.

Conclusions: The measured redshift allows us to discuss the optical beaming factor and the absorption of the high energy spectrum by the extragalactic background light.

Title: ESO Very Large Telescope Optical Spectroscopy of BL Lacertae Objects. IV. New Spectra and Properties of the Full Sample

Authors: Landoni, M.; Falomo, R.; Treves, A.; Sbarufatti, B.; Barattini, M.; Decarli, R.; Kotilainen, J.

Publication: The Astronomical Journal, Volume 145, Issue 4, article id. 114, 12 pp. (2013). (AJ Homepage)

Publication Date: 04/2013

Origin: IOP

Astronomy Keywords: BL Lacertae objects: general, instrumentation: spectrographs, quasars: absorption lines

DOI: 10.1088/0004-6256/145/4/114

Bibliographic Code: 2013AJ....145..114L

Abstract: We present the last chapter of a spectroscopy program aimed at deriving the redshift or a lower limit to the redshift of BL Lac objects using medium-resolution spectroscopy. Here we report new spectra for 33 BL Lac object candidates obtained in 2008-2009, confirming the BL Lac nature of 25 sources and obtaining new redshifts for 5 objects. These new observations are combined with our previous data in order to construct a homogeneous sample of 70 BL Lac objects with high-quality spectroscopy. All these spectra can be accessed at the Web site <http://www.oapd.inaf.it/zblac/>. The average spectrum, beaming properties of the full sample, discussion of intervening systems, and future perspectives are addressed.

Title: Spectroscopy of Optically Selected BL Lac Objects and their gamma-ray emission

Authors: Sandrinelli, A.; Treves, A.; Falomo, R.; Farina, E. P.; Foschini, L.; Landoni, M.; Sbarufatti, B.

Publication: eprint arXiv:1310.1837 (AJ in press)

Publication Date: 10/2013

Keywords: Astrophysics - Cosmology and Extragalactic Astrophysics

Comment: Accepted for publication in AJ

Bibliographic Code: 2013arXiv1310.1837S (AJ, in press)

Abstract: We present Very Large Telescope optical spectroscopy of nine BL Lac objects of unknown redshift belonging to the list of optically selected radio loud BL Lacs candidates. We explore their spectroscopic properties and the possible link with gamma ray emission. From the new observations we determine the redshift of four objects from faint emission lines or from absorption features of the host galaxy. In three cases we find narrow intervening absorptions from which a lower limit to the redshift is inferred. For the remaining two featureless sources, lower limits to the redshift are deduced from the very absence of spectral lines. A search for gamma counterpart emission shows that six out of nine are Fermi gamma-ray emitters with two new detections. Our analysis suggests that most of the BL Lac still lacking of redshift information are most probably located at high redshift.

Title: Speckle observations with PISCO in Merate (Italy) - XII. Astrometric measurements of visual binaries in 2011

Authors: Scardia, M.; Prieur, J.-L.; Pansecchi, L.; Argyle, R. W.; Span, P.; Riva, M.; Landoni, M.

Publication: Monthly Notices of the Royal Astronomical Society, Volume 434, Issue 4, p.2803-2813 (MNRAS Homepage)

Publication Date: 10/2013

Origin: OUP

Astronomy Keywords: techniques: interferometric, astrometry, binaries: close, binaries: visual

DOI: 10.1093/mnras/stt1140

Bibliographic Code: 2013MNRAS.434.2803S

Abstract: We present relative astrometric measurements of visual binaries, made in 2011 with the Pupil Interferometry Speckle camera and COronagraph (PISCO) at the 102-cm Zeiss telescope of the Brera Astronomical Observatory in Merate (Italy). Our observing list contains orbital couples as well as binaries whose motion is still uncertain. We obtained new measurements of 469 objects, with angular separations in the range 0.14-8.1 arcsec, and an average accuracy of 0.02 arcsec. The mean error on the position angles is 0.7. Most of the position angles were

determined without the usual 180 deg ambiguity with the application of triple-correlation techniques and/or by inspection of the long integration files. Thanks to a new low-magnification option included in PISCO, we have been able to observe fainter stars than previously. The limiting magnitude of our instrumentation on the Zeiss telescope is now close to $m_V = 10-12$, which permits the observation of some red dwarfs. Finally, we present new revised orbits for ADS 8739, 9182 Aa,Ab, 9626 Ba,Bb, 12880 and 14412, partly derived from those observations. The corresponding estimated values for the masses of those systems are compatible with the spectral types.

Title: Supernova 2013fj in Pgc 68419 = Psn J22152851+1534041

Authors: Ciabattari, F.; Mazzoni, E.; Parker, S.; Brimacombe, J.; Zanutta, A.; Landoni, M.; Bianco, A.; Spiro, S.; Benetti, S.; Pastorello, A.; Cappellaro, E.; Tomasella, L.; Ochner, P.; Turatto, M.

Publication: Central Bureau Electronic Telegrams, 3654, 1 (2013). Edited by Green, D. W. E.

Publication Date: 09/2013

Origin: CBAT

Objects: 2013fj

Bibliographic Code: 2013CBET.3654....1C

Title: ESPRESSO front end opto-mechanical configuration

Authors: Riva, M.; Landoni, M.; Zerbi, F. M.; Mgevand, D.; Cabral, A.; Cristiani, S.; Delabre, B.

Publication: Ground-based and Airborne Instrumentation for Astronomy IV. Proceedings of the SPIE, Volume 8446, article id. 84469E, 7 pp. (2012). (SPIE Homepage)

Publication Date: 09/2012

Origin: SPIE

Comment: ISBN: 9780819491473

DOI: 10.1117/12.924978

Bibliographic Code: 2012SPIE.8446E..9ER

Abstract: This paper presents the Espresso Front End mechanical and optical configuration. ESPRESSO, Echelle Spectro-graph for Rocky Exoplanets and Stable Spectroscopic Observations, will combine the efficiency of modern echelle spectrograph design with extreme radial-velocity precision. It will be installed on ESO's VLT and it is expected to achieve a gain of two magnitudes with respect to its predecessor HARPS. The instrumental radial-velocity precision will also be improved to reach cm/s level. The Front End is a modular subsystem that collects the light coming from the Coude Trains of all the Four Telescope Units (UT), provides Field and Pupil stabilisation via piezoelectric tip tilt devices and inject the beam into the Spectrograph fiber. The Front End will also inject the calibration light coming from the calibration unit. There will be four Front End modules, one per UT. A rotary Stage will provide the toggling between different observation mode: Single UT Ultra High resolution (SUT-UHR), Single UT High resolution (SUT-HR) and multiple UTS Mid Resolution (MUT-MR). The field and pupil guiding is obtained through a reimaging system that elaborates the halo of the light out of the Injection Fiber and a telescope pupil beacon. A dedicated guiding algorithm has been studied in order to provide proper image stability even with faint objects (mv=20).

Title: ESPRESSO front-end guiding algorithm

Authors: Landoni, M.; Riva, M.; Zerbi, F. M.; Mgevand, D.; Cabral, A.; Cristiani, S.

Publication: Software and Cyberinfrastructure for Astronomy II. Proceedings of the SPIE, Volume 8451, article id. 84512X, 14 pp. (2012). (SPIE Homepage)

Publication Date: 09/2012

Origin: SPIE

Comment: ISBN: 9780819491527

DOI: 10.1117/12.924980

Bibliographic Code: 2012SPIE.8451E..2XL

Abstract: This paper presents the Espresso Front End Guiding Algorithm. ESPRESSO, the Echelle SPectrograph for Rocky Exoplanets and Stable Spectroscopic Observations, will be installed on ESO's Very Large Telescope (VLT). The Front End (FE) is the subsystem that collects the light coming from the Coud Trains of all the Four Telescope Units (UTs), provides Field and Pupil stabilisation via piezo-electric tip tilt devices and inject the beams into the Spectrograph fibers. The field and pupil guiding is obtained through a re-imaging system that elaborates the halo of the light out of the Injection Fiber and a telescope pupil beacon. The first guiding algorithm that we evaluated splits the FP in four areas and computes the sum of the photon counting of each pixel in that area. The unbalancing of the photon sums will give the centroid misalignment information that will be handled by the Instrument Control Software (ICS). Different algorithms and controllers architectures have been evaluated and implemented in order to select a strategy that enables the FE to guide up to 20 apparent magnitude in V band.

Title: ESPRESSO: the ultimate rocky exoplanets hunter for the VLT

Authors: Mgevand, Denis; Zerbi, Filippo M.; Cabral, Alexandre; Di Marcantonio, Paolo; Amate, Manuel; Pepe, Francesco; Cristiani, Stefano; Rebolo, Rafael; Santos, Nuno C.; Dekker, Hans; Abreu, Manuel; Affolter, Michael; Avila, Gerardo; Baldini, Veronica; Bristow, Paul; Broeg, Christopher; Carvas, Pedro; Cirami, Roberto; Coelho, Joo.; Comari, Maurizio; Conconi, Paolo; Coretti, Igor; Cupani, Guido; D'Odorico, Valentina; De Caprio, Vincenzo; Delabre, Bernard; Figueira, Pedro; Fleury, Michel; Fragoso, Ana; Genolet, Ludovic; Gomes, Ricardo; Gonzalez Hernandez, Jonay; Hughes, Ian; Iwert, Olaf; Kerber, Florian; Landoni, Marco; Lima, Jorge; Lizon, Jean-Louis; Lovis, Christophe; Maire, Charles; Manetta, Marco; Martins, Carlos; Moitinho, Andr; Molaro, Paolo; Monteiro, Manuel; Rasilla, Jos Luis; Riva, Marco; Santana Tschudi, Samuel; Santin, Paolo; Sosnowska, Danuta; Sousa, Sergio; Span, Paolo; Tenegi, Fabio; Toso, Giorgio; Vanzella, Eros; Viel, Matteo; Zapatero Osorio, Maria Rosa

Publication: Ground-based and Airborne Instrumentation for Astronomy IV. Proceedings of the SPIE, Volume 8446, id. 84461R-84461R-15 (2012). (SPIE Homepage)

Publication Date: 09/2012

Origin: SPIE

Comment: ISBN: 9780819491473

DOI: 10.1117/12.924602

Bibliographic Code: 2012SPIE.8446E..1RM

Abstract: ESPRESSO, the VLT rocky exoplanets hunter, will combine the efficiency of modern echelle spectrograph with extreme radial-velocity precision. It will be installed at Paranal on ESO's VLT in order to achieve a gain of two magnitudes with respect to its predecessor HARPS, and the instrumental radial-velocity precision will be improved to reach 10 cm/s level. We have constituted a Consortium of astronomical research institutes to fund, design and build ESPRESSO on behalf of and in collaboration with ESO, the European Southern Observatory. The project has passed the preliminary design review in November 2011. The spectrograph will be installed at the so-called "Combined Coud Laboratory" of the VLT, it will be linked to the four 8.2 meters Unit Telescopes (UT) through four optical "Coud trains" and will be operated either with a single telescope or with up to four UTs. In exchange of the major financial and human effort the building Consortium will be awarded with guaranteed observing time (GTO), which will be invested in a common scientific program. Thanks to its characteristics and the ability of combining incoherently the light of 4 large telescopes, ESPRESSO will offer new possibilities in many fields of astronomy. Our main scientific objectives are, however, the search and characterization of rocky exoplanets in the habitable zone of quiet, near-by G to M-dwarfs, and the analysis of the variability of fundamental physical constants. In this paper, we present the ambitious scientific objectives, the capabilities of ESPRESSO, the technical solutions for the system and its subsystems, enlightening the main differences between ESPRESSO and its predecessors. The project aspects of this facility are also described, from the consortium and partnership structure to the planning phases and milestones.

Title:ESPRESSO Front End Exposure Meter - A chromatic approach to radial velocity correction

Authors: Marco Landoni , Marco Riva , Francesco Pepe , Paolo Conconi , Filippo

M. Zerbi , Alexandre Cabral , Stefano Cristiani and Denis Megevand

Publication: SPIE Optics and Photonics 2013 in press

Publication Date: In press

Origin: SPIE

DOI: 10.1117/12.2023227

Abstract: This paper presents the Espresso Exposure Meter (EM) implementation. ESPRESSO, the Echelle SPectrograph for Rocky Exoplanets and Stable Spectroscopic Observations, will be installed on ESOs Very Large Telescope (VLT). The light coming from the Telescope through a Coud Focus4 of all the Four Telescope Units (UTs) will be collected by the Front End Unit that provides Field and Pupil stabilisation and injects the beams into the Spectrograph fibers. An advanced Exposure Meter system will be used to correct RadialVelocity (RV) obtained from the scientific spectrum for the Earth relative motion. In this work we will present the performance of an innovative concept for the Exposure Meter system based on a Charge Coupled Device (CCD) with a chromatic approach for the calculation of the Mean Time of Exposure (MTE). The MTE is a crucial quantity used for the correction of RV for the Earth relative motion during the exposure. In particular, splitting the light in different chromatic channels on the CCD, we will probe for potential chromatic effects on the calculation of the MTE in each channel and how they could be used in order to perform the correction of RV. The paper is accompanied by a fully described numerical analysis that keeps into view a key performance evaluation for different stellar spectral types (B to M spectral main sequence classes).

Title: ESPRESSO APSU: simplify the life of pupil slicing

Authors: Conconi, P.; Riva, M.; Pepe, F.; Zerbi, F. M.; Cabral, A.; Cristiani, S.; Megevand, D.; Landoni, M.; Span, P.

Publication: Proceedings of the SPIE, Volume 8842, id. 88420P 9 pp. (2013). (SPIE Homepage)

Publication Date: 09/2013

Origin: SPIE

Comment: ISBN: 9780819496928

DOI: 10.1117/12.2024843

Bibliographic Code: 2013SPIE.8842E..0PC

Abstract: This paper presents the Espresso Anamorphic pupil Slicer (APSU) implementation. ESPRESSO, the Echelle SPectrograph for Rocky Exoplanets and Stable Spectroscopic Observations, will be installed on ESOs Very Large Telescope (VLT). In this work we will present the design and trade-off for the pupil slicing system introduced in order to increase the resolving power, effectively decreasing slit width. Its based onto simplified optical component that introduce large anamorphism while keeping low aberrations by means of cylindrical optics. We describe here the trade-off between slicing through two adjacent squared doublets and two achromatic prisms.

References

- A. Baglin, M. Auvergne, L. Boisnard, T. Lam-Trong, P. Barge, C. Catala, M. Deleuil, E. Michel, and W. Weiss. CoRoT: a high precision photometer for stellar evolution and exoplanet finding. In *36th COSPAR Scientific Assembly*, volume 36 of *COSPAR Meeting*, page 3749, 2006. [7](#)
- K. Banse, D. Ponz, C. Ounnas, P. Grosbol, and R. Warmels. The MIDAS Image Processing System. In L. B. Robinson, editor, *Instrumentation for Ground-Based Optical Astronomy*, page 431, 1988. [26](#)
- A. Baranne, M. Mayor, and J. L. Poncet. CORAVEL - A new tool for radial velocity measurements. *Vistas in Astronomy*, 23:279–316, 1979. doi: 10.1016/0083-6656(79)90016-3. [8](#)
- T. Boroson. Blueshifted [O III] Emission: Indications of a Dynamic Narrow-Line Region. *AJ*, 130:381–386, August 2005. doi: 10.1086/431722. [141](#)
- A. Cabral, A. Moitinho, J. Coelho, J. Lima, G. Ávila, B.-A. Delabre, R. Gomes, D. Mégevand, F. Zerbi, P. Di Marcantonio, C. Lovis, and N. C. Santos. ESPRESSO: design and analysis of a Coudé-train for a stable and efficient simultaneous optical feeding from the four VLT unit telescopes. In *Society of Photo-Optical Instrumentation Engineers (SPIE) Conference Series*, volume 8444 of *Society of Photo-Optical Instrumentation Engineers (SPIE) Conference Series*, September 2012. doi: 10.1117/12.926093. [ix](#), [14](#), [15](#)
- J. A. Cardelli, G. C. Clayton, and J. S. Mathis. The relationship between infrared, optical, and ultraviolet extinction. *ApJ*, 345:245–256, October 1989. doi: 10.1086/167900. [108](#)

- H.-W. Chen, J. E. Helsby, J.-R. Gauthier, S. A. Smetman, I. B. Thompson, and J. L. Tinker. An Empirical Characterization of Extended Cool Gas Around Galaxies Using Mg II Absorption Features. *ApJ*, 714:1521–1541, May 2010. doi: 10.1088/0004-637X/714/2/1521. [162](#)
- W. D. Cochran and A. P. Hatzes. A high-precision radial-velocity survey for other planetary systems. *APSS*, 212:281–291, February 1994. doi: 10.1007/BF00984532. [8](#)
- C. W. Danforth, B. A. Keeney, J. T. Stocke, J. M. Shull, and Y. Yao. Hubble/COS Observations of the Ly α Forest Toward the BL Lac Object 1ES 1553+113. *ApJ*, 720:976–986, September 2010. doi: 10.1088/0004-637X/720/1/976. [170](#)
- R. Decarli, M. Dotti, and A. Treves. Geometry and inclination of the broad-line region in blazars. *MNRAS*, 413:39–46, May 2011. doi: 10.1111/j.1365-2966.2010.18102.x. [xv](#), [128](#), [129](#)
- A. Domínguez, J. R. Primack, D. J. Rosario, F. Prada, R. C. Gilmore, S. M. Faber, D. C. Koo, R. S. Somerville, M. A. Pérez-Torres, P. Pérez-González, J.-S. Huang, M. Davis, P. Guhathakurta, P. Barmby, C. J. Conselice, M. Lozano, J. A. Newman, and M. C. Cooper. Extragalactic background light inferred from AEGIS galaxy-SED-type fractions. *MNRAS*, 410:2556–2578, February 2011. doi: 10.1111/j.1365-2966.2010.17631.x. [143](#)
- R. Falomo. Host galaxy and close environment of BL Lacertae objects. *MNRAS*, 283:241–250, November 1996a. [xvi](#), [136](#), [138](#), [141](#), [142](#)
- R. Falomo. Host galaxy and close environment of BL Lacertae objects. *MNRAS*, 283:241–250, November 1996b. [98](#)
- R. Falomo, J. Melnick, and E. G. Tanzi. On the close environment of BL Lacertae objects. *Nature*, 345:692–694, June 1990. doi: 10.1038/345692a0. [143](#)
- R. Falomo, M. Bersanelli, P. Bouchet, and E. G. Tanzi. The optical to near-infrared emission of BL Lac objects - Simultaneous observations. *AJ*, 106:11–27, July 1993a. doi: 10.1086/116616. [136](#)

-
- R. Falomo, M. Bersanelli, P. Bouchet, and E. G. Tanzi. The optical to near-infrared emission of BL Lac objects - Simultaneous observations. *AJ*, 106:11–27, July 1993b. doi: 10.1086/116616. [98](#)
- R. Falomo, R. Scarpa, and M. Bersanelli. Optical spectrophotometry of blazars. *ApJ Supplement Series*, 93:125–143, July 1994a. doi: 10.1086/192048. [136](#)
- R. Falomo, R. Scarpa, and M. Bersanelli. Optical spectrophotometry of blazars. *ApJ Letters*, 93:125–143, July 1994b. doi: 10.1086/192048. [98](#)
- R. Falomo, R. Scarpa, A. Treves, and C. M. Urry. The Hubble Space Telescope Survey of BL Lacertae Objects. III. Morphological Properties of Low-Redshift Host Galaxies. *ApJ*, 542:731–739, October 2000. doi: 10.1086/317044. [98](#)
- J. H. Fan and R. G. Lin. Optical Variability and Periodicity Analysis for Blazars. I. Light Curves for Radio-selected BL Lacertae Objects. *ApJ*, 537:101–122, July 2000. doi: 10.1086/308996. [138](#)
- E. P. Farina, R. Decarli, R. Falomo, A. Treves, and C. M. Raiteri. The optical spectrum of PKS 1222+216 and its black hole mass. *MNRAS*, 424:393–398, July 2012. doi: 10.1111/j.1365-2966.2012.21209.x. [129](#)
- G. Ghisellini, A. Celotti, G. Fossati, L. Maraschi, and A. Comastri. A theoretical unifying scheme for gamma-ray bright blazars. *MNRAS*, 301:451–468, December 1998. doi: 10.1046/j.1365-8711.1998.02032.x. [96](#)
- P. Giommi, M. T. Menna, and P. Padovani. The sedentary multifrequency survey - I. Statistical identification and cosmological properties of high-energy peaked BL Lacs. *MNRAS*, 310:465–475, December 1999. doi: 10.1046/j.1365-8711.1999.02942.x. [100](#)
- P. Giommi, S. Piranomonte, M. Perri, and P. Padovani. X-ray/radio data of high energy peaked BL Lacs (Giommi+, 2005). *VizieR Online Data Catalog*, 343:40385, January 2005. [100](#)
- P. Giommi, P. Padovani, G. Polenta, S. Turriziani, V. D’Elia, and S. Piranomonte. A simplified view of blazars: clearing the fog around long-standing selection

- effects. *MNRAS*, 420:2899–2911, March 2012. doi: 10.1111/j.1365-2966.2011.20044.x. [170](#)
- P. Goldoni, F. Royer, P. François, M. Horrobin, G. Blanc, J. Vernet, A. Modigliani, and J. Larsen. Data reduction software of the X-shooter spectrograph. In *Society of Photo-Optical Instrumentation Engineers (SPIE) Conference Series*, volume 6269 of *Society of Photo-Optical Instrumentation Engineers (SPIE) Conference Series*, July 2006. doi: 10.1117/12.669986. [135](#)
- M. R. S. Hawkins, P. Veron, R. W. Hunstead, and A. M. Burgess. Two BL Lacertae objects discovered through their optical variability. *A&A*, 248:421–425, August 1991. [159](#)
- A. Heger and S. E. Woosley. Nucleosynthesis and Evolution of Massive Metal-free Stars. *ApJ*, 724:341–373, November 2010. doi: 10.1088/0004-637X/724/1/341. [18](#)
- A. Hewitt and G. Burbidge. A revised and updated catalog of quasi-stellar objects. *ApJ Supplement Series*, 87:451–947, August 1993. doi: 10.1086/191811. [101](#)
- S. Howell. *Handbook of CCD astronomy - Second edition*. 2006. [47](#)
- G. G. Kacprzak, C. W. Churchill, E. J. Barton, and J. Cooke. Halo Gas and Galaxy Disk Kinematics of a Volume-limited Sample of Mg II Absorption-selected Galaxies at $z \sim 0.1$. *ApJ*, 733:105, June 2011. doi: 10.1088/0004-637X/733/2/105. [143](#)
- S. Kaspi, D. Maoz, H. Netzer, B. M. Peterson, M. Vestergaard, and B. T. Jannuzi. The Relationship between Luminosity and Broad-Line Region Size in Active Galactic Nuclei. *ApJ*, 629:61–71, August 2005. doi: 10.1086/431275. [90](#), [94](#)
- A. L. Kinney, D. Calzetti, R. C. Bohlin, K. McQuade, T. Storchi-Bergmann, and H. R. Schmitt. Template Ultraviolet to Near-Infrared Spectra of Star-forming Galaxies and Their Application to K-Corrections. *ApJ*, 467:38, August 1996. doi: 10.1086/177583. [119](#), [164](#)

- D. G. Koch, W. Borucki, L. Webster, E. Dunham, J. Jenkins, J. Marriott, and H. J. Reitsema. Kepler: a space mission to detect earth-class exoplanets. In P. Y. Bely and J. B. Breckinridge, editors, *Society of Photo-Optical Instrumentation Engineers (SPIE) Conference Series*, volume 3356 of *Society of Photo-Optical Instrumentation Engineers (SPIE) Conference Series*, pages 599–607, August 1998. [7](#)
- A. Kolmogorov. The Local Structure of Turbulence in Incompressible Viscous Fluid for Very Large Reynolds' Numbers. *Akademiia Nauk SSSR Doklady*, 30: 301–305, 1941. [22](#)
- J. K. Kotilainen, R. Falomo, and R. Scarpa. The host galaxies of BL Lac objects in the near-infrared. *A&A*, 336:479–489, August 1998. [138](#)
- J. E. Krist, R. N. Hook, and F. Stoehr. 20 years of Hubble Space Telescope optical modeling using Tiny Tim. In *Society of Photo-Optical Instrumentation Engineers (SPIE) Conference Series*, volume 8127 of *Society of Photo-Optical Instrumentation Engineers (SPIE) Conference Series*, September 2011. doi: 10.1117/12.892762. [161](#)
- M. Landoni, R. Falomo, A. Treves, B. Sbarufatti, R. Decarli, F. Tavecchio, and J. Kotilainen. On the redshift of the bright BL Lacertae object PKS 0048-097. *A&A*, 543:A116, July 2012a. doi: 10.1051/0004-6361/201219114. [129](#)
- M. Landoni, M. Riva, F. M. Zerbi, D. Mégevand, A. Cabral, and S. Cristiani. ESPRESSO front-end guiding algorithm. In *Society of Photo-Optical Instrumentation Engineers (SPIE) Conference Series*, volume 8451 of *Society of Photo-Optical Instrumentation Engineers (SPIE) Conference Series*, September 2012b. doi: 10.1117/12.924980. [70](#)
- M. Landoni, R. Falomo, A. Treves, B. Sbarufatti, M. Barattini, R. Decarli, and J. Kotilainen. ESO Very Large Telescope Optical Spectroscopy of BL Lacertae Objects. IV. New Spectra and Properties of the Full Sample. *AJ*, 145:114, April 2013. doi: 10.1088/0004-6256/145/4/114. [xiv](#), [100](#), [101](#), [108](#)
- H. Landt, P. Padovani, E. S. Perlman, and P. Giommi. The Emission Line Properties of DXRBS Blazars. In P. Padovani and C. M. Urry, editors, *Blazar*

-
- Demographics and Physics*, volume 227 of *Astronomical Society of the Pacific Conference Series*, page 73, 2001. [98](#)
- H. Landt, P. Padovani, E. S. Perlman, and P. Giommi. A physical classification scheme for blazars. *MNRAS*, 351:83–100, June 2004. doi: 10.1111/j.1365-2966.2004.07750.x. [97](#)
- L. Lindegren and D. Dravins. The fundamental definition of “radial velocity”. *A&A*, 401:1185–1201, April 2003. doi: 10.1051/0004-6361:20030181. [58](#)
- L. Lindegren and M. A. C. Perryman. GAIA: Global astrometric interferometer for astrophysics. *A&A*, 116:579–595, May 1996. [7](#)
- D. Lutz, E. Sturm, R. Genzel, A. F. M. Moorwood, T. Alexander, H. Netzer, and A. Sternberg. ISO-SWS Spectroscopy of NGC 1068. *ApJ*, 536:697–709, June 2000. doi: 10.1086/308972. [xiii](#), [94](#), [95](#)
- M. Mayor and D. Queloz. A Jupiter-mass companion to a solar-type star. *Nature*, 378:355–359, November 1995. doi: 10.1038/378355a0. [8](#), [10](#)
- M. Mayor, A. Duquenooy, J.-L. Halbwachs, and J.-C. Mermilliod. CORAVEL Surveys to Study Binaries of Different Masses and Ages. In H. A. McAlister and W. I. Hartkopf, editors, *IAU Colloq. 135: Complementary Approaches to Double and Multiple Star Research*, volume 32 of *Astronomical Society of the Pacific Conference Series*, page 73, 1992. [8](#)
- M. Mayor, F. Pepe, D. Queloz, F. Bouchy, G. Rupprecht, G. Lo Curto, G. Avila, W. Benz, J.-L. Bertaux, X. Bonfils, T. Dall, H. Dekker, B. Delabre, W. Eckert, M. Fleury, A. Gilliotte, D. Gojak, J. C. Guzman, D. Kohler, J.-L. Lizon, A. Longinotti, C. Lovis, D. Megevand, L. Pasquini, J. Reyes, J.-P. Sivan, D. Sosnowska, R. Soto, S. Udry, A. van Kesteren, L. Weber, and U. Weilenmann. Setting New Standards with HARPS. *The Messenger*, 114:20–24, December 2003. [13](#), [73](#)
- M. T. Murphy, T. Udem, R. Holzwarth, A. Sismann, L. Pasquini, C. Araujo-Hauck, H. Dekker, S. D’Odorico, M. Fischer, T. W. Hänsch, and A. Manescau. High-precision wavelength calibration of astronomical spectrographs with laser

- frequency combs. *MNRAS*, 380:839–847, September 2007. doi: 10.1111/j.1365-2966.2007.12147.x. [14](#)
- R. Narayan and I. Yi. Advection-dominated accretion: A self-similar solution. *ApJ Letters*, 428:L13–L16, June 1994. doi: 10.1086/187381. [97](#)
- J. B. Oke. Faint spectrophotometric standard stars. *AJ*, 99:1621–1631, May 1990. doi: 10.1086/115444. [108](#)
- P. Padovani and P. Giommi. The connection between x-ray- and radio-selected BL Lacertae objects. *ApJ*, 444:567–581, May 1995. doi: 10.1086/175631. [100](#)
- M. V. Penston, A. Robinson, D. Alloin, I. Appenzeller, I. Aretxaga, D. J. Axon, T. Baribaud, P. Barthel, S. A. Baum, C. Boisson, A. G. de Bruyn, J. Clavel, L. Colina, M. Denefeld, A. Diaz, M. Dietrich, F. Durret, J. E. Dyson, P. Gondhalekar, E. van Groningen, P. Jablonka, N. Jackson, W. Kollatschny, E. Laurikainen, A. Lawrence, J. Masegosa, I. McHardy, E. J. A. Meurs, G. Miley, M. Moles, P. O’Brien, C. O’Dea, A. del Olmo, A. Pedlar, J. Perea, E. Perez, I. Perez-Fournon, J. Perry, G. Pilbratt, M. Rees, I. Robson, P. Rodriguez-Pascual, J. M. Rodriguez Espinosa, M. Santos-Lleo, R. Schilizzi, G. Stasińska, G. M. Stirpe, C. Tadhunter, E. Terlevich, R. Terlevich, S. Unger, V. Vila-Vilaro, J. Vilchez, S. J. Wagner, M. J. Ward, and G. J. Yates. The extended narrow line region of NGC 4151. I - Emission line ratios and their implications. *A&A*, 236:53–62, September 1990. [91](#)
- F. A. Pepe, S. Cristiani, R. Rebolo Lopez, N. C. Santos, A. Amorim, G. Avila, W. Benz, P. Bonifacio, A. Cabral, P. Carvas, R. Cirami, J. Coelho, M. Comari, I. Coretti, V. de Caprio, H. Dekker, B. Delabre, P. di Marcantonio, V. D’Odorico, M. Fleury, R. García, J. M. Herreros Linares, I. Hughes, O. Iwert, J. Lima, J.-L. Lizon, G. Lo Curto, C. Lovis, A. Manescau, C. Martins, D. Mégevand, A. Moitinho, P. Molaro, M. Monteiro, M. Monteiro, L. Pasquini, C. Mordasini, D. Queloz, J. L. Rasilla, J. M. Rebordão, S. Santana Tschudi, P. Santin, D. Sosnowska, P. Spanò, F. Tenegi, S. Udry, E. Vanzella, M. Viel, M. R. Zapatero Osorio, and F. Zerbi. ESPRESSO: the Echelle spectrograph for rocky exoplanets and stable spectroscopic observations. In *Society of Photo-Optical In-*

- strumentation Engineers (SPIE) Conference Series*, volume 7735 of *Society of Photo-Optical Instrumentation Engineers (SPIE) Conference Series*, July 2010. doi: 10.1117/12.857122. [12](#)
- B. Peterson. *An introduction to Active Galactic Nuclei*. 1997. [95](#), [96](#)
- A. J. Pica and A. G. Smith. Optical variability, absolute luminosity, and the Hubble diagram for QSOs. *ApJ*, 272:11–25, September 1983. doi: 10.1086/161257. [136](#)
- R. M. Plotkin, S. F. Anderson, W. N. Brandt, A. M. Diamond-Stanic, X. Fan, P. B. Hall, A. E. Kimball, M. W. Richmond, D. P. Schneider, O. Shemmer, W. Voges, D. G. York, N. A. Bahcall, S. Snedden, D. Bizyaev, H. Brewington, V. Malanushenko, E. Malanushenko, D. Oravetz, K. Pan, and A. Simmons. Optically Selected BL Lacertae Candidates from the Sloan Digital Sky Survey Data Release Seven. *AJ*, 139:390–414, February 2010. doi: 10.1088/0004-6256/139/2/390. [97](#), [170](#)
- T. A. Rector and J. T. Stocke. The Properties of the Radio-Selected 1 Jy Sample of BL Lacertae Objects. *AJ*, 122:565–584, August 2001. doi: 10.1086/321179. [98](#), [141](#)
- I. Ribas, A. Font-Ribera, and J.-P. Beaulieu. A $\sim 5 M_{\oplus}$ Super-Earth Orbiting GJ 436? The Power of Near-Grazing Transits. *ApJ*, 677:L59–L62, April 2008. doi: 10.1086/587961. [ix](#), [6](#)
- M. Riva, M. Landoni, F. M. Zerbi, D. Mégevand, A. Cabral, S. Cristiani, and B. Delabre. ESPRESSO front end opto-mechanical configuration. In *Society of Photo-Optical Instrumentation Engineers (SPIE) Conference Series*, volume 8446 of *Society of Photo-Optical Instrumentation Engineers (SPIE) Conference Series*, September 2012. doi: 10.1117/12.924978. [ix](#), [14](#), [16](#), [70](#)
- M. Sarazin, J. Melnick, J. Navarrete, and G. Lombardi. Seeing is Believing: New Facts about the Evolution of Seeing on Paranal. *The Messenger*, 132:11–17, June 2008. [23](#)

- B. Sbarufatti, A. Treves, and R. Falomo. Imaging Redshifts of BL Lacertae Objects. *ApJ*, 635:173–179, December 2005a. doi: 10.1086/497022. [97](#), [98](#), [118](#)
- B. Sbarufatti, A. Treves, R. Falomo, J. Heidt, J. Kotilainen, and R. Scarpa. ESO Very Large Telescope Optical Spectroscopy of BL Lacertae Objects. I. New Redshifts. *AJ*, 129:559–566, February 2005b. doi: 10.1086/427138. [108](#), [118](#), [119](#)
- B. Sbarufatti, A. Treves, R. Falomo, J. Heidt, J. Kotilainen, and R. Scarpa. ESO Very Large Telescope Optical Spectroscopy of BL Lacertae Objects. II. New Redshifts, Featureless Objects, and Classification Assessments. *AJ*, 132:1–19, July 2006. doi: 10.1086/503031. [xiv](#), [xvii](#), [100](#), [101](#), [108](#), [118](#), [119](#), [136](#), [145](#), [159](#), [165](#)
- B. Sbarufatti, S. Ciprini, J. Kotilainen, R. Decarli, A. Treves, A. Veronesi, and R. Falomo. European Southern Observatory Very Large Telescope Optical Spectroscopy of BL Lacertae Objects. III. An Extension of the Sample. *AJ*, 137:337–346, January 2009. doi: 10.1088/0004-6256/137/1/337. [108](#), [118](#)
- R. Scarpa and R. Falomo. Are high polarization quasars and BL Lacertae objects really different? A study of the optical spectral properties. *A&A*, 325:109–123, September 1997. [97](#)
- D. J. Schlegel, D. P. Finkbeiner, and M. Davis. Maps of Dust Infrared Emission for Use in Estimation of Reddening and Cosmic Microwave Background Radiation Foregrounds. *ApJ*, 500:525, June 1998. doi: 10.1086/305772. [108](#)
- W. Seifert, I. Appenzeller, W. Fuertig, O. Stahl, E. Sutorius, W. Xu, W. Gaessler, R. Haefner, H.-J. Hess, W. Hummel, K.-H. Mantel, W. Meisl, B. Muschielok, K. Tarantik, H. E. Nicklas, G. Rupprecht, C. Cumani, T. Szeifert, and J. Spyromilio. Commissioning of the FORS instruments at the ESO VLT. In M. Iye and A. F. Moorwood, editors, *Society of Photo-Optical Instrumentation Engineers (SPIE) Conference Series*, volume 4008 of *Society of Photo-Optical Instrumentation Engineers (SPIE) Conference Series*, pages 96–103, August 2000. [108](#)
- M. S. Shaw, R. W. Romani, G. Cotter, S. E. Healey, P. F. Michelson, A. C. S. Readhead, J. L. Richards, W. Max-Moerbeck, O. G. King, and W. J. Potter.

- Spectroscopy of Broad-line Blazars from 1LAC. *ApJ*, 748:49, March 2012. doi: 10.1088/0004-637X/748/1/49. [129](#)
- M. S. Shaw, R. W. Romani, G. Cotter, S. E. Healey, P. F. Michelson, A. C. S. Readhead, J. L. Richards, W. Max-Moerbeck, O. G. King, and W. J. Potter. Spectroscopy of the Largest Ever γ -Ray-selected BL Lac Sample. *ApJ*, 764:135, February 2013. doi: 10.1088/0004-637X/764/2/135. [159](#)
- Y. Shen, G. T. Richards, M. A. Strauss, P. B. Hall, D. P. Schneider, S. Snedden, D. Bizyaev, H. Brewington, V. Malanushenko, E. Malanushenko, D. Oravetz, K. Pan, and A. Simmons. A Catalog of Quasar Properties from Sloan Digital Sky Survey Data Release 7. *ApJ Supplement Series*, 194:45, June 2011. doi: 10.1088/0067-0049/194/2/45. [131](#)
- P. Spanò, B. Delabre, H. Dekker, F. Pepe, F. M. Zerbi, P. Di Marcantonio, S. Cristiani, and D. Mégevand. Very high-resolution spectroscopy: the ESPRESSO optical design. In *Society of Photo-Optical Instrumentation Engineers (SPIE) Conference Series*, volume 8446 of *Society of Photo-Optical Instrumentation Engineers (SPIE) Conference Series*, September 2012. doi: 10.1117/12.925947. [ix](#), [13](#), [61](#)
- M. Stickel, P. Padovani, C. M. Urry, J. W. Fried, and H. Kuehr. The complete sample of 1 Jansky BL Lacertae objects. I - Summary properties. *ApJ*, 374: 431–439, June 1991. doi: 10.1086/170133. [101](#)
- M. Stickel, J. W. Fried, and H. Kuehr. The complete sample of 1 Jy BL Lac objects. II - Observational data. *A&A*, 98:393–442, May 1993. [98](#), [136](#), [143](#)
- J. T. Stocke and T. A. Rector. An Excess of Mg II Absorbers in BL Lacertae Objects. *ApJ Letters*, 489:L17, November 1997. doi: 10.1086/310962. [98](#), [132](#), [133](#)
- O. Svelto. *Principles of lasers*. 2010. [24](#)
- F. Tavecchio, L. Maraschi, and G. Ghisellini. Constraints on the Physical Parameters of TeV Blazars. *ApJ*, 509:608–619, December 1998. doi: 10.1086/306526. [127](#), [143](#)

- F. Tavecchio, G. Ghisellini, G. Ghirlanda, L. Foschini, and L. Maraschi. TeV BL Lac objects at the dawn of the Fermi era. *MNRAS*, 401:1570–1586, January 2010. doi: 10.1111/j.1365-2966.2009.15784.x. [xvi](#), [143](#), [144](#)
- L. Ubeda and et al. *Advanced Camera for Surveys Instrument Handbook for Cycle 21 v. 12.0*. December 2012. [161](#)
- C. M. Urry and P. Padovani. Unified Schemes for Radio-Loud Active Galactic Nuclei. *PASP*, 107:803, September 1995. doi: 10.1086/133630. [96](#)
- C. M. Urry, R. Scarpa, M. O’Dowd, R. Falomo, J. E. Pesce, and A. Treves. The Hubble Space Telescope Survey of BL Lacertae Objects. II. Host Galaxies. *ApJ*, 532:816–829, April 2000. doi: 10.1086/308616. [98](#)
- M. Uslenghi and R. Falomo. AIDA: a software package for 2D model fitting analysis of astronomical images. In *Society of Photo-Optical Instrumentation Engineers (SPIE) Conference Series*, volume 8135 of *Society of Photo-Optical Instrumentation Engineers (SPIE) Conference Series*, September 2011. doi: 10.1117/12.913305. [162](#)
- J. Vernet, H. Dekker, S. D’Odorico, L. Kaper, P. Kjaergaard, F. Hammer, S. Randich, F. Zerbi, P. J. Groot, J. Hjorth, I. Guinouard, R. Navarro, T. Adolfse, P. W. Albers, J.-P. Amans, J. J. Andersen, M. I. Andersen, P. Binetruy, P. Bristow, R. Castillo, F. Chemla, L. Christensen, P. Conconi, R. Conzelmann, J. Dam, V. de Caprio, A. de Ugarte Postigo, B. Delabre, P. di Marcantonio, M. Downing, E. Elswijk, G. Finger, G. Fischer, H. Flores, P. François, P. Goldoni, L. Guglielmi, R. Haigron, H. Hanenburg, I. Hendriks, M. Horrobin, D. Horville, N. C. Jessen, F. Kerber, L. Kern, M. Kiekebusch, P. Kleszcz, J. Klougart, J. Kragt, H. H. Larsen, J.-L. Lizon, C. Lucuix, V. Mainieri, R. Manuputy, C. Martayan, E. Mason, R. Mazzoleni, N. Michaelsen, A. Modigliani, S. Moehler, P. Møller, A. Norup Sørensen, P. Nørregaard, C. Péroux, F. Patat, E. Pena, J. Pragt, C. Reinero, F. Rigal, M. Riva, R. Roelfsema, F. Royer, G. Sacco, P. Santin, T. Schoenmaker, P. Spano, E. Sweers, R. Ter Horst, M. Tintori, N. Tromp, P. van Dael, H. van der Vliet, L. Venema, M. Vidali, J. Vinther, P. Vola, R. Winters, D. Wistisen, G. Wul-

-
- terkens, and A. Zacchei. X-shooter, the new wide band intermediate resolution spectrograph at the ESO Very Large Telescope. *A&A*, 536:A105, December 2011. doi: 10.1051/0004-6361/201117752. [134](#)
- M.-P. Veron-Cetty and P. Veron. Spectroscopic observations of sixteen BL Lacertae candidates. *A&A*, 100:521–529, September 1993. [98](#)
- M.-P. Véron-Cetty and P. Véron. A catalogue of quasars and active nuclei: 11th edition. *A&A*, 412:399–403, December 2003. doi: 10.1051/0004-6361:20034225. [101](#)
- B. J. Wills, D. Wills, M. Breger, R. R. J. Antonucci, and R. Barvainis. A survey for high optical polarization in quasars with core-dominant radio structure - Is there a beamed optical continuum? *ApJ*, 398:454–475, October 1992. doi: 10.1086/171869. [136](#)
- A. Wolszczan and D. A. Frail. A planetary system around the millisecond pulsar PSR1257 + 12. *Nature*, 355:145–147, January 1992. doi: 10.1038/355145a0. [8](#)
- G. Zhu and B. Ménard. The JHU-SDSS Metal Absorption Line Catalog: Redshift Evolution and Properties of Mg II Absorbers. *ApJ*, 770:130, June 2013. doi: 10.1088/0004-637X/770/2/130. [xv](#), [132](#), [133](#)

Acknowledgements

Only formal

I would like to thank all of my supervisors (rigorously only in alphabetic order) Renato Falomo, Aldo Treves and Filippo Zerbi who followed and helped me from the first day to the end of this long journey. It is also a pleasure to thank all the other people in OABr Merate while a special mention goes to Marco Riva for all of our long discussion and the overall support. I am also grateful to Paolo Di Marcantonio (OATs) for the careful reading of a significant part of this manuscript. Moreover, I have to be indebt with Francesco Pepe (Geneva Observatory) for the extremely professionalism in his review of the Thesis as commissary. His fruitful comments greatly helped to improve the quality of my work. Next, many thanks goes also to the other astrophysics students in Como (especially to Emanuele and Angela) and obviously I could not forget all my friends that supported me during these 9 years. Finally, I thank my family and parents for their continuos and unconditioned support.